

---

Concentration polarization enabled hydrogel coating of desalination  
membranes using crosslinkable zwitterionic polymeric building blocks

---

**Dissertation**

zur Erlangung des akademischen Grades

Doktor der Naturwissenschaften

Doctor rerum naturalium

(Dr. rer. nat.)

Fakultät für Chemie der  
Universität Duisburg-Essen

von

**Patrick May**

geboren

in Kamen

Essen, 2020

# DuEPublico

Duisburg-Essen Publications online

UNIVERSITÄT  
DUISBURG  
ESSEN

*Offen im Denken*

ub | universitäts  
bibliothek

Diese Dissertation wird über DuEPublico, dem Dokumenten- und Publikationsserver der Universität Duisburg-Essen, zur Verfügung gestellt und liegt auch als Print-Version vor.

**DOI:** 10.17185/duepublico/71985

**URN:** urn:nbn:de:hbz:464-20200708-095713-9

Alle Rechte vorbehalten.

Tag der Disputation: 17.06.2020

Gutachter: Universitätsprofessor Dr. Mathias Ulbricht

Universitätsprofessor Dr. Stefan Panglisch

Vorsitzender: Universitätsprofessor Dr. Christian Mayer



Die vorliegende Arbeit wurde in der Zeit von April 2016 bis Juni 2019 am Lehrstuhl für Technische Chemie II von Herrn Prof. Dr. Mathias Ulbricht in der Fakultät für Chemie der Universität Duisburg-Essen angefertigt.

Hiermit versichere ich, dass ich die vorliegende Arbeit selbst verfasst und keine außer den angegebenen Hilfsmitteln und Quellen benutzt habe. Des Weiteren wurde die Arbeit in dieser oder ähnlicher Form noch bei keiner anderen Universität eingereicht.

Patrick May



## Acknowledgments

Worte zu verfassen ist ein bescheidener Versuch, Gefühle der Dankbarkeit auszudrücken. Dennoch hoffe ich, dass diese Zeilen die Leser dort erreichen, wo dies beabsichtigt ist.

Vielen Dank Prof. Ulbricht – Sie hatten es sicher nicht immer leicht mit mir, dennoch haben Sie mich stets sachlich und geduldig bei diesem Unterfangen unterstützt. Ohne Ihre konstruktive Art wäre diese Arbeit nicht möglich gewesen. Ich habe es genossen, mit Ihnen Gespräche zu führen und immer wieder Neues zu lernen. Dankbar bin ich auch, dass Sie es mir ermöglicht haben, meine Arbeit im Ausland vorzustellen. Sie sind ein Vorbild für mich geworden und ich kann mich glücklich schätzen, bei Ihnen promoviert zu haben.

Prof. Panglisch danke ich für die Übernahme des Koreferats. Ich habe auch mit Ihrem Arbeitskreis angenehme und großartige Erfahrungen gemacht und möchte Ihnen für die gemeinsame Zeit danken.

Danke an Prof. Mayer für die Übernahme des Prüfungsvorsitzes.

Ein großer Teil der Arbeit resultiert aus der Unterstützung durch Master und Bachelorabsolventen – Philipp Jahn, Didem Denizer, Marcel Kaufmann, Marcel Matthias, Dimitri Vorrat, Katrin Stamer, Niko Brodt, Wanyu Wang – Euch allen möchte ich für eure großartige Arbeit danken. Es hat mir viel Freude bereitet, gemeinsam mit euch zu arbeiten. Ich habe viel von euch gelernt!

Ein großer Dank geht ebenfalls an alle TCII Promovierenden – besonders an Derek Koch, Soraya Laghmari, Mohamed ElLeithy, Qirong Ke, Ibrahim ElSherbiny, Ahmed Abdelsamad – Ihr wart nicht nur für fachliche Ratschläge oder Korrekturen zu haben, sondern auch immer zwischenmenschlich eine Bereicherung für mein Leben – Danke dafür!

Danke auch an Tobias Kallweit, Inge Danielzik und Jackelyn Aragon-Gomez – Ihr wart euch nie zu schade zu helfen!

Wenn eine Freundschaft mehr als 7 Jahre hält, hält sie ein Leben, heißt es – In diesem Sinne Danke an dich, Adnan. Du bist ein Freund, dem ich unbegrenzt vertraue. Danke für das Begleiten durch diesen Lebensabschnitt.

Danke auch an dich, Kevin. Du hast eine positiv-verrückte Natur und ich glaube, da haben wir vieles gemeinsam. Wer weiß, was daraus noch wird.

Dr. Boukercha möchte Ich für die Aufnahme der REM-Bilder danken. Die Gespräche mit Ihnen waren immer angenehmer und abwechslungsreicher Natur.

Dr. Schaller und Dr. Niemann möchte Ich für die Aufnahme der NMR-Proben und interessante Diskussion danken.

Danke auch an euch Basti, Nam, Hassan, Jetmir und Armin – Egal welche Atmosphäre ich mitgebracht habe, eure Zeit für Worte und Ablenkungen waren sehr wertvoll für mich und haben stets meinen Horizont erweitert.

Ich bedanke mich bei Mama und Papa. Ohne euch wäre diese Zeit so nie möglich gewesen. Eure liebevolle, an mich glaubende Unterstützung hat mich immer begleitet und mir oft in zweifelnden Momenten während des gesamten Studiums Kraft geschenkt. Ihr habt einen großen Anteil am Erfolg!

Der größte Dank geht an meine Liebe – ohne dich wäre ich nichts, mein Herz. Du hast mich, in der nicht immer leichten Zeit, unterstützt und mir trotz meiner teilweisen sehr anstrengenden Launen viel Vertrauen entgegengebracht.

## Abstract

Although membrane-based separations became tailor-made for several applications in recent years, they still suffer from limited separation performance, i.e. the relation between permeability and selectivity and are also highly affected by fouling processes. Fouling can be generally divided into three categories, namely biofouling, colloidal fouling (especially by natural organic matter) and inorganic fouling (scaling). Besides operational conditions as well as feed water and foulant characteristics, membrane properties are a crucial factor for fouling mechanisms. Despite that many membrane functionalizations show improved anti-fouling behavior, their application is still limited to lab-scale or implementation during membrane fabrication.

This project therefore focuses on surface-selective, reactive anti-fouling hydrogel coatings, which were applied in situ to nanofiltration membranes. To obtain such protective layer systems, first free radical polymerization of a zwitterionic copolymeric building block, which can be crosslinked to a hydrogel on surfaces by using a second crosslinkable functionality, was established with molecular weights in the range of 60-100 kDa. The gelation reaction of zwitterionic copolymer was initiated and studied in presence of radical initiator system (APS and TEMED) in free bulk. Critical gelation concentration was found to be above 5 wt.% and gelation time was in the range of 1-25 minutes, decreasing with higher polymer and initiator concentration.

To apply such a zwitterionic hydrogel coating onto membranes, concentration polarization was utilized. According to the film model, filtration through a membrane will lead to a concentration gradient of retained substances, resulting from a balance of convective and diffusive mass transport. Thus, dead end filtration of crosslinkable building blocks and redox-initiator system, which were rejected by nanofiltration membranes (NF90 and NF270), lead to an increase of concentration at the membrane surface and enabled modification of membranes when critical concentrations were exceeded at the membrane surface. Additionally, the extent of concentration polarization during modification was modelled in order to discuss gelation in boundary layer and allow comparison to free bulk gelation conditions.

Furthermore, the gelation reaction at membrane surface and its impact on membrane performance was studied in dependence of polymer and initiator feed concentration as well as filtration/reaction time. First, below a critical APS feed content (APS<0.06 wt%) gelation was

not initiated. Moreover, results indicate that at low polymer feed concentrations ( $>0.005$  wt.%) only dense gelation in NF90 membrane hot-spots may occur, causing strong decline of permeability ( $\sim 50\%$ ) without showing beneficial anti-fouling properties. Above this threshold concentration, hydrogel layers covered membrane surface completely. Furthermore, hydrogel layer thicknesses could be adjusted in NF270 membrane modification by higher polymer concentration and filtration time. For example, modifications performed below 15 minutes, resulted in layer thicknesses thinner than 100 nm and decreased membrane permeability only up to about 15%. Increasing filtration time to 40 minutes, lead to hydrogel layer thicknesses of approximately  $2\mu\text{m}$  and a reduction in permeability up to 80%. Finally, hydrogel modified NF270 membranes showed higher permeability during protein filtration experiments compared to unmodified membranes.

## List of contents

Acknowledgments .....	i
Abstract .....	iii
1 Introduction .....	1
2 Theoretical background.....	3
2.1 Membrane processes .....	3
2.1.1 Membrane transport .....	4
2.1.2 Pore-flow model.....	5
2.1.3 Solution-diffusion model.....	7
2.1.4 Donnan effect and dielectric exclusion .....	8
2.2 Polyamide TFC membranes .....	9
2.3 Membrane fouling .....	10
2.3.1 Colloidal fouling .....	12
2.3.2 Organic fouling .....	13
2.3.3 Inorganic fouling .....	14
2.3.4 Biofouling.....	15
2.4 Concentration polarization .....	15
2.5 Anti-fouling strategies.....	18
2.6 Zwitterionic polymers .....	20
2.6.1 Anti-fouling properties .....	23
2.7 Hydrogels .....	25
2.7.1 Structure .....	25
2.7.2 Anti-fouling properties .....	27
2.7.3 Transport through and resistance of hydrogels .....	30
2.8 Zwitterionic hydrogel membrane surface modifications .....	32
2.8.1 Zwitterionic hydrogels .....	32
2.8.2 Membrane surface modifications .....	35

3 Scope of the work.....	39
3.1 Concept.....	39
3.2 Goals.....	40
3.3 Work plan.....	41
4 Materials and methods .....	45
4.1 Chemicals and membrane materials.....	45
4.2 Polymer synthesis.....	46
4.2.1 Free radical copolymerization of DMAEMA and HEMA.....	46
4.2.2 Acrylation of P(DMAEMA-co-HEMA).....	47
4.2.3 Sulfobetainization of P(DMAEMA-co-MAMMA).....	47
4.2.4 Quaternization of P(DMAEMA-co-MAMMA).....	48
4.3 Polymer characterization.....	48
4.3.1 NMR spectroscopy.....	48
4.3.2 Size exclusion chromatography (SEC) .....	49
4.4 Polymer in solution .....	51
4.4.1 Polymer solubility .....	51
4.4.2 Viscosity measurements.....	51
4.4.3 Dynamic light scattering .....	52
4.5 Free bulk gelation.....	53
4.6 Membrane performance and modification .....	54
4.6.1 Pretreatment .....	54
4.6.2 Surface linker adsorption .....	55
4.6.3 Membrane modification and modified membranes' permeability .....	56
4.6.4 Critical and limiting flux .....	57
4.7 Calculation of concentration polarization .....	58
4.7.1 Estimation of boundary layer thickness .....	58
4.7.2 Estimation of dynamic CP.....	59
4.8 Membrane fouling.....	62

4.8.1 Protein adsorption .....	62
4.8.2 Protein filtration .....	62
4.9 Membrane characterization .....	63
4.9.1 Scanning electron microscopy .....	63
4.9.2 Attenuated total reflection infrared spectroscopy (ATR-IR) .....	63
4.9.3 Zeta potential.....	64
4.9.4 Contact angle measurement .....	66
5 Results .....	67
5.1 Free radical copolymerization.....	67
5.1.1 Characterization of P(DMAEMA-co-HEMA).....	67
5.1.2 Determination of conversion and polymerization rate .....	68
5.1.3 Influence of initiator concentration on molecular weight .....	71
5.1.4 Influence of monomers' concentration on molecular weight of resulted copolymers .....	75
5.2 Polymer functionalization .....	77
5.2.1 Introducing crosslinkable methacrylate groups.....	77
5.2.2 Sulfobetainization.....	78
5.2.3 Quaternization .....	79
5.3 Polymer in solution .....	82
5.3.1 Solubility behavior .....	82
5.3.2 Size analysis .....	83
5.3.3 Viscosity.....	88
5.4 Free Bulk gelation .....	91
5.4.1 Kinetics.....	91
5.4.2 Mechanical properties .....	95
5.4.3 Free bulk gelation summary .....	99
5.5 In situ NF90 membrane modification .....	100
5.5.1 Pristine membrane characteristics .....	100

5.5.2 Membrane modification .....	100
5.5.3 Membrane fouling .....	107
5.5.4 Zwitterionic hydrogel modified NF90 membrane characteristics.....	111
5.5.5 NF90 membrane modification summary.....	114
5.6 In situ NF270 membrane modification .....	115
5.6.1 Pristine membrane characteristics .....	115
5.6.2 Membrane modification .....	116
5.6.3 Hydraulic resistance and Darcy permeabilities .....	135
5.6.4 Membrane fouling .....	139
5.6.5 Discussion of CP model .....	141
5.6.6 Zwitterionic hydrogel modified NF270 membrane characteristics.....	144
5.6.7 NF270 membrane modification summary.....	147
6 Conclusion.....	149
7 Outlook.....	151
8 Literature .....	154
9 Appendix .....	161
9.1 List of figures .....	161
9.2 List of tables .....	167
9.3 List of abbreviations.....	168
9.4. List of equations .....	170
9.5 List of Symbols .....	172

# 1 Introduction

Around 70% of earth's surface is covered by water, hence it is also commonly known as the blue planet. However, most of that water is contained in oceans and seas as salt water or stored in frozen form in ice caps and glaciers. The amount of easily accessible freshwater found in groundwater, lakes, and rivers is limited to around 1-3%.<sup>1</sup>

Therefore, scarcity of freshwater resources presents a major global challenge in the 21<sup>st</sup> century towards sustaining life and economy. Current reports indicate that one third of world's population is facing temporary water stresses over the year.<sup>2</sup> The demand for freshwater supplies is expected to increase since world population is growing by ~80 million people per year, in addition to other global threats to freshwater sources, e.g., industrialization and climate change.<sup>3</sup> By 2025, it is assumed that almost two thirds of world's population will live temporarily in water stressed regions.<sup>4</sup> Hence, to tackle water scarcity problem is essential to maintain global stability and public health as well as to preserve biodiversity.<sup>5</sup>

Several international policies, regulations and plans have been set to control freshwater resources treatment, transportation and consumption. Innovative and low cost new separation technologies are crucial to properly address freshwater shortage and improve the access to drinkable water. Tremendous efforts have been devoted to offer new freshwater resources; a very promising and well-developed example is water desalination. Inspired by nature, nowadays science and industry focus primarily on the improvement of membrane technology to desalinate water from oceans or treat contaminated freshwater resources.<sup>6,7</sup>

In general, a membrane represents a semi-permeable barrier between two liquid or gaseous phases. Separation is achieved since non-permeable substances are retained, while permeable substances, e.g., water or other solvents can pass through the membrane. Unlike conventional water desalination techniques, e.g., distillation and crystallization, pressure driven membrane-based technologies are less energy consuming and potentially more attractive. Further advantages including excellent separation, efficiency, feed water tailor-made processes, and high quality water, make membrane-based separation process a key technology for overcoming freshwater shortage.<sup>8</sup>

The most promising approaches are reverse osmosis (RO) and nanofiltration (NF). These processes use membranes that possess very small pore-sizes in thin, active separation layers, ultimately allowing separation of ions while maintaining a high water flux. Recent progress

during last decades, made RO plants the most energy efficient desalination technology, compared to thermal separation techniques.<sup>9</sup>

However, such thin-film composite (TFC) membranes are facing two major obstacles. First, TFC membranes exhibit a trade-off between permeability and selectivity.<sup>10</sup> While permeability describes the permeation rate through the membrane, selectivity deals with the capacity of a membrane to separate two or more different species. Usually materials that are more selective are less permeable and vice versa.<sup>11</sup>

Additionally, RO membranes are subjected to fouling phenomena that is usually caused by the accumulation of retained substances on membrane surface. The blocking of permeation channels causes a decay in membrane performance; accordingly, more energy is needed to maintain permeability and RO plant productivity. High energy demands, pretreatment procedures, as well as periodic modules replacement increase the operation costs.<sup>12</sup>

Hence, membrane fouling creates environmental and economic incentives to develop more advanced membrane technologies with improved anti-fouling properties. The number of publications focusing on anti-fouling research has increased exponentially during the last decade, improving our understanding of fouling phenomena and creating strategies to manipulate membrane surface characteristics.<sup>13</sup>

Promising anti-fouling behavior has been demonstrated for hydrophilic surfaces, which show resistance towards organic matter and biofouling. In particular, zwitterionic structures are now in the core of development of new anti-fouling coatings/materials, which is owing to their ability to form strong hydrogen bonds with water while maintaining low surface energy. Their unique combination of properties can inhibit non-specific adsorption, making zwitterionic surface chemistry a promising and attractive approach to create novel anti-fouling surfaces.<sup>14, 15</sup>

Although several surface functionalization approaches have already demonstrated improved anti-fouling behavior, their application in industrial scale is limited to modification during membrane fabrication. This project aims at establishing a reactive polyzwitterionic, anti-fouling layer, which can be applied in situ during filtration processes inside membrane modules and thus, avoid manufacturing process changes and make use of already existing modules.

## 2 Theoretical background

### 2.1 Membrane processes

A membrane acts as a barrier between two fluid phases and allows separation of substances in the size range from a fraction of a few nanometers, like ions or molecules with low molecular weights, or to several micrometers, like bacteria and algae. Mass transport and exchange between two separated liquids is generally induced by differences in chemical potential, which is comprised of gradients in concentration, pressure, temperature and electrical potential.

However, transport in fluid membrane separations is mainly driven by pressure differential between feed and permeate side and hence are less energy consuming than thermal separation processes.<sup>16</sup> Both, the broad separation spectra as well as economic reasons, allow membrane technologies to cover a wide range of industrial and medical applications, varying from water desalination and purification of food products to hemodialysis and drug delivery systems.<sup>16</sup>

While membrane materials are not limited to polymers, this chapter will mainly focus on synthetic polymeric membranes. Generally, membrane types can be characterized by their average pore size or their cross-section morphology. Pore diameter characterization allows differentiation between microfiltration (MF), ultrafiltration (UF), nanofiltration (NF) and reverse osmosis (RO) membranes as illustrated in Fig. 2.1.

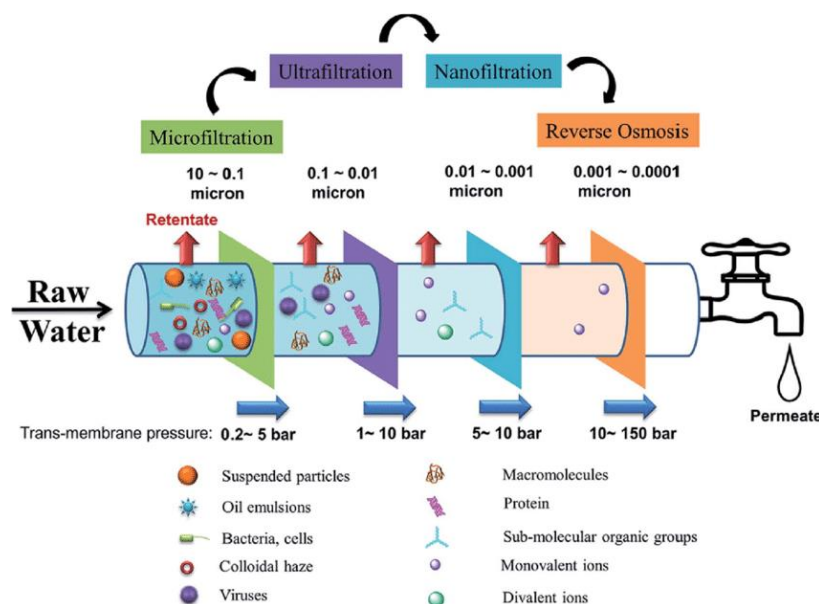


Figure 2.1 Pressure driven membrane processes and their characteristic separation range.<sup>17</sup>

Microfiltration separation processes usually target to sieve colloidal particles and bacteria in the range of 0.1 to 10  $\mu\text{m}$ . UF membranes filter smaller organic molecules like proteins and

viruses in the range of 2 to 100 nm. For separation of divalent ions and molecules up to 2 nm, NF is used, while RO membranes are able to retain monovalent ions.

Another typical characterization is determined by membrane cross-section morphology. Thereby, the membrane can be categorized along with two types: symmetric and asymmetric. Symmetric or isotropic membranes show a homogenous porous structure across their cross-section and possess a uniform chemical composition. Typical isotropic membranes are microporous filter used in UF or MF, dense and non-porous materials are used for gas separation and electrically charged membranes.<sup>16</sup>

Asymmetric or anisotropic membranes exhibit a heterogeneous cross-section morphology or are made of different polymer materials. They usually have a layered structure, e.g., thin-film composite membranes, with an ultrathin selective layer. Such membranes demonstrate high performance since hydraulic resistance, and consequently, permeation rate is inversely proportional to active layer thickness. Hence, anisotropic membranes are commonly employed in the industry by virtue of their superior performance properties.<sup>16, 18</sup>

#### 2.1.1 Membrane transport

This section introduces an overview on permeation and selection mechanisms in membrane processes. Two basic models are used to describe permeation through a membrane, known as Pore-flow and Solution-diffusion models. Furthermore, Coulomb-based mechanisms, so-called Dielectric effect and Donnan exclusion, between charged membranes and ions will be explained.

In general, mass transport through a membrane is derived by a difference in chemical potential between feed and permeate side, while permeation rate is influenced by membranes structural parameters, e.g., pore size distribution, porosity and tortuosity. Chemical potential can be expressed as a function of various driving forces such as pressure, concentration and electrical potential gradient across the membrane. However, pressure is most commonly applied in membrane processes to induce flux.<sup>16</sup> Flux through a membrane can thus be described by equation 2.1:

$$J = P \frac{\Delta p}{l} \quad (2.1)$$

Where  $P$  is membrane permeability coefficient,  $\Delta p$  is the transmembrane pressure difference across the membrane,  $J$  is transmembrane flux, and  $l$  is active layer thickness.

### 2.1.2 Pore-flow model

In porous membranes, pores are assumed to be cylindrical channels and hence flux through a pore can be described via Hagen-Poiseuille equation:

$$\dot{V} = \frac{\pi r^4 \Delta p}{8 \eta l} \quad (2.2)$$

Where  $\dot{V}$  is volume flow,  $r$  is radius of channel,  $\Delta P$  pressure difference,  $\eta$  is viscosity and  $l$  is channel length.

Nevertheless, due to the heterogeneous nature of most of porous membranes, no unified theory can describe mass transport through the membrane accurately. In addition, different membrane materials possess different chemical nature, i.e., hydrophilic, hydrophobic or charged membranes, which influence membrane-solvent interactions. Thus, structural parameters were found to be crucial for interpreting transport in porous membranes. Fundamental structural properties are depicted in Fig. 2.2.

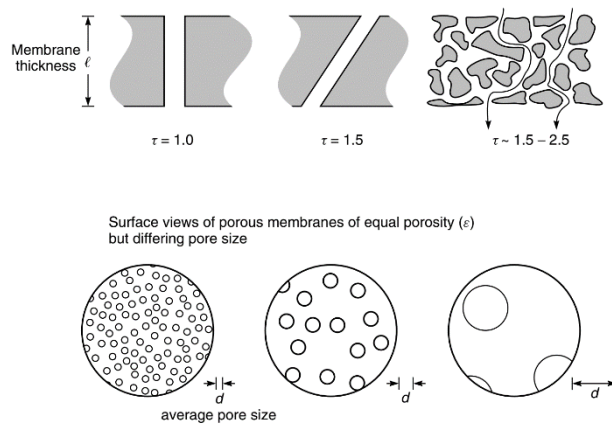


Figure 2.2 Schematic representation of membrane tortuosity (top), porosity and pore size (bottom).<sup>16</sup>

The tortuosity of a membrane describes the ratio of pore length to selective layer thickness and is usually between 1.5 and 2.5. When tortuosity is low, molecules permeate quicker, due to shorter channel length. Membrane porosity reflects the void volume compared to the total bulk volume of a membrane and is in the range of 0.3 to 0.8. While higher porosity allows more molecules to permeate, it also decreases mechanical stability.<sup>16</sup>

In an ideal membrane, pores would be distributed and sized evenly, accordingly, flux of a porous membrane could be therefore predicted by a capillary, porosity considering Hagen-Poiseuille equation:

$$J = \frac{\varepsilon_{mem} d_p^2 \Delta p}{32 \eta l} \quad (2.3)$$

However, calculation of mass transport is even further complicated due to irregular pore shapes and connectivity.<sup>19</sup>

Membrane selectivity is also mainly dependent on pore diameter and its distribution. In the pore flow model, retention of a membrane can be explained by size exclusion effects. Solutes are impermeable, if their size is bigger than the biggest pore diameter of the membrane, see Fig. 2.3. This separation mechanism is called screening effect since compounds are filtered at the membrane surface.<sup>16</sup>

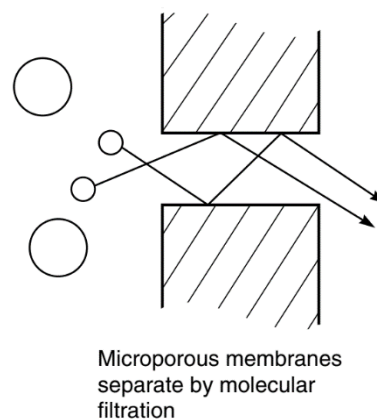


Figure 2.3 Size exclusion mechanism in a porous membrane.<sup>16</sup>

Furthermore, different separation phenomena take place when compounds are captured or adsorbed at the membrane-fluid interface. This depth filtration mechanism occurs when solutes are small enough to enter the membrane, but they are hindered from permeating completely because of four scenarios, see Fig. 2.4.<sup>16</sup> Briefly, in addition to regular sieving mechanism in deeper membrane structures, solutes may be captured inside membrane pores by either inertial effect, Brownian diffusion or electrostatic adsorption/adhesion.

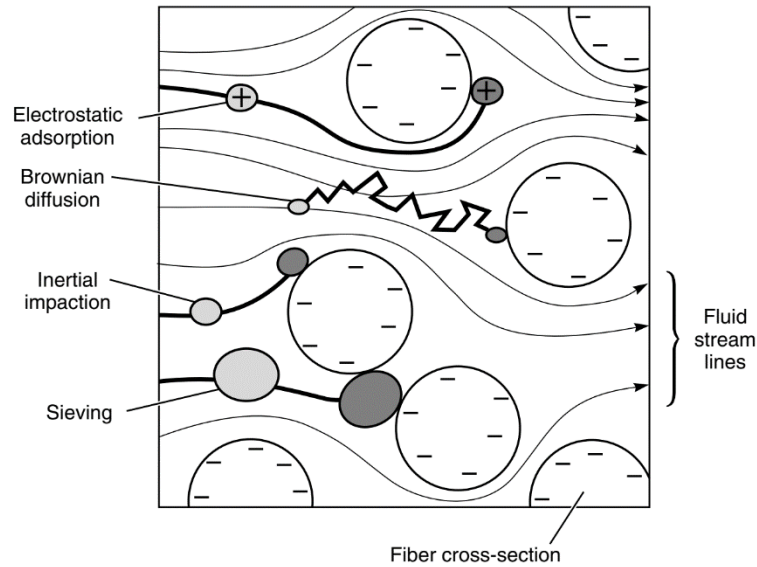


Figure 2.4 Capture mechanisms inside a membrane.<sup>16</sup>

### 2.1.3 Solution-diffusion model

In contrast, dense polyamide (PA) films, present in RO and NF membranes, exhibit different transport and separation mechanism, involving solubility and diffusion mechanisms.

First, solutes are adsorbed at the membrane surface and dissolve into the non-porous layer, before molecular diffusion occurs. Subsequently, solutes enter into free small volumes or cavities existing in the dense polymer film with sizes are up to 0.6 nm and then diffuse through polymer matrix. Finally, when solutes reach the barrier at permeate side, they are desorbed from membrane polymer. Hence, this transport mechanism is commonly called solution-diffusion model.<sup>16</sup>

Since diffusion through the membrane is the flux determining process (ad- and desorption rate are much faster), and is induced by a concentration gradient between two phases, it can be described by Fick's Law given in equation 2.4:

$$J_i = -D_i \frac{dc_i}{dx_i} \quad (2.4)$$

As described in section 2.1.1, the transport through a membrane is induced by difference in chemical potential between feed and permeate side. However, for water no concentration gradient exists and hence transport is solely driven by pressure difference. Water flux can thus be mathematically described with following equation:

$$J_{water} = A_m(\Delta p - \Delta\mu) \quad (2.5)$$

With  $A_m$  as water permeability constant,  $\Delta p$  transmembrane pressure difference,  $\Delta\mu$  osmotic pressure difference across the membrane.

In contrast, salt concentrations between feed and permeate differ due to rejection of ions by the membrane layer. Salt flux is therefore pressure independent and can be described by concentration differences, as shown in equation 2.6:

$$J_{salt} = B_m(c_f - c_p) \quad (2.6)$$

With  $J_{salt}$  as salt flux,  $B_m$  as salt permeation constant,  $c_f$  as salt concentration in feed and  $c_p$  as salt concentration in permeate.

Based on these equations, the solution-diffusion model decouples salt and water permeation, and membrane performance could therefore be enhanced by higher pressure differentials. Although understanding based on solution-diffusion is simplified and advanced theories regard salt and water transport coupled, solution diffusion model is often sufficient to quantify mass transport through a selective dense layer.<sup>16, 20</sup>

#### 2.1.4 Donnan effect and dielectric exclusion

Charged membranes, exemplary for NF/RO polyamide barriers, exhibit a further partitioning mechanism, based on Coulomb repulsion. A polymer film with fixed charges in its structure will cause a potential difference at the fluid and membrane interface when exposed to an electrolyte solution. This is known as Donnan potential and results in an additional separation mechanism.<sup>21, 22</sup>

First, counter ions from bulk will adsorb at the membrane surface due to attractive electrostatic Coulomb forces, in order to balance net charge. Therefore, concentration of both counter-and co-ions will be unequal in bulk solution and membrane phase. This imbalance of charges will result in a potential difference at solid-liquid interfaces, generating Donnan potential. Subsequently, when a water flux is induced through the membrane, co-ions will be repelled due to Coulomb repulsion forces. Additionally, in order to sustain charge balance at the feed side, counter-ions will also be rejected. This repulsion mechanism is called Donnan exclusion.<sup>22</sup>

However, when feedwater contains a mixture of impermeable divalent and permeable monovalent salt, e.g.  $\text{Na}_2\text{SO}_4$  and  $\text{NaCl}$ , also negative retention (higher ion concentration in permeate than in feed) may occur and is utilized in water softening processes. Divalent ions ( $\text{SO}_4^{2-}$ ) will be rejected, and in order to maintain charge neutrality, monovalent ions with same charge ( $\text{Cl}^-$ ) are encouraged to permeate through the membrane.<sup>23</sup>

However, high rejection values, especially for multivalent ions, cannot be explained solely by Donnan exclusion. Hence, the influence of another charge effect, so-called Dielectric exclusion, is causing separation of electrolytes. Ions in contact with highly polarizable solvents, e.g., water, may cause orientation of solvent molecules resulting in same charge polarization sign. Since ions will also interact with the barrier layer, which possesses a much lower dielectric constant, the interaction at the interface between hydrated ions and ions accumulated at the interface will always be repulsive, independent of its sign.<sup>24, 25</sup> The magnitude of this effect is a function of ion valence, dielectric constant and pore geometry. Consequently, NF membranes allow the rejection of ions, with sizes lower than membranes' average pore size.<sup>26, 27</sup>

## 2.2 Polyamide TFC membranes

TFC NF and RO membranes are nowadays dominating the water desalination market. Such membranes typically comprise three different layer structures:<sup>28</sup>

- a) non-woven polyester, which introduces mechanical stability (120-150  $\mu\text{m}$  in thickness)
- b) asymmetric UF/MF micro/macroporous polysulfone (40-50  $\mu\text{m}$ ) that acts as a support layer
- c) ultrathin and highly selective polyamide layer (100-200 nm) that acts as active barrier

The small and symmetric pore sizes or voids (up to 2 nm for NF, below 1 nm for RO) of polyamide films are responsible for separation of low MW substances (200-1000 Da) and inorganic salts. Nevertheless, the ultrathin selective layer still guarantees relatively high fluxes, which was among primary reasons for the growth of commercial use of PA TFC membranes and its well-established application in desalination industry.<sup>21, 29</sup>

PA films are commonly prepared using interfacial polymerization (or polycondensation) technique, where polymerization reaction occurs, typically between diamine and di- or trifunctional acid chloride monomers, at the liquid-liquid interface of two completely immiscible phases. First, a certain portion of aqueous solution containing diamine monomers, e.g., m-phenylenediamine (MPD) or piperazine, is absorbed by the macroporous membrane support. Afterwards, the support is immersed into an organic solution containing acid chlorides, typically trimesoyl chloride (TMC); consequently, a step growth polymerization is initiated upon diffusion of monomers to the interface. Due to diamines' partial solubility in organic solvents, the condensation kinetics are controlled by diamine diffusion into the organic phase. A general scheme for the interfacial polymerization of PA is depicted in Fig. 2.5.<sup>30-32</sup>

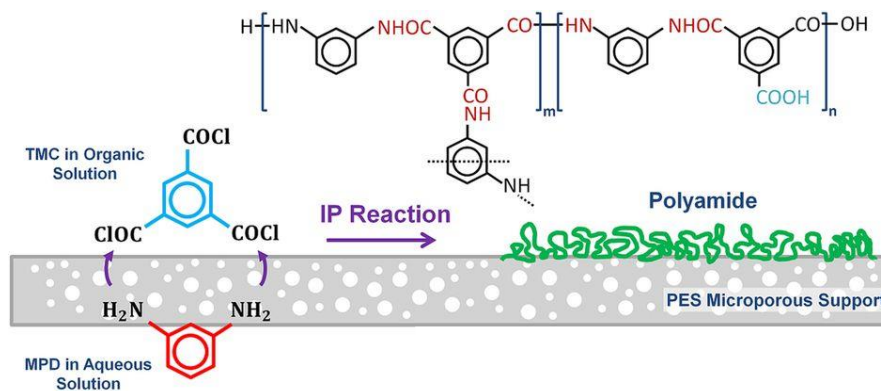


Figure 2.5 Schematic representation of PA film formation between TMC and MPD.<sup>30</sup>

Early PA formation at the interface is nearly instantaneous, yet reaction rates decrease due to the growth and aggregation of a dense PA layer in the organic phase. Consequently, interpenetration for monomers becomes more impaired. This self-limiting nature of PA polymerization is the main reason behind its ultrathin film thickness. In later reaction phases, changes in surface morphology are contributed to crosslinking of PA clusters, resulting in rough, ridge and valley topographies with reduced amide bond densities between such covalently merged PA clusters.<sup>33, 34</sup> Additionally, unreacted acid chlorides will experience hydrolysis, generating free carboxylic groups and thus negatively charged groups in the PA film. More findings include a heterogeneous distribution of carboxylic and amine groups related to the different location of monomer in immiscible phases. However, specific membrane physico-chemical properties of PA films (topography, layer thickness, chain rigidity, crosslinking degree and surface charge) can be tailored by reaction parameters, e.g., type of monomers, concentration, solvents, curing temperature, additives and UF support.<sup>28, 35-37</sup>

### 2.3 Membrane fouling

Membrane fouling describes the deposition of retained and undesired species on a membrane surface or inside the pores. It causes a permeate flux decline and contributes strongly to increasing operating costs, as a result of more intense chemical cleaning methods and membrane replacement. Fouling is, thus, still a bottleneck challenge in membrane technology.<sup>38, 39</sup>

Generally, membrane fouling can be understood as a thermodynamic system between foulant, membrane surface and solvent. According to thermodynamic principles, every system tries to minimize its Gibbs free energy. Thermodynamic fouling processes for different surface types are demonstrated in Fig. 2.6.<sup>40</sup>

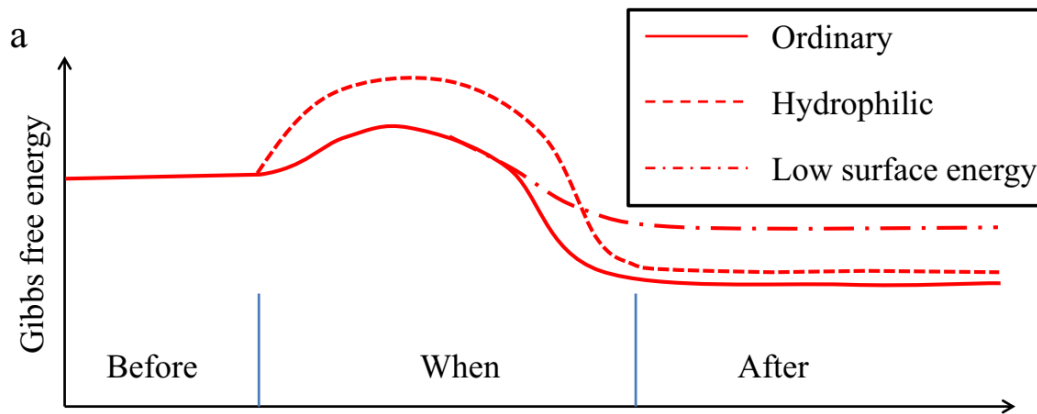


Figure 2.6 Course of Gibbs free energy in stepwise adsorption of a protein onto different surface types.<sup>40</sup>

If, for example, an in water dissolved protein approaches a membrane surface, protein's tertiary structure will be disordered and, consequently, it loses its integrated water molecules. The loss of water molecules is accompanied by a temporary increase in Gibbs free energy. However, when new attractive interactions, e.g., electrostatic interactions, hydrogen bonds or van-der-Waals forces, between foulant and membrane surface are formed, the Gibbs free energy of the system will overall decrease. The protein adsorption is therefore driven by thermodynamics but is varying for different physico-chemical surface properties. Ordinary or hydrophobic surfaces demonstrate biggest gain in free Gibbs energy after adsorption. In contrast, hydrophilic surfaces strongly disturb restructuring of approaching protein, which can be understood as imposing an activation barrier for the foulant. Complementary, neutral zero charge surfaces behave thermodynamically like ordinary surfaces during protein approach but do not impose strong attractive forces and hence decrease in Gibbs free energy is smaller. A schematic example for protein adsorption onto a surface is demonstrated in Fig. 2.7.<sup>40</sup>

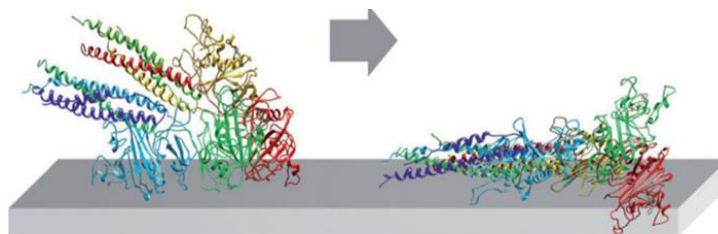


Figure 2.7 Adsorption of a protein onto a surface and change of its conformation.<sup>40</sup>

Although there are different types of fouling, all can be described by thermodynamics and reduction of Gibbs free energy as the driving force. However, many parameters, including feed water characteristics, foulant type, operating and hydrodynamic conditions as well as

membrane properties, may influence fouling behavior and turn membrane fouling to a complex phenomenon.<sup>41</sup>

To simplify the fouling phenomenon, it is usually classified into four types:

- a) Colloidal
- b) Organic
- c) Inorganic
- d) Biofouling

### 2.3.1 Colloidal fouling

Colloids include silt and clay, precipitated crystals, iron and aluminum, as well as colloidal silica and sulfur, can vary in size between few nanometers to several micrometers. When particles are similar in size to membrane pores, they can block pores and cause severe flux decline. This initial pore blocking can be divided into three different types.<sup>16, 42, 43</sup>

Standard pore blocking describes the constriction of pores. Colloids accumulate at pore opening and narrow pore channels when their diameter is smaller than the pore diameter. Complete pore block, or pore sealing, occurs when particles' size exceeds membranes' pore diameter and cause plugging of a pore. Intermediate pore blocking represents a combination of both previous blockings; here, pore entries are blocked by several particles.<sup>38, 42, 44</sup>

Initial blocking mechanisms mostly precede a formation of filtration cake and have a stronger influence on permeate flux. As filtration proceeds, additional particles are deposited onto the membrane surface; a cake layer will grow gradually and affect membrane permeability and selectivity, depending on colloid properties, e.g. size, morphology and deformability. The formation of a filter cake is followed by its consequent compression. A skin and compact layer is formed and contributes up to 90 % of overall resistance. Pore blocking filtration models are schematically illustrated in Fig. 2.8.<sup>38, 42, 45</sup>

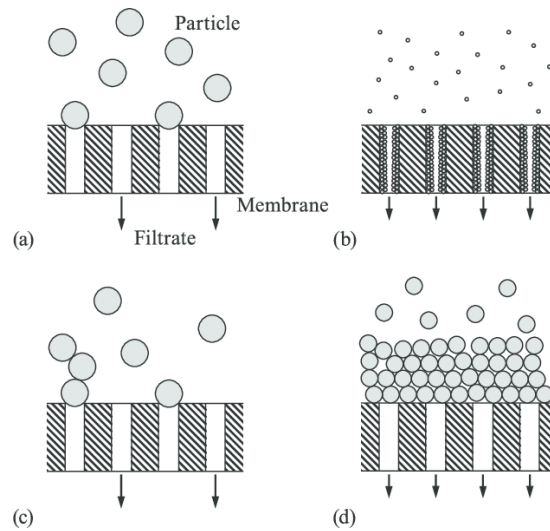


Figure 2.8 Colloid Fouling mechanism – a) complete blocking, b) standard pore blocking, c) intermediate pore blocking, d) cake layer formation.<sup>42</sup>

The dynamic fouling process is also understood as a resistance-in-series model, in which overall membrane resistance is mathematically demonstrated using Darcy's law:

$$J = \frac{\Delta P}{\eta (R_m + R_{ad} + R_{pp} + R_{cake})} \quad (2.7)$$

Where  $J$  is flux through the membrane,  $\Delta P$  is transmembrane pressure,  $\mu$  is dynamic viscosity,  $R_m$  is hydraulic membrane resistance,  $R_{ad}$  is resistance caused by adsorbed species,  $R_{pp}$  is resistance caused by plugged pores and  $R_{cake}$  is resistance caused by filter cake.

### 2.3.2 Organic fouling

Due to their diverse nature, organic foulants in water treatment are hard to categorize and therefore their contribution to fouling is poorly understood. In general, organic matter is composed of humic substances, proteins, polysaccharides, microbial products, endocrine disrupting compounds and pharmaceuticals, often cataloged as natural (NOM) and effluent organic matter (EfOM). The fouling phenomena of this material class are governed by attractive physico-chemical interactions between surface and foulant and/or foulant and foulant. Furthermore, studies suggest polysaccharides are the most relevant organic foulants in water treatment, even though their concentration is low in usual waste and surface waters.<sup>39, 46, 47</sup>

In general, organic substances can contribute in several ways to the RO/NF fouling phenomena:

a) adsorption

Adsorption often results in a first conditioning layer, upon which a cake layer or a biofilm is formed. It can also initiate pore narrowing and subsequently pore plugging when substances are able to enter the membrane matrix. However, dependent on the foulants physico-chemical nature, adsorption does not necessarily cause a flux decline in membrane processes. Charged NOM, for example, was found to increase membrane hydrophilicity and consequently water permeation rate. In contrast, proteins were found to massively reduce membrane flux.<sup>46, 48</sup>

b) gel or cake layer formation

Gel layer is formed when solubility limits of organic matter is exceeded at the membrane surface. Either this happens due to precipitation in presence of salts or increasing surface concentration due to retention and concentration polarization. Consequently, high cross-flow velocities are expected to inhibit gel layer formation by decreasing the extent of CP.<sup>46</sup>

c) nutrients for microorganisms resulting in biofouling (see section 2.3.4)

### 2.3.3 Inorganic fouling

Scaling and inorganic fouling occur at the membrane surface, when the concentration of sparingly soluble inorganic salts, e.g.,  $\text{CaSO}_4$ ,  $\text{CaCO}_3$ ,  $\text{SiO}_2$  and  $\text{BaSO}_4$ , is exceeding their solubility product. Due to concentration polarization effect, described in section 2.4, NF and RO membranes exhibit 4 to 10 times higher concentrations of salts near the membrane surface compared to bulk-solution.<sup>38, 49</sup>

Studies suggest a formation of a scale cake layer is based on two main mechanisms: crystallization and particulate fouling. Crystallization describes the deposition of inorganic matters via nucleation of ions and precipitation at the membrane surface. In contrast, particulate fouling is caused by the deposition of crystallized colloidal matters from the bulk.<sup>38, 50</sup>

Whether surface or bulk crystallization might occur is dependent on several parameters, e.g., membrane properties, salt type, module and operating conditions. Shirazi et al. proposed that surface precipitation is more probable at low cross-flow velocities and high operating pressures, due to low shear rate and, consequently, high CP.<sup>51</sup>

#### 2.3.4 Biofouling

Biofouling is a serious drawback of membrane processes, due to living and reproduction nature of microorganisms. Even at minor concentrations of bacterial cells, a biofilm is formed at the membrane surface. Generally, biofouling is divided into four steps:<sup>52, 53</sup>

- i) formation of a conditioning film by adsorption of organic compounds (proteins and other macromolecules)
- ii) transport and attachment of microorganisms
- iii) metabolism and subsequent growth of microbial cells
- iv) development of a biofilm

Living microorganisms are embedded in a three-dimensional matrix of hydrated extracellular polymer substances (EPS). EPS consist of various chemistries, e.g., carboxylic and amino acids, proteins as well as polysaccharides, acting as nutrients for microbial matters. Since EPS contributes up to 80% of overall biofilm, they are mainly responsible for flux decline by deposition and attachment onto membranes. Furthermore, amphoteric character of EPS allows adsorption on hydrophilic as well as on hydrophobic surfaces, making biofouling a non-specific fouling phenomenon.<sup>38, 54, 55</sup>

#### 2.4 Concentration polarization

In membrane filtration processes, matters in the feed are transported by convection towards the active separation layer. When transported components are rejected by the membrane through size exclusion, insolubility in dense film or charged-induced mechanisms, they are concentrated within a laminar boundary layer with thickness  $\delta$  near the membrane surface. Consequently, the increased concentration near the membrane surface will induce a diffusive transport of retained solutes back into bulk solution. It is assumed that convective transport towards and diffusion away from membrane will be in balance in a continuous filtration process and hence a steady state of mass transport will be achieved. The formation of such a concentration gradient between boundary layer near the membrane surface and bulk is known as concentration polarization phenomena (CP) and is depicted in Fig. 2.9.<sup>56-58</sup>

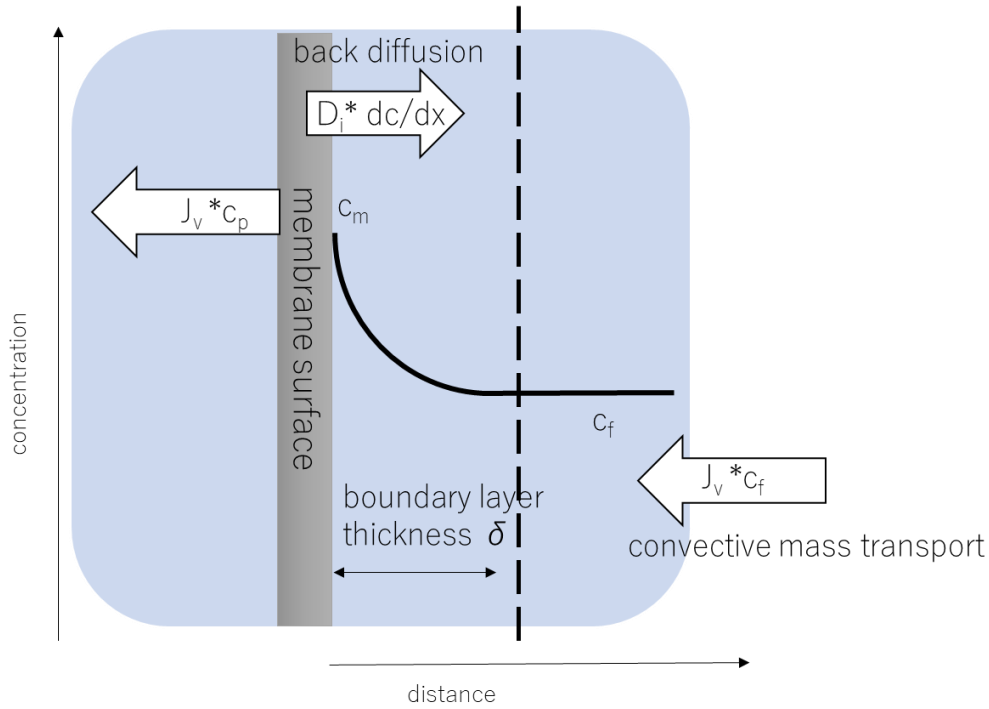


Figure 2.9 Schematic representation of concentration polarization during filtration.

High retained solute concentration in the boundary layer can increase salt permeation through the membrane and, hence, reduce membrane selectivity. Furthermore, CP adds additional resistance to membrane filtration and, therefore, decreases membrane permeability. The higher the solute concentration at the membrane surface, the higher is the probability of precipitation of rejected solutes. Hence, CP is a critical precursor for membrane fouling.<sup>56</sup>

A mathematical description of mass transport balance and CP can be generated by the Film theory model:<sup>16, 56</sup>

$$Jc_p = Jc_f - D_i \frac{dc}{dx} \quad (2.8)$$

Where  $J_v$  is the permeate flux,  $D_i$  is the diffusion coefficient of solute  $i$ ,  $c_p$  is permeate concentration of solute  $i$ ,  $c_f$  is feed concentration of solute  $i$ ,  $x$  is the distance from the membrane surface and  $c$  is the concentration.

Integration over the boundary layer thickness  $\delta$  will lead to the following equation of CP:

$$\frac{c_m - c_p}{c_f - c_p} = e^{\frac{J\delta}{D}} \quad (2.9)$$

With  $c_m$  as the concentration at the membrane surface.

For complete rejection of solute i,  $c_p$  equals 0 and thus equation 2.10 gives:

$$\frac{c_m}{c_f} = e^{\frac{J\delta}{D}} \quad (2.10)$$

When CPM is 1, there is no concentration polarization occurring and membrane performance is not affected. In contrast, a high CPM has a substantial impact on permeability and rejection. Typical RO applications demonstrate CPM values between 4-10, while UF processes can lead to modulus up to 70.<sup>16</sup>

As CP influences membrane separation, calculation of membrane rejection is highly relevant. However, many researchers focus only on observed rejection  $R_{obs}$ , regarding feed or bulk concentration<sup>56</sup>:

$$R_{obs} = \left(1 - \frac{c_p}{c_f}\right) * 100\% \quad (2.11)$$

Nevertheless,  $R_{obs}$  underestimates real rejection  $R_0$ , as solute concentration next to the membrane surface will be higher than in the bulk or feed. Therefore, it should be distinguished between observed and real rejection:

$$R_0 = \left(1 - \frac{c_p}{c_m}\right) * 100\% \quad (2.12)$$

Considering that the concentration at membrane surface  $c_m$  cannot be measured directly, a different approach is necessary to gain knowledge about real membrane selectivity. Koyuncu and Topacik developed an estimation of real rejection by considering velocity dependent mass transfer coefficients. Relationship between observed and real rejection can then be derived by equation 2.13:<sup>59</sup>

$$\ln \left[ \frac{1-R_{obs}}{R_{obs}} \right] = \ln \left[ \frac{1-R_0}{R_0} \right] + \frac{J}{k} \quad (2.13)$$

With  $k$  as the mass transfer coefficient.

Even though CP exacerbates membrane fouling, its impact on permeability and rejection is considered reversible. To minimize CP, its contribution to fouling and decay of membrane performance, several techniques and adjustments of operating parameters are suggested. Methods like higher cross-flow velocities, feed pulsation, membrane spacers or electric fields potentially can influence hydrodynamic conditions, enhance shear stress at boundary layer and, hence, reduce the concentration at membrane surface.<sup>16</sup>

## 2.5 Anti-fouling strategies

This section discusses the main approaches to minimize fouling phenomena. Membrane related modifications will be discussed in more details in section 2.8.2. Due to specific nature of foulant-membrane interactions, fouling mitigation and release of foulants require a versatile range of strategies. In general, anti-fouling approaches are classified between active and passive approaches.<sup>14</sup>

Active mechanisms are mostly relevant to bacterial fouling. They inhibit biological activity and growth of microorganisms by the release from the membrane surface (off-surface anti-fouling), or implementation of antibacterial agents onto the membrane surface (on-surface anti-fouling). Hence, active strategies aim at preventing biofouling formation.<sup>14</sup>

Off-surface approaches act in two possible ways, either by leaching metallic antimicrobial nanomaterials or by releasing reactive oxygen species (ROS).<sup>60, 61</sup> Silver nanomaterials, in the form of nanoparticles or polymer-composites, are well-known biocidal materials deposited on membrane surfaces or incorporated in its support.<sup>62</sup> According to Choi et al., silver ions are released through reaction of silver nanomaterials with oxygen, existing in feed water solutions. The release is followed by inactivation of living matters, mainly due to inhibiting adenosine triphosphate (ATP) production and deoxyribonucleic acid (DNA) replication.<sup>14, 63</sup>

Another off-surface mechanism against fouling is introduced by so-called reactive oxygen species (ROS) such as oxygen, hydroxyl radicals and hydrogen peroxide. They are generated by a reaction of water or oxygen with metal-based nanocatalyst and can cause oxidative stress to microorganisms.<sup>14</sup> ROS show anti-microbial properties by deconstructing lipid membranes and consequent damage of DNA as well as ribonucleic acid (RNA).<sup>64</sup> Besides Ag nanoparticles, a commonly used nanomaterial and ROS generating agent that exhibits low toxicity, good thermo- as well as chemical stability is photoactive TiO<sub>2</sub>.<sup>61, 65</sup>

Nevertheless, off-surface metallic strategies have some drawbacks since leaching of ROS or nanomaterials is uncontrolled. Furthermore, their depletion and practical limits, such as air and light isolation, disrupt their applicability. Additionally, metal nanomaterials may give rise to mutated bacteria that are resistant to heavy metals and pose another threat to human health because of their toxicity.<sup>14, 66, 67</sup>

In contrast, on-surface methods integrate anti-fouling agents into membrane structure and thus do not suffer from the release of toxic biocides or depletion. The inhibition of fouling and

biological growth results from interrupting contact between surface-active membranes and microbial matters.<sup>14</sup>

Generally speaking, anti-bacterial properties are commonly reported for cationic polymeric material (CPM), carbon nanotubes (CNT) and graphene oxide (GO).<sup>68-71</sup> Their cell toxicity stems from different mechanisms, such as decomposition of membrane walls through electrostatic interaction or physical collision, oxidative stress and disruption of metabolic pathways.<sup>14, 64, 69, 72</sup>

While active strategies rely on biologically active matters, passive anti-fouling approaches focus on weakening foulant-membrane interactions by manipulating physico-chemical and topological properties of membrane surfaces. Passive methods are divided into fouling resistance and fouling release mechanisms. Fouling resistant materials prohibit contact between foulants and membrane, while fouling release mechanisms aim at releasing the attached foulants at low shear forces.<sup>14</sup> Both mechanisms are illustrated schematically in Fig. 2.10.

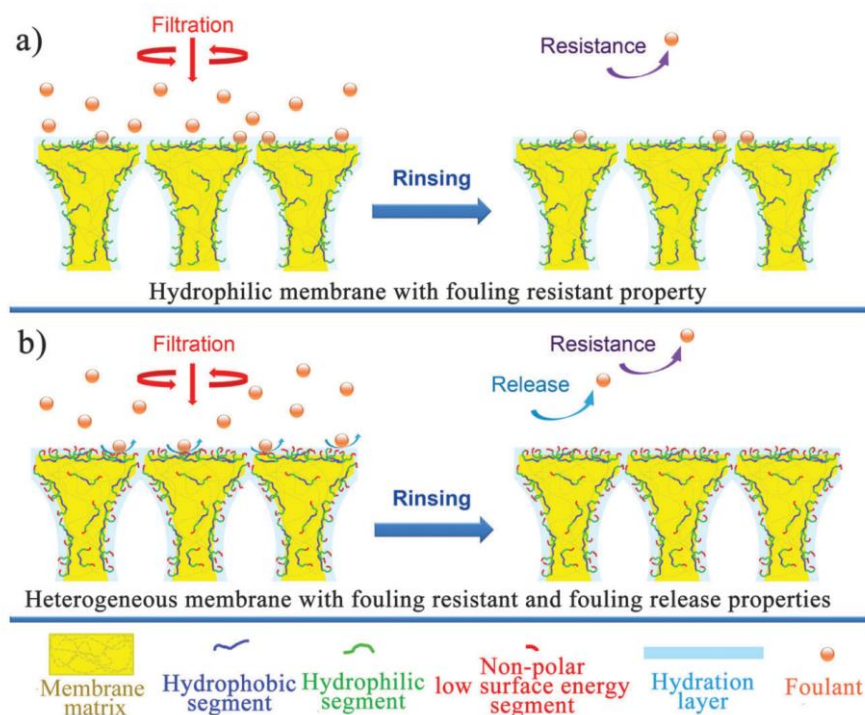


Figure 2.10 Passive anti-fouling strategies: a) fouling resistance; b) fouling release.<sup>73</sup>

Foulant resistant membranes represent the most common anti-fouling approach. Such membranes are designed to be hydrophilic, electrically neutral and possess hydrogen bond acceptors, but not donors. Common materials are poly(ethylene glycol)-based (PEG) or zwitterionic polymers, introduced onto membrane surfaces as polymer brushes or hydrogel networks (see section 2.7).<sup>14, 74</sup>

Fouling resistant behavior of hydrophilic membrane surfaces is mainly attributed to steric repulsion effects and dense hydration layer. Steric effects disfavor adsorption since foulants would cause an entropy loss by compression and decrease polymer chain mobility.<sup>40</sup> Nevertheless, hydration seems to be more relevant in the construction of anti-fouling surfaces. For instance, hydrophilic surfaces with unperturbed water networks, e.g., zwitterionic moieties, are superior in preventing protein adsorption since “releasing” of water molecules from hydration shell would not lead to an increase in entropy.<sup>40, 75, 76</sup> In contrast, PEG modified surfaces possess ordered water molecules with higher hydration energy.<sup>40</sup> The superior anti-fouling qualities of zwitterionic polymers were discussed in detail in section 2.6.

While chemistry is a critical factor in designing fouling resistant membranes, structural aspects, e.g., brush (density, side chain length) or hydrogel (elasticity), are also considered. High brush density as well as steric side groups always result in more expanded structures that enable water penetration and hence, show improved fouling resistance. In low elastic hydrogels, water sorption is more pronounced, causing a stronger hydration shell and better prevention of foulant attachment.<sup>77-80</sup>

However, hydrophilic membrane modification by macromolecules often includes flux decline and an inability to circumvent fouling caused by oil.<sup>81</sup> To overcome such challenges, fouling release membranes focus on weakening attractive foulant-membrane interactions.<sup>14</sup> Conventional releasing membranes have been inspired from marine applications and have incorporated fluoro- and silicone-containing materials.<sup>82</sup> Nevertheless, such materials are not matching water filtration conditions, as adsorption is caused by a plethora of different physico-chemical types of foulants.<sup>14</sup>

Modern promising approaches aim at establishing amphiphilic surfaces by combining hydrophilic (PEG and zwitterionic) and hydrophobic domains. Essentially, the self-cleaning effect of hydrophilic and hydrophobic surfaces is driven by synergistic effects reducing interfacial free energy. This allows low shear stress to segregate foulants from membrane surfaces.<sup>14, 82, 83</sup>

## 2.6 Zwitterionic polymers

In recent years a class of macromolecules, so-called polyzwitterions, have gained significant attention in a wide range of material research including anti-fouling coatings, hydrogels and drug delivery carriers.<sup>84</sup> Poly-zwitterions (or polybetaines) contain the same number of cationic and anionic groups within a repeating unit and are widely represented in nature. The most

prominent example is phosphatidylcholine that acts as zwitterionic head group of bilipid layers in cell membranes.<sup>85, 86</sup>

Polyzwitterions exhibit a unique combination of properties that make them highly attractive for several biological applications. Since oppositely charged groups undergo Coulomb interactions, polyzwitterions possess, analogous to conventional non-ionic polymers, charge neutrality over a broad pH range.<sup>86</sup> However, zwitterionic polymers also demonstrate high hydrophilic abilities due to their polar nature, which is typical for charged species.<sup>87</sup> Furthermore, they show responsive behavior in presence of salts.<sup>88</sup>

From a chemical perspective, polyzwitterions can exist in many different structural arrangements. Ionic/charged units can be implemented in the backbone of a polymer as well as in its side units. The most commonly used arrangements, because of their facile synthesis, are depicted in Fig. 2.11.<sup>86</sup> Such structures are mostly covered by three popular types of polybetaines, namely carbo-, sulfo- and phosphobetaines. All of them contain positively charged quaternary ammonium units coupled with complementary anionic carboxylic, sulfonic or phosphatic units.<sup>88</sup>

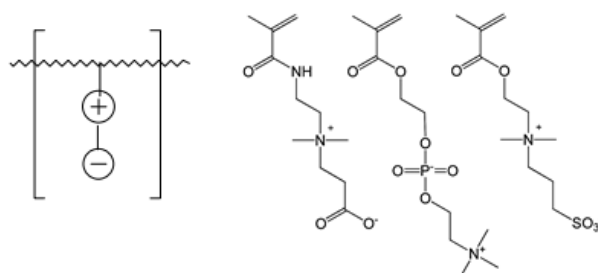


Figure 2.11 Most frequent type and examples for polybetaines.<sup>86</sup>

In water, attractive electrostatic Coulomb interactions promote self-assembled cyclic or crosslinked conformations of polybetaines. Cyclic associations can either be formed by charged units within a side chain (intragroup) or intrachain interactions of the macromolecule. Additionally, intermolecular orientations (interchain) can lead to a crosslinked type network with gel-like properties.<sup>88</sup>

Usually, ring formation requires bending and thus, intrachain interactions are disfavored by entropic means.<sup>15</sup> Consequently, monomeric zwitterionic compounds show no intramolecular interactions when investigated by molecular mechanic models.<sup>89</sup> In contrast, polymer-polymer associations may be sterically hindered and hence, force polybetaines to undergo intrachain

pairing. In principle, the equilibrium state for polyelectrolytic conformation is dependent on attractive enthalpic forces and inner entropic energy, which are a function of pH, alkyl spacer length, molecular weight and type of ionic groups.<sup>15, 87, 88</sup>

The ability to build intra- and interchain pairing is resulting in a collapsed state and ultralow solubility in pure water, especially at the isoelectric point (IEP). IEP is defined as the pH, at which the overall charge of a zwitterionic macromolecule is zero and hence, ionic interactions are most attractive.<sup>90, 91</sup> However, in the presence of low molecular weight salts, polybetaines become soluble showing higher viscosity and exhibiting distinctive responsive properties.<sup>84, 91</sup> Primarily, screening of charged units allows to disturb and weaken intra- and intermolecular attractive Coulomb forces and hence improves solubility.<sup>90</sup>

Furthermore, shielding electrolytes induce the so-called anti-polyelectrolyte effect, which describes the expansion of zwitterionic chains. Wang et al. have proposed that the primary mechanism behind anti-polyelectrolyte effect and polymer swelling is a break up of zwitterionic pairing.<sup>91</sup> The proposed mechanism of salt presence is illustrated in Fig. 2.12.<sup>92</sup>

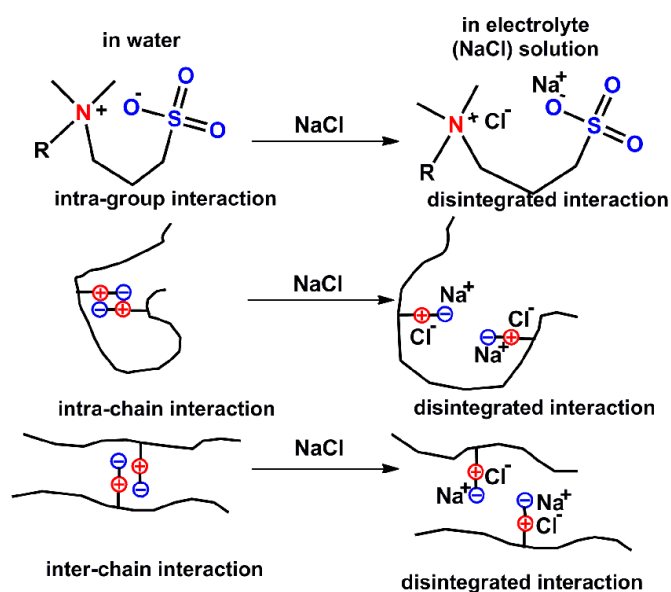


Figure 2.12 Anti-polyelectrolyte effect of NaCl – Impact on intra- and intermolecular interactions and polyelectrolytic swelling.<sup>92</sup>

The impact of electrolytes on polyelectrolytic behavior is often following the so-called Hofmeister series, which is a representation of hydration strength of ions (Fig. 2.13) or water-“philicity” and their consequent influences on water-water interactions.<sup>88, 93</sup> They are generally divided into two types: chaotropic and kosmotropic.

Chaotropic ions are usually large in size and possess a low charge density and disturb water structures by breaking or weakening hydrogen bonds. Consequently, chaotropic salts induce salting-in or dissolution of charged macromolecules like proteins or polyelectrolytes. In contrast, kosmotropes refer to smaller and high charge density electrolytes, which exhibit strong interactions with water allowing water structures to remain and causing salting-out or precipitation of polyelectrolytes.<sup>93-95</sup>

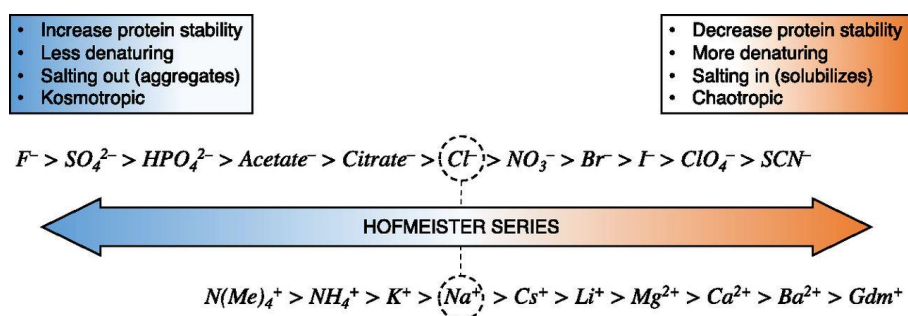


Figure 2.13 Hofmeister series.<sup>94</sup>

The impact of different salts on polyelectrolytic expansion was demonstrated by de Groot et al. using dynamic swelling experiments. Results showed that swelling degree and rate for zwitterionic copolymers are influenced by salt type as well as salt concentration. Moreover, the swelling ability, attributed to the anti-polyelectrolyte effect, followed Hofmeister series for anions. However, the effect was more arbitrary and less significant for cations.<sup>96</sup>

### 2.6.1 Anti-fouling properties

Zwitterionic coatings possess extraordinary anti-fouling properties that are generally related to their low surface energy and their strong hydration shell. However, a more precise interpretation regards the contribution of water hydration, coating morphology, excluded volume effects as well as no ion evaporation as relevant for their superior fouling resistance.<sup>15</sup>

First, a hydrophilic surface is able to bind water molecules and form a tight hydration shell. If water is bound in a state comparable to water in bulk, adsorption of a foulant and consequent release of water molecules will not lead to a gain of Gibbs free energy (see section 2.3). Since polyelectrolytes counterbalance their charge and exhibit a minimized polarity due to their charge proximities, they can maintain such a disoriented hydrogen bond network with superior interaction energy. Fouling is, therefore, more disfavored for an unperturbed water hydration shell compared to polyelectrolytic or uncharged hydrophilic surfaces.<sup>15, 40, 97</sup> The orientation of water molecules is demonstrated in Fig. 2.14.

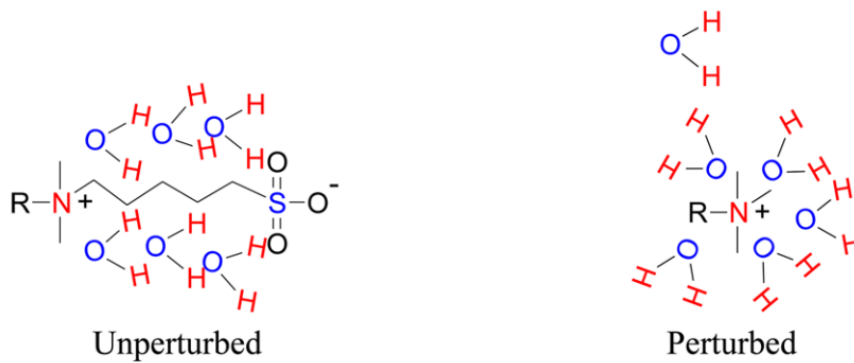


Figure 2.14 Water orientation in zwitterionic and positively charged side groups.<sup>15</sup>

Additional resistance to adsorption phenomena is attributed to steric resistance. When hydrophilic macromolecules, i.e., polybetaines, exist in a swollen state, they possess high motility and a large excluded volume. Compression of brushes attached to a surface or crosslinked network by foulants' particles and other species would result in steric repulsion between macromolecular chains. Hence, compression of polyzwitterions by foulants is inhibited by entropy.<sup>15, 40</sup>

Furthermore, charged surfaces can lead to a release of counter-ions, when an oppositely charged protein is approaching it (Fig. 2.15). Such freeing of ions is called “counterion evaporation”. However, neutral and low energy polybetaines do not possess many surface ions since their charge is balanced by internal ion pairing. In addition, many ions are trapped in the depth of the macromolecule making them hard to access. Consequently, polyzwitterionic surfaces do not gain enough energy from releasing counterions to promote sorption of foulants.<sup>15</sup>

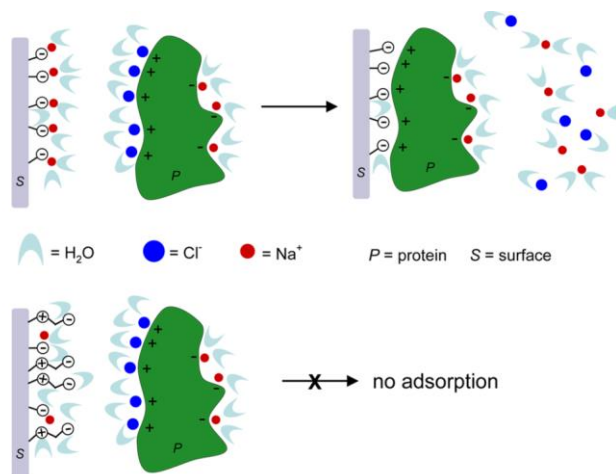


Figure 2.15 Protein adsorption and “counterion evaporation” for polyzwitterionic and negatively charged brushes.<sup>15</sup>

## 2.7 Hydrogels

### 2.7.1 Structure

Three-dimensionally crosslinked and hydrophilic polymer networks represent a class of soft materials known as hydrogels. They are generally insoluble, yet their mass consists of up to 99 % of water as a result of swelling in aqueous media. Due to the combination of high water uptake, elastomeric, soft, rubber-like properties and highly porous networks, hydrogels exhibit low friction with surrounding matter and are highly permeable. Such characteristics make hydrogels an attractive biocompatible material used in contact lenses, diapers or drug delivery applications with proven anti-fouling abilities.<sup>98, 99</sup>

Classification of hydrogels can occur according to the type of bonding. They can be chemically (non-reversible) or physically (reversible) crosslinked. Chemical bonds between monomers or polymers origin from a radical or click reaction using a bridging crosslinker.<sup>98</sup> Mostly, chemical crosslinking is initiated via a radical mechanism. A common initiator, also used in this work, representing a redox system, is ammonium persulfate (APS) in which radicals are generated by its decomposition. Amines, such as tetramethylethylenediamine (TEMED), catalyze the formation of radicals. The reaction mechanism is depicted in Fig. 2.16.

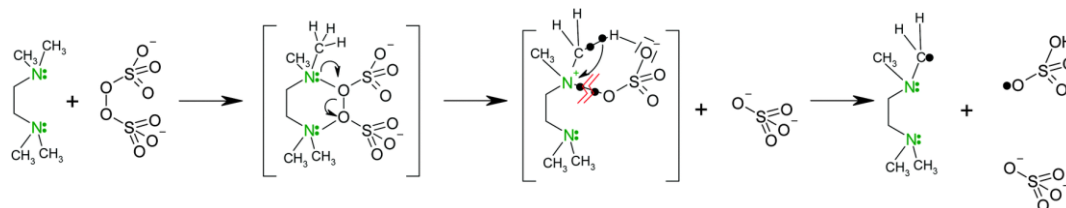


Figure 2.16. Redox reaction of APS and TEMED and formation of radicals.<sup>100</sup>

Free radicals start crosslinking reaction by attacking electron rich double bonds, e.g., methacrylate groups present in monomers or respective polymers. This step leads to a carbon radical that allows propagation and consequent chemical crosslinking of polymer chains. When a bifunctional crosslinking agent is used, often a three-dimensional network is produced. Thereafter, exhaustion of crosslinkable units and/or termination by combination of radicals will end the gelation reaction.

In addition, network formation requires that the reactive agents are sufficiently high concentrated. In macromolecular solutions DeGennes introduced the concept of overlap concentration, at which polymer coils are in direct contact with each other. Below overlap concentration average space between neighboring macromolecules is big. Hence,

polymer-polymer interactions are negligible and do not contribute additionally to solutions viscosity. Exceeding overlap concentration is a precondition for gelation between crosslinkable polymers.<sup>101</sup> Macromolecular solutions can therefore be divided into three concentration regions (Fig. 2.17):

*Diluted polymer solution ( $c < c^*$ ):* Polymers are not in direct contact with each other.

*Overlap concentration ( $c = c^*$ ):* Polymers are in contact with each other.

*Concentrated polymer solution ( $c > c^*$ ):* Solution is highly concentrated, and coils are entangled.

Where  $c$  is polymer concentration and  $c^*$  is overlap concentration.

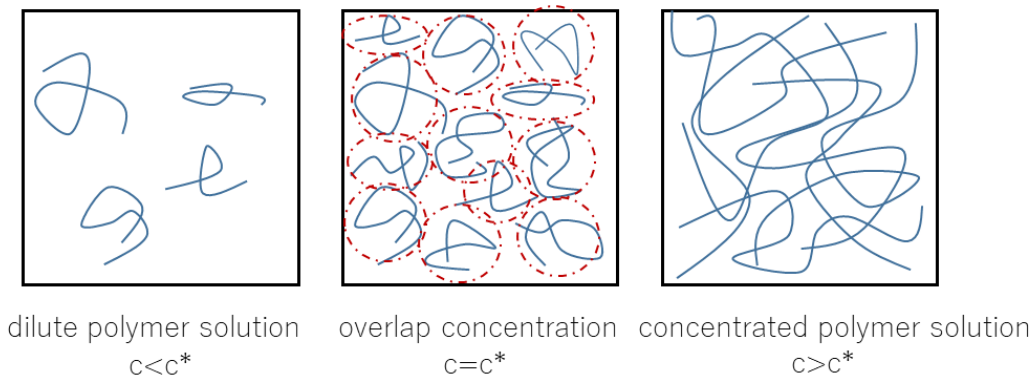


Figure 2.17 Concentration areas in polymer solution after deGennes.<sup>101</sup>

Beside covalently bound networks, physical interconnection in hydrogels can stem either from molecular forces, e.g., Coulomb, hydrophobic, van-der-Waals interactions and hydrogen bonds, or from physical entanglement without undergoing a chemical reaction.<sup>99, 102, 103</sup>

The uncontrollable nature of coupling asymmetric components via radical mechanisms forms high mobility networks that are often possessing irregular and random microscopic morphologies, including loops, dangling chains or defects in gel structures. Inhomogeneities in three-dimensional network types are classified as spatial, connectivity, topological or mobility. They are depicted in Fig. 2.18.<sup>98</sup>

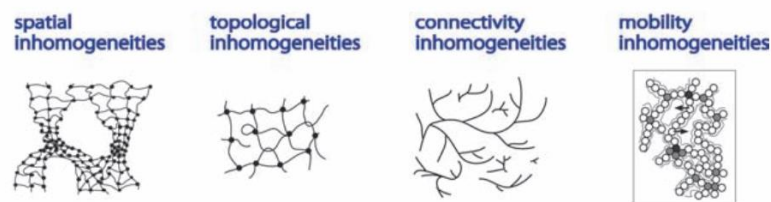


Figure 2.18 Irregular hydrogel network types.<sup>98</sup>

Because of such structural and chemical heterogeneities, no universal theory regarding physico-chemical parameters was able to be established to explain and predict the viscoelastic properties of hydrogels. Nevertheless, this chapter will try to point out relationships between structural characteristics and mechanical properties, besides their relevance for anti-fouling hydrogel coatings.

Since hydrogel can be understood as soft and rubber-like materials, understanding of hydrogels' mechanical properties is based on the theory of rubber elasticity. Rubbers are regarded as lightly crosslinked networks that can show elongation up to 1000% when mechanical stress is applied, but still demonstrate absolute and immediate reversible behavior when external strain is removed.<sup>79, 102</sup>

The most important and impactful structural aspect of gel networks is the crosslinking density that is proportionally linked to mechanical strength and glass transition temperature. Hence, all irregularities in network structure will lower mechano-physical strength.<sup>98</sup>

Furthermore, highly concentrated reaction solutions may also lead to a high crosslinking density. Therefore, mechanical properties can also be influenced by reaction conditions, e.g., crosslinker concentration. Nevertheless, there is a trade-off relationship between crosslinking density, and consequent mechanical stability, as well as other network parameters, i.e., diffusivity and swelling degree, which decrease when network structure has high material density.<sup>98, 99</sup>

Studies also suggested that hydrogels show higher mechanical strength when incorporating monomers with sterically more demanding backbones (e.g., acrylate vs. methacrylate). Furthermore, the hydrophilicity of chain units was found to decrease mechanical strength of networks due to enhanced swelling properties.<sup>99</sup>

### 2.7.2 Anti-fouling properties

Even though hydrogels demonstrate good anti-fouling behavior, especially regarding biofouling, its underlying mechanisms are still not well understood. Nevertheless, researchers have agreed on the crucial contribution of low elastic modulus and high water uptake in reducing drag forces and surface energies. Irrespective of gel chemistry, optimal water uptake of 85-90 % was related to a trade-off between low adhesion forces and increased penetration into the gel by living organisms.<sup>79</sup>

Fig. 2.19 demonstrates the impact of various chemistries present in hydrogels on the five day settlement of barnacles. While either hydroxyl groups or sulfonate groups present in hydrogels show minimizing effects on barnacle attachment, a combination of both tend to increase settlement. This activity is not yet understood. Furthermore, amine containing gels tend to decrease anti-fouling properties. However, no correlation between hydrogel charge and barnacle settlement can be observed in seawater conditions that indicate cancellation of charge effects by ionic strength.<sup>79</sup>

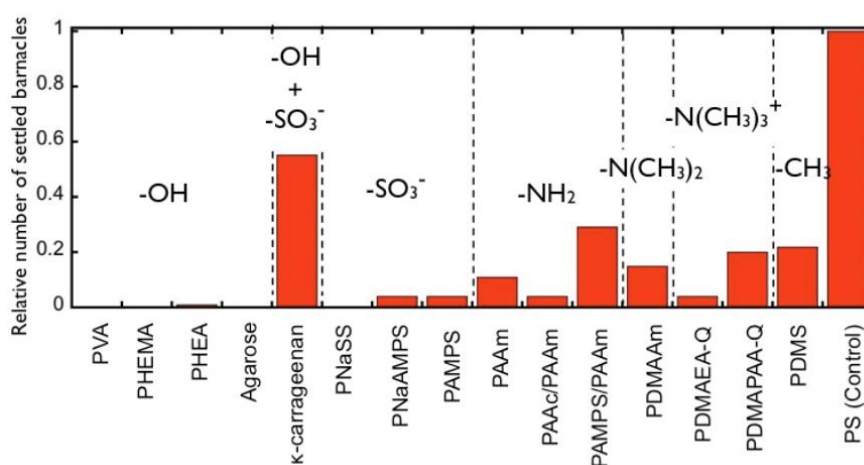


Figure 2.19 Relative settlement of barnacles onto hydrogel with different chemical groups.<sup>79</sup>

Additionally, hydrogel chemistry may influence different phases in biofouling phenomena. While for polyelectrolyte hydrogels germination seems to be inhibited, polysaccharide gels demonstrate adhesion resistance against protein and algae. Other works by Bowen et al. revealed a positive correlation between alkyl chain length in a hydrogel and its anti-fouling behavior.<sup>79, 104</sup>

Considering physico-mechanical hydrogel properties, fouling propensity increases generally with higher gel elasticity. However, the impact of mechanical properties also depends on gel chemistry. Fig. 2.20. shows the settlement of barnacles after five days exposure for hydrogels with different elastic modulus and various functional groups.<sup>79</sup>

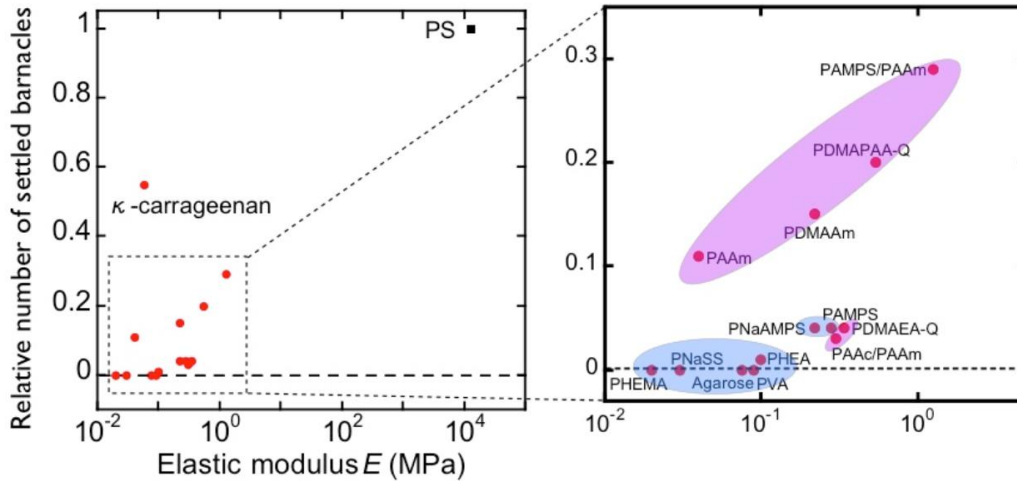


Figure 2.20 Barnacle settlement in dependence of elastic modulus.<sup>79</sup>

Hydroxyl- or sulfonic containing networks exhibit strong anti-fouling abilities regardless of their viscoelastic properties. In contrast, elasticity and number of barnacle settlement are positively correlated when the hydrogel structure contains amine functionalities. Again, understanding of the relationship between chemistry and physico-mechanical properties is complex and their impact on anti-fouling abilities is not fully developed.<sup>79</sup>

Additionally, to understand hydrogels' anti-fouling abilities, specific parameters, e.g., type of foulant, feed water characteristics and hydrogel chemistry, have to be considered. Nevertheless, an approximation concerning surface wettability and water uptake of hydrogels is crucial. High elasticity results in low water uptake. Hence, Murosaki et al. argued that settlement of barnacles was promoted due to low water content, which is analogous to a less pronounced hydration shell.<sup>79</sup>

Likewise, Eshet et al. provided an understanding about specific physical and chemical factors of hydrogels in bacterial deposition and biofouling phenomena. More precisely, they were able to show that the anti-fouling properties increase with hydrogels swelling abilities independent of networks chemical functionalities.<sup>105</sup> Nevertheless, chemistry does have an impact on fouling properties. PEGMA (poly(ethylene glycol methacrylate)) networks showed significantly lower bacterial deposition rates compared to zwitterionic PSPE (poly(2-(methacryloyloxy)ethyl dimethyl-(3-sulfopropyl methacrylate)) and PAAm (poly(acrylamide)) gels. Impact of swelling ability and chemistry on bacterial deposition is depicted in Fig. 2.21.

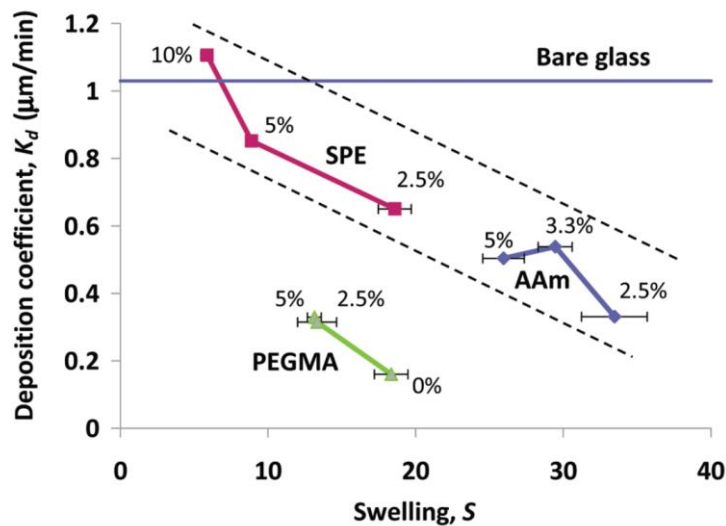


Figure 2.21 Deposition coefficient of *Pseudomonas fluorescens* in dependence of swelling degree and chemistry.<sup>105</sup>

In organic fouling, contribution of physical factors to nonspecific adsorption properties becomes more complex because it is additionally influenced by hydrogels sieving effects (networks mesh size).<sup>106</sup> While deposition is generally reduced in less crosslinked and hence more swollen gels (with bigger mesh sizes), it is counterbalanced by facile penetration and permeation of smaller biomolecules into and through the network. Hence, bigger network pores are less effective retaining biomolecules, which allows them to approach the underlying surface and therefore enable fouling. In contrast, denser crosslinked networks show improved rejection of biomolecules onto hydrogel layer and therefore decrease accumulation on substrates surface, although possessing lower swelling degrees.<sup>107, 108</sup>

### 2.7.3 Transport through and resistance of hydrogels

Hydrogels applied in membranes represent an additional transport barrier and therefore influence membrane performance. The precise nature and magnitude of imposed influence depends on type of base membrane (porous: pore size and structure; or non-porous) in combination with location of incorporated hydrogel (onto surface or within pores) as well as gel characteristics (i.e. crosslinking/swelling degree, layer thickness, functional groups). To simplify the understanding of hydrogels' impact on membrane properties, categorization into porous and non-porous membrane is beneficial.<sup>109</sup>

In porous membranes, the overall hydraulic resistance is relatively low and therefore they often demonstrate high water flux. In contrast, the resistance introduced by a hydrogel can be relatively high compared to intrinsic membranes resistance. Porous membranes modified with

hydrogels may therefore experience a decrease in permeability, while simultaneously becoming more selective. Hence, UF/MF hydrogel modified membranes often possess two complementary functions, in which the polymeric membrane provides mechanical stability and the gel network introduces additional sieving mechanisms (and/or anti-fouling properties).<sup>110</sup>

A more detailed understanding of transport and resistance properties distinguishes between specific location of applied hydrogel (either within pores or on membrane surface) and its physico-chemical properties. However, for this research project it is sufficient to focus on hydrogels applied onto membrane surfaces, which is more relevant for dense membranes.

Contrary to porous structures, dense selective layers of NF/RO membranes already demonstrate high hydraulic resistances in combination with high selectivity properties. Subsequently surface hydrogels can only be applied onto membrane surfaces due to non-porous material structure and show less pronounced influence on membrane permeability and size exclusion than identical hydrogels in porous membranes. Hydrogels applied in NF/RO membranes are therefore mostly intended to introduce anti-fouling properties.<sup>110</sup>

However, each layer (hydrogel and active membrane layer) is contributing separately to total membrane resistance  $R_{tot}$  and can therefore be described by Darcy's law and a resistance-in-series model.<sup>111</sup> The compartmentalization of hydraulic barriers is commonly used to quantify additional resistances introduced by concentration polarization and various membrane blocking/fouling phenomena.<sup>112</sup> Analogous the series model can be utilized in hydrogel modified membranes:

$$R_{tot} = R_m + R_{hyd} \quad (2.14)$$

$$R_{tot} = \frac{\Delta P}{J \eta_{water}} \quad (2.15)$$

Where  $R_{mem}$  is intrinsic membrane resistance,  $R_{hyd}$  is the resistance of the hydrogel,  $\Delta P$  is transmembrane pressure,  $J$  is water flux through membrane and  $\eta_{water}$  is dynamic viscosity of water.

The hydraulic resistance and transport through hydrogels are mainly discussed in terms of their physico-chemical properties. As described in chapter 2.7.1, hydrogels represent swollen three-dimensional crosslinked networks, in which mass transport must occur through mobile polymer chains with fluctuating pore sizes. The permeation is therefore strongly dependent on the microstructure of the gel network. More specific, water flux correlates with the free volume present in the hydrogel matrix, equivalent to mean mesh size and hydrogel water uptake.<sup>113, 114</sup>

In contrast, gels with high polymer volume fraction will experience more friction between water and the gel matrix and consequently, flux through the network will be reduced.

As a result of mobile and flexible chains, no fixed pores are assumed to exist, therefore water flux cannot be calculated using “regular” Hagen-Poiseuille model.<sup>113</sup> Instead, water transport depends on penetration into and through the mobile polymer matrix, described by solution-diffusion model (see section 2.1.3). Mathematically transport through hydrogels is expressed as hydraulic permeability  $K_{hyd}$  (equation 2.16) or, for comparison, as Darcy permeability  $\kappa$  (equation 2.17).<sup>115, 116</sup>

$$K_{hyd} = J * \frac{\Delta x}{\Delta p} \quad (2.16)$$

In which  $J$  is flux,  $\Delta x$  is hydrogel thickness and  $\Delta p$  is pressure differential across the hydrogel.

$$\kappa = \frac{K}{\mu} \quad (2.17)$$

With  $\mu$  as dynamic viscosity of the solution.

High flux hydrogels can generally be obtained when crosslinking densities are decreased (in chemically equivalent hydrogels). A looser network is accompanied by an increase in swelling ability as well as water and salt transport. However, hydrogels water-salt selectivity is also influenced by network characteristics. More precise, bigger mesh sizes result in lower selectivity and vice versa.<sup>117, 118</sup>

## 2.8 Zwitterionic hydrogel membrane surface modifications

### 2.8.1 Zwitterionic hydrogels

The combination of zwitterionic chemistry and hydrogels represent a novel type of material with promising anti-fouling and biocompatible properties. In general, zwitterionic networks can be generated in various chemical or physical pathways, which influences networks characteristics such as mechanical properties and mesh size as well as anti-fouling abilities. However, the focus of this section will be solely on chemical crosslinking and adaption in membranes.

Chemically crosslinked hydrogels are mostly obtained via free radical polymerization induced by a redox- or photo-initiation system, in which zwitterionic monomers or crosslinkable polyzwitterions form a three-dimensional network with a matching crosslinker.<sup>119</sup>

Common reported zwitterionic monomers for hydrogel synthesis are carboxybetaine methacrylate (CBMA), carboxybetaine acrylamide (CBAA), 2-methacryloyloxyethyl phosphorylcholine (MPC) and sulfobetaine methacrylate (SBMA), each influencing network structure and hydrogel properties (see Tab. 2.1).<sup>120</sup>

Table 2.1 Zwitterionic chemistry and its influence on network properties.

<i>Zwitterionic functionality</i>	<i>Network properties</i>
<i>CBMA</i>	highest elasticity
<i>CBAA</i>	highest hydration and water diffusion coefficient
<i>MPC</i>	largest mesh size
<i>SBMA</i>	fastest degradation (with degradable crosslinker)

However, the understanding of underlying physico-chemical structure-properties relationship is poor, although it helps to develop of well-tailored networks for specific purposes. Already minor changes in crosslinker length and concentration as well as amount and type of zwitterionic groups are discussed to affect non-fouling abilities in an unpredictable and complex manner.<sup>121</sup>

In addition, many zwitterionic hydrogel networks are chemically bound by a non-zwitterionic crosslinker or possess additional side functionalities. Non-zwitterionic chemistry in zwitterionic hydrogels is reported to impact network regularity, water uptake and transport, degradability/reversibility as well as biocompatibility due to different incorporation rates as well as complex interactions between various functional groups and water.<sup>122</sup> For example, polycarboxybetaine and polysulfobetaine based networks bridged by chemically similar crosslinkers were shown to possess enhanced non-fouling properties and higher mechanical stabilities, compared to gels coupled by commercially available, non-zwitterionic crosslinkers. The beneficial properties were related to increased hydrophilicity and homogeneity of the networks.<sup>122, 123</sup>

In addition, the random nature of radical propagation makes it difficult to control crosslinking reaction properly. Consequently, radical mechanism complicates formation of well-defined and homogenous networks with adjustable mesh sizes. The most common network irregularities are danglings, loops or permanently entangled chains (see section 2.7.1).

Hence, controllability of hydrogel properties, which is relevant in membrane or drug-releasing applications, is still a bottleneck problem in free radical crosslinking of monomers. Therefore, click-type reactions of polyzwitterionic macromolecules are increasingly discussed as a



### 2.8.2 Membrane surface modifications

Due to their anti-fouling abilities, application of zwitterionic materials in membranes have increased in last decades. Even though zwitterionic free bulk networks of different chemical and physically properties are already synthesized and regarded as highly attractive fouling resistant materials, their implementation in membranes is not very well established and still challenged by facile, controllable and scalable preparation strategies.

First, the versatile zwitterionic chemistry is almost entirely limited to sulfobetaine functionalities, because they maintain their neutral character over a broad pH range and monomers are easily available. Furthermore, research often focuses on incorporation of zwitterionic polymer brushes rather than investigating hydrogel modifications. However, when zwitterionic hydrogels are introduced in commercial membranes, the reported techniques solely utilize radical polymerization of zwitterionic monomers, although macromolecular crosslinking and click reaction possess many advantages.<sup>121, 127, 128</sup>

Nevertheless, this section will summarize reported zwitterionic hydrogel membrane modifications, which are mainly based on photo-, redox-, or macro-initiated grafting-from techniques as well as CP-enhanced crosslinking and underline their advantages and drawbacks. Generally, grafting-from refers to chemical polymerization initiated at the membrane surface and therefore allows adjusting of grafting density. However, random polymerization mechanism disables proper control of network structure.

In photo-irradiation radical species are generated in the membrane material or by previously adsorbed photo initiators. The reactive species then allow radical chain propagation with monomers and crosslinkers, leading to the formation of hydrogel networks. The main advantage of photo-grafting is its simplicity, surface-selectivity and applicability in one step. One of the first partially zwitterionic hydrogel modified membranes were developed by Susanto et al. utilizing photo-crosslinking of PEGMA and SPE in various ratios, with and without crosslinker MBAA (N,N-methylenebisacrylamide) onto UF PES (polyethersulfone) membranes. Interestingly, composite materials with higher portion of PEGMA, showed better anti-fouling properties, than membranes with more zwitterionic chemistry.<sup>129</sup>

Similarly, Zhang et al. established thin-film polyampholyte hydrogel layers onto PES membrane by first coating and subsequently copolymerizing a mixture containing monomers vinylsulfonic acid (VSA), 2-(methacryloyloxy)ethyl trimethylammonium chloride (METMA) and the crosslinker MBAA via UV-irradiation. The composite membranes showed improved

resistance to protein adhesion, especially for neutral membrane surfaces, which were obtained for a monomer ratio of 3:1 (VSA:METMA). In addition, the degree of grafting and layer thickness were shown to be tunable by varying irradiation time.<sup>127</sup>

However, using radiation may also lead to a degradation of polymer material and weaken its mechanical stability. Therefore, optimized modification conditions have to be tailored to specific membrane type.<sup>130</sup> Furthermore, UV-grafting is limited to light accessible membrane areas and hence difficult to implement in hidden surfaces as well as in membrane modules. Once coatings are damaged or sheared from the surface, membrane filtration processes need either to be stopped, in order to be remodified, or materials need to be replaced, which comes along with higher operational costs.<sup>110</sup>

The challenges were partially addressed by Lu et al., who incorporated N-(3-methacryloylimino)propyl-N,N-(dimethylamino) propanesulfonate (SPP) hydrogels into UF PES membrane via redox-initiated grafting method. Instead of using photo-initiation, radical are generated in a redox reaction. The zwitterionic coating enhanced virus removal and was introduced by filtration of aqueous reactive solution containing redox initiator system and zwitterionic monomers. It was speculated that the PSPP hydrogel layer was mainly grafted onto membrane surface and exerted repulsion toward viruses approaching the membrane. However, hydrogel modification was not well-controlled in terms of location. More precise, gelation reaction was not limited to the membrane surface but occurred also within pores.<sup>131</sup> Additionally, hydrogels attachment to the surface may be weak because radicals are formed in solution and not by the membrane material (or adsorbed photo-initiators).

Complementary, the location selectivity and stronger attachment to the surface was faced by Quilitzsch et al., who established a novel surface selective coating method for porous membranes by adsorbing a copolymeric macromolecular initiator, containing hydrophobic linker functionalities N-butylmethacrylate (BMA) and redox-catalyzing functionalities N,N-(dimethylamino)ethyl methacrylate (DMAEMA) onto membrane surface. Due to its molecular weight, the macroinitiator was not able to enter membrane pores during filtration and was therefore physically adsorbed as a monolayer onto outer PES surface. The premodified surface was subsequently brought in contact (by wetting the surface) with a co-reactive solution containing SPP as zwitterionic monomer, MBAA as crosslinker and ammonium persulfate, functioning as radical initiator. Due to the complete retention of macroinitiator, gelation was limited to membrane surfaces and did not occur within pores. The degree of modification could be adjusted by crosslinker or respective monomer concentration as well as reaction time and

influenced permeability reduction, MWCO (molecular weight cut-off) and anti-fouling properties.<sup>132</sup>

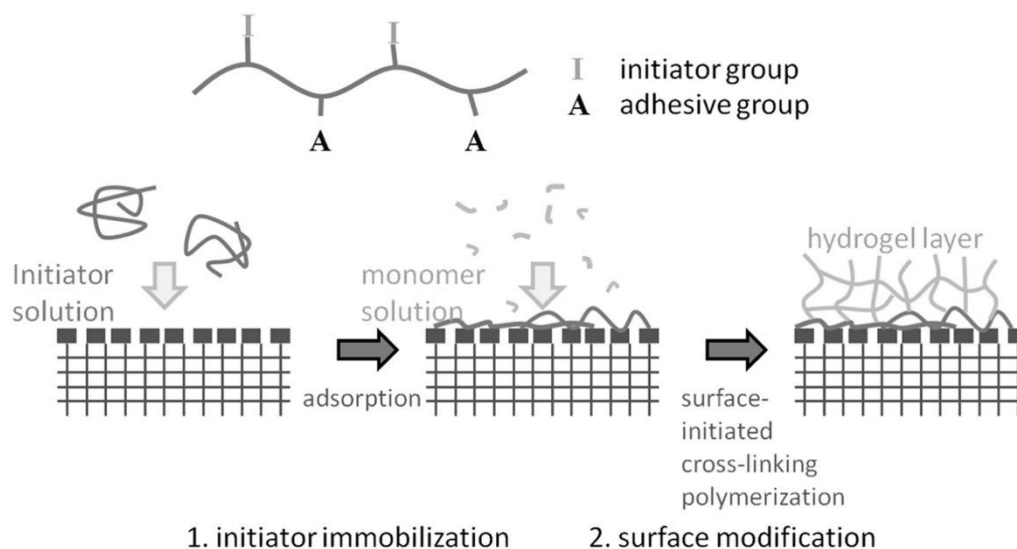


Figure 2.23 Surface initiated crosslinking developed by Quilitzsch et al.<sup>107, 132</sup>

The method was also adapted to hollow fiber membrane modules, demonstrating its superiority compared to UV-photo grafting in accessing and coating hidden surfaces. Hereby, the gelation components flushed the lumen after initial macroinitiator adsorption representing a facile, in situ hydrogel modification of membranes.<sup>128</sup>

In RO/NF membranes surface-selectivity is already given due to dense PA films, which retain small molecules. Therefore, PA layers allow even more advanced modification with monomeric units during on-going filtration. As described in section 2.4, membrane filtration causes an exponential increase of retained molecules next to the membrane surface. This fact was utilized by Freger et al., who coated commercially available PA membranes via in situ concentration polarization enhanced modification. During dead end filtration, concentration of reactive agents (monomers) and redox initiator system, were increased at the membrane surface. Once necessary concentration of reacting compounds in boundary layer was reached, hydrogel formation was initiated. Generally, the obtained hydrogel composite membranes were proven to reduce biofouling propensity by reducing bacterial deposition. Moreover, modified membranes showed permeabilities in the range of commercial brackish water membranes with improved salt rejection.<sup>133</sup>

The concept was also adapted to crossflow modular platforms, emphasized potential use and scalability of CP-enhanced radical graft polymerization for industrial applications. By adjusting feed composition and operational conditions such as time, flux and cross-flow velocities,

concentration polarization induced gelation could decrease the consumption of modifying chemicals in a simple one step process.<sup>134</sup>

However, several challenges regarding in situ membrane surface modification still exist. Primarily, surface-selective CP-enhanced modification with monomeric compounds is limited to dense RO/NF membranes. In porous membranes, small reactants will not be retained by membrane surface. Consequently, concentration polarization may be weak and essentially not initiate (or delay) crosslinking reaction onto membrane surface since necessary threshold concentrations are not achieved in boundary layer. Furthermore, monomers will be able to penetrate porous membrane structure and may cause polymerization reaction within pores.

In addition, the discussed zwitterionic network is only loosely anchored to the membrane surface due to non-tailored interactions between hydrogel and membrane material. Hence, modification may be easily washed away from surface, when strong shearing forces are applied.

Finally, not much is known about the critical gelation conditions and the extent of CP. Thus, crosslinking reaction in boundary layer is rather arbitrary performed and not well-controlled. In order to develop tailored membrane modifications by mimicking free bulk gelation conditions, a proper understanding of hydrogel formation and CP is crucial.

The challenges define the research gaps, which were intended to be well-understood and addressed in this thesis. The concept, goals and work plan are described in the following chapter.

### 3 Scope of the work

#### 3.1 Concept

The main goal of this research project was to establish a facile in situ anti-fouling hydrogel coating for NF/RO TFC membranes based on crosslinkable zwitterionic polymeric building blocks (see Fig. 3.1).

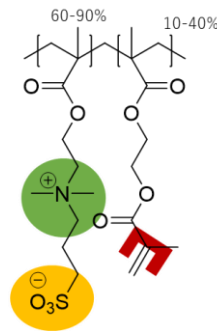


Figure 3.1 Zwitterionic crosslinkable target molecule.

Ideally, such coating should be applied during filtration, enabled by the concentration polarization phenomenon, with the purpose of mimicking free bulk gelation conditions in the boundary layer. Tight anchoring of hydrogel onto negatively charged membrane surfaces is guaranteed by retention of a positively charged macromolecular linker, previous to surface selective gelation. Ultimately, this approach aimed at addressing the challenges of stable anchoring, surface-selectivity and scalability. The general idea of CP enabled polymerization is depicted in Fig. 3.2.

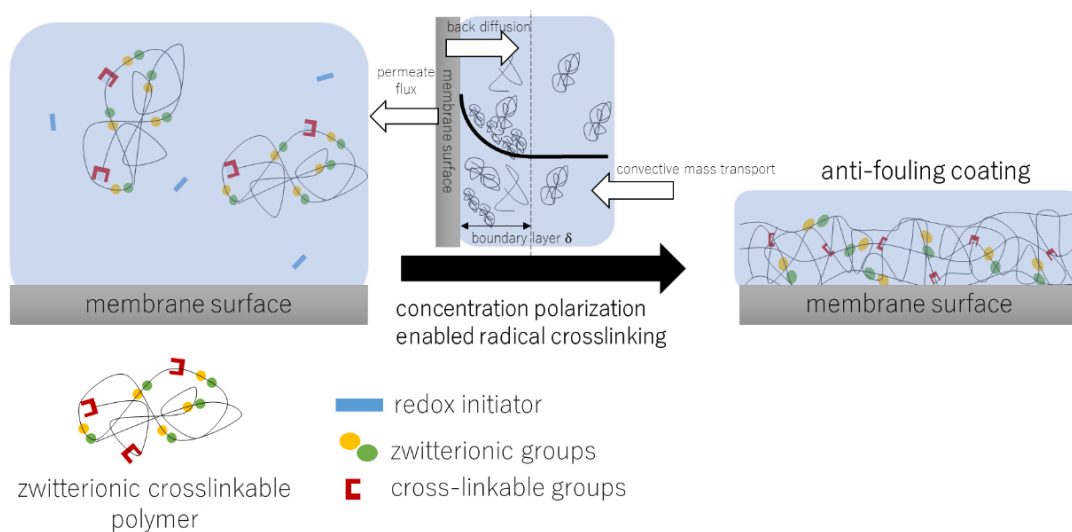


Figure 3.2 Concentration polarization enabled modification of membrane surface with polyzwitterionic and crosslinkable macromolecules.

The objectives and goals of this thesis are therefore:

- a) development of a polyzwitterionic (and cationic surface linker) material and demonstrate its general crosslinking possibility in free bulk
- b) investigation of hydrogel formation onto membrane surface during filtration via concentration polarization enabled radical polymerization
- c) demonstration of the possibility to control the coating degree by modifying gelation conditions
- d) modeling concentration polarization based on iterative mass transport and compare free bulk gelation with surface crosslinking

This project therefore may act as a first step towards mimicking free bulk gelation and therefore represent a pioneering work towards well-controlled (or more precise duplication of) hydrogel networks onto (dense) membrane surfaces.

### 3.2 Goals

The sub-goals of this research project can be grouped into two main categories:

- a) material development
- b) application onto dense membranes

#### Material development

(i) *Synthesis of crosslinkable zwitterionic polymer and surface linker*

The first goal of this research project is to establish a synthesis method for a polyzwitterionic macromolecule containing crosslinkable units. In addition, synthesis and adsorption of a macromolecular surface linker containing anchoring and crosslinkable side functionalities should guarantee tight linking of hydrogel coating to membrane surface.

(ii) *Free bulk zwitterionic hydrogel formation*

After successful building block synthesis, gelation reaction, initiated by APS and TEMED, should be studied in free bulk via rheological measurements (gelation time, critical gelation concentration, mechanical properties).

## Application in membranes

### *(iii) Surface modification of NF membranes via CP enabled crosslinking*

The crosslinking in free bulk is followed by establishing the hydrogel network onto dense polyamide membranes surfaces. Moreover, the coating is applied in situ during dead end filtration, enabled via concentration polarization of polyzwitterionic building blocks and previous adsorption of cationic macromolecular surface linker onto negatively charged PA membrane surface. Additionally, several modification parameters are varied in order to tailor coating degree (hydrogel layer thickness).

### *(iv) Investigation of modified membrane properties*

The successfully implemented zwitterionic hydrogel modified membranes should be discussed and compared to non-modified, pristine PA membranes in terms of their permeability and selectivity characteristics in combination with their anti-fouling abilities.

### *(v) Estimation of CP*

Finally, insights into the extent of CP are gained by modelling the polymer concentration at the membrane surface. The approximation of CP allows to discuss and compare gelation reaction on membrane surface to free bulk crosslinking. Furthermore, the model may lead to improved control of gelation reaction by simulating the impact of operational conditions (feed concentration, flux, filtration time) on CP. Ultimately, improved understanding and controllability could enable to generate ultrathin hydrogel layers in situ with minor water permeability reduction but sufficient anti-fouling properties.

## 3.3 Work plan

### *(i) Synthesis of crosslinkable zwitterionic polymer and surface linker*

The synthesis of zwitterionic macromolecule was based on free radical copolymerization of two monomers, DMAEMA and HEMA (hydroxyethyl methacrylate). The ratio and amount of HEMA (10-40%) and DMAEMA (60-90%) as well as initiator Azobisisobutyronitrile (AIBN) content (0.05-0.6 wt.%) were varied and its impact on the macromolecular weight, distribution and composition were analyzed via SEC size exclusion chromatography and <sup>1</sup>H-NMR.

Introduction of methacrylate groups with MAC, which act as crosslinkable functionalities, was followed by well-reported sulfobetainization with 1,3-propanesultone. Conversion into functional units was investigated via <sup>1</sup>H-NMR (nuclear magnetic resonance). The whole

reaction scheme is presented in Fig. 3.3. Additionally, the hydrodynamic diameter of the target molecules is measured via dynamic light scattering (DLS).

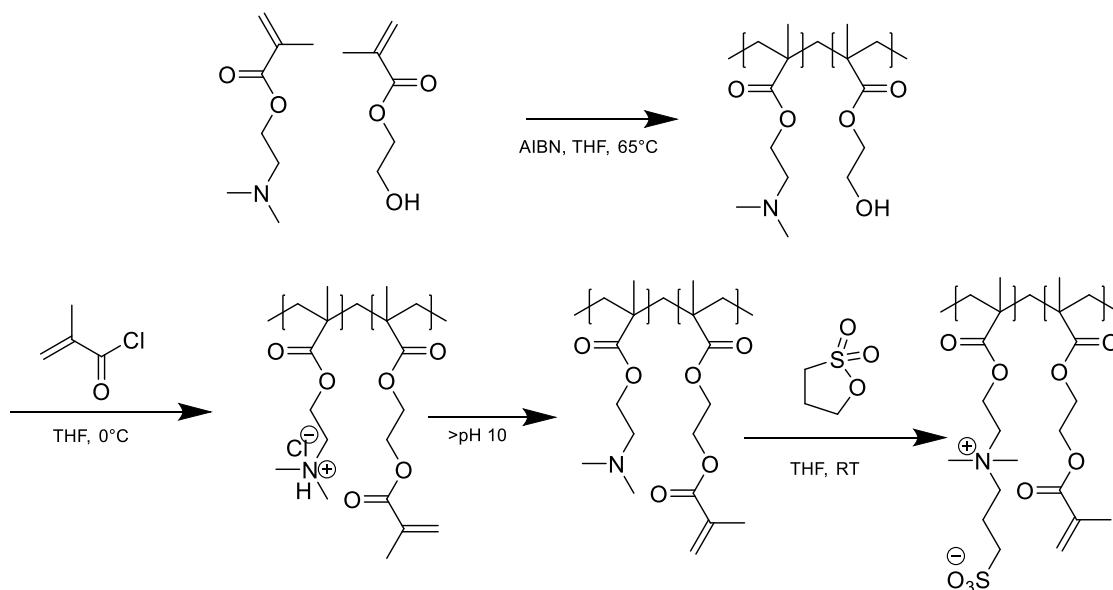


Figure 3.3 Polymer synthesis reaction scheme.

The synthesis of macromolecular surface linker was obtained by a similar synthetic pathway, only differing in the last functionalization step. Instead of possessing zwitterionic side functionalities, the synthesis of macromolecular linker introduced cationic charged groups by nucleophilic reaction with methyl iodide (see Fig. 3.4).

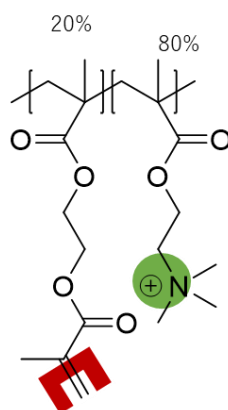


Figure 3.4 Cationic macromolecular surface linker.

### (ii) Free bulk zwitterionic hydrogel formation

Dissolved in water, above overlap concentration and in presence of radicals, polyzwitterionic, crosslinkable polymers should form a hydrogel network. The necessary conditions and their

impact on gelation reaction as well as network properties were studied via rheological measurements in following order.

First, overlap concentration was studied by measuring viscosities of variously concentrated polymer solutions (0-10 wt.%). The gelation was initiated by adding redox system APS and TEMED to variously concentrated polymer solutions above overlap concentration. The crosslinking reaction was studied via rheological measurements with the purpose to investigate the influence of polymer and radical content on mechanical properties and gelation time.

*(iii) Application onto membranes via CP enabled coating*

After studying hydrogel formation in free bulk, hydrogel coating was applied onto membranes surface. Commercially available NF90 and NF270 Dow Filmtec membranes with selective polyamides layers were used. Before hydrogel coating, cationic surface linker was first adsorbed on negatively charged PA films. Thereafter, crosslinking reaction was initiated on membrane surface via dead end filtration of the gelation solution (containing polyzwitterionic building blocks and redox-initiator below overlap concentration). Due to complete retention of macromolecules, the concentration of reactive agents were increased at the membrane surface. Consequently, when polymer and radical content exceeds critical gelation concentrations in boundary layer, gelation was initiated at membrane surface. Membrane modification was therefore studied in dependence of polymer and initiator feed concentration as well as filtration/reaction time.

*(iv) Investigation and characterization of hydrogel modified membrane properties*

After modification, changes in water permeability and salt rejection were studied in order to verify successful coating. In addition, membranes were analyzed via several methods including infrared spectroscopy (IR), scanning electron microscope (SEM), zeta potential and contact angle measurements. Furthermore, anti-fouling properties were evaluated via both static adsorption and filtration experiments using protein solutions (Myoglobin and Bovine serum albumin). Results were discussed and compared to characteristics of pristine membranes. Furthermore, hydraulic resistances and Darcy permeabilities of hydrogel layers were calculated.

*(v) Modelling of CP and comparison between surface and free bulk gelation*

Polymer concentration in boundary layer was estimated by modeling mass transport during dead end filtration. For that purpose, a mathematical approximation based on Film model

presuppositions was developed. However, it is important to notice that steady state of CP conditions cannot be obtained during dead end mode, due to permanent change in feed volume and concentration. Thus, CP cannot be calculated using equations derived from common Film model. Instead, mass transport for short time intervals (convective flux towards and diffusive flux away from the membrane surface) was considered to estimate CP. Furthermore, the iteration of mass transport allows to model the extent of dynamic CP (course of CP over time). The model and its fundamental assumptions are explained in more detail in section 4.7.2.

The gained insights into quantitative nature of CP for macromolecules allowed to adjust polymer feed concentration, flux as well as filtration/reaction time during surface modification of NF270 membranes and investigate their influences on estimated CP. By comparing free bulk gelation conditions with estimated concentrations at the membrane surface, the model is critically discussed in terms of its reliability to predict in situ gelation in boundary layer.

## 4 Materials and methods

### 4.1 Chemicals and membrane materials

Table 4.1 Chemicals used in this work.

Chemicals	Abbreviation	Company
1,3-Propanesultone	PS	Sigma Aldrich
2-(Dimethyl amino)ethyl methacrylate	DMAEMA	Sigma Aldrich
2-(Hydroxyethyl) methacrylate	HEMA	Sigma Aldrich
Azobisisobutyronitrile	AIBN	Sigma Aldrich
Ammonium persulfate	APS	Sigma Aldrich
Chloroform	CHCl <sub>3</sub>	Acros Organics
Deuterated water	D <sub>2</sub> O	Sigma Aldrich
Deuterated chloroform	CDCl <sub>3</sub>	Sigma Aldrich
Diethylether	-	Fisher Scientific
Ethanol	EtOH	Fisher Scientific
Iodomethane	-	Sigma Aldrich
Magnesiumchloride	MgCl <sub>2</sub>	Sigma Aldrich
Methacryloyl chloride	MAC	Sigma Aldrich
Potassium chloride	KCl	Sigma Aldrich
Potassium hydroxide	KOH	Bernd Kraft
Sodium chloride	NaCl	Sigma Aldrich
Sodium hydroxide	NaOH	Bernd Kraft
Sodium sulfate	Na <sub>2</sub> SO <sub>4</sub>	Sigma Aldrich
Tetrahydrofuran	THF	Acros Organics
Tetramethylenediamine	TEMED	Acros Organics
Triethylamine	TEA	Acros Organics

In this work, two PA TFC flat sheet membranes, NF270 or NF90 Dow Filmtec membranes were used. Both NF membrane types consist of three common polymeric layers, explained in section 2.2. However, the active PA layers are different for each membrane. NF270 has a semi-aromatic nature, resulting from interfacial polymerization of TMC and piperazine. In contrast, barrier layer of NF90 membranes is made by interfacial polymerization of TMC and MPD and is therefore fully aromatic. Consequently, both membranes demonstrate different physico-chemical surface properties, which will affect membrane performance and fouling propensity. The membrane properties will be discussed in more detail in section 5.5 and respectively 5.6.

## 4.2 Polymer synthesis

### 4.2.1 Free radical copolymerization of DMAEMA and HEMA

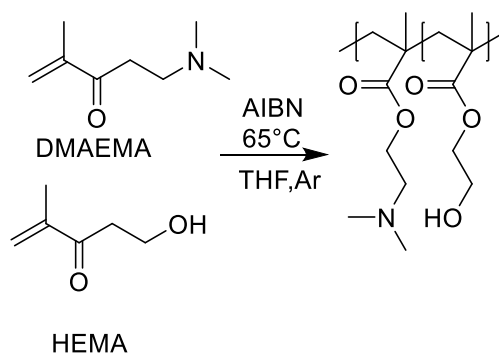


Figure 4.1 Free radical polymerization of HEMA and DMAEMA.

A solution containing HEMA (constituting 10-40 mol.% of monomer portion) and DMAEMA (constituting 90-60 mol.% of monomer portion) were dissolved in Tetrahydrofuran (THF) in a 100 mL two neck round bottom flask so that the monomer concentration was set at 2.5 mol/L. The mixture was subsequently degassed for 15 minutes with Argon gas before AIBN (0.05-0.6 wt.%) was added to the monomers' mixture. The temperature was increased to 65 °C and the reaction was performed under reflux. After 24 h, the viscous solution was let to cool down to room temperature. Thereafter, the copolymer was precipitated in cold diethyl ether. Finally, poly((dimethylamino)ethyl methacrylate-co-hydroxyethyl methacrylate) copolymer (P(DMAEMA-co-HEMA)) was dried at 40°C in a vacuum oven for 24 h. The copolymer composition was characterized using NMR-spectroscopy, and average molecular weight (MW) was determined using SEC.

#### 4.2.2 Acrylation of P(DMAEMA-co-HEMA)

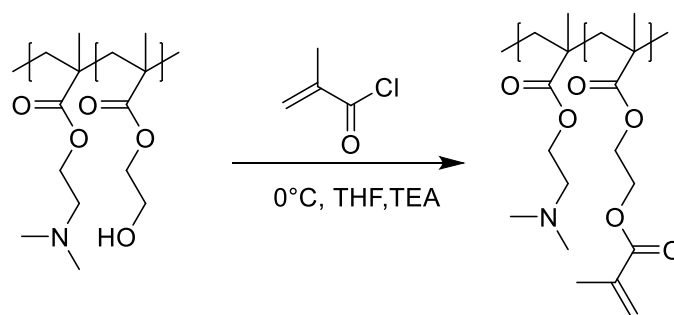


Figure 4.2 Acrylation of HEMA side functionalities.

3.0 g of P(DMAEMA-co-HEMA) was dissolved in 75 mL THF in a 250 mL two-neck round bottom flask and cooled down to 0°C. Subsequently, triethylamine (1,3-fold excess compared to HEMA units) was added. Afterwards, methacryloyl chloride (MAC) (10-fold excess compared to HEMA units) was first dissolved in 51 mL THF and then added to the polymer solution dropwise for one hour. The reaction mixture turned white immediately. After an additional hour, the ice bath was taken away so that the reaction could proceed for two days at room temperature. Thereafter, water was added to quench the reaction and THF was removed via rotary evaporation. The polymer was then precipitated by adding NaOH (1 mol/L) until the pH was approximately 10. The aqueous solution was discarded and the functionalized polymer was dried in vacuum oven at 40°C. Finally, successful conversion and composition of poly(dimethyl amino)ethyl methacrylate-co-(2-methacryloylmethyl) methacrylate (PDMAEMA-co-MAMMA) was analyzed via NMR.

#### 4.2.3 Sulfobetainization of P(DMAEMA-co-MAMMA)

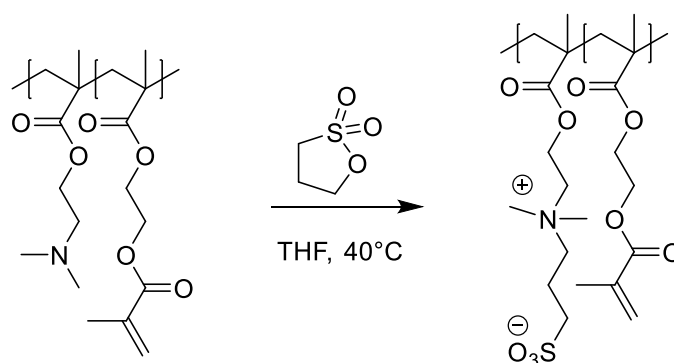


Figure 4.3 Sulfobetainization of DMAEMA side units.

2.0 g of P(DMAEMA-co-MAMMA) was dissolved in 48 mL THF in a 100 mL one-neck round bottom flask and heated up to 40°C under reflux. Subsequently, 1,3-propanesultone (1.5-fold

excess compared to DMAEMA units) was added to the solution. The polymer mixture was precipitated and swelled overnight, before it was dissolved again by adding water. Removal of THF by rotary evaporation was followed by removal of 1,3-propanesultone via dialysis washing (12-14 kDa) for three days. Finally, poly(sulfobetainethyl) methacrylate-co-(2-methacryloylmethyl) methacrylate) (PSBMA-co-MAMMA) was obtained by freeze-drying and zwitterionic functionalization was verified using NMR-spectroscopy.

#### 4.2.4 Quaternization of P(DMAEMA-co-MAMMA)

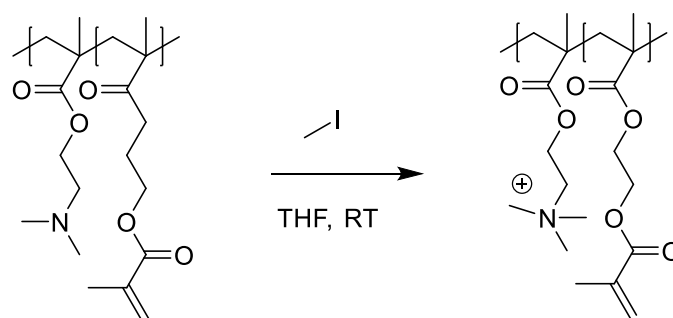


Figure 4.4 Quaternization of DMAEMA units.

2.0 g of P(DMAEMA-co-MAMMA) was dissolved in 48 mL THF in a 100 mL one-neck round bottom flask. Subsequently, iodomethane (1.3-fold excess compared to DMAEMA units) dissolved in 10 mL THF was added dropwise to the solution. The polymer mixture was immediately precipitated and the reaction was terminated after 3 hours. The cationic polymer was dissolved by adding water. The removal of iodomethane was performed with the aid of a cooling trap. THF was subsequently evaporated via rotary evaporator and cationic macromolecular linker was obtained by freeze-drying. Finally, successful conversion of DMAEMA units was confirmed via NMR-spectroscopy

### 4.3 Polymer characterization

#### 4.3.1 NMR spectroscopy

NMR spectroscopy was used to identify the composition and functionalization degree of polymers. Briefly, synthesized polymer (20 mg) was dissolved in deuterated solvents (0.8 ml) and samples were analyzed in DRX300 spectrometer (*Bruker*). Polymer structure was investigated using *MestreNova software*. The integration of spectra peaks allowed the determination of macromolecular composition. Furthermore, free radical reaction kinetics were studied. Briefly, the conversion of HEMA and DMAEMA was investigated by taking reaction mixture samples and comparing ratio of monomer to polymer peaks over time.

#### 4.3.2 Size exclusion chromatography (SEC)

Size exclusion chromatography is a method to determine molecular weights and size distribution of a solution containing macromolecules. Briefly, an aqueous or organic solvent containing polymer (mobile phase) is pumped through a column (stationary phase), which is filled with porous beads. Dependent on their hydrodynamic volumes, analytes can diffuse into bead pores. Small molecules can enter into more pores and hence, travel a longer distance than large macromolecules, which pass by the pores. Consequently, elution time is a function of polymer size or hydrodynamic volume. Ideally, influence of physico-chemical interactions on elution time can be neglected, so that retention is solely dependent on particle size. The overall principle is demonstrated schematically in Fig. 4.5.<sup>135, 136</sup>

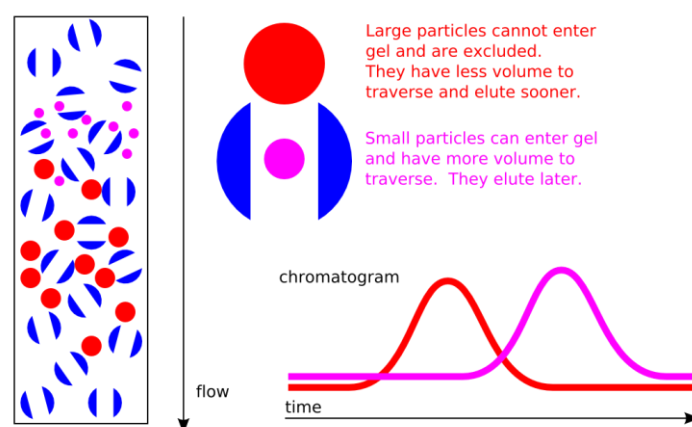


Figure 4.5 Principle of SEC and example for obtained chromatogram.<sup>137</sup>

To derive molecular weight from retention time, two calibration methods are known, and both have been used in this work: relative and universal. Relative calibration allows determining MW of an unknown sample by comparing retention times of standards with known molecular weights possessing a narrow distribution. Typical narrow standards are represented by poly(methyl methacrylate) (PMMA), polystyrene (organic system), or poly(ethylene oxides) and poly(ethylene glycols) (aqueous system). After several measurements for standard polymer samples and a polynomial fitting, a calibration plot between  $\log MW$  vs. retention time can be obtained.<sup>135, 138</sup>

To determine the polymer concentration at different elution times, mostly refractive index or UV-spectroscopy is applied. By knowing polymer concentration, the number weighted average  $M_n$  and mass weighted average  $M_w$  can be calculated. Furthermore, the ratio of  $M_n$  and  $M_w$

gives polydispersity index (PDI), which is a unitless term that describes the “non-uniformity” of a polymer distribution.<sup>135</sup>

Since SEC is dependent on hydrodynamic volume, relative calibration may differ from correct MW. For a known standard and a chemically different sample with the same molecular weight, hydrodynamic volumes are not equal. This is due to differences in solvent-polymer interactions and their effect on polymer expansion. Hence, elution time will vary for two chemically different, but same MW polymers and limit application of relative calibration to macromolecules with similar chemistry. For example, in a polar eluent a less polar polymer (compared to standard) will exhibit smaller hydrodynamic size, which will enhance diffusion into pores. This will result in longer retention and consequently underestimation of the MW.

In contrast, universal calibration is based on the proportional relation between the product of intrinsic viscosity and molecular weight,  $[\eta]M$ , and the hydrodynamic volume. Benoit et al. have shown that plotting  $\log [\eta]M$  against retention for a variety of narrow distributed standard samples results in one calibration line. Consequently, the molecular weight of any polymer coil can be determined by using universal calibration method.<sup>139</sup>

Sometimes logarithm of intrinsic viscosity is plotted against the log MW. This fit is the so-called viscosity-law or Mark-Houwink plot. The Mark-Houwink plot is linear and is given by:

$$[\eta] = K M^\alpha \quad (4.1)$$

Whereby  $[\eta]$  represents intrinsic viscosity,  $M$  is mass weighted molecular weight,  $K$  and  $\alpha$  are polymer-solvent dependent constants.

Both  $\alpha$  and  $K$  can provide information about polymer-solvent interactions as well as polymer shape. They are derived from slope ( $\alpha$ ) and intercept ( $K$ ) of linear fit. Experimental values often demonstrate inverse correlation between  $\alpha$  and  $K$ .<sup>140</sup>

$\alpha$  indicates the morphology of a macromolecule in solution. Generally, a higher  $\alpha$  value means more attractive solvent-solute interactions presents. For a complete spherical coil (minimization of interactions),  $\alpha$  is 0. When  $\alpha$  is maximal ( $\alpha = 2$ ), the polymer expands and can be visualized as a rigid rod. In contrast,  $K$  gives the extent of polymer-solvent interactions.<sup>135, 140</sup>

In this work, both calibration methods were used to determine molecular weight and PDIs for synthesized copolymer P(DMAEMA-co-HEMA). Samples were first dissolved in dimethylacetamide (DMAc) containing LiBr (0.01 mol/L), so that polymer concentration was

4 g/L. The solution was injected into an organic based *PSS GRAM* column, which was filled with polyester copolymer beads (separation range 0.5-1000 kDa) and elution rate was adjusted to 1 mL/min via *PU-2080 Plus pump (Jasco)*. The temperature during measurement was kept constant at 60 °C and detection was finally performed with *ETA-2020 (WEG Dr. Bures)*. For relative calibration method narrow distributed PMMA standards (0.1-1000 kDa, *PSS Polymers*) were used.

#### 4.4 Polymer in solution

##### 4.4.1 Polymer solubility

The solubility of zwitterionic copolymer P(SBMA-co-MAMMA) in water was determined via cloud point measurements. A copolymer solution with 10 wt.% was used as stock solution. By adding specific and calculated amount of water, concentration was reduced step wise for 0.5 or 1 wt.%. After each reduction in polymer concentration, the solution was visually investigated for persistent turbidity. Dilution was proceeded until no turbidity could be observed and corresponding concentration was determined as solubility limit.

##### 4.4.2 Viscosity measurements

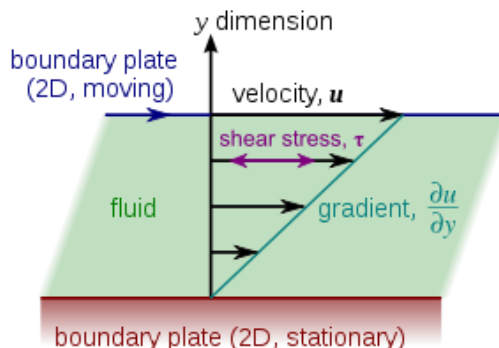


Figure 4.6 Schematic representation of planar Couette flow and consequent resistance of a fluid to shear deformation.<sup>141</sup>

Rheology studies the flow and deformation properties of materials, especially of fluids. Generally, viscosity  $\eta$  of a fluid is defined as its resistance to deformation, or the ratio of shear stress  $\tau$  to shear rate  $\gamma$  in a simple shear flow, see equation 4.2. The resistance results from inner friction by adjacent moving layers and can be illustrated with planar Couette flow.<sup>142</sup>

$$\eta = \frac{\tau}{\gamma} \quad (4.2)$$

When a fluid is trapped between a moving plate with constant velocity  $u$  and a fixed plate with a distance  $h$ , the fluid will be sheared causing shear stress. As fluid layers will experience inner friction, the velocity of fluid layers will gradually decrease as they approach the stationary plate. Shear stress  $\tau$  and rate  $\gamma$  are defined by the following equations:

$$\tau = \frac{F}{A} \quad (4.3)$$

$$\gamma = \frac{u}{h} \quad (4.4)$$

With  $F$  is applied force,  $A$  as cross-sectional area of the material,  $u$  velocity of the moving plate and  $h$  distance between the moving and the stationary plate.

In this work, the viscosity of polymer solutions with various concentrations (0-10 wt.%) was studied via a rotary viscosimeter *Physica MCR301 (Anton Paar)* using cone-plate geometry. This allows determining the overlap concentration of the polymer solution, at which the slope of viscosity against concentration increases.

In detail, 200  $\mu\text{L}$  polymer solution was added to the plate and homogeneously distributed. Before the experiment was started, the gap between the two plates was adjusted down to 0.1  $\mu\text{m}$ . Finally, viscosity was measured at room temperature (25  $^{\circ}\text{C}$ ) by applying a shear rate, which was varied from 0.01 to 800  $\text{s}^{-1}$ , in order to categorize polymer solution as Newtonian or non-Newtonian fluid.

#### 4.4.3 Dynamic light scattering

Dynamic light scattering is a non-invasive optical method to analyze the Brownian motion of particles in solution (size range from 0.3 nm-10  $\mu\text{m}$ ), in order to determine particle size. Monochromatic laser light is scattered in all directions (Rayleigh scattering) when it passes through a dispersion due to different refractive indexes. However, due to size dependency of Brownian motion, scattering intensity is fluctuating over time. Furthermore, scattered light will interfere constructively or destructively with scattered light of other particles in the surroundings. Consequently, interference and Brownian movement will cause a dynamic light pattern, which can be analyzed via autocorrelation and various mathematical approaches.<sup>143</sup>

In this work, polymer solutions (0.1 g/L) were analyzed in pure water or KCl solutions (1-5 mM) using *Zetasizer Nano ZS (Malvern Instruments)*. 750  $\mu\text{L}$  of sample solution was placed in a capillary cell (DTS1070) and laser light was generated by a HeNe laser (4 mW,  $\lambda=633$  nm) with a scattering angle of 173 $^{\circ}$ . The refractive index of synthesized polymers was

assumed to be similar to PMMA (1.49). Every sample was measured 30 times, ten seconds each, to obtain an average value for the hydrodynamic diameter.

Besides measuring untreated samples, scattering of solutions was also performed after prefiltration of zwitterionic copolymers in order to reduce possible agglomeration. Therefore, polymer solutions with two different concentrations (0.1 and 0.2 g/L) were filtered at 1 bar with an MF PES membrane (Sartorius, pore size 0.1  $\mu\text{m}$ ), before DLS measurements were performed as described above.

#### 4.5 Free bulk gelation

Besides determination of viscosity, polymer gelation was also studied using oscillatory experiments, in which non-stationary sinus like input signal is applied in the form of stress. As response a sinus-like and by the angle  $\delta$  shifted deformation is measured. The ratio of applied deformation and monitored shear stress is called dynamic (or complex) shear modulus and is exemplary for viscoelastic material properties:

$$G^* = \frac{\tau(t)}{\gamma(t)} \quad (4.5)$$

With  $G^*$  is complex shear modulus,  $\tau(t)$  as time dependent shear stress and  $\gamma(t)$  as time dependent shear rate.

The dynamic shear modulus can be divided into two variables, storage and loss modulus ( $G''$  and  $G'$ ). Storage modulus  $G'$  is a measure for the elastic properties of a material and its capability to store energy in its structure. Hence, the elasticity of a sample is responsible for reversible mechanical impact, which allows a material to regain its original form after mechanical stress and subsequently undergo relaxation. In contrast, loss modulus  $G''$  represents viscous material portion, whereby mechanical stress results in energy dissipation, mostly in the form of heat caused by friction. Therefore, viscous materials experience an irreversible deformation.<sup>142</sup>

The ratio of loss to storage modulus is known as the damping factor, which is a measure for a sample capability to absorb energy. It is defined as:

$$\tan \delta = \frac{G''}{G'} \quad (4.6)$$

Based on the viscoelastic properties, samples can be divided into liquid ( $G'' > G'$ ), gel- or sol-transition ( $G'' \approx G'$ ) and gel or solid-state ( $G' \gg G''$ ).

In this work, the gelation reaction was monitored by measuring storage and loss modulus for 120 min at const. angular frequency 10 Hz and an amplitude deflection of 0,1 mrad. For that purpose, zwitterionic crosslinkable polymer was dissolved in water at different concentrations (5, 7.5 and 10 wt.%). The reaction was initiated by adding APS and TEMED in various ratios to amount of methacrylate groups (see Tab. 4.2) into polymer solution and thorough homogenization of reaction sample by using Vortex mixer. Subsequently, measurement was started by placing 400  $\mu$ L of liquid mixture onto rheological setup and adjusting plate-cone gap to 0.101 mm. Crosslinking or gelation point was reached when storage equals loss modulus. However, gelation was performed for 120 minutes and was considered as completed when storage modulus did not further increase. If formation of hydrogel did not occur within 2 hours, gelation reaction was considered unsuccessful.

Table 4.2 Free bulk gelation conditions.

Polymer concentration [wt.%]	APS:Acrylate ratio	APS:TEMED ratio
4	1:2	1:8
5	1:10	1:8
5	1:5	1:8
5	1:2	1:8
5	1:10	1:2
5	1:10	1:16
7.5	1:10	1:8
7.5	1:5	1:8
7.5	1:2	1:8
10	1:10	1:8
10	1:5	1:8
10	1:2	1:8

## 4.6 Membrane performance and modification

### 4.6.1 Pretreatment

Before use, flat sheet NF270 or NF90 Dow Filmtec membranes were cut into circular samples with a diameter of 48 mm. Afterwards, membranes were washed first for 1 h in 1:1 EtOH-water mixture, followed by washing overnight using pure water. Then, membranes have been placed into a stainless-steel dead end cell and compacted at 15 bar until permeability was constant (~90 minutes).

Membrane performance of modified and unmodified NF membranes was evaluated by measuring water permeability as well as salt rejection. For that purpose, flat sheet membranes with a diameter of 48 mm were placed with the active layer facing upwards in a dead end stainless-steel cell with a permeation area of about 9.62 cm<sup>2</sup> and a feed volume of about 100 mL. Pure water was introduced and flux was measured at a pressure of approximately 15 bar. The membrane permeability was measured every 30 minutes for 3 minutes until permeability was constant (usually, 90 minutes). Water permeability was determined using equation 4.7 by weighing permeated water mass in a given filtration time:

$$P_{water} = \frac{m_{water}}{\rho_{water} \cdot A \cdot t \cdot \Delta p} \quad (4.7)$$

Where  $P_{water}$  is permeance,  $m_{water}$  is permeated water mass,  $\rho$  is water density at room temperature (0.997 g/cm<sup>3</sup>),  $A$  is effective membrane area (9.89 cm<sup>2</sup>) and  $\Delta p$  is the transmembrane pressure.

Rejection measurements were performed for different salt and organic solutions. Salt and organic solutions of NaCl (2000 ppm), Na<sub>2</sub>SO<sub>4</sub> (2000 ppm) and MgCl<sub>2</sub> (2000 ppm), APS (1000 ppm) and TEMED (1000 ppm) were filtrated at a stirring rate of about 300 rpm. In order to determine salt rejection, 10 mL of permeate was collected and the conductivity was measured by using conductometer *Lab 960 (Schott Instruments)*. Subsequently, the rejection was calculated using equation 4.8 by comparing feed and permeate conductivity:

$$R_{salt} = \frac{\sigma_f - \sigma_{pe}}{\sigma_f} * 100 \quad (4.8)$$

Where  $R$  is the rejection in %,  $\sigma_f$  and  $\sigma_p$  are the conductivities of feed or respectively permeate.

In addition, the rejection of organic TEMED was determined using total organic carbon measurements (*TOC-analyzer, Shimadzu*) and the following equation:

$$R_{TOC} = \frac{TOC_f - TOC_p}{TOC_f} * 100 \quad (4.9)$$

Where  $R$  is the rejection,  $TOC_f$  and  $TOC_p$  is total organic carbon of feed or respectively permeate sample.

#### 4.6.2 Surface linker adsorption

To guarantee tight anchoring of hydrogel to the membrane surface, a macromolecular linker was firstly adsorbed onto PA layer. For that purpose, surface linker was dissolved in pure water

(1 g/L) and 25 mL was introduced into the cell. The solution was stirred at 300 rpm and adsorption was allowed to take place for one hour. Thereafter, solution was discarded and the membrane was washed five times with pure water and one time with NaCl solution (2000 ppm).

#### 4.6.3 Membrane modification and modified membranes' permeability

For membrane modification, P(SBMA-co-MAMMA) was dissolved in 100 mL of pure water. Then, redox-initiators APS and TEMED were added directly before the solution was introduced to the cell. Afterwards, a constant pressure of approximately 12 to 15 bar was applied, so that the initial flux was adjusted between 18 and 22 L/hm<sup>2</sup>. The membrane modification was monitored by measuring permeability. To terminate the modification reaction, the pressure was released, and the membrane was washed 10x using pure water and 2x using NaCl solution (2000 ppm). An example of a typical membrane modification procedure and its corresponding flux course is given in Fig. 4.7.

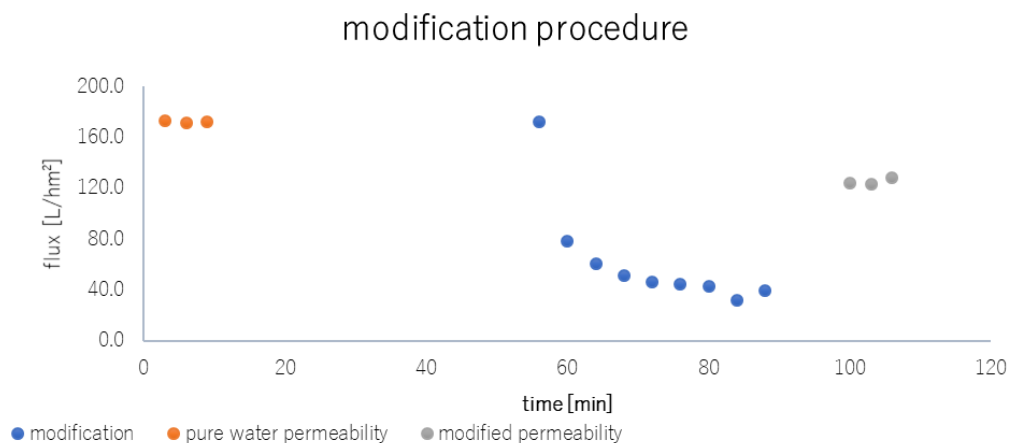


Figure 4.7 Membrane modification procedure: flux in dependence of time with rinsing after adsorption and modification step.

For each membrane type a different approach was pursued. For NF90 membranes a specific experimental approach was followed, in which the portions of reacting compounds in the boundary layer were not estimated before modification. Initiator concentration was kept constant for each modification and only polymer feed concentrations were varied. This approach should prove general possibility of CP enhanced surface selective gelation and investigate influence of polymer feed concentration on modification degree. Used parameters in NF90 modification are shown in Tab. 4.3.

Table 4.3 NF90 membrane modification feed parameter.

Polymer feed concentration [wt.%]	APS feed concentration [wt.%]	TEMED feed concentration [wt.%]
0.0001	0.01	0.025
0.0002	0.01	0.025
0.0005	0.01	0.025
0.001	0.01	0.025
0.002	0.01	0.025
0.005	0.01	0.025
0.0075	0.01	0.025

In contrast, the portions of polymer and initiator in the boundary layer were calculated prior to modification process for NF270 membranes. This is explained in detail in section 4.7. Both concentrations were varied in order to investigate the influence of redox-initiator feed amount as well as polymer feed content on hydrogel layer thickness and permeability reduction. In addition, modified membranes are named in the following manner: “ZHMMX NF90/NF270 yy”, which is the abbreviation for *zwitterionic hydrogel modified membrane X* (number of polymer batch) with yy as polymer feed concentration and NF90 or NF270 as pristine membrane.

To determine the degree of modification, membrane performance was tested after the modification process via measuring of water permeability and salt rejection for NaCl (2 g/L) and MgCl or respectively Na<sub>2</sub>SO<sub>4</sub> (2000 ppm). The maintained permeability was determined by the ratio of modified permeability ( $P_{mod}$ ) and pristine permeability ( $P_0$ ):

$$\text{Maintained permeability [\%]} = \frac{P_{mod}}{P_0} \quad (4.10)$$

#### 4.6.4 Critical and limiting flux

Additionally, critical and limiting flux measurements were performed (for NF270 membranes) for various concentrated polymer feed solutions. Therefore, flux was measured 3 times for 1 minute at different applied pressures (3 up to 15 bar). After every measurement, cell was refilled with polymer solution in order to perform measurements with same feed conditions.

In addition, filtrations for different concentrated polymer solutions were performed for 30 minutes at highest pressures. The filtrations were performed to determine, if irreversible fouling occurs.

## 4.7 Calculation of concentration polarization

### 4.7.1 Estimation of boundary layer thickness

First, to generate any information regarding the extent of CP, boundary layer thickness has to be estimated indirectly by calculating the mass transfer coefficient. However, since the polymer is entirely rejected by the membrane, mass transfer coefficient and consequently boundary layer thickness can only be measured for a semi-permeable compound (see section 2.4).<sup>59</sup>

Hence, for determination of boundary layer thickness, dead end filtration with semi-permeable monomer HEMA was performed. Observed rejection  $R_{ob}$  as well as volume flux was determined at different stirring rates (0-1000 rpm) and constant pressure (15 bar). Feed concentration of HEMA was kept relatively low (90 ppm) in order to minimize sorption effects onto the membrane and not to exceed solubility limits in the boundary layer. The rejection was determined by measuring permeate and feed concentration 3 times for each stirring rate via TOC-measurements. Flux was monitored for three minutes. After every filtration step, cell was filled with a 45 ppm HEMA solution, which was approximately the permeate concentration and allowed to guarantee constant feed concentration. After taking three samples, stirring rate was increased about 200 rpm and measurements were repeated.

The rejection  $R$  of HEMA is a function of stirring rate and follows equation 2.12 (see section 2.4).

The stirring rate dependent mass transfer coefficient  $k_d$  was assumed to follow the relationship developed by Opong and Zydney<sup>144</sup>:

$$k_d = k'_d \omega^{0.567} \quad (4.11)$$

Where  $\omega$  is stirring velocity and  $k'_d$  is cell-specific solute dependent mass transfer coefficient. Additionally, for HEMA filtration without stirring a finite value of  $\omega = 10.6$  rpm was assumed.<sup>133</sup>

Inserting the mass transfer coefficient relationship in equation 2.12,  $R$  and  $k'_d$  give intercept and slope in  $\ln(R/1-R)$  vs.  $J_v \omega^{-0.567}$  plot. Finally, boundary layer thickness could be calculated with the aid of Film model, resulting in equation 4.12:

$$\delta = \frac{D_{HEMA}}{k_d} \quad (4.12)$$

Whereas  $D_{HEMA}$  is the diffusion coefficient of HEMA ( $5.9 \cdot 10^{-10}$  m<sup>2</sup>/s in water at room temperature).

#### 4.7.2 Estimation of dynamic CP

Ideally, transferring free bulk gelation conditions into membrane modules would allow control over crosslinking reaction and consequent adjustment of hydrogel properties like thickness and mechanical properties. To mimic free bulk gelation, knowledge of concentration polarization is essential. However, since modifications were performed in dead end mode, a steady state for CP cannot be achieved.

As proposed by the Film model, a defined laminar boundary layer of rejected compounds will be formed in a stirred cell due to the balancing of convective mass transport towards and diffusive transport away from membrane surface. Thus, to estimate the extent and course of concentration polarization over time in a continuous process, convective flux towards membrane surface and diffusion back into bulk were calculated iteratively for short intervals by utilizing experimental flux data obtained during membrane modification.

Calculation of CP by an iterative approach was developed independently and was based on the following assumptions:

- 1) boundary layer thickness is constant over the whole filtration procedure and was estimated by a separate experiment (see section 4.7.1)
- 2) back diffusion is solely viscosity dependent; viscosities for different polymer concentrations are derived from rheological measurements (see section 4.4.2)
- 3) concentration was first considered constant in whole boundary layer (see Fig. 4.8 (b))

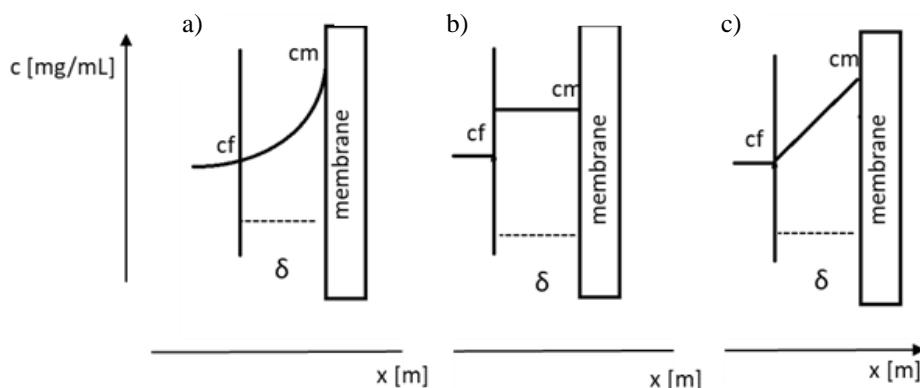


Figure 4.8 Concentration polarization – a) exponential course resulting from the Film model; b) homogenous distribution in the boundary layer; c) linear increase in boundary layer used in this work.

First, convectively transported mass towards the membrane was calculated:

$$m(t_i) = V(t)_i * c_f * R_i \quad (4.13)$$

Where  $m(t_j)$  is transported mass in time interval  $t_j$ ,  $V(t_j)$  is permeated volume in time interval  $t_j$  obtained by experimental values,  $c_f$  is feed concentration and  $R_i$  is rejection of component  $j$  ( $R_p = 1$ ).

Subsequently, the solute concentration at the membrane surface was determined using equation 4.14:

$$c_m(t_j) = \frac{m(t_j)}{A * \delta} + c_f \quad (4.14)$$

Where  $c_m$  is the concentration at the membrane surface,  $A$  is the effective membrane area and  $\delta$  is boundary layer thickness estimated from HEMA filtration experiment (see section 4.6.1). As back diffusion is assumed to be driven only by the concentration gradient, an average interval concentration  $\bar{c}_m$  at the membrane surface was needed and calculated with the following equation:

$$\bar{c}_m(t_j) = \frac{c_m(t_j) + c_m(t_{j-1})}{2} \quad (4.15)$$

Back diffused mass can then be derived by time extended Fick's law:

$$m_D = \frac{\bar{c}_m - c_f}{\delta} * D_i * t_j * A \quad (4.16)$$

Where  $m_D$  is back diffused mass and  $D_i$  is the diffusion coefficient of component  $i$ .

For polymer diffusion,  $D_p$  was determined by Stokes-Einstein equation and separate measurement of the radius by DLS measurements and concentration dependent viscosity:

$$D_P(t_j) = \frac{k_B T}{6\pi\eta(t_j)r} \quad (4.17)$$

Where  $k_b$  is Boltzmann constant,  $T$  is room temperature,  $r$  is polymer radius and  $\eta(t_j)$  is time dependent dynamic viscosity.

Viscosity was obtained by separate rheological measurements of polymer solutions and calculated for average concentration at the membrane surface with equation 4.18:

$$\eta(t_j) = \bar{c}_m(t_j) * \frac{d\eta}{dc} \quad (4.18)$$

Where  $\frac{d\eta}{dc}$  is the change of viscosity with concentration obtained in rheological measurements (see section 4.4.2).

With the aid of back diffused mass, a net transported mass  $m_{net}$  was obtained with equation 4.19 and consequently a corrected concentration at the membrane surface  $c_{m,corr}$  was calculated:

$$m_{net}(t_j) = m(t_j) - m_D(t_j) \quad (4.19)$$

$$c_{m,corr}(t_j) = \frac{m_{net}(t_j)}{A*\delta} \quad (4.20)$$

Finally, iterative concentration conditions for the following interval could be determined with the following equations:

$$c_m(t_{j+1}) = \frac{m(t_{j+1})}{A*\delta} + c_f(t_{j+1}) \quad (4.21)$$

$$c_f(t_{j+1}) = c_f(t_j) + \frac{m_D}{V(t_{j+1})} \quad (4.22)$$

Where  $V(t_{j+1})$  is feed volume at time interval  $t_{j+1}$ .

Compared to the ordinary Film model, where mathematical derivation gives an exponential function for concentration gradient, iterative calculation of CP, as seen above, is limited since it assumes a homogenous mass and concentration distribution in the boundary layer. However, to improve such limited representation of boundary conditions, a linear concentration gradient was assumed to exist (see Fig. 4.8 (c)).

A linear relationship between concentration in the boundary layer and distance  $x$  is given by:

$$c(x) = ax + b \quad (4.23)$$

Where  $m$  is the slope and  $b$  represents the intercept.

For  $x=0$ , it applies that the concentration at the beginning of the boundary layers is equal to the feed concentration  $c_f$ :

$$c(0) = b = c_f \quad (4.24)$$

Additionally, integration over the boundary layer volume gives the whole transported mass in the boundary layer:

$$\int_0^{V\delta} ax + c_f = m_{net} \quad (4.25)$$

$$\Rightarrow a = \frac{2m_{net}}{V_{\delta}^2} - \frac{2c_f}{V_{\delta}} \quad (4.26)$$

Where  $V_{\delta}$  is volume of boundary layer.

Inserting  $m$  and  $b$  into equation 4.23 allows determination of corrected linear concentration at the membrane surface:

$$c_{corr,m} = \left( \frac{2m_{net}}{V_{\delta}^2} - \frac{2c_f}{V_{\delta}} \right) V_{\delta} + c_f \quad (4.27)$$

The estimation of CP can help to adapt concentrations in the boundary layer to match free bulk gelation conditions by adjusting convective mass transport in membrane modification via flux or feed concentration variations. In addition, adjustment of filtration parameters and consequently control over CP is supposed to generate controllability of modification degree by influencing hydrogel layer thickness.

The alignment of CP to free bulk conditions was performed to evaluate the model by predicting whether gelation should occur on membrane surface or not and compare prediction to real outcome, i.e. reduced permeability attributed to successful gelation. Finally, the comparison led to judgment about validity of proposed model.

## 4.8 Membrane fouling

### 4.8.1 Protein adsorption

After measuring permeability and salt rejection of modified or unmodified membranes, 20 mL a protein solution (10 g/L bovine serum albumin (BSA), in 0.01 mol/L phosphate buffered saline (PBS) at pH 4.8 or Myoglobin, in 0.01 mol/L PBS at pH 7.0) was added to the dead end cell. The solution was stirred at 300 rpm for 1 h before the solution was discarded. Afterwards, the membrane was cleaned 10 times with MilliQ water and the permeability was determined a second time in order to evaluate the relative flux reduction caused by static adsorption.

$$RFR = \frac{P_{SA}}{P_0} * 100 \quad (4.28)$$

Equation 4.28 was used to calculate the relative flux reduction (RFR) where  $P_{SA}$  is the permeability after static adsorption and  $P_0$  is the initial permeability.

### 4.8.2 Protein filtration

Besides surface adsorption, also protein filtration experiments were performed. After determining permeability and salt rejection of modified or unmodified membranes, 100 mL

protein solution (1 g/L BSA, in 0.01 mol/L PBS at pH 4.8 or Myoglobin, in 0.01 mol/L PBS at pH 7.0) was introduced into the dead end cell. The pressure was adjusted so that the experiments for modified and unmodified membranes were started at the same flux rate of approximately 40 L/hm<sup>2</sup>. During filtration, decline in flux was monitored by measuring permeate volume until 50 mL of protein solution was filtered. The residual solution was removed and the membrane surface was washed 10 times with pure water and 2 times with NaCl solution (2000 ppm). Water permeability was measured again and fouling resistance was determined using equation 4.29:

$$RFR = \frac{P_{FF}}{P_0} * 100 \quad (4.29)$$

Where  $P_{FF}$  is the permeability after filtration of foulant.

## 4.9 Membrane characterization

### 4.9.1 Scanning electron microscopy

Scanning electron microscopy generates high resolution (below 2 nm) images of sample topographies. Conductive materials are scanned via a focused electron beam, which interacts with surface atoms and results in emitted secondary and backscattered electrons. An Everhart-Thornley detector allows extracting information of surface characteristics by analyzing the quantity and intensity of scattered electrons as well as emitted X-rays, which gathers information about surface atoms.<sup>145</sup>

In this work, SEM (*Quanta 400 FEG, FEI*) was used for imaging of modified and unmodified membrane surfaces and cross-section morphologies in order to evaluate the modification process and measure the hydrogel layer thickness. The samples were prepared for cross-section imaging by rinsing and then freeze-drying the membranes in liquid nitrogen, before breaking them. Subsequently, membranes were sputtered with an alloy containing 80% Au and 20% Pd to guarantee electron conductivity. Images of cross-sections and membrane surfaces were recorded under vacuum conditions.

### 4.9.2 Attenuated total reflection infrared spectroscopy (ATR-IR)

Light in the electromagnetic range of 14000 to 10 cm<sup>-1</sup> is considered as infrared and used to determine functional groups of a molecule. Molecules can be described as harmonic oscillators and thus possess vibrational character. The vibrational state is depending on bonding type and atom properties. When the frequency of IR light matches the frequency of a functional group, its energy is absorbed, and the vibrational state of the molecule is excited. The resonance results

in characteristic adsorption bands and allows to extract information about samples' chemical structure.<sup>146</sup>

In this work, an attenuated total reflection spectrometer (*Type IRAffinity-1S, Shimadzu*) was used to determine the surface chemistry of modified and unmodified membranes. ATR method uses an evanescent wave, which is generated when an IR-beam is reflected within a ZnS crystal. The penetration depth  $pd$  is mainly dependent on angle of incidence, refractive index of sample and crystal as well as on specific IR wavelength. Penetration depth can be calculated with following equation:

$$pd = \frac{\lambda}{2\pi \sqrt{\sin^2(\theta) - \left(\frac{n_2}{n_1}\right)^2}} \quad (4.30)$$

With  $\lambda$  is wavelength,  $\theta$  is angle of incidence,  $n_1$  is refractive index of crystal and  $n_2$  is refractive index of the sample.

With an incident angle of  $45^\circ$  typical penetration depth are in the range of 1-3  $\mu\text{m}$ , varying with the wavelength.<sup>147</sup> Before measurement, samples have been washed and freeze-dried. Every samples' top layer was scanned 32 times in the range of 4000 to 600  $\text{cm}^{-1}$  with a resolution of 1  $\text{cm}^{-1}$ .

#### 4.9.3 Zeta potential

Electrokinetic properties of surfaces are crucial to understand adsorption and fouling phenomena. They can be analyzed via zeta potential measurements. At a solid-liquid interface, ions will adsorb on the surface due to Coulomb interactions and form an electric double layer. This electric double layer is often considered as a combination of a Stern and a diffusive layer, which exhibits a distance dependent decay of electrical potential.

Stern proposed a simple two layer model, in which the internal layer (Stern layer) can be accounted to tightly anchored oppositely charged ions and the second can be described as a diffusive layer with loosely associated charged species, see Fig. 4.9. Due to strong attractive Coulomb interactions at the surface, the potential cannot be measured. Instead, zeta potential is obtained by shearing ions from the slipping lane.<sup>148</sup>

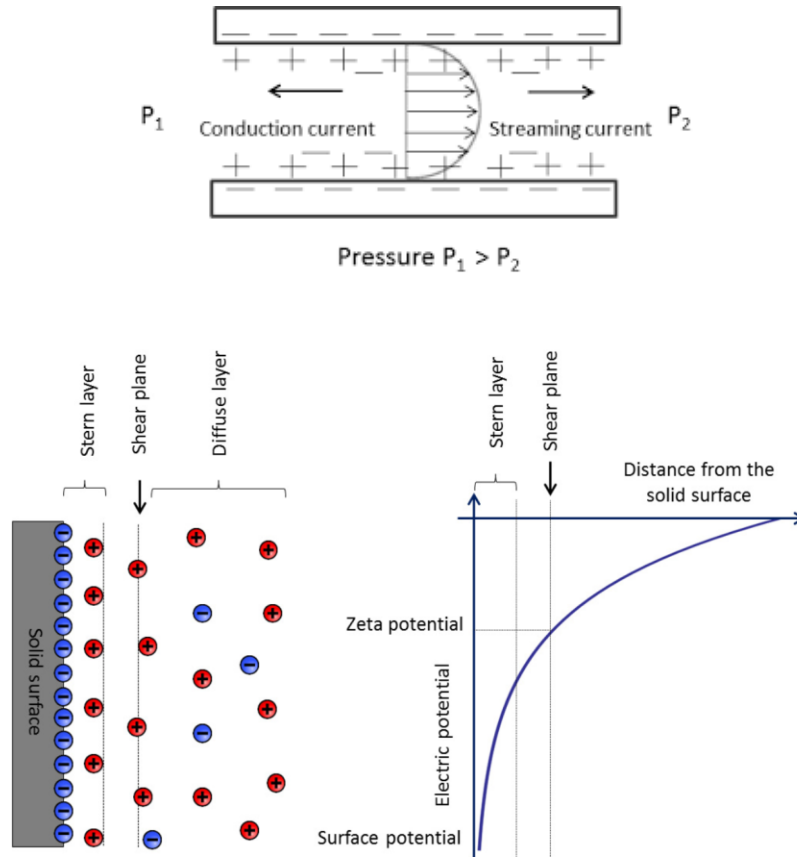


Figure 4.9 Development of streaming and conduction current in a channel(top); schematic representation of electrical double layer and distance dependence of electrical potential (bottom).<sup>149</sup>

When a flow at such interface is induced by external pressure, mobile ions from the diffusive layer will be transported in the flow direction, resulting in a streaming current and consequently in a potential difference. This potential difference is counterbalanced by back diffusion of ions the called leak or conduction current (Fig. 4.9). In steady state, difference of streaming and leak current results in streaming potential, from which zeta potential can be obtained using the Helmholtz-Smoluchowski equation:

$$\zeta = \frac{\Delta U_S}{\Delta P} \cdot \frac{\eta}{\varepsilon \varepsilon_0} \cdot \frac{\Delta x}{AR_{ch}} \quad (4.31)$$

Where  $\zeta$  is the zeta potential,  $\frac{\Delta U_S}{\Delta P}$  is the slope of streaming current versus pressure,  $\eta$  is the electrolyte viscosity,  $\varepsilon_0$  is the vacuum permittivity,  $\varepsilon$  is the relative permittivity,  $\Delta x$  is the height of the streaming channel,  $A_{ch}$  is the cross-section of the streaming channel and  $R_{ch}$  is the electrical resistance of the channel.

For all zeta potential measurements of modified and unmodified membranes, a *SurPASS electrokinetic analyzer (Anton Paar)* was used. Flat sheet membranes were first immersed for

at least 20 min in 1 mM KCl solution, before fixed to the measuring cell. The gap between two membranes was adjusted to  $100 \pm 5 \mu\text{m}$  and measurements were started at pH of around 2.5 with a differential target pressure of 400 mbar. After each measurement, pH was increased incrementally with automatic titration of 0.1 M KOH solution and zeta potential was again determined.

#### 4.9.4 Contact angle measurement

Investigation of membrane hydrophilicity was performed by contact angle measurements using *OCA 15 plus system (Dataphysics)*. The contact angle was measured at the membrane surface between the liquid-vapor interface via captive bubble method. Thereby an air bubble with a volume of  $5\mu\text{L}$  was dispensed onto membrane surface with the active layer facing downwards, while the membrane is submerged in water. Generally, in captive bubble mode small contact angles indicate high surface hydrophilicity and vice versa.<sup>150</sup>

Measurements were performed five times at three different spots for each freeze-dried membrane sample. All samples were placed in pure water and measured at room temperature. Modified and unmodified membranes were fixed to a glass slide and an air bubble was released via Hamilton syringe. The attached bubble was analyzed with a charge-coupled device camera employing ellipse fitting.

## 5 Results

### 5.1 Free radical copolymerization

#### 5.1.1 Characterization of P(DMAEMA-co-HEMA)

All synthesized copolymers are composed of DMAEMA and HEMA monomer units. The copolymer structure was verified via  $^1\text{H-NMR}$ -spectroscopy, depicted in Fig. 5.1. NMR analysis allows investigating the chemical composition of the copolymer and quantifying the amounts of HEMA and DMAEMA side units.

Polymer backbone peaks, present for each monomer side chains in form of methyl group (a) and methylene protons (b), are both represented by two broad signals at 0.9 ppm and 1.8 to 2.1 ppm, respectively. The split of backbone group into two or more peaks is attributed to the magnetically inequivalent protons resulting from polymer tacticity. Here, the NMR spectra of P(DMAEMA-co-HEMA) indicates atactic orientation of polymer backbone.<sup>151</sup> Additionally, broadening of peaks and consequent lack of resolution are caused by slow spin-spin relaxation of macromolecules compared to spin-lattice relaxation.<sup>152</sup>

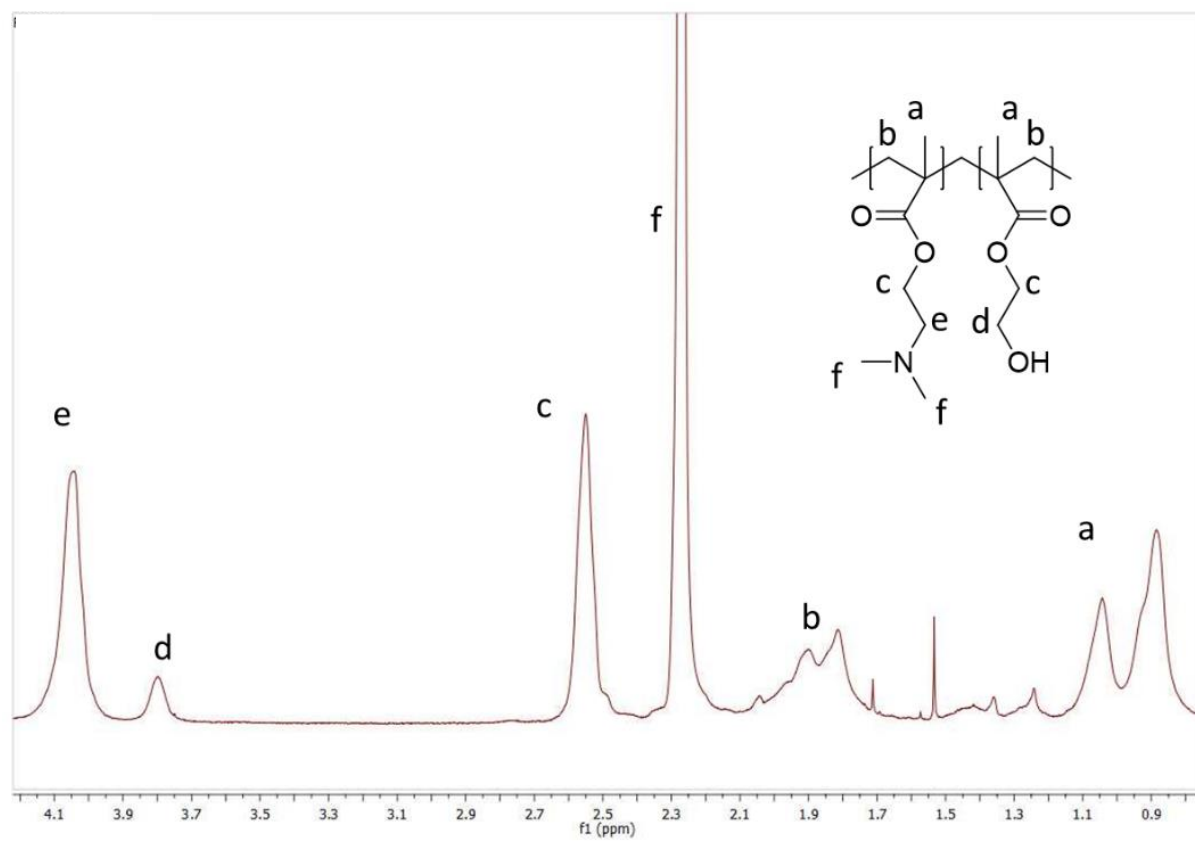


Figure 5.1 NMR Spectra of P(DMAEMA-co-HEMA).

Signal (c), at 2.6 ppm, represents methylene protons for both side units next to ester functionality. Individual signals, which allow distinction of monomer composition in polymers, are given by signal (f), at 2.3 ppm assigned to dimethyl group in DMAEMA, signal (d), at 3.8 ppm assigned to methylene protons next to alcohol functionality in HEMA, as well as peak (e), at 4.0 ppm assigned to methylene-group next to amine-functionality in DMAEMA.

In order to determine copolymer composition, a characteristic peak belonging to HEMA (d) and another representative peak for both side chains (c) were integrated and subsequently, the ratio of integrals gives HEMA-contribution to the macromolecule:

$$PHEMA[\%] = \frac{\int d}{\int c} \quad (5.1)$$

$$PDMAEMA[\%] = 100\% - PHEMA[\%] \quad (5.2)$$

The obtained results are shown in following sections.

#### 5.1.2 Determination of conversion and polymerization rate

Although NMR analysis of P(DMAEMA-co-HEMA) copolymers allows determining composition, it does not provide any information about sequential order of side chains. To acquire knowledge about the side chain regularity, conversion rates for each monomer were obtained by measuring NMR spectra of reaction mixtures at different times and subsequent comparison of signals related to monomers (HEMA at 6.05 ppm and DMAMEMA at 6.00 ppm) and polymer (methyl group in backbone at 0.8-1.1 ppm). The three corresponding peaks are shown in Fig. 5.2.

The time dependent conversion was calculated with following equation:

$$conv. (t) [\%] = \frac{\int a_{t\frac{1}{3}}}{\int a_{t\frac{1}{3}} + \int HEMA_t + \int DMAEMA_t} \quad (5.3)$$

The monomer conversion results for different AIBN contents and an initial HEMA content of 20% is finally depicted in Fig. 5.3.

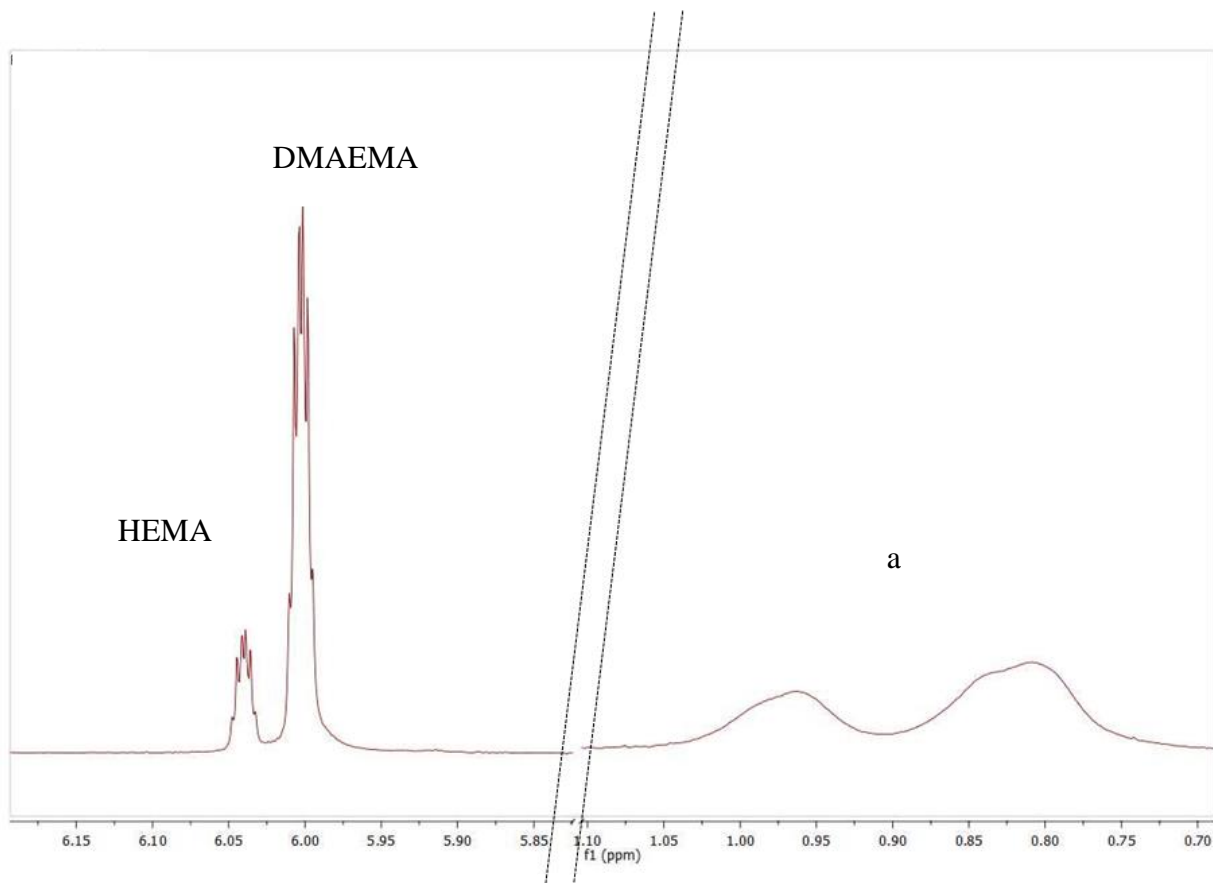


Figure 5.2 NMR peaks for monomers and polymer backbone.

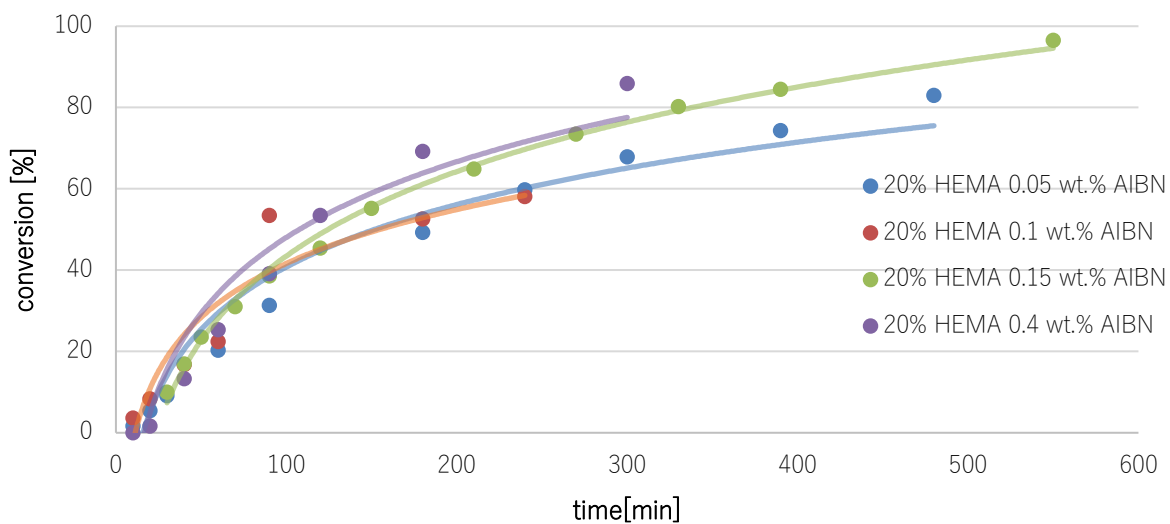


Figure 5.3 Monomer conversion over time.

Generally, all polymerization reactions showed an exponential decrease in conversion rate with time. Furthermore, the initial polymerization phase and kinetics until approximately 60 minutes, equivalent to an average conversion of 25%, were found to be independent of AIBN content and showed all a linear conversion rate. Nevertheless, above 60 minutes, the monomer

conversion rate differs for various initiator concentrations. Longer periods of linear conversion rates were observed in case of using 0.4 wt.% AIBN until approximately 120 minutes, and until 80 minutes only upon using 0.15 wt.% AIBN.

Additionally, later polymerization phases (>60 minutes) showed AIBN concentration dependent decrease in reaction rates. For higher contents of AIBN (>0.15 wt.%), the conversion was slightly quicker, which should be explained by more available radicals and different solution viscosities. This will be further discussed in section 5.1.3.

Exemplarily relative conversion rates of each monomer at AIBN content of 0.15 wt.% are depicted in Fig. 5.4. Values were calculated using equation 5.4, whereby overall conversion was multiplied by ratio of monomers at the beginning compared to time t resulting in relative HEMA conversion:

$$conv. (HEMA) [\%] = conv. (t) \frac{\frac{f_{HEMA_0}}{f_{HEMA_0} + f_{DMAEMA_0}}}{\frac{f_{HEMA_t}}{f_{HEMA_t} + f_{DMAEMA_t}}} \quad (5.4)$$

The differences in conversion rates appeared after the initial reaction phase (<60 min.). While for the first 50 minutes conversion rates for DMAEMA and HEMA monomers showed no significant difference, HEMA is reacting slightly faster at later reaction times.

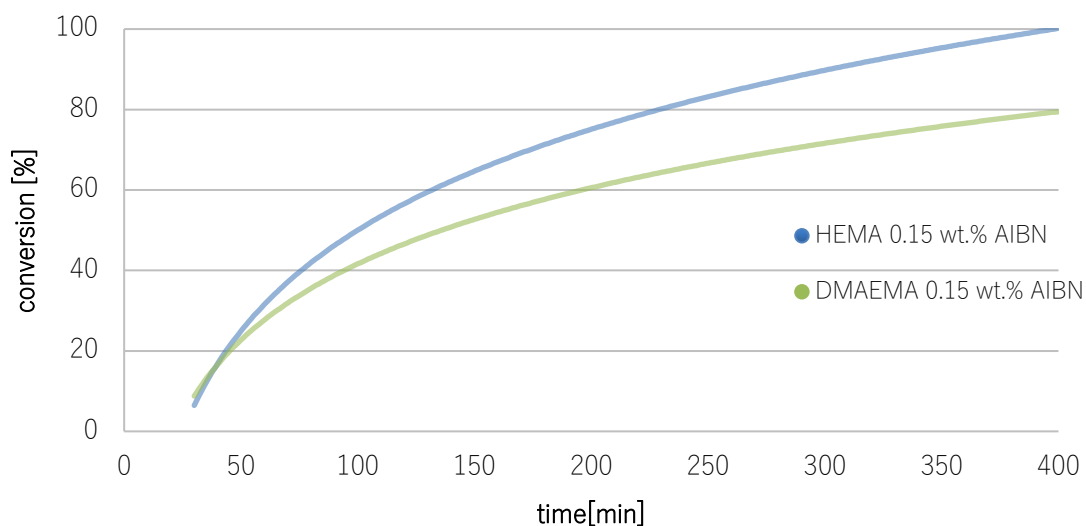


Figure 5.4 Relative conversion of HEMA and DMAEMA for polymerization with 0.15 wt. % AIBN.

The difference in conversion rates may be explained by different molecular sizes and unequal mobilities of DMAEMA and HEMA are expected. Due to the bigger hydrodynamic radius, attributed to dimethyl amino groups, DMAEMA diffuses slower into polymer network and

hence, polymerization rates drop faster than for HEMA. As polymerization proceeds, viscosity of reaction mixture increases over time and consequently, the diffusion phenomenon becomes more relevant for further propagation reactions.<sup>153</sup> Furthermore, because diffusion is viscosity dependent, differences in reaction rates for each monomer increased with reaction time. Therefore, monomer conversion rates diverged in later reaction phases for all polymerizations irrespective of their initial AIBN content.

Moreover, monomer interactions, i.e., hydrogen bonds dipole forces for HEMA and DMAEMA, differ from thermodynamic perspective and can shift the statistical random distribution of monomers in reaction mixture towards a more ordered one. Hydrogen bonds and dipole interactions in HEMA-HEMA are enthalpically more favorable ( $\Delta H \approx -10.6$  kcal/mol) than DMAEMA-DMAEMA or DMAEMA-HEMA ( $\Delta H \approx -3.3$  kcal/mol) interactions.<sup>154</sup> Hence, HEMA monomers may be associated with each other causing cascading effects during radical propagation and therefore HEMA conversion may be slightly faster. Nevertheless, the thermodynamic interaction effect on relative conversion rates will be weaker compared to its impact on monomer conversion derived by diffusion transport. However, the overall differences in relative conversion rates are small enough to result in statistical distribution of side units, which is an essential criterion for the formation of regular hydrogel networks.

### 5.1.3 Influence of initiator concentration on molecular weight

Size exclusion chromatography was performed to determine alteration in polymers' molecular weight (universal and PMMA calibrated) in dependence of initial monomer composition and AIBN content. In Fig. 5.5 the influence of AIBN amount on molecular weight  $M_n$ , for polymers with 20% HEMA units is presented. Generally, molecular weights are in range of 20 to 45 kDa. Higher  $M_n$  were obtained using PMMA calibration up until an AIBN amount of 0.15 wt.%. In contrast, higher molecular weights for higher initiator concentrations (>0.2 wt.%) were found when universal calibration was used. However, in most cases no significant difference in molecular weights can be observed.

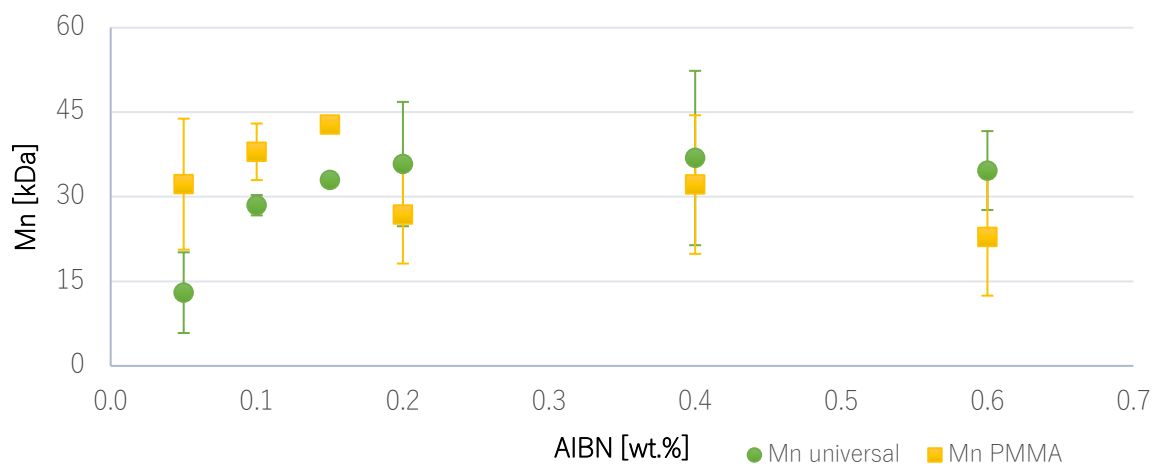


Figure 5.5 Molecular weight in dependence of AIBN concentration for 20% HEMA content.

Generally, molecular weight obtained via SEC is a function of molecular size and polymer-solvent interactions. In relative SEC calibration, P(DMAEMA-co-HEMA) will undergo different physico-chemical interactions and therefore, it possesses different solubility in DMAc than PMMA. Consequently, different hydrodynamic volumes for the same molecular weight are expected for PMMA and synthesized copolymer. The interactions and the influence on copolymer solubility can be estimated using Hansen-solubility parameters, i.e., dispersive  $\delta_d$ , polar  $\delta_p$  and hydrogen bond interaction energies  $\delta_h$  between solvent and polymer. The interaction energies result in a distance parameter  $R_a$ , given by following equation:

$$R_a = 4 (\delta_{d2} - \delta_{d1}) + (\delta_{p2} - \delta_{p1}) + (\delta_{h2} - \delta_{h1}) \quad (5.5)$$

The lower the distance, the better the solubility. For PMMA, PDMAEMA, PHEMA and DMAc, Hansen solubility parameters as well as  $R_a$ , are given in Tab. 5.1.<sup>155, 156</sup>

Table 5.1 Hansen solubility parameter for PHEMA, PDMAEMA and PMMA in DMAc

Name	$\delta_d$	$\delta_p$	$\delta_h$	$R_a$
PHEMA	17.1	5.0	12.1	9.6
PDMAEMA	17.2	4.4	6.2	12.7
PMMA	10.5	18.8	5.7	37.0
DMAc	16.8	11.5	10.2	-

Tab. 5.1 reveals that P(DMAEMA-co-HEMA) is much better soluble than PMMA in DMAc, which may result in a more pronounced expansion of chains. Bigger hydrodynamic diameter of P(DMAEMA-co-HEMA) compared to that of PMMA may cause lower retention times during SEC and inevitably lead to overestimation of copolymers molecular weights. This overestimation phenomena of  $M_n$  using relative calibration should explain higher values of  $M_n$  using PMMA calibration compared to  $M_n$  values using universal calibration at lower AIBN concentrations. However, it is unclear why expectations are not matched for higher initiator content.

Furthermore, an increase in  $M_n$  was observed upon increasing of AIBN concentrations up to 0.15 wt.%. Such trend is unexpected since higher initiator content and consequently, more available free radicals should lead to more initiation reactions and more parallel growing chains. Hence, more chains were theoretically expected to compete for propagation, which should result in smaller macromolecules. However, only above an initiator concentration of 0.2 wt.%, expectations are matched, since the molecular weight drops for relative and is at least constant for universal calibration.

Investigation of PDI helps to clarify, why bigger polymer chains are obtained for lower AIBN content (see Fig. 5.6). PDI describes molecular mass distribution and can be calculated by equation 5.6:

$$PDI = \frac{\bar{M}_w}{\bar{M}_n} \quad (5.6)$$

Generally, PDI for both calibration methods are decreasing with increasing initiator concentration. For instance, polymerization reactions at AIBN concentration of 0.05 wt.% resulted in a broad distribution of molecular weight (PDI of 9.2 vs. 5.2 for PMMA and universal calibration, respectively), which means that most of macromolecules are small and others are extraordinarily large. For concentrations above 0.15 wt.%, all PDI are comparable, dropping to approximately 2.8 and 2.2 for universal and PMMA calibrations, respectively.

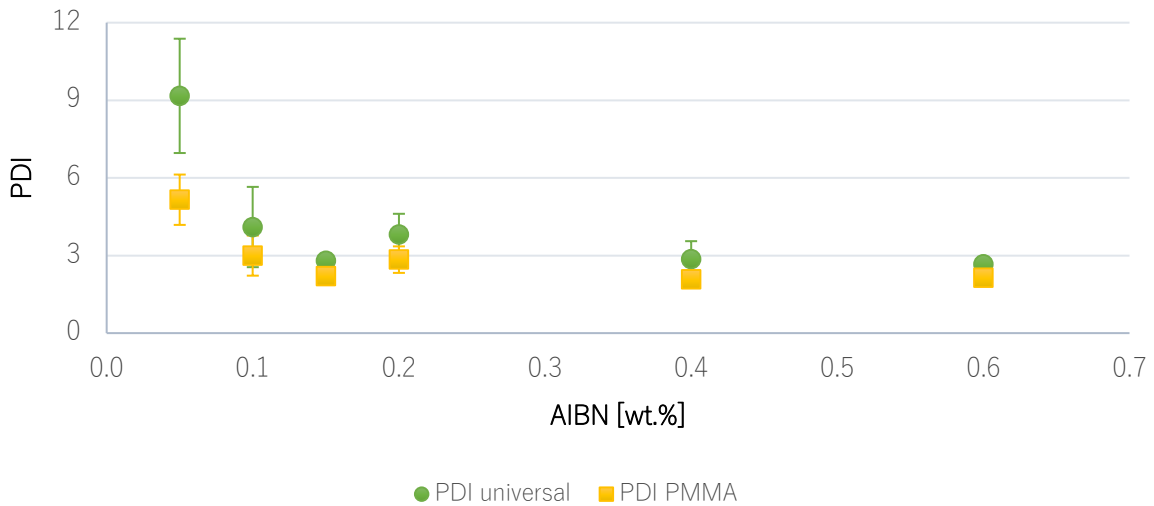


Figure 5.6 PDI of copolymers with 20% HEMA content and different initiator concentrations.

Such a big contrast in polymer growth can also be explained by free radical scavenging or quenching, in which radicals are reacting to inactive products. A well-known inhibitor reported for radical polymerization reactions is oxygen, which stops further propagation of chains.<sup>157</sup> Hence, quenched (inactive) polymer chains will not compete for monomers and only some chains can incorporate monomers, resulting in long chains. The impact of radical quenching is found to be stronger for low initiator concentrations since the amount of inactive and quenched polymers, compared to regular growing chains, become more dominant. Consequently, broader molecular weight distribution is usually found when AIBN concentration is low.

The influence of radical initiator content on polymer characteristics can also be demonstrated by the Mark-Houwink parameters and intrinsic viscosities, as depicted in Fig. 5.7.

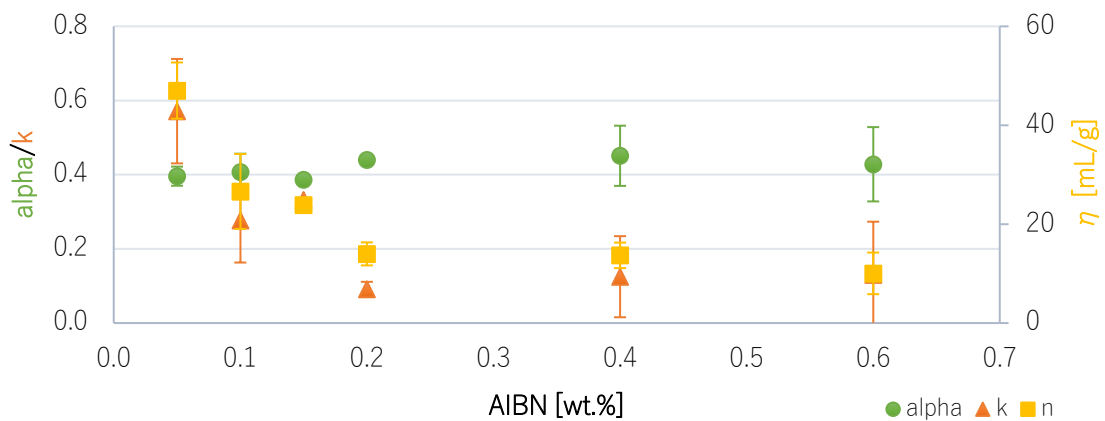


Figure 5.7 Intrinsic viscosities and Mark-Houwink parameters for copolymers with 20% HEMA side units at different AIBN concentrations.

In the same way, a sharp distinction between AIBN concentrations above and below 0.2 wt.% was observed. At lower AIBN concentration, intrinsic viscosities and  $k$  values for copolymers with 20% HEMA side units are three times higher than those at initiator concentrations  $>0.2$  wt.%. As intrinsic viscosities represent solutes contribution to the viscosity, the increase can be attributed to some extraordinary long macromolecules, which influence viscosity stronger than smaller polymer chains due to their more pronounced physical entanglement.

#### 5.1.4 Influence of monomers' concentration on molecular weight of resulted copolymers

Besides the influence of radical initiator concentration on molecular weight, also dependency on monomer concentration was studied. In Fig. 5.8 molecular weight of P(DMAEMA-co-HEMA) is shown for different initial HEMA content and constant AIBN amount of 0.2 wt.%. All synthesized polymers exhibit comparable average molecular weights between 20 and 40 kDa. In general, universal calibration resulted in higher  $M_n$  than PMMA calibration. Furthermore, a slight increase in  $M_n$  with higher HEMA amount can be observed and may be attributed to higher conversion rates of HEMA (see section 5.1.2).

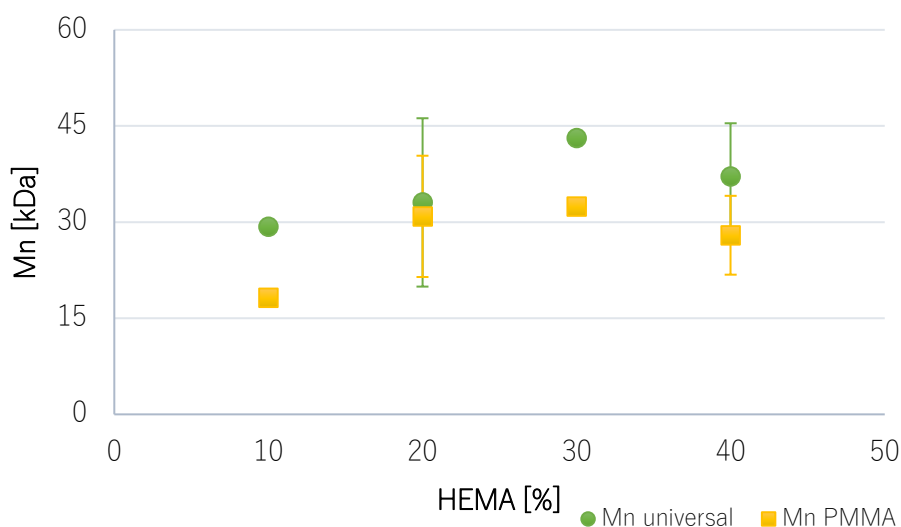


Figure 5.8 Influence of HEMA content on molecular weight of P(DMAEMA-co-HEMA) at constant AIBN amount of 0.4 wt.%.

The PDI of polymer samples at constant AIBN amount (0.2 wt.%) are represented in Fig. 5.9. PDI for universal calibration are generally higher than for PMMA calibration, in the range of 2.6 to 3.9 and 2.2 to 2.9 in case of universal and PMMA calibrations, respectively. In addition, a slight increase in PDI for more heterogeneous compositions can be observed.

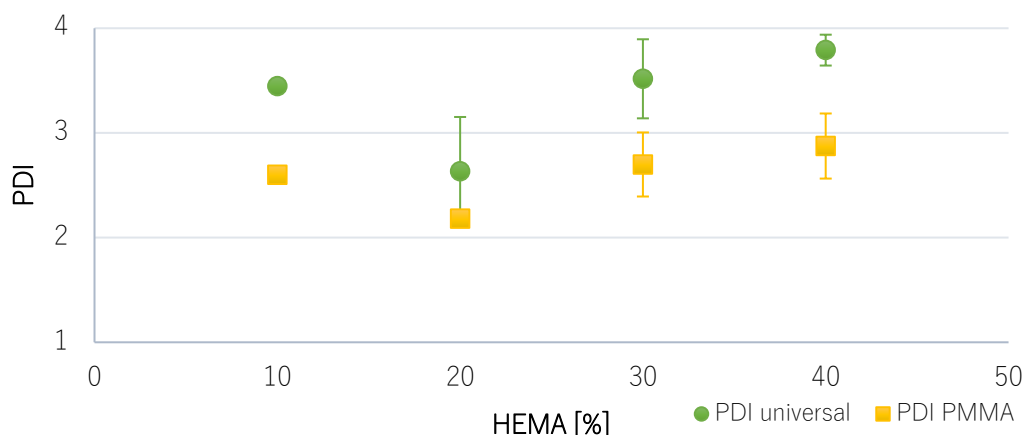


Figure 5.9 Influence of HEMA content on PDI.

Nevertheless, the influence of monomer concentration on molecular weight and PDI is less pronounced than the impact of initiator concentration. Both monomers, DMAEMA and HEMA, have comparable radical stability, reactivity and structure so that they behaved similarly during the polymerization reaction. Only the slight differences in size and their impact on diffusion properties are responsible for higher conversion rates for HEMA monomer (see section 5.1.2). This leads to minimal differences in molecular weight and PDI.

Additionally, no significant influence of polymers' composition on Mark-Houwink parameters and intrinsic viscosities at constant AIBN (0.2 wt.%) was observed (see Fig. 5.10). Alpha was in range of 0.45, representing almost ideal chain conformation (theta conditions, alpha=0.5), while K possesses values of about 0.08. Intrinsic viscosities vary from 9.0 to approximately 15.0 ml/g for polymers with more than 10% HEMA side units. Hence, the influence of monomer composition on polymerization reaction is insignificant and negligible.

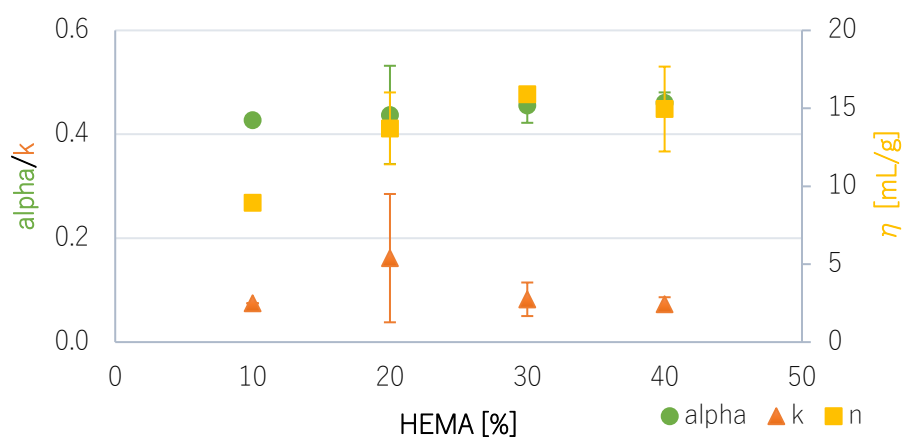


Figure 5.10 Influence of HEMA content on the Mark-Houwink parameter.

## 5.2 Polymer functionalization

### 5.2.1 Introducing crosslinkable methacrylate groups

After free radical polymerization, hydroxyl containing side groups were functionalized in order to obtain methacrylate functionalities that act as crosslinkable groups.  $^1\text{H-NMR}$  spectrum and structural verification of P(DMAEMA-co-MAMMA) is depicted in Fig. 5.11.

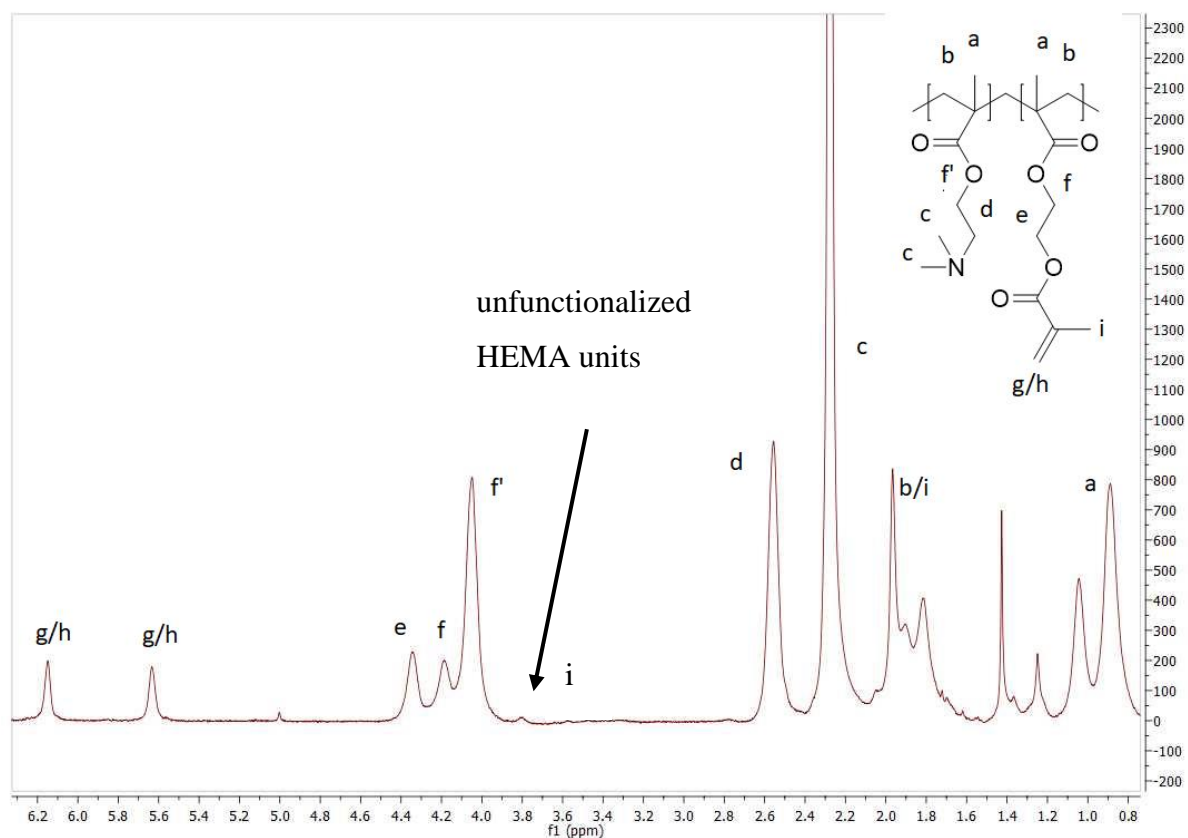


Figure 5.11  $^1\text{H-NMR}$  spectroscopy and structural analysis of P(DMAEMA-co-MAMMA).

The percentage of methacrylate units could be calculated with equation 5.7:

$$\text{methacrylate units}[\%] = \frac{f_g}{f_a} \quad (5.7)$$

However, peak at 3.8 ppm indicates that a small percentage of HEMA units remained unfunctionalized. Reaction of MAC with hydroxyl group of HEMA is susceptible to non-quantitative conversion. Hence, polymer functionalizations can be incomplete and result in a copolymer with three different side units. The portion of HEMA units was calculated by equation 5.8 and was up to 3%:

$$\text{HEMA units}[\%] = \frac{f_i}{f_a} \quad (5.8)$$

### 5.2.2 Sulfobetainization

Finally, the introduction of zwitterionic units was performed by ring opening reaction using 1,3-propanesultone, as described in section 4.2.3. Fig 5.12 shows  $^1\text{H-NMR}$  spectroscopy and structural analysis of P(SBMA-co-MAMMA).

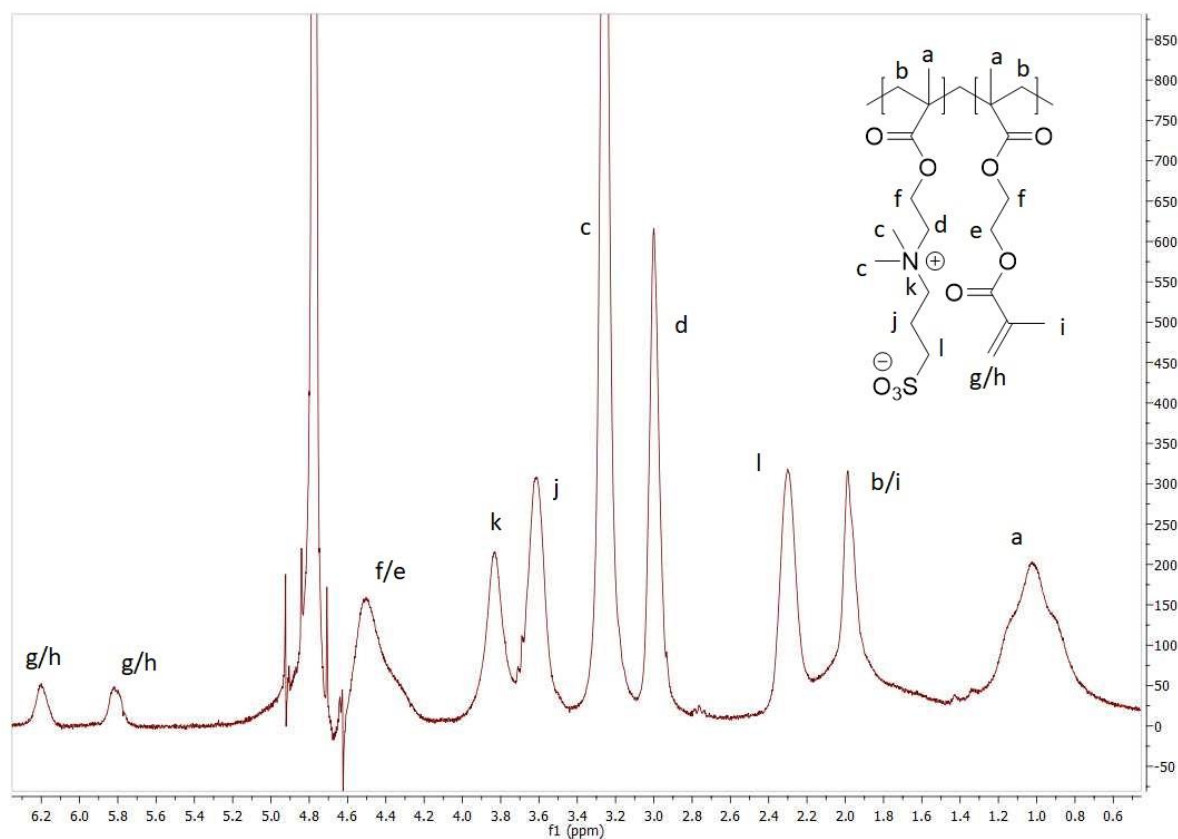


Figure 5.12  $^1\text{H-NMR}$  spectroscopy and structural analysis of P(SBMA-co-PMAMMA).

The sulfobetainization of P(DMAEMA) is reported to maintain a small amount of uncharged dimethyl amine units. However, the absence of the signal at 4.0 to 4.2 ppm points to quantitative conversion and quaternization of dimethyl amino groups.<sup>158</sup> Additionally, complete shift of signal for dimethyl amino units from 2.4 to 3.3 ppm verifies successful conversion of P(DMAEMA). Copolymer composition was finally calculated by equation 5.9:

$$\text{zwitterionic units}[\%] = \frac{\int_{\frac{c}{6}}}{\int_{\frac{a}{3}}} \quad (5.9)$$

Molecular weight of zwitterionic, crosslinkable copolymer was determined by equation 5.10, in which  $M_n$  of P(DMAEMA-co-HEMA) was multiplied by the ratio of functionalized average side chain molar mass to average molar mass of DMAEMA and HEMA functionalities:

$$M_{n,functionalized} = M_{n,0} * \frac{\overline{MW}_{side-chain} (PSBMA-co-MAMMA)}{\overline{MW}_{side-chain} (PDMAEMA-co-HEMA)} \quad (5.10)$$

Where  $M_{n,functionalized}$  is the MW of P(SBMA-co-MAMMA),  $M_{n,0}$  is the MW of P(DMAEMA-co-HEMA) and  $\overline{MW}_{side-chain}$  is the average molar mass of P(SBMA-co-MAMMA) or respectively P(DMAEMA-co-HEMA) side units.

Following zwitterionic copolymer (ZP) batches, shown in Tab. 5.2, were used for free bulk gelation and membrane modification experiments.

Table 5.2 Molecular weight, PDI and composition of used polymer batches.

Name	Mn (PMMA) [kDa]	Mn (univ.) [kDa]	methacrylate [%]	PDI (univ.)
ZP1	63.7	87.8	21	2.6
ZP2	88.2	122.2	20	2.3
ZP3	44.1	77.9	11	3.4

### 5.2.3 Quaternization

In order to obtain the cationic macromolecular linker, the quaternization of tertiary amine units of P(DMAMEA-co-MAMMA) was performed with methyl iodide. The  $^1\text{H-NMR}$ -spectrum is shown in Fig. 5.13.

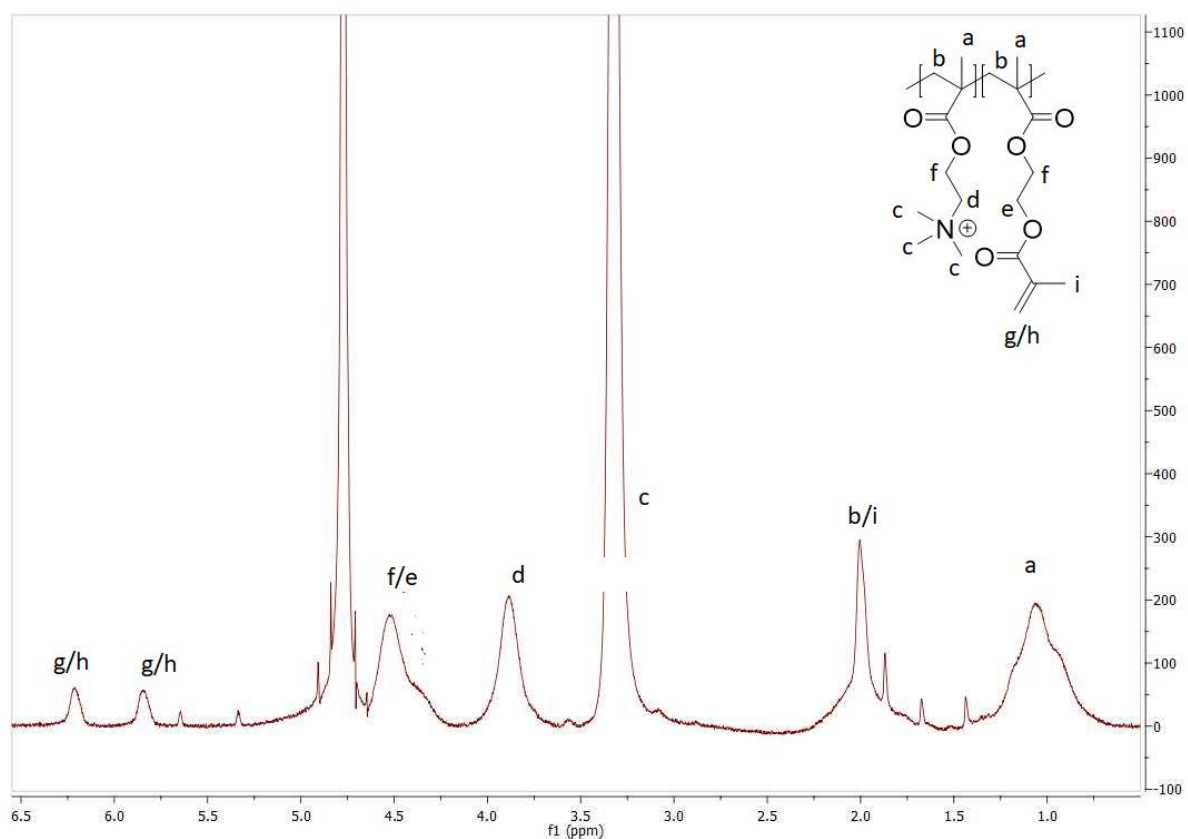


Figure 5.13  $^1\text{H-NMR}$  spectroscopy and structural analysis of surface linker.

Again, quantitative conversion of amino units was confirmed by the absence of peak at 4.2 ppm and compositions were analyzed by comparing integrals of methacrylate units at 5.8 ppm (g/h) or respectively 6.2 ppm (g/h) and of trimethyl ammonium group at 3.3 ppm (c).

$$\text{ammonium units [\%]} = \frac{\int_{6.2}^c}{\int_{3.3}^a} \quad (5.11)$$

Molecular weight of cationic surface linker was determined by equation 5.12, in which  $M_n$  of P(DMAEMA-co-HEMA) was multiplied by the ratio of average side chain molar mass of surface linker to average molar mass of DMAEMA and HEMA functionalities:

$$M_{n,\text{cationic}} = M_{n,0} * \frac{\overline{MW}_{\text{side-chain}}(\text{surface linker})}{\overline{MW}_{\text{side-chain}}(\text{PDMAEMA-co-HEMA})} \quad (5.12)$$

Where  $M_{n,\text{cationic}}$  is the molecular weight the surface linker,  $M_{n,0}$  is the molecular weight of P(DMAEMA-co-HEMA) and  $\overline{MW}_{\text{side-chain}}$  is the average molar mass of the surface linker or respectively P(DMAEMA-co-HEMA).

Surface linker batches, shown in Tab. 5.3, were used in membrane modification experiments.

*Table 5.3 Molecular weights, PDIs and compositions of macromolecular surface linker.*

<b>Name</b>	<b>Mn (PMMA) [kDa]</b>	<b>Mn (univ.) [kDa]</b>	<b>methacrylate [%]</b>	<b>PDI (univ.)</b>
SL1	26.4	39.7	20	2.4
SL2	49.8	58.3	21	2.5

### 5.3 Polymer in solution

This section discusses the behavior and characteristics of P(SBMA-co-MAMMA) in aqueous solution. Three different polymers with methacrylate side unit percentage in range of 10 to 20 % and zwitterionic functionalities in range of 80 to 90 % were investigated (see Tab. 5.2 in section 5.2.2).

While ZP1 and ZP2 exhibited similar copolymer composition (~20 % methacrylate units), ZP2 had about 35% higher molar mass. Moreover, ZP3 possessed slightly smaller  $M_n$  than ZP1 and had lowest methacrylate content (~11%).

#### 5.3.1 Solubility behavior

Generally, the solubility of polymers is determined by thermodynamics, more precise by the balance of cohesive forces between molecules and the solvation energy. For macromolecules, the solvation process takes longer time than for small molecular weight substances, since additional transport processes in form of solvent diffusion into polymer structure and chain disentanglement must occur.<sup>159</sup> Thus, besides physico-chemical properties, molecular weight and its distribution are crucial for slow dissolution of polymers.<sup>159, 160</sup>

In this work, solubility properties of copolymer P(SBMA-co-MAMMA) (ZP1) are investigated by solubility measurements, see Fig. 5.14. The cloud point is defined as the concentration, at which a polymer solubility is exceeded and the solution becomes heterogeneous (turbid).

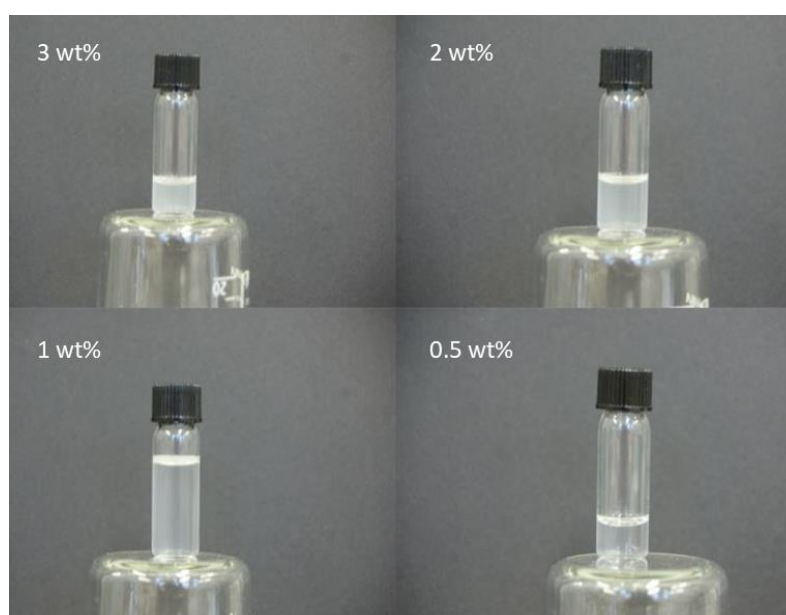


Figure 5.14 Polymer solubility: Cloud point measurements of various concentrated copolymer solutions.

In pure water, the solubility limit at room temperature is already exceeded at approximately 1 wt.%. As described in chapter 2.5, polyelectrolytes undergo several intra- and intermolecular Coulomb interactions. Furthermore, methacrylate side units possess hydrophobic character and consequently, they minimize interactions with water molecules by collapsing and reducing the interacting surface area. Hence, zwitterionic and methacrylate side groups disfavor dissolution in pure water and may lead to agglomeration of macromolecules in order to minimize water-polymer interactions.

### 5.3.2 Size analysis

With the aid of DLS measurement, a deeper understanding of polymers' solubility behavior was gained. Fig. 5.15 shows the intensity and number percentage plot vs. hydrodynamic diameter for P(SBMA-co-MAMMA) batches in water (1 g/L) with different MW or respectively number of methacrylate units.

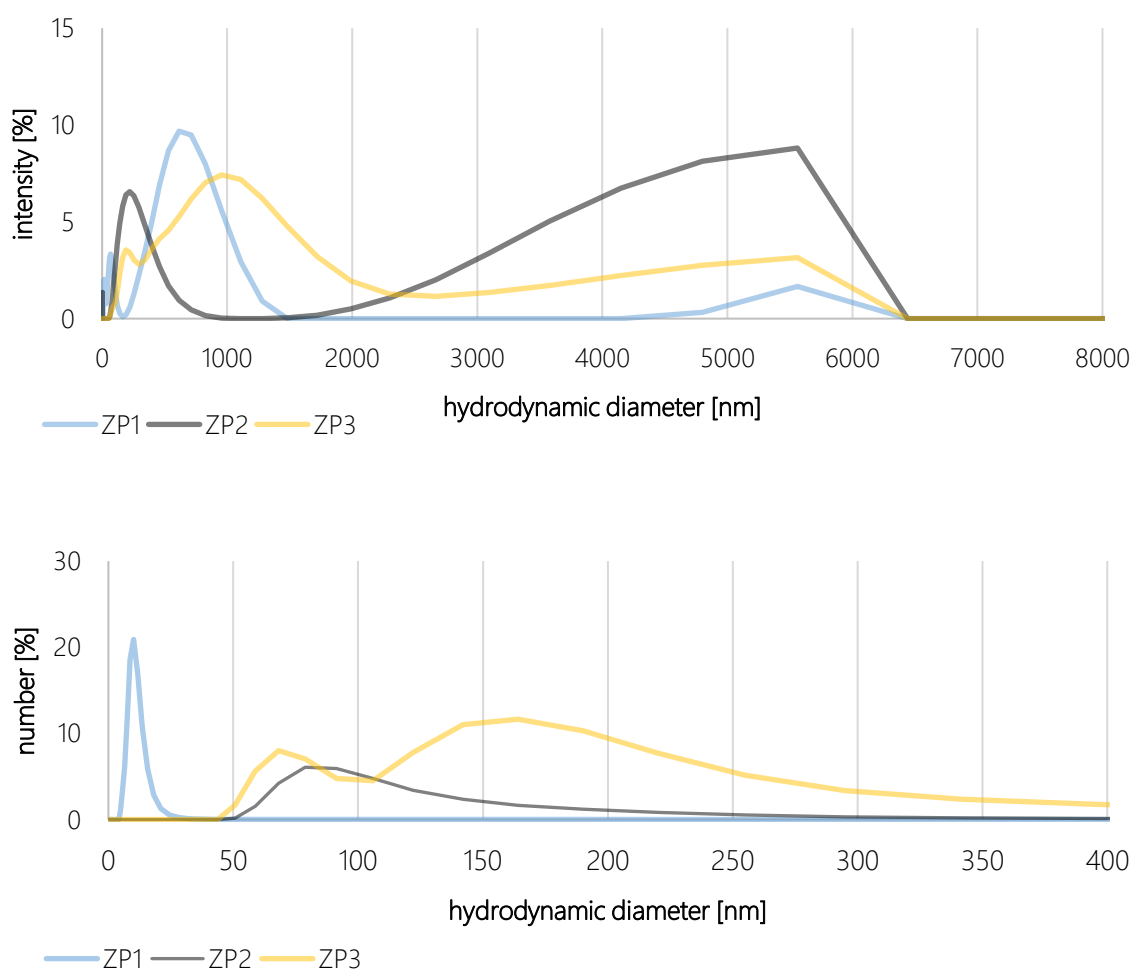


Figure 5.15 DLS intensity (top) and number (bottom) plot for different zwitterionic polymers in water.

First, the intensity plots for all samples, independent of their MW and composition, are polydisperse and show two smaller particle regions at approximately 10 nm and in between 200-1000 nm. Moreover, copolymers seem to form structures with big diameters (up to 7  $\mu\text{m}$ ), pointing to the extensive agglomeration of polymer chains. The agglomeration of macromolecules may result from attractive interchain Coulomb forces and explain why solubility is low.

Nevertheless, the intensity plot highly overestimates the number of agglomerates since light is scattered much more heavily for big particles (intensity $\sim r^6$ ). Therefore, plotting numbers against hydrodynamic size allows more accurate judgment of polymer conformation in solution. In the bottom Fig. 5.15 a monodisperse solution with a diameter of about 10 nm can be observed for the batch (ZP1) with 21% MAMMA units and average  $M_n$  of 87.8 kDa.

For a copolymer with a similar side group composition (ZP2) but higher  $M_n$  of 122.2 kDa, the sample exhibits broad monodispersity. However, the hydrodynamic diameter (approximately 80 nm) is much bigger compared to sample ZP1. The significant increase in diameter cannot be solely attributed to higher  $M_n$  (longer macromolecules). DLS measurement of ZP2 hints strongly to agglomeration of ZP2 in water.

The third sample ZP3, which is similar in  $M_n$  with ZP1 (77.9 kDa) but with a lower number of methacrylate groups (11%), showed a polydisperse size distribution with two broad signals at approximately 70 and 160 nm. On first sight, increase in hydrodynamic diameter compared to ZP1 (10 nm) may be caused by higher degree of agglomeration. Nevertheless, bigger polydispersity is unexpected because lower number of hydrophobic side units and a small  $M_n$  should both contribute to better dissolution properties.

However, such an observation points also to strong attractive Coulomb interactions between charged side segments. The higher amount of zwitterionic groups, present in sample ZP3 (90% compared to 80%), can possess lower tendency to dissolve due to more attractive Coulomb interactions and enhance agglomeration processes.

A full understanding of macromolecular solubility properties is complicated since dissolution phenomena are a multivariant and interdependent function of size, polymer composition and alternation of side units. As shown in section 5.2.1, conversion of alcohol groups is non-quantitative and hence percentage of side units and their alternation may differ between batches. Hence, multiple and partially competing inter- and intramolecular polymer interactions may complicate comparison.

In order to examine anti-polyelectrolyte effects on hydrodynamic volume and agglomeration, DLS measurements for sample ZP2 were performed in KCl solutions (1 and 5 mM). The intensity and number against diameter are plotted in Fig. 5.16.

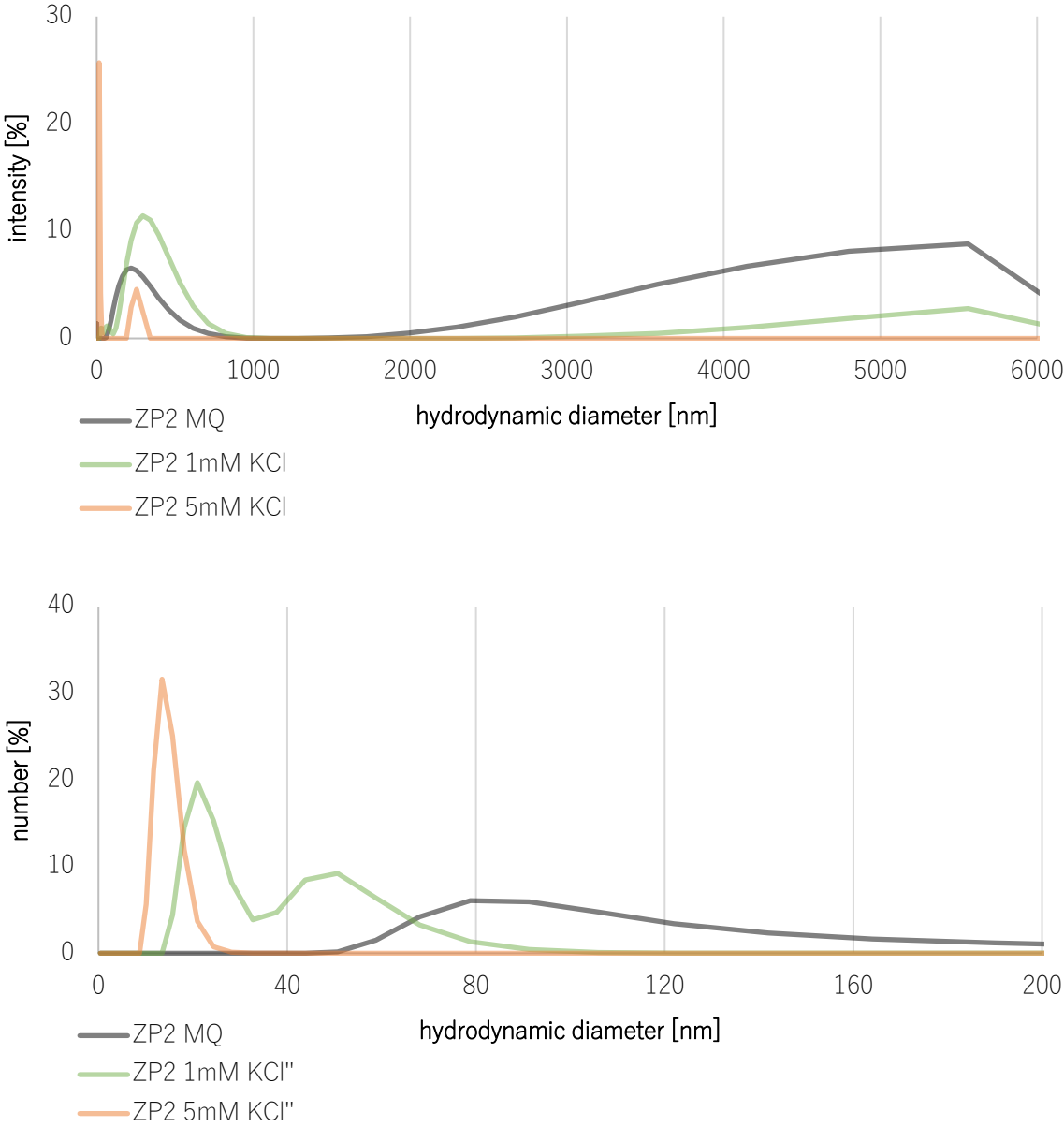


Figure 5.16 DLS intensity and number plot for ZP2 in water and KCl solutions.

With increasing salt concentration, the number of big particles is reduced significantly. For a 5 mM KCl solution, no particles bigger than 255 nm can be observed. Furthermore, the highest intensity is achieved for particles with a size of about 15 nm.

In contrast, sample ZP2 exhibits in water as well as in 1 mM KCl solution a broad distribution at large hydrodynamic diameters (up to 6 μm), hinting again to attractive interchain interactions,

which can cause agglomeration of macromolecules. Nevertheless, already a small amount of salt (1 mM) can partially shield charges and decrease the percentage of large structures.

The more relevant number plot demonstrates the gradual impact of screening in relation to salt concentration even more profoundly. Here, ZP2 exhibits largest particles in the range of 60 to 160 nm in water.

Although adding a small amount of KCl (1 mM) decreases the size of agglomerates, the sample still possesses a broad distribution in the range of 20 to 80 nm. The polydispersity and hydrodynamic size still indicate that polymer chains may agglomerate. However, when further increasing KCl concentration to 5 mM, screening of zwitterionic charges seems to become sufficient to obtain a monodisperse distribution and a sharp peak at approximately 14 nm. Schematically charge screening and break down of agglomerates in presence of salt is presented in Fig. 5.17.<sup>161</sup>

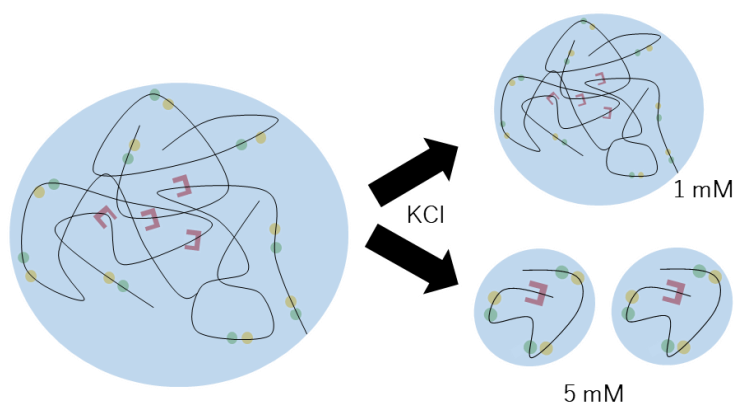


Figure 5.17 Break down of zwitterionic agglomerates by addition of salt and screening of interchain interactions.

In order to understand if agglomeration is a dynamic phenomenon or instead caused by some specific polyzwitterionic chains, also prefiltered ZP2 solutions (see section 4.4.3) were measured by DLS.

Fig. 5.18 shows the intensity plot of pretreated ZP2 samples. Like previous intensity measurements, polyzwitterions show agglomeration into huge structures. Nevertheless, the peak intensity in water decreases from about 9 for untreated to approximately 3% for prefiltered samples. The reduction of agglomerates is even more pronounced for salt solutions of ZP2 and proportional to salt concentration. In 5 mM KCL solution, for example, no particles in the range of several  $\mu\text{m}$  are present.

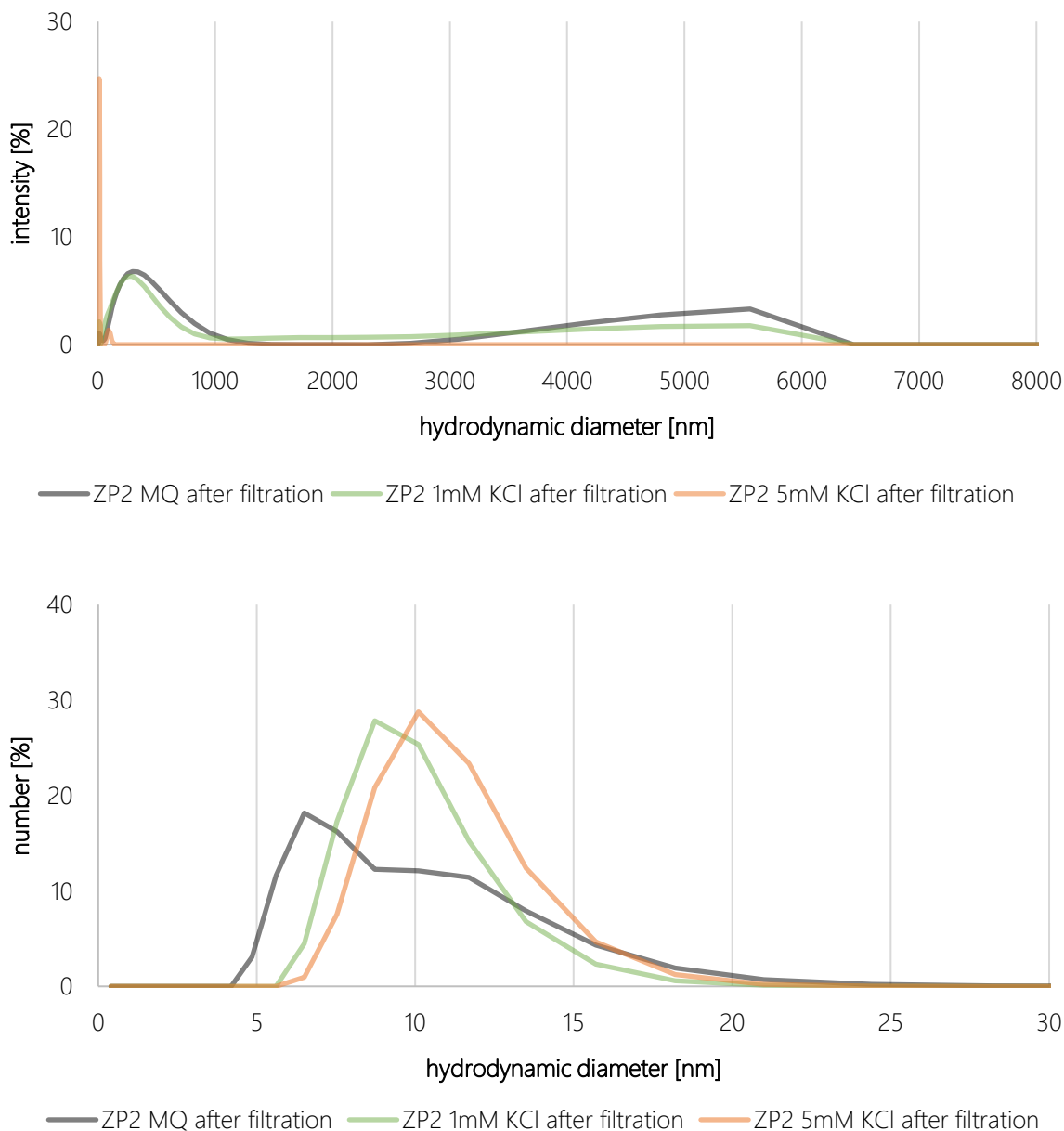


Figure 5.18 DLS intensity and number plot for ZP2 in water and KCl solutions after prefiltration.

More interestingly, number plots before and after filtration differ significantly from each other. Pretreated samples show no particles bigger than 20 nm for all aqueous solutions. This observation indicates that rather some copolymers, which can be prefiltered, contribute to agglomeration of chains. Instead of understanding agglomeration as a dynamic process, some specific polymeric matter may be responsible for large conglomerates. Such chains may have a very high molecular weight and hence hydrodynamic volume, due to branching and/or possession a multifunctional composition, which significantly lowers solubility and promotes agglomeration.

Furthermore, pretreated sample ZP2 demonstrates a gradual increase in hydrodynamic diameter in dependence of salt concentration. The lowest diameter is obtained for ZP2 in pure water. Adding salt results in shielding of inter- and intrachain Coulomb forces of polyelectrolyte ZP2 and consequent expansion of chains, well-known as anti-polyelectrolyte effect, schematically demonstrated in Fig. 5.19. Hence, the diameter meets expectations and increases from about 6 to 9 and up to 10 nm with higher salt concentration.

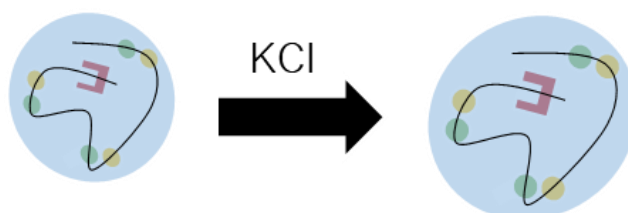


Figure 5.19 Schematic representation of the anti-polyelectrolyte effect.

Size analysis of polymers is relevant in order to estimate the diffusion coefficient by the Stokes-Einstein equation. A polydisperse distribution in hydrodynamic diameter would cause complications in estimation of CP since diffusion would be unequal for differently sized particles. Furthermore, agglomeration would hinder regular hydrogel building.

Hence, a pretreatment of polyelectrolytes or addition of salt to samples before membrane modification may be necessary, to enhance monodispersity and allow control over CP by adjusting filtration variables. However, membrane modifications and gelation experiments, described in sections 5.4 to 5.6, were performed with untreated (unfiltered) samples.

### 5.3.3 Viscosity

The viscosity of polymer solutions was studied via rheological measurements with purpose of determining overlap concentration. In Fig. 5.20 shear stress is plotted against strain rate for sample ZP1 (0.5-10 wt.%) in pure water. All solutions behave like Newtonian fluids with proportionally rising shear stress and strain rate.

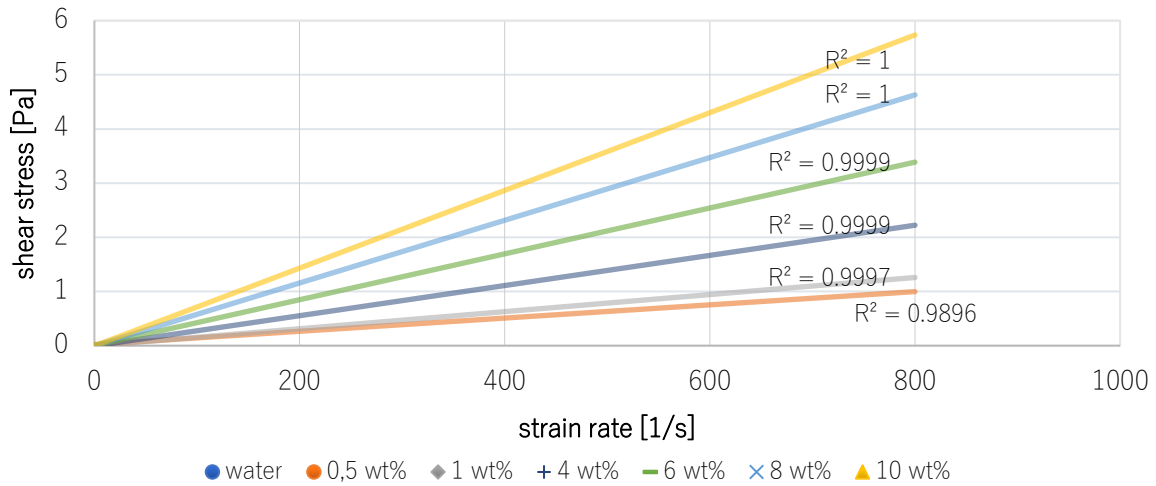


Figure 5.20 Shear stress vs. strain rate of ZP1 samples with different concentrations.

The viscosity of aqueous solutions containing ZP1 and ZP2 is depicted against polymer concentration in Fig. 5.21. Generally, with higher polymer content, viscosity rises proportionally because of increasing friction between polymer chains.

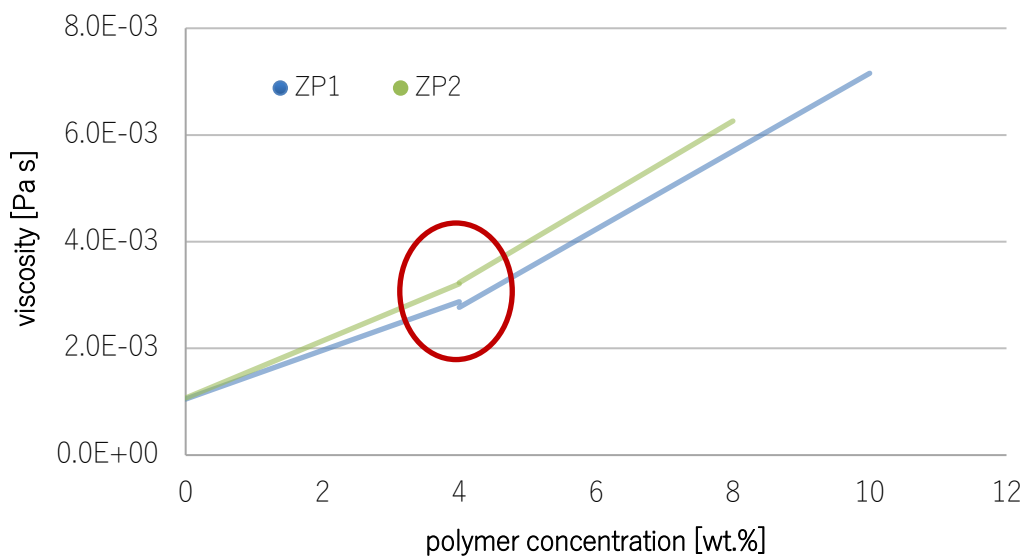


Figure 5.21 Viscosity of aqueous polymer solutions (ZP1 and ZP2) in dependence of polymer concentration with strain rate of  $800 \text{ s}^{-1}$ .

More specific, two linear regions with different slopes can be observed. For low concentrated solutions (0-3 wt.%), increases in viscosity are relatively low compared to highly concentrated polymer samples (4-10 wt.%). In addition, ZP2 solutions show slightly higher viscosities than samples containing smaller ZP1. The difference is small ( $\sim 10\%$ ) but significant and stems from higher molecular weight. Consequently, it leads to bigger hydrodynamic volume and more

pronounced friction between ZP2 macromolecules. However, both solutions show similar change in slope at around 4 wt.%, which corresponds to overlap concentration.

In general, polymer solutions at different concentration ranges can be divided after de Gennes into three regions: a) dilute, b) overlapping c) concentrated (see Fig. 2.17 in section 2.6.1).<sup>101</sup>

Below the overlap concentration, solutions are diluted, meaning that solutes are not in direct contact with each other and viscosities are solely a product of solvent-polymer interactions. Due to big average spacing between macromolecules, diluted polymer solutions cannot form interpenetrated network structures when crosslinking agents are added. Instead, in diluted solutions, polymer diffusion of reactive chains can lead to cyclic structures or gel particles.<sup>162</sup>

In contrast, for concentrations at overlap region, number of physical interactions between chains increase and viscosity becomes a sum of solvent-polymer and polymer-polymer interactions. Hence above overlap region, polymer amount contributes stronger to rise in viscosities. In addition, proximity of chains allows formation of regular gel networks.<sup>162, 163</sup> The zwitterionic crosslinkable P(SBMA-co-MAMMA) solutions must therefore exceed at least 4 wt.% to guarantee hydrogel formation, which will be discussed in the following section.

## 5.4 Free Bulk gelation

### 5.4.1 Kinetics

After determination of overlap concentration, free bulk gelation was studied for polymer solutions ZP1 (4, 5, 7.5 and 10 wt.%) in dependence of APS and TEMED amount. An example of a crosslinking reaction measured via rheology is given in Fig. 5.22.

Relevant information for hydrogel formation was extracted by intersection between storage ( $G'$ ) and loss modulus ( $G''$ ), which represents gelation point and completed gelation time, at which no further increase in storage can be observed. Furthermore, mechanical properties for different gelation conditions were evaluated by damping factor  $\delta$  and final storage modulus.

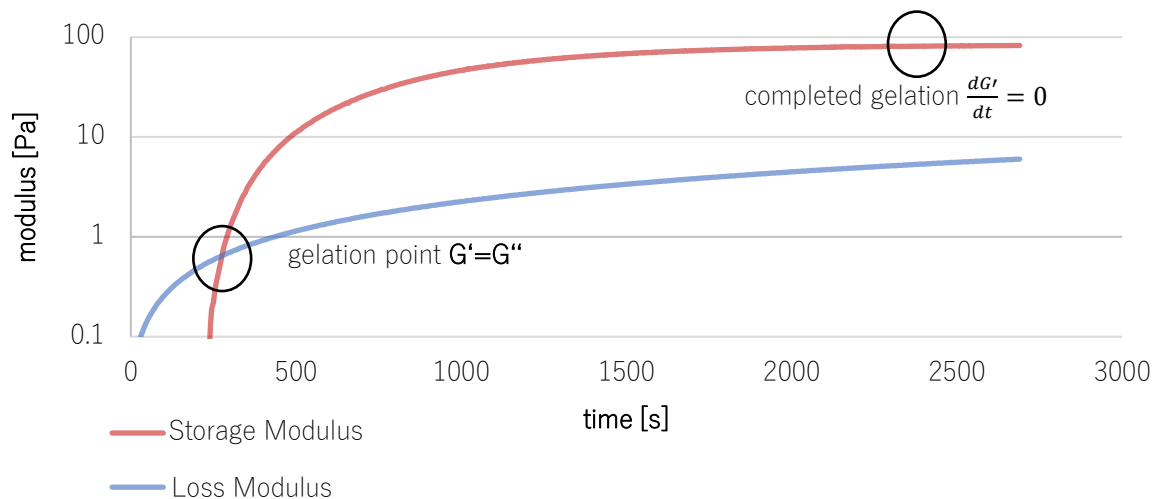


Figure 5.22 Rheological investigation of gelation reaction; ZP1 (5 wt.%), APS:Acrylate ratio (1:2) and APS:TEMED ratio (8:1).

In Fig.5.23, the gelation time is plotted in dependence of APS:Acrylate ratio for various concentrated polymer solutions. The amount of TEMED was kept constant in relation to APS concentration (APS:TEMED ratio 8:1). For solutions with a macromolecular content of 4 wt.% no gelation could be observed, supporting viscosity results that overlap concentration is not yet reached.

Generally, gelation time is affected by the collision of methacrylate radicals with other polymer crosslinking functionalities. Hence, the impact on crosslinking gelation is twofold by:

- a) increasing number of radicals
- b) increasing number of polymer collisions

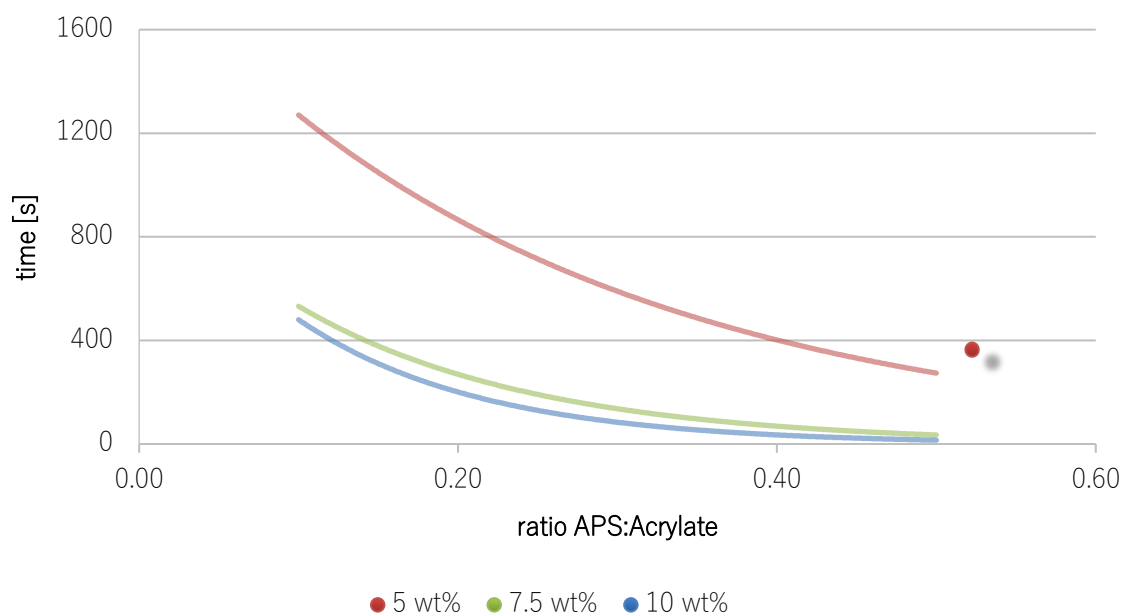


Figure 5.23 Gelation time in dependence of the APS:Acrylate ratio.

Gel formation occurs faster with higher APS content since more radicals are available and thus, more crosslinking points can arise simultaneously. Like expected, highest gelation time (approximately 22 minutes) was observed at lowest APS:Acrylate ratio (0.1) and minimal polymer concentration (5 wt.%). In contrast, almost instantaneous hydrogel formation (16 s) is obtained for highest initiator content and a 10 wt.% solution. Moreover, impact of APS on gelation follows logarithmic scale.

The change in gelation time for various polymer concentrations is demonstrated in Fig. 5.24. For all initiator concentrations, slowest gelation is observed for solutions with minimal polymer content of 5 wt.%, varying from approximately 22 down to 5 minutes. When concentration is increased to 7.5 wt.%, gelation time drops significantly, indicating that more collisions between crosslinkable methacrylate segments occur. In addition, when a substantial amount of APS is present (APS:Acrylate ratio >0.1), hydrogel formation occurs relatively fast within 2.5 minutes.

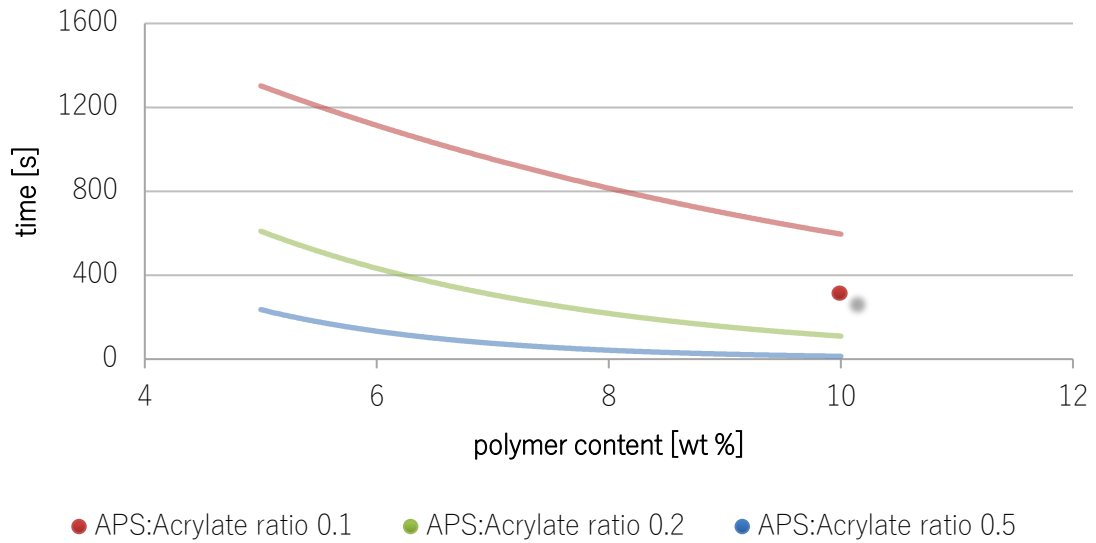


Figure 5.24 Gelation time in dependence of polymer concentration.

Such a massive decrease cannot be noticed when polymer concentration is further increased, especially for higher APS content (0.2 and 0.5 APS:Acrylate ratio). While gelation time reduces from approximately 13 minutes to 2.5 minutes from lowest to middle polymer concentration, additional polymer content does not influence hydrogel formation time. At first sight, higher polymer content should lead to more collisions between chains. Nevertheless, gelation may be counterbalanced by a simultaneous increase in viscosity, hence decreasing chain mobility and the number of crosslinking reactions. Both effects may result in a lower limit for gelation time, at which crosslinking becomes almost independent of polymer concentration.

In Fig. 5.25, completion time for crosslinking is plotted against the APS:Acrylate ratio. A substantial decrease in reaction time is observed for a doubling of APS content. For lowest initiator content crosslinking reaction is completed in between 80 and 100 minutes. When APS content is increased, completion of reaction reduces to approximately 20 minutes (7.5 and 10 wt.%) or respectively 45 minutes (5 wt.%). Although additional initiator still causes a decrease in reaction time, the impact is less pronounced, with completion in between 13 or respectively 29 minutes. Again, higher radical concentrations can explain faster completion of network formation, due to more simultaneously occurring crosslinking reactions between macromolecular chains.



Figure 5.25 Completion of hydrogel reaction in dependence of APS:Acrylate ratio.

Interestingly, polymer concentration only has a minor and inconsistent impact on the completion of hydrogel formation, see Fig. 5.26. For lowest radical amount, no tendency is observed and crosslinking reactions occur for more than 80 minutes. With higher APS content (0.2 APS:Acrylate ratio), completion of reaction is halving down from 45 minutes to approximately 22 minutes when concentration is increased from 5 to 7.5 wt.%. Nevertheless, higher polymer content does not further reduce reaction time. In contrast, for highest radical initiator concentration (APS:Acrylate ratio 0.5) a linear drop in crosslinking completion is observed, varying from 29 minutes for a polymer content of 5 wt.% down to 13 minutes for a 10 wt.% polymer solution.

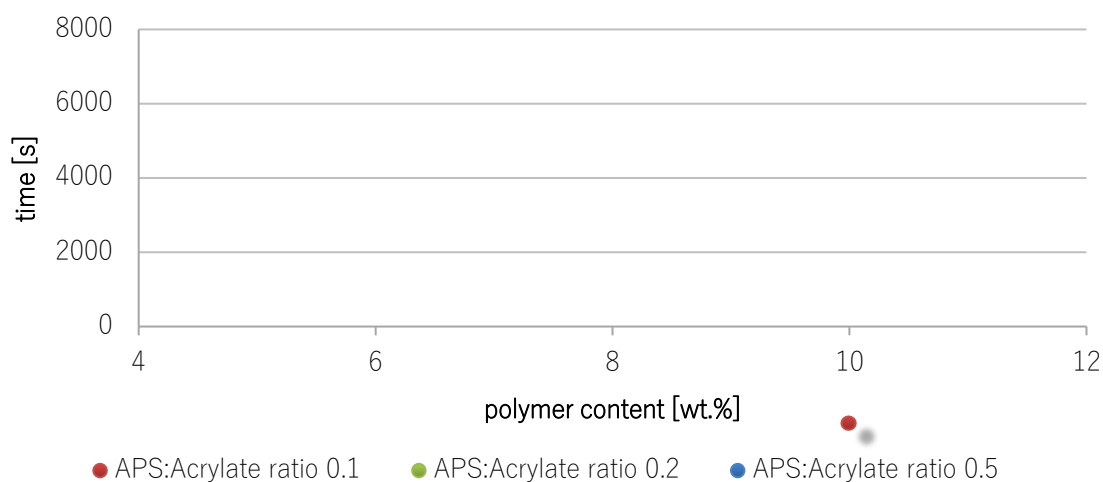


Figure 5.26 Completion of gelation in dependence of polymer concentration.

Since measurements have only been performed once, any reasoning why the completion of hydrogel formation in dependence of polymer content shows unequal tendencies for different initiator amounts, must be taken carefully. Nevertheless, lower impact of polymer concentration is observed.

As seen above, early stages of crosslinking (gelation points) are strongly affected by polymer concentration, due to more collision between chains. However, on-going reactions lead to a highly chemically crosslinked network with a sudden change in viscosity, which will inhibit chain diffusion into gel matrix and continuously decrease the number of collisions.<sup>164, 165</sup> Hence, influence of polymer concentration is strongly observed until early gel formation, but not for completion of reaction.

This effect is more pronounced for low APS concentration since diffusion of macromolecules is more relevant to crosslinking reaction when the number of radicals is low. In contrast, higher free radical content seems to be capable of compensating low mobility of macromolecules for creating three-dimensionally crosslinked structures.

#### 5.4.2 Mechanical properties

Besides studying the impact of solution conditions on gelation time, also influence on mechanical properties was investigated. Fig. 5.27 shows the damping factor in dependence of APS:Acrylate ratio. Generally, elasticity of samples slightly increases with rising initiator content. Lowest damping factor (0.11) is obtained for an APS:Acrylate ratio of 0.1. A higher amount of radical starter decreases damping factor down to 0.06. However, all damping factors are similar in range (~0.1) and were only measured once.

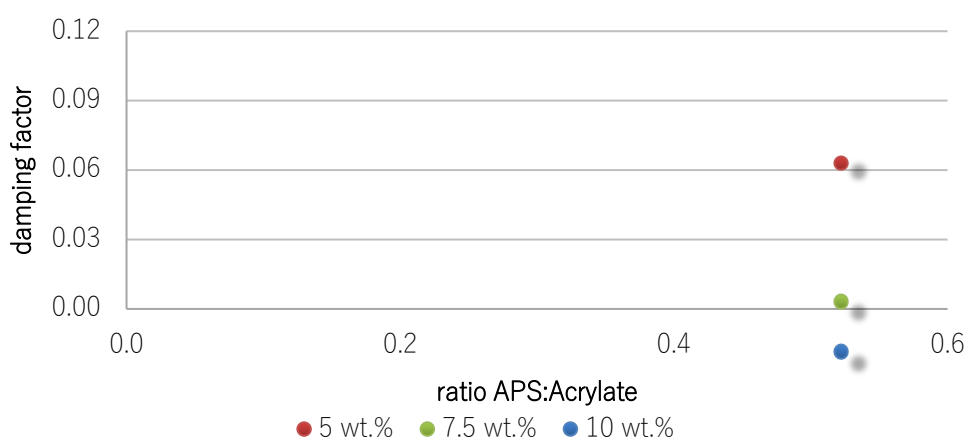


Figure 5.27 Damping factor in dependence of APS:Acrylate ratio for various polymer concentrations.

Thus, a more accurate description of viscoelastic properties can be achieved by additionally including storage modulus at the end of the crosslinking reaction, depicted in Fig. 5.28. Here, different tendencies are observed concerning polymer concentration. For a 10 wt.% solution, storage modulus is rising from approximately 9000 up to 20000 Pa with higher APS content. However, for lower concentrated solutions elastic proportions of hydrogel are less developed (~100-5000 Pa) and seem to be independent of initiator concentration.

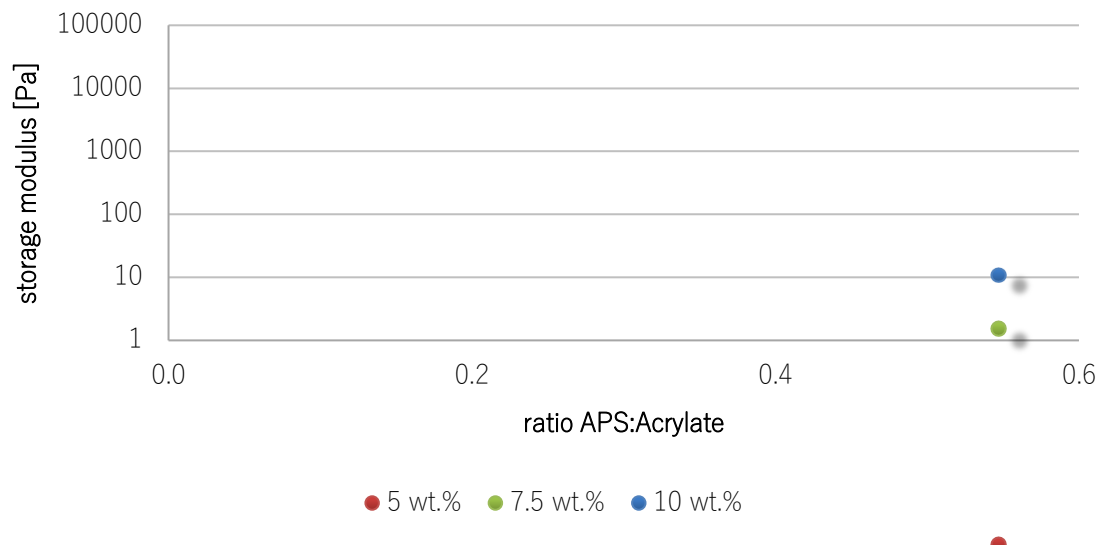


Figure 5.28 Final storage modulus in dependence of APS:Acrylate ratio.

The change in storage modulus in dependence of APS:Acrylate ratio is shown in Fig. 5.29, whereby storage ratio is calculated with the following equation:

$$\text{storage ratio} = \frac{G'(\text{APS/Acrylate ratio } x)}{G'(\text{APS/Acrylate ratio } 0.1)} \quad (5.13)$$

Contrasting gelation behavior for various polymer concentrations indicates differences in hydrogel crosslinking and network properties. In general, higher initiator concentrations increase the possibility of radical combination. Free TEMED or APS radicals can move more freely than macromolecules through the formed network, due to their smaller size. Consequently, a combination of radicals may occur more frequently than chemical crosslinking of methacrylate units.

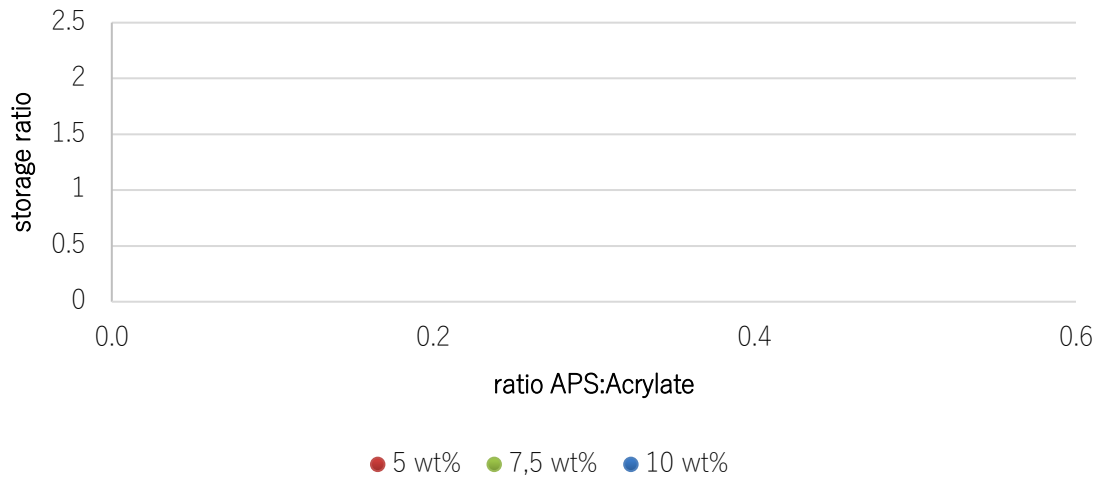


Figure 5.29 Change in storage modulus in dependence of APS:Acrylate ratio.

However, for a highly polymer concentrated solution, chain-chain crosslinking is still more probable due to higher number of collisions between chains. In contrast, solution with lower polymer concentration experience less collision between chains. Thus, impact of radical combination may be enhanced, essentially forming fewer crosslinking points and elastic gel networks.

Independent of initiator concentration, all hydrogels formed with high polymer concentration possess similar damping factors (see Fig. 5.30).

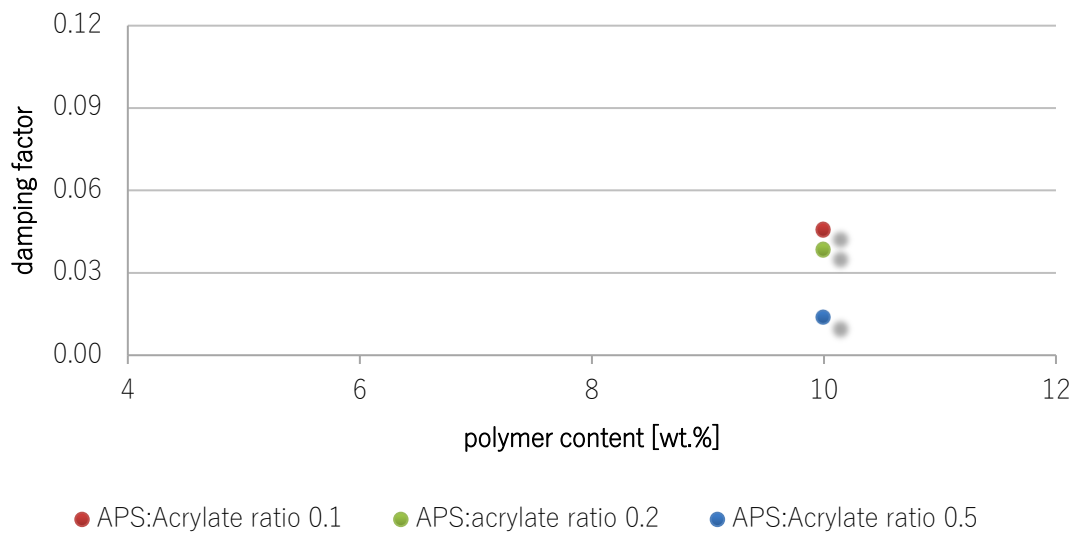


Figure 5.30 Damping factor in dependence of polymer content.

However, storage modulus rises exponentially from several hundred for a 5 wt.% solution up to 20000 Pa for highest polymer concentration (see Fig. 5.31). First, high amount of polymer will lead to more matter integrated into the hydrogel network and thus, gels possess more solid proportions. Furthermore, competition between interchain and intrachain crosslinking points is influenced by polymer concentration. While for high polymer contents interchain collision is more probable, low amount of polymer may favor intrachain crosslinking. Hence, low polymer concentration could result in hydrogels with irregularities regarding material density and consequently, reduce sample elasticity, schematically depicted in Fig. 5.32.

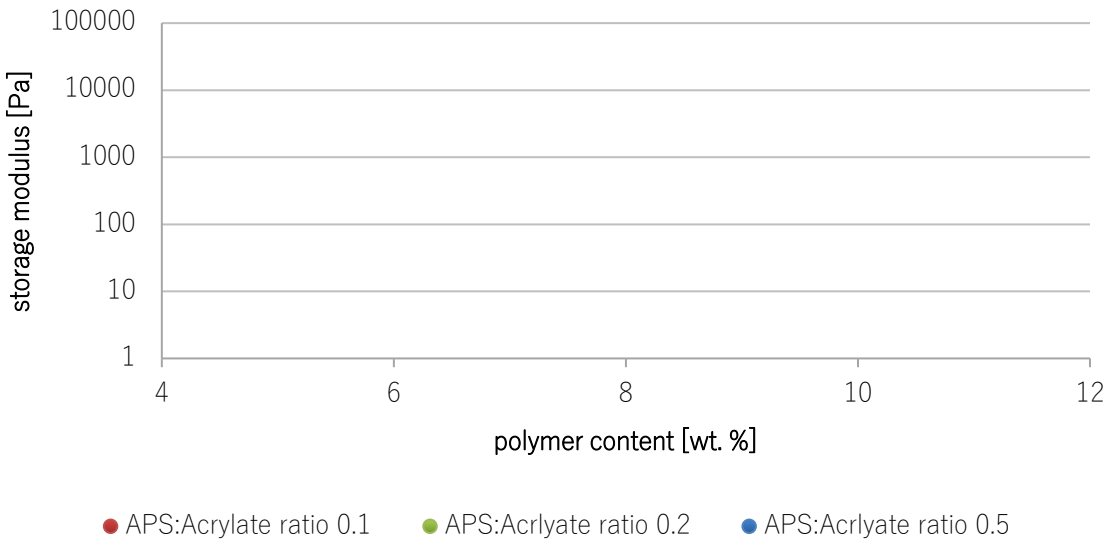


Figure 5.31 Storage modulus in dependence of polymer concentration

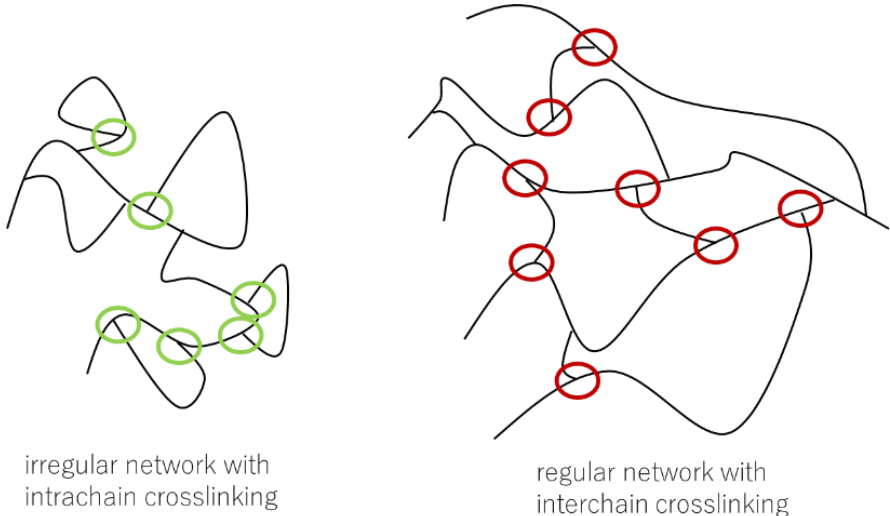


Figure 5.32 Intra- and interchain crosslinking and its impact on network structure.

### 5.4.3 Free bulk gelation summary

An overall analysis of free bulk gelation lead to the following conclusions:

- 1) Elastic hydrogels with storage modulus above 1000 Pa are only obtained for gelations with a polymer concentration above 7.5 wt.%.
- 2) The influence of initiator concentration on mechanical properties is dependent on polymer concentration. For high polymer concentrations, elastic portions of hydrogel increase with higher initiator content and vice versa.
- 3) The gelation time decreases exponentially with higher APS and polymer content.
- 4) A sharp reduction for time to completion of the crosslinking reaction is observed when APS:Acrylate ratio is increased from 0.1 to 0.2.
- 5) The impact of polymer concentration on completion of the crosslinking reaction is much less pronounced, probably due to inhibited macromolecular diffusion into hydrogel matrix.

## 5.5 In situ NF90 membrane modification

### 5.5.1 Pristine membrane characteristics

Pure water permeance, rejection of various substances as well as contact angle were measured according to section 4.5 and are given in Tab. 5.4.

Table 5.4 NF90 characteristics from experiments and literature.

NF90 characteristics	exp.	lit. <sup>166-169</sup>
rejection NaCl [%]	91.5 ± 6.6	90-96
rejection MgCl <sub>2</sub> [%]	95.1 ± 5.0	-
rejection Na <sub>2</sub> SO <sub>4</sub>	96.4 ± 2.1	> 98
rejection TEMED [%]	98.9 ± 0.7	-
rejection APS [%]	98.2 ± 1.1	-
zwitterionic polymer rejection [%]	100	-
permeance [L/hm <sup>2</sup> bar]	2.4 ± 0.7	3.6
contact angle	47.2±1.1	50.9 ± 4.9

In general, obtained results are in a similar range compared to literature. Differences can be attributed to the specific production of used batches. Pure water permeance is low (2.4 L/hm<sup>2</sup>bar) and the NF90 membrane possesses high monovalent and even higher divalent salt rejection, which is caused by tight and negatively charged and PA network surface due to size and charge exclusion phenomena.

For redox-initiator APS, a divalent organic ion, rejection is very high (>98%) and consequently it is continuously accumulated at the membrane surface during modification. Interestingly, almost complete rejection for TEMED can be observed, although MWCO of NF90 is about 200 Da and TEMED has only a molecular weight of 116 Da. Additionally, as expected, the synthesized zwitterionic polymer is entirely retained by the active PA surface. Essentially, rejection values of redox-initiator system and polymer indicate large extent of CP and hence, surface selective gelation conditions are most likely to be achieved during membrane modification.

### 5.5.2 Membrane modification

#### *Polymer concentration dependency*

NF90 membrane was modified by varying feed concentration of zwitterionic building block ZP1 and keeping the amount of APS and TEMED and filtration time (30 minutes) constant.

The initial feed characteristics are given in Tab. 4.3. The maintained permeability after modification procedure, calculated according to section 4.6.3, is depicted in dependence of polymer concentration in Fig. 5.33.

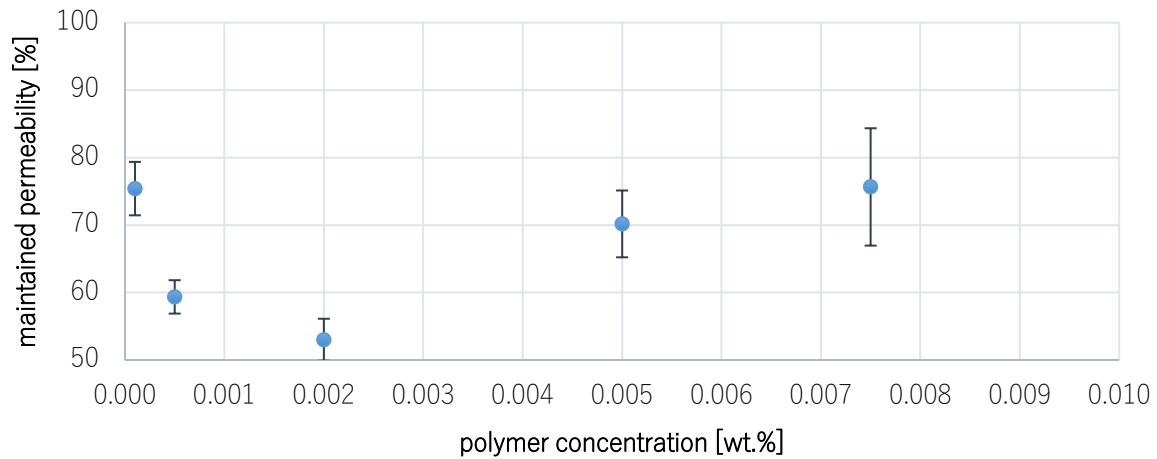


Figure 5.33 NF90 membrane modification: maintained permeability in dependence of polymer and redox-initiator feed concentrations.

In general, two different areas of concentration dependency are observed. First, for low polymer concentrations ( $c_f < 0.005$  wt.%), permeability is declining logarithmically with a maximal reduction of up to 50%. Counterintuitively, with higher feed concentrations ( $c_f > 0.005$  wt.%) maintained permeability again increases up to the range of ~70%. For low concentrations, a hydrogel may not be regularly formed since necessary gelation conditions may not be reached in the boundary layer. Hence, the initial severe decline might be related to defect blocking or “valley clogging” rather than by an uniformed hydrogel.<sup>170, 171</sup> A schematic representation of valley modification is depicted in Fig. 5.34.

Typically, PA possesses a ridge and valley topography and will experience heterogenous flux dependent on the layer thickness. Thinner valley regions enable higher mass transport and are therefore known as “hot spots”.<sup>172, 173</sup> For these areas, it is speculated that they are more prone to deposition of organic and colloidal matter.<sup>174</sup> Similarly, the higher flux at valleys can lead to heterogenous concentration polarization across membrane surface area. Consequently, for low feed concentration, a hydrogel may only be built in the PA valleys, in which CP reaches critical conditions. In addition, “hot spot” modification may lead to more dense hydrogels, compared to regularly formed networks and decrease membrane permeability more pronounced. Maintained permeability results therefore lead to the assumption that only feed concentrations

around and above 0.005 wt.% achieve a sufficiently high concentration polarization across whole membrane surface and hence, can initiate regular gel network formation.

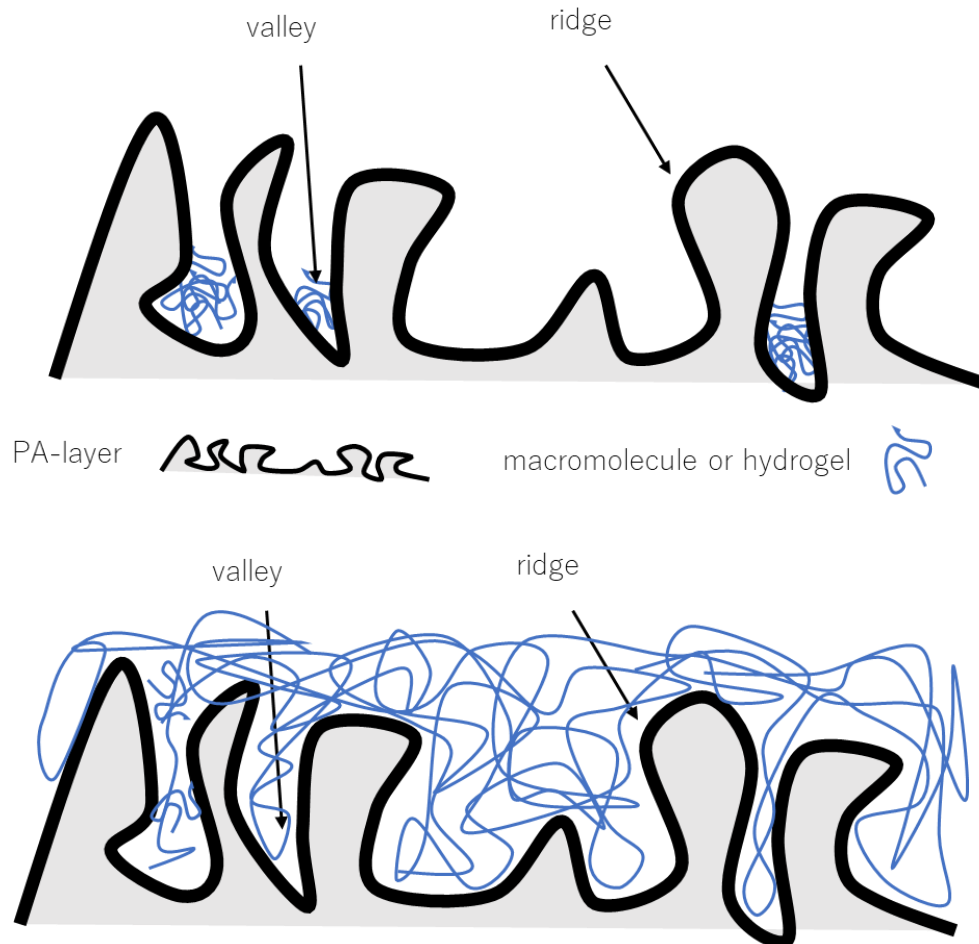


Figure 5.34 Schematic representation of heterogenous hot spot (top) and regular hydrogel modification (bottom) onto ridge and valley topographies.

The assumption that there seems to exist a certain threshold concentration between 0.002 and 0.005 wt.% is supported by SEM images, see Fig. 5.35. In contrast to typical ridge and valley structure, modified membranes showed a smoother top layer. However, degree of modification is dependent on polymer feed concentration. For very low concentrations (0.0005 wt.%), no regular zwitterionic hydrogel on top of polyamide layer can be observed. Nevertheless, polymeric matter is heterogeneously distributed in agglomerated form on the membrane surface and is either blocking some defects on the membrane surface or solely forms hydrogel in PA valley regions. This may explain the strong decrease in permeability after modification (approximately 40%).

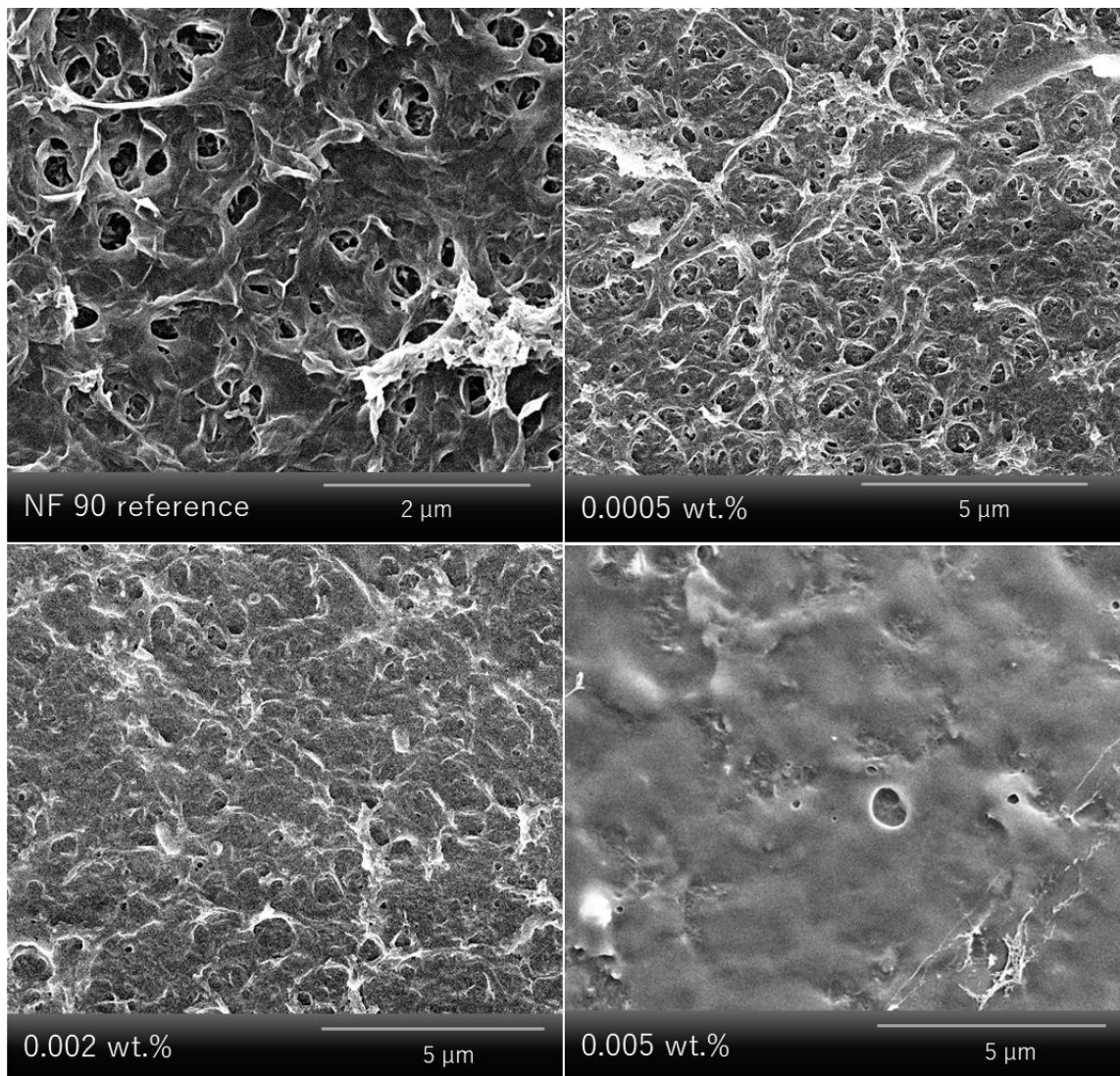


Figure 5.35 SEM images of NF90 membrane and zwitterionic hydrogel modified membranes (ZHMM1 NF90) at different polymer feed concentrations.

For a polymer feed concentration of about 0.002 wt.%, PA surface coverage is even more pronounced. However, the ridge and valley structure can be still detected. The hydrogel is not entirely smoothening PA ridge and valley structures, which supports the hypothesis that concentration polarization is not sufficiently high.

In contrast, a modification performed using a feed concentration of 0.005 wt.% resulted in an almost complete covering and smoothening of the rough and original polyamide structure. Nevertheless, the surface is not covered homogeneously, which might be attributed to filtration conditions because no stirring was applied during modification. Initially, modification with no additional shearing forces was thought to increase CP. However, no stirring is also accompanied by an undefined boundary layer and hence, hydrogel coatings still show irregularities in form of “patchy” patterns on top of PA layer.

The superior permeation of regular hydrogel crosslinking compared to defect blocking is even more pronounced when feed concentration of 0.0075 wt.% was used during membrane modification (see Fig. 5.36). The hydrogel covered the PA layer more dominantly than in case of modifications using lower concentrations. Although entire membrane is coated, permeability reduction is only 20%, pointing to superior permeation abilities and low hydraulic resistance imposed by hydrogel, compared to accumulation of polymeric matter in PA valleys.

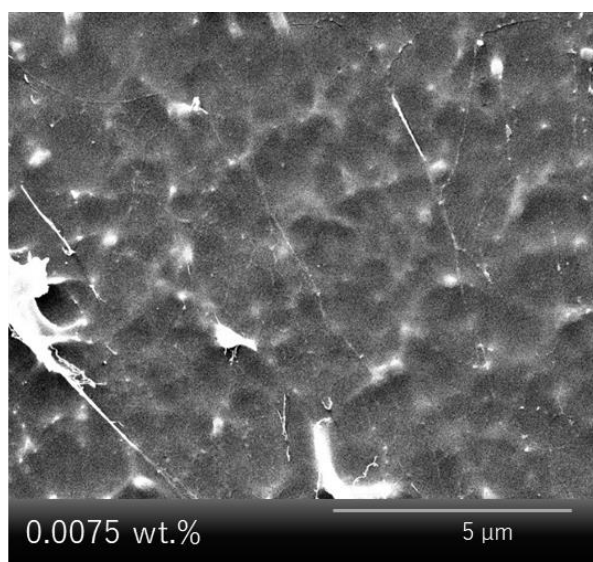


Figure 5.36 SEM images of NF90 membrane and zwitterionic hydrogel modified membranes (ZHMM1 NF90) at a feed concentration of 0.0075 wt.%.

The argumentation that feed concentration and CP are more relevant for successful gelation onto the membrane surface rather than overall transported mass per area is supported by Fig. 5.37. Shown data is calculated with by equation 5.14:

$$m/A = V_p * c_f \quad (5.14)$$

With  $m$  as convectively transported mass,  $A$  as membrane surface area,  $V_p$  as filtrated volume and  $c_f$  as polymer feed concentration.

Analogous to concentration dependency, a first exponential decrease up to 50% in permeability is observed when transported mass towards membrane rises up to 0.03 mg/cm<sup>2</sup>.

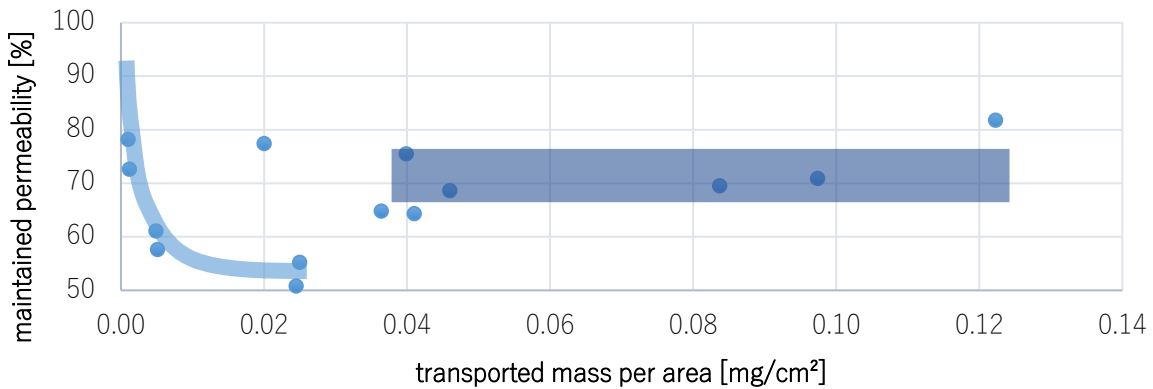


Figure 5.37 NF90 membrane modification: Maintained permeability in dependence of transported mass per area.

For higher concentrated feed solutions in the range of 0.005 wt.%, transported mass varies between 0.04 and 0.05 mg/cm<sup>2</sup>, due to slightly different membrane fluxes. However, permeability reduction is less pronounced (~30%), compared to modifications with lower transported mass and feed concentration. These results support the above-mentioned hypothesis about different reaction locations in dependence of polymer feed concentration. While for low concentrations polymerization solely occurs at valleys immediately at the membrane surface, higher polymer content can lead to regular crosslinking further away from membrane surface.

Interestingly, reduction in permeability remains constant, even though concentration and transported mass are increased (see Fig. 5.37, blue plateau). Once a critical threshold concentration in the boundary layer is exceeded, reaction may form hydrogel with similar density and thickness, independent of transported mass. Furthermore, the similarity of hydrogel thicknesses and permeability reductions may refer to fast gel formation, in which further mass transport is only integrated into network structure to a minor portion.

#### *Filtration time dependency*

More supportive data for this hypothesis are obtained by Fig. 5.38 and 5.39. In this experiment, concentration for modification was kept constant (0.005 wt.%, ZP1) and only filtration time was varied from 9 to 60 minutes. These experiments help to investigate the influences of reaction time and transported mass on the modification degree.

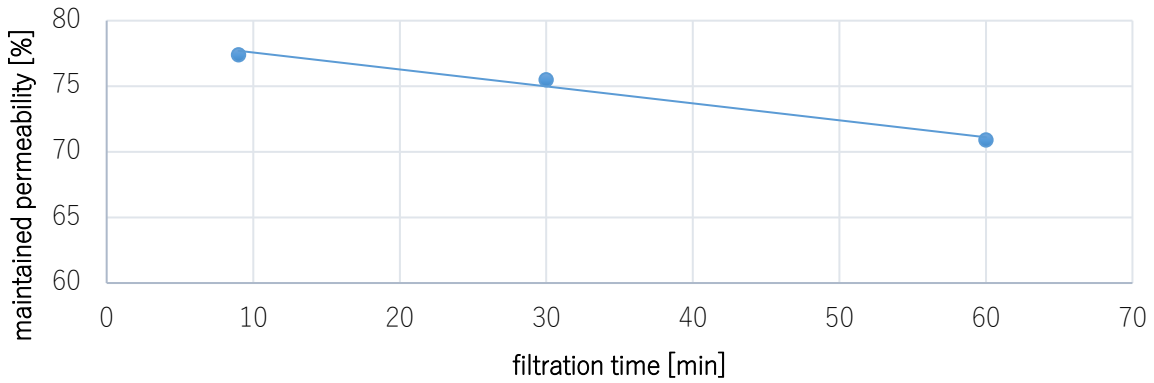


Figure 5.38 NF90 membrane modification: Maintained permeability in dependence of filtration time and a constant polymer feed concentration (0.005 wt.%).

Fig 5.38. shows only a slight declining trend, when filtration time is varied from 9 to 60 minutes. All membranes showed a permeability decline in the range of 25%. Consequently, a filtration time of 9 minutes is already long enough to lead to regular hydrogel on the PA layer, assuming a morphology described in Fig. 5.35 (bottom right).

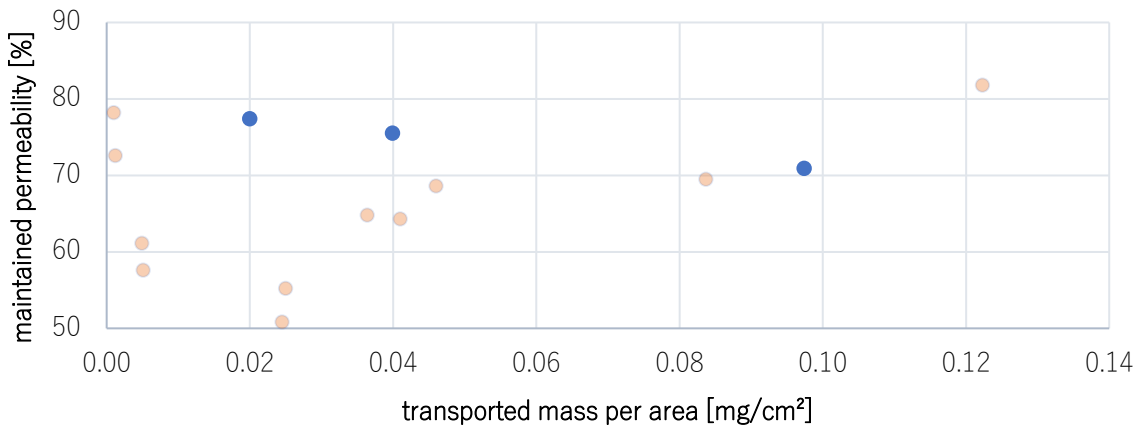


Figure 5.39 Comparison of NF90 membrane modification: Maintained permeability in dependence of transported mass per area and constant polymer feed concentration (0.05 wt.%, blue) and different polymer feed concentration (orange).

Hence, modification was already successful at short filtration times and a low amount of transported mass, which is strongly indicating that concentration polarization is causing crosslinking reaction on membrane surface. Comparison with membranes, modified with different feed concentrations strengthens this argument (see orange points in Fig. 5.39). Moreover, the initial reaction phase is already creating a crosslinked hydrogel network and longer modification time has only slight impact on degree of modification.

On the other hand, the reduction in permeability with higher transported mass may be caused by a slightly thicker and/or denser hydrogel, which is formed twofold:

- a) Filtration time is prolonged and more material can be incorporated due to convective polymer transport.
- b) Reaction time is prolonged and more chemical crosslinking can occur, leading to a denser hydrogel matrix.

However, conclusions must be made carefully, since time dependent experiments have only been performed once.

### 5.5.3 Membrane fouling

In order to evaluate surface gelation and its influence on anti-fouling properties, static protein adsorption experiments using BSA were performed. In Fig. 5.40, reversible fouling recovery is shown in the dependency of polymer feed concentration. For pristine polyamide layer a decrease of about 50% was observed, which points to the strong fouling propensity of rough ridge and valley topography, characteristic for NF90 membranes.<sup>170, 175</sup>

However, when membranes are modified by hydrogel, RFR increases logarithmically with higher feed concentrations. For low polymer concentration ( $c_f < 0.002$  wt.%), in which only valley clogging or irregular gelation occurred, RFR already increases to about 70%. For feed concentration in the range of 0.002 wt.% RFR was approximately 90%, while for modifications with concentrations at 0.005 wt.% or higher, almost no reduction in permeability caused by fouling can be observed due to smoothing of membrane surface and introduction of zwitterionic surface chemistry.

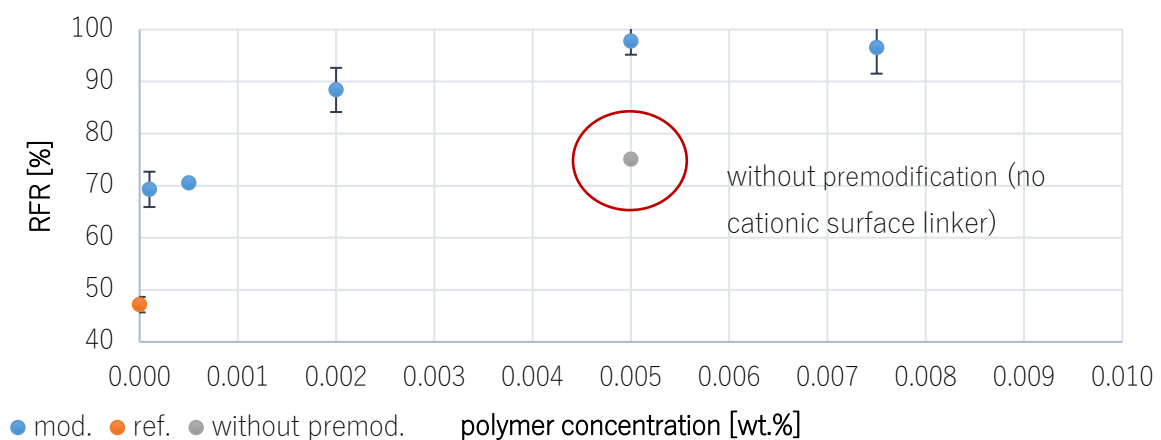
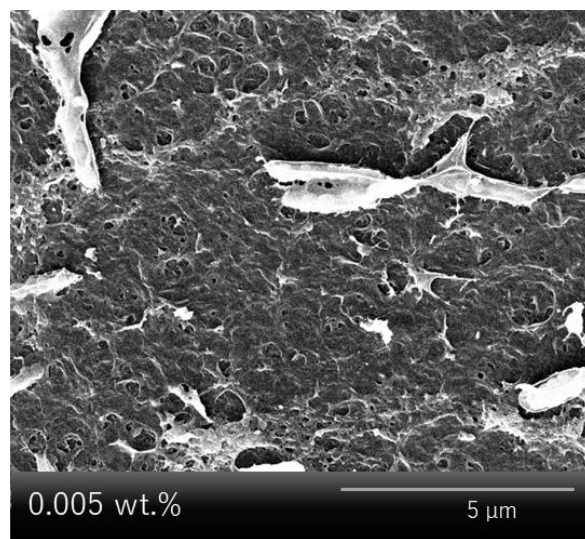


Figure 5.40 RFR in dependency of polymer feed concentration for static BSA adsorption.

Interestingly, a coating procedure (0.05 wt.%), in which membrane was not premodified with the cationic linker, did only show minor beneficial anti-fouling properties (RFR~70%), but still reduced membrane permeability up to approximately 20%. The result may indicate that zwitterionic hydrogel is washed from membrane surface since adhesion forces between zwitterionic polymer and membrane are weaker than in the case of cationic macromolecular linker and negatively charged PA. In addition, SEM images show clumped structures that may hint to a delamination process during freeze-drying, which is again indicating no tight anchoring between zwitterionic hydrogel and membrane due to the absence of surface linker (see Fig. 5.41).



*Figure 5.41 SEM images of NF90 membrane and zwitterionic hydrogel modified membranes (ZHMM1 NF90) at a feed concentration of 0.005 wt.% but without premodification (no cationic surface linker).*

Furthermore, independency of transported mass on modification and impact on fouling abilities is demonstrated via variation of filtration time experiments, see Fig. 5.42. All membranes show almost no static fouling (RFR>98%). Consequently, a filtration time of 9 minutes is already sufficient to form an anti-fouling hydrogel covering the active PA layer.

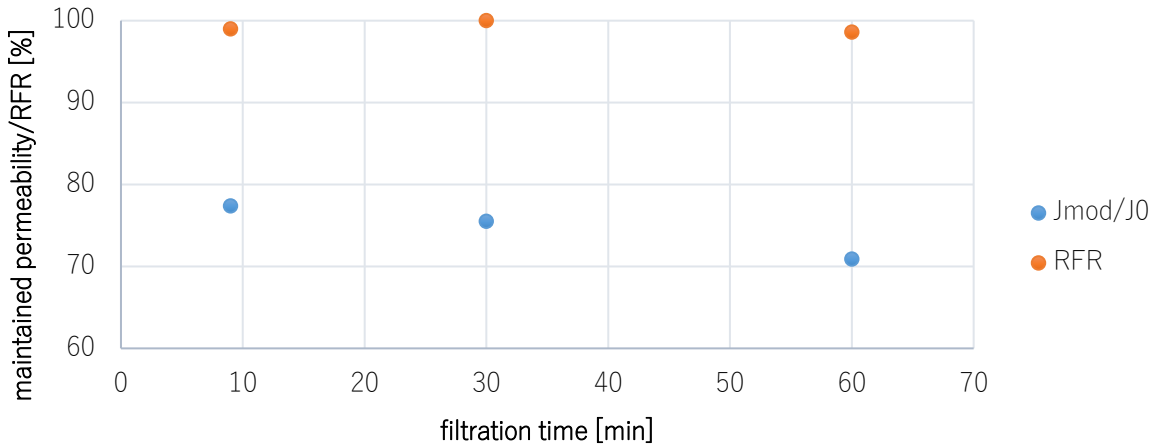


Figure 5.42 RFR in dependency of filtration time with constant polymer feed concentration (0.005 wt.%)

In summary, fouling results strengthen the hypothesis that concentration polarization is causing membrane modification rather than overall transported polymer mass. Moreover, fouling test support the argument that a gel is already formed during initial filtration phase when concentration is sufficiently high. Increased reaction time and further convective mass transport have no significant impact on performance parameters such as permeability and AF properties.

The minor impact of modification time on the imposed resistance by the hydrogel layer may indicate that radical gelation is kinetically fast and quickly completed. Alternatively, chain termination reaction can occur, which will inhibit further network growth. As seen in free bulk gelation experiments, completion of gelation reaction is rather a function of APS content than of polymer concentration. Hence, a high concentration of APS near the membrane surface could cause a significant decrease in gelation time and may explain why longer filtration time did not show an influence on network and permeation abilities. However, this hypothesis is only speculative since concentration of APS, TEMED and polymer in the boundary layer are unknown for NF90 membrane modification and were not varied.

#### *Trade off*

For evaluation of membrane performance, a trade-off parameter regarding permeability reduction caused by the zwitterionic hydrogel coating and the introduced anti-fouling abilities by equation 5.15:

$$trade\ off\ [\%] = \frac{P_{mod}}{P_o} * RFR \quad (5.15)$$

An ideal membrane coating would only minimally reduce membrane permeability, while simultaneously introduce sufficiently pronounced anti-fouling properties. Hence, a high trade-off represents excellent anti-fouling properties while still maintaining high permeation rates.

The trade-off for given modifications is shown in Fig. 5.43. Pristine membranes possess a high fouling propensity (RFR~50%) and consequently show a low trade-off. While membrane coatings prepared using low polymer feed concentrations ( $c_f < 0.002$  wt.%) slightly improved fouling recovery (RFR~70%), the permeability reduction is so dramatic (~30%) that resulting trade-off is not improved and still comparable to pristine NF90 membrane (~50%). However, when feed concentration is increased above 0.005 wt%, both parameters (maintained permeability and RFR) improve. Hence, the trade-off is highest for concentrations bigger than 0.005 wt.% with values of almost 80%.

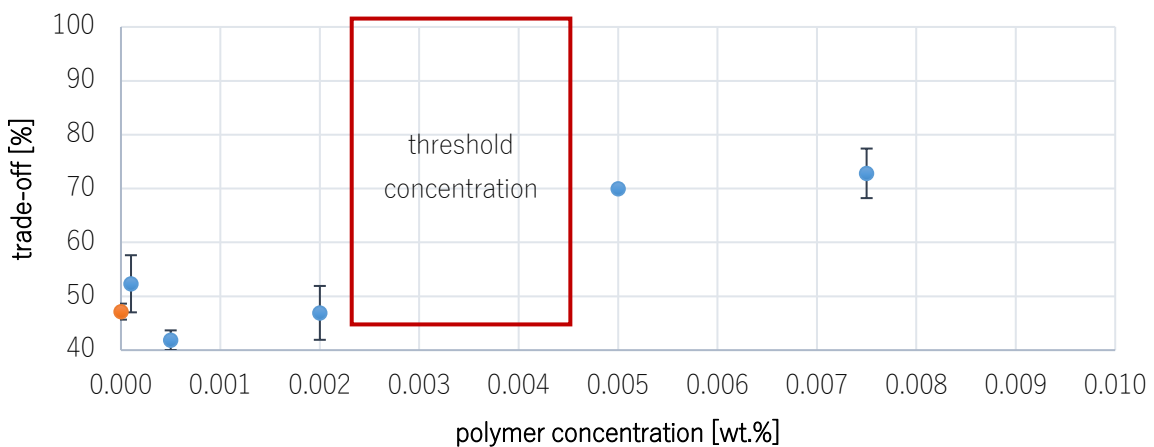


Figure 5.43 Trade-off in dependence of polymer concentration.

Additionally, since RFR and permeability reduction are almost independent of filtration time, trade-off values are not correlating with filtration time, see Fig. 5.44. It can therefore be concluded that hydrogel was formed during the first 10 minutes of filtration and more extended modification procedure did not improve membrane performance significantly.

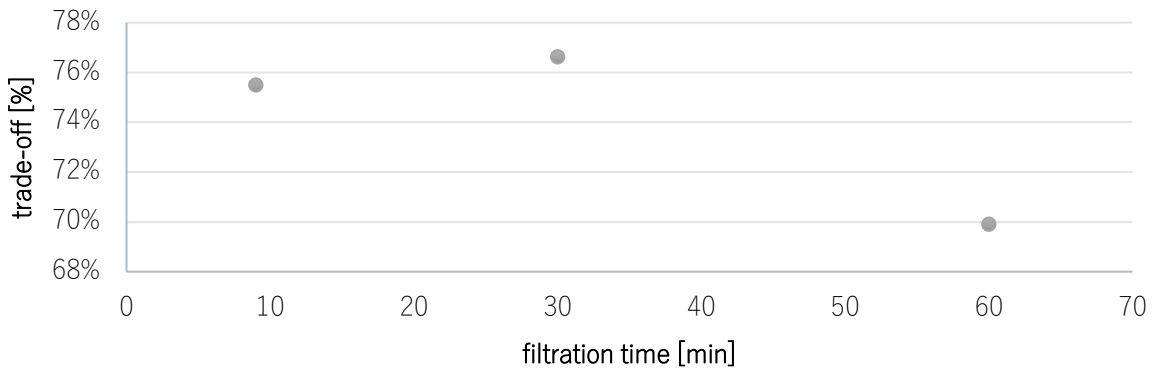


Figure 5.44 Trade-off in dependence of filtration time.

#### 5.5.4 Zwitterionic hydrogel modified NF90 membrane characteristics

##### *Impact on salt rejection*

The impact of zwitterionic hydrogel onto membrane rejection was evaluated for membranes, which were modified using feed concentrations of approximately 0.005 wt.%. The results are summarized in Tab. 5.5. Compared to pristine membrane, no additional rejection influence can be observed when the hydrogel is applied onto PA membranes.

Since hydrogel possesses a neutral surface charge, it does not introduce additional charge exclusion phenomena for various salts. Moreover, no size exclusion rejection mechanism is added to the membrane, which indicates that mesh sizes of polymeric hydrogel networks seem to be significantly bigger than ion diameters. Hence, the PA layer still represents main rejection barrier and is the limiting factor for salt permeation.

Table 5.5 Comparison of salt rejection for pristine NF90 and zwitterionic hydrogel modified membranes.

NF 90 characteristics	ZHMM1	pristine
rejection NaCl [%]	89.6 ± 4.4	91.5 ± 6.6
rejection MgCl <sub>2</sub> [%]	94.1 ± 3.6	95.1 ± 5.0
rejection Na <sub>2</sub> SO <sub>4</sub> [%]	97.3 ± 1.3	96.4 ± 2.1

##### *Zeta potential*

Hydrogel coating was also investigated by zeta potential measurements. Since polyamide possesses free carboxylic groups, its overall charge is negative with an IEP at a pH of approximately 4. At pH >9 membranes show a zeta potential below -100 mV. However, after adsorption of cationic macromolecular linker, the zeta potential becomes more positive due to coverage of polyamide layer and its negatively charged groups. At low pH zeta potential for premodified membrane almost reaches 70 mV, while at pH 10 much less negative zeta

potential (-60 mV) than pristine NF90 membrane was found. Additionally, IEP shifts to pH 7.8, which can also be attributed to the adsorption of cationic linker. The difference compared to unmodified membrane indicates that adsorption of macromolecular linker is stable over whole pH range with sufficiently strong attractive Coulomb forces between negatively charged carboxylate groups of PA layer and quaternary ammonium units.

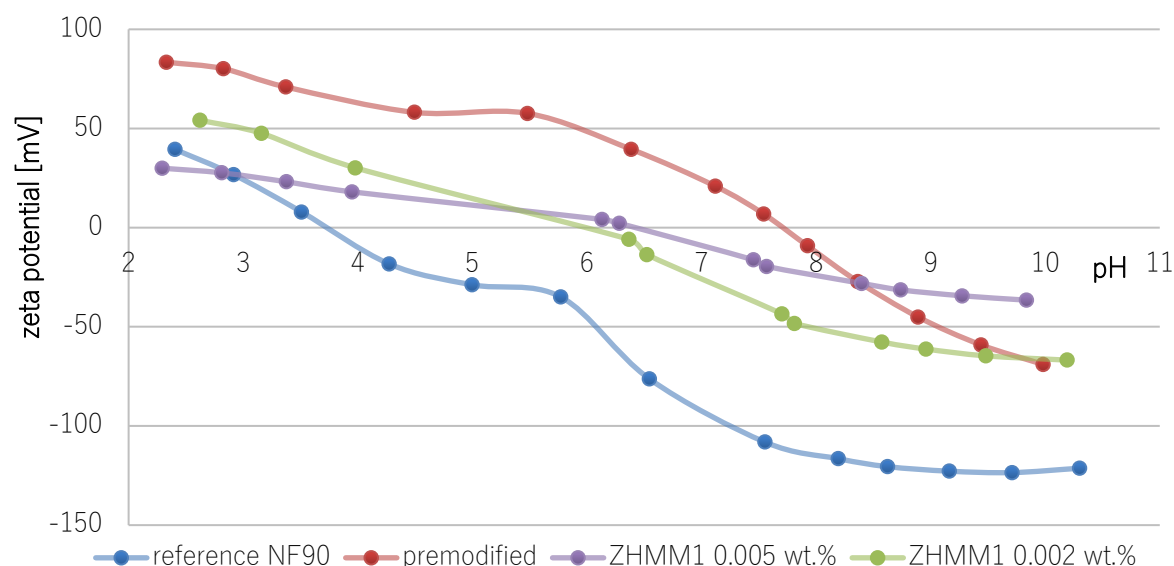


Figure 5.45 Zeta potential measurements for pristine NF90, pre-modified and ZHM1 hydrogel coated membranes.

After zwitterionic modification using two different concentrations (0.002 and 0.005 wt.%), the membrane becomes more neutral with less extreme swings in acidic as well as in basic aqueous media. The difference points to a successful membrane coating by the zwitterionic network, in which inter- and intramolecular Coulomb interactions lead to surface neutrality.

Nevertheless, differences in zeta potential for both concentrations can be observed. First, higher polymer concentration is leading to lower extremes in zeta potential (40 and -35 mV) than a feed concentration of 0.002 wt.% (55 and -65 mV). The differences in zeta potential support previous argumentation that higher polymer concentration was explained to cause a more pronounced CP and consequently lead to more homogenous gelation on the membrane surface. In contrast, concentration below 0.005 wt.% did not form regular gels over whole membrane area and hence, showed more swings in zeta potential measurements, attributed to premodified, cationic and unmodified membrane areas. However, IEP of modified membranes is around pH 6 and independent of feed concentration, which suggests that also lower concentration is partially covering polyamide surface area.

## IR spectroscopy

IR spectroscopy was only performed for ZHM1 membrane (0.005 wt.%) in order to prove the existence of hydrogel on membrane surface. Compared to pristine membrane, two main differences in the IR spectra can be detected. First, carbonyl group, present in the zwitterionic polymer, appears at typical wavenumber range of  $1724\text{ cm}^{-1}$ . Second, a broad signal in the range of  $3200\text{ to }3400\text{ cm}^{-1}$  is more visible in pristine membrane, usually representing N-H-stretching.<sup>146</sup> The intense amine signal is assigned to unreacted amine functionalities in PA layers of m-phenylenediamine monomer during interfacial polymerization. However, when the membrane was covered with zwitterionic hydrogel amine functionalities disappeared or at least sharply decreased in intensity. Moreover, C-H stretching vibrations in the range of  $\sim 2900\text{ cm}^{-1}$  decreased as well in intensity, compared to pristine membrane spectra.

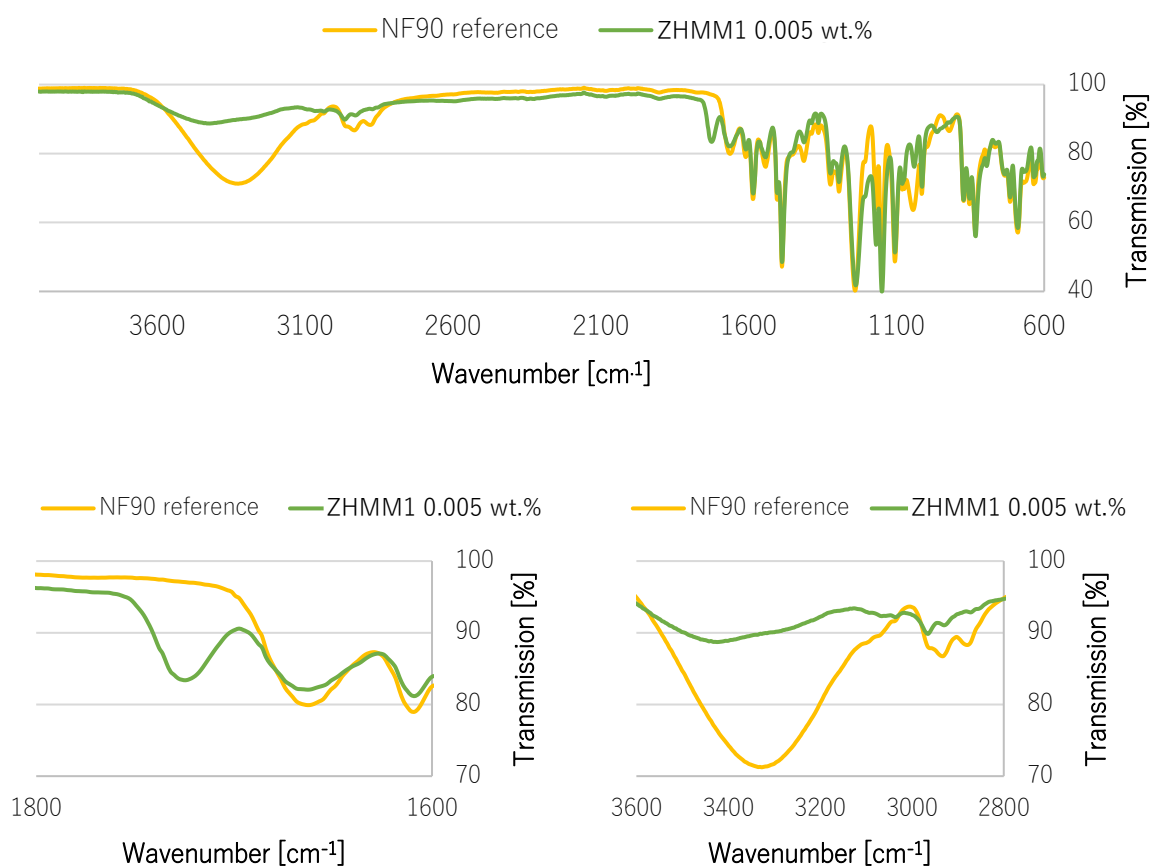


Figure 5.46 IR spectra and enlargement of two IR ranges showing differences between NF90 and ZHMM1 (0.005 wt.%) membrane (left: Carbonyl stretching vibration of the zwitterionic hydrogel at  $1726\text{ cm}^{-1}$ ; right: N-H stretching vibration of pristine PA membrane).

### Contact angle

Contact angle measurements were performed for pristine, premodified and modified membranes. Pristine NF90 membrane is made by interfacial polymerization of m-phenylenediamine and trimesoylchloride, which results in a fully aromatic polyamide layer.<sup>176</sup> As expected, aromatic PA surface possess lowest hydrophilic character and a contact angle of about 47°, which is in similar range as reported in literature (~51°).<sup>169</sup>

When cationic macromolecular linker or zwitterionic hydrogel is adsorbed, the aromatic PA layer is covered and the surface becomes more hydrophilic. Due to charged groups, contact angle decreases down to approximately 25° for premodification as well as for hydrogel layer. In Fig. 5.47 the various contact angle for different surfaces is summarized.

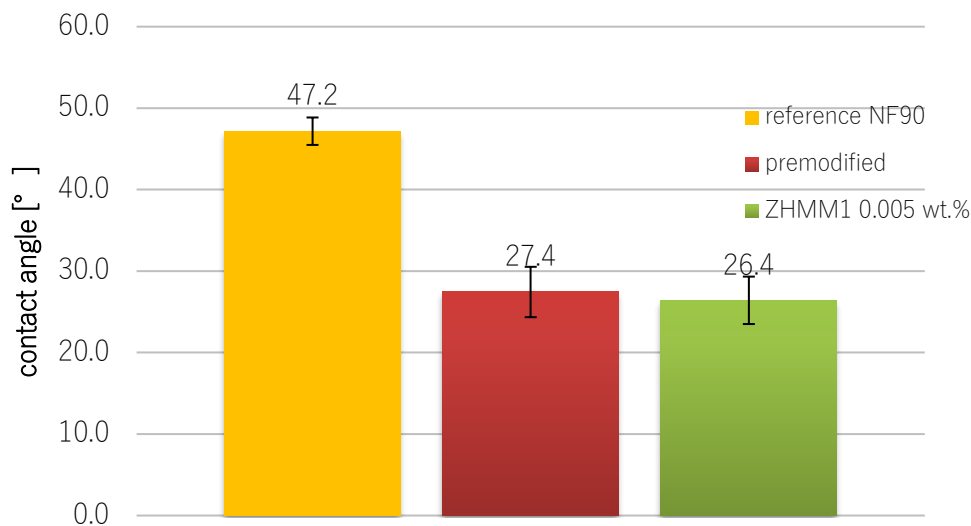


Figure 5.47 Contact angle of NF90 reference, premodified and ZHM1 membranes (0.005 wt.%).

#### 5.5.5 NF90 membrane modification summary

Results allow to make the following conclusions regarding NF90 membrane modification:

- 1) For low concentrations ( $c_f < 0.002$  wt.%), no hydrogel coating on membrane can be observed. However, permeability reduction was unexpectedly high and was related to local gelation as valley clogging or dense hot spot modification.
- 2) For feed concentration of 0.005 wt.%, membranes were almost entirely covered and showed no fouling propensity in static adsorption experiments. Maintained membrane permeabilities were in the range of 70 to 80 % and are not further decreasing when higher feed concentrations were used. Hence, ideal membranes possess a trade-off up to 80%, compared to approximately 50% for pristine membranes.

- 3) Higher polymer feed concentration is more relevant for successful modification rather than overall transported mass, indicating that CP is probably leading to critical conditions in the boundary layer and causing a crosslinking reaction.
- 4) Higher reaction times only marginally impact permeability and anti-fouling properties. The minor influence indicated fast reaction kinetics due to high radical concentration in the boundary layer. Alternatively, chain propagation may be quickly terminated by radical combination, disproportionation or quenching reactions and explain why the impact of filtration time is neglectable.

In general, NF90 gelation experiments prove that membranes can be modified by the zwitterionic hydrogel. However, no estimation of CP was performed. Hence, more detailed insights and investigation of CP are gained by modification experiments of NF270 membranes.

## 5.6 In situ NF270 membrane modification

### 5.6.1 Pristine membrane characteristics

Water permeance and rejection of NF270 membrane for various substances as well as contact angle were measured according to section 4.6 and are given in Tab. 5.6.

Table 5.6 NF270 characteristics from experiments and literature.

NF270 characteristics	exp.	Lit. <sup>177-181</sup>
NaCl rejection [%]	37.7 ± 7.8	50-52
Na <sub>2</sub> SO <sub>4</sub> rejection [%]	89.7 ± 2.8	90-95
TEMED rejection [%]	36.5 ± 9.5	-
APS rejection [%]	75.9 ± 3.1	-
zwitterionic polymer rejection [%]	100	-
pure water permeance [L/hm <sup>2</sup> bar]	11.3 ± 1.0	17.0 ± 0.8
contact angle [°]	32.5 ± 1.3	29-55

Overall, the investigation of membrane properties gives similar results compared to literature. However, permeability was lower in used membranes, which may be attributed to specific membrane production batch. In comparison with other NF membranes, NF270 membranes possess a relatively high permeation rate, due to its extremely thin top lay (~21 nm).<sup>178</sup>

In comparison with NF90 membrane, NF270 showed less retention of monovalent ions. Lower rejection of NaCl can be attributed to bigger pores in NF270 membrane, also suggested by higher MWCO (400 vs. 200 Da).<sup>182</sup> In contrast, negatively charged divalent sulfate anions are

retained by Donnan and dielectric exclusion phenomena, resulting in much higher rejection, typical for PA membranes. Therefore, NF270 is often regarded as loose NF membrane.<sup>183</sup>

As expected, the zwitterionic polymer is completely retained by the membrane. However, significant permeation for redox-initiator compounds can be observed and will substantially decrease CP of initiator. As a result, the incomplete rejection may complicate gelation in the boundary layer since kinetics of decomposition into radicals and consequent initiation of chain growth will compete with compounds permeation time.

### 5.6.2 Membrane modification

#### *Estimation of boundary later thickness*

In order to acquire information about the extent of CP, boundary layer thickness was firstly calculated by using filtration experiment based on Film model theory, in which mass transfer coefficient for a semi-permeable compound (here HEMA, see section 4.7.1) was employed. Tab. 5.7 gives rejection of HEMA in dependence of stirring rate.

*Table 5.7 HEMA rejection in dependence of stirring rate.*

stirring rate [rpm]	rejection HEMA [%]
200	24.7 ± 8.2
400	35.4 ± 3.7
600	44.5 ± 3.9
800	46.3 ± 8.1
1000	42.9 ± 18.0

Overall observed rejection of HEMA increases with a higher stirring rate. Stirring introduces more pronounced shearing forces on boundary layer and lowers extent of CP and concentration at the membrane surface. Due to the lowered concentration at the liquid-membrane interface, less solute permeation can occur, which essentially leads to decreasing permeate concentration with higher stirring rates. Hence, observed rejection, which only considers bulk and permeate concentration, will show rising rejection for more pronounced shearing stress.<sup>56</sup>

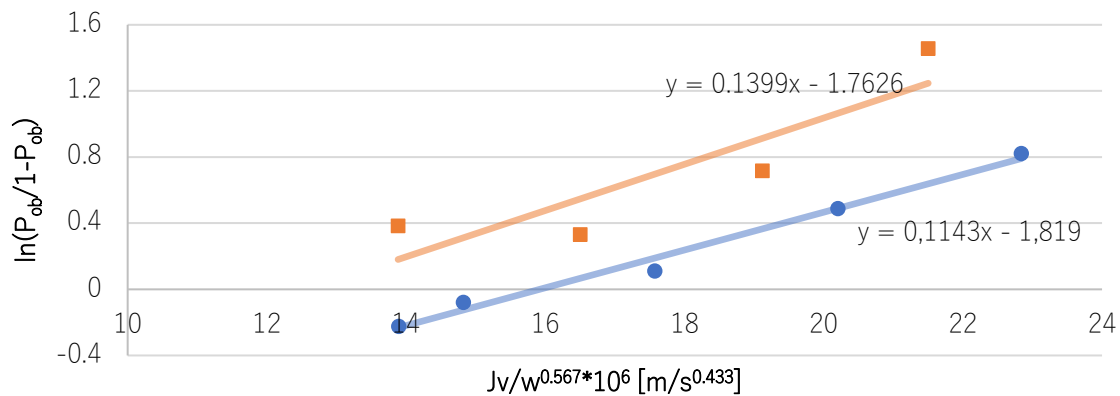


Figure 5.48 Permeation of HEMA as a function of flux and stirring rate.

Two experiments, in which permeation of HEMA in dependence of flux and stirring rate was investigated, are shown in Fig. 5.48. With the aid of the average slope of linear plot, which is equal to  $1/k'_d$ , boundary layer thickness can be obtained, according to section 4.7.1. Mass transfer coefficient and boundary layer thicknesses in dependence of stirring rate are then given by Tab. 5.8.

Table 5.8 Mass transfer coefficient and boundary layer thickness in dependence of stirring rate.

stirring rate [rpm]	mass transfer coefficient [ $10^{-6}$ m/s]	boundary layer thickness [ $\mu\text{m}$ ]
0	0.3	194
200	1.6	38
400	2.3	25
600	2.9	20
800	3.5	17
1000	3.9	15

Layer thicknesses are in a reasonable range of several  $\mu\text{m}$  and decrease logarithmically with a higher stirring rate. The decrease of boundary layer thickness as a result of more intense shearing stress imposed hydrodynamic conditions near to the membrane surface.

Although CP layer thicknesses have been used to estimate extent of concentration polarization, it must be considered that polymer solutions are expected to show profoundly different hydrodynamic conditions in the boundary layer compared to solutions of monomer HEMA. More concretely, continuous macromolecular mass transport towards the membrane surface will strongly increase viscosity causing overall thicker boundary layers. However, for purpose

of simplification, boundary layer thickness for membrane modification was assumed to be controlled by the stirring rate.

### *Critical and limiting flux*

Fig. 5.49 shows flux for various polymer concentrations in dependence of pressure and allows to determine critical and limiting flux.

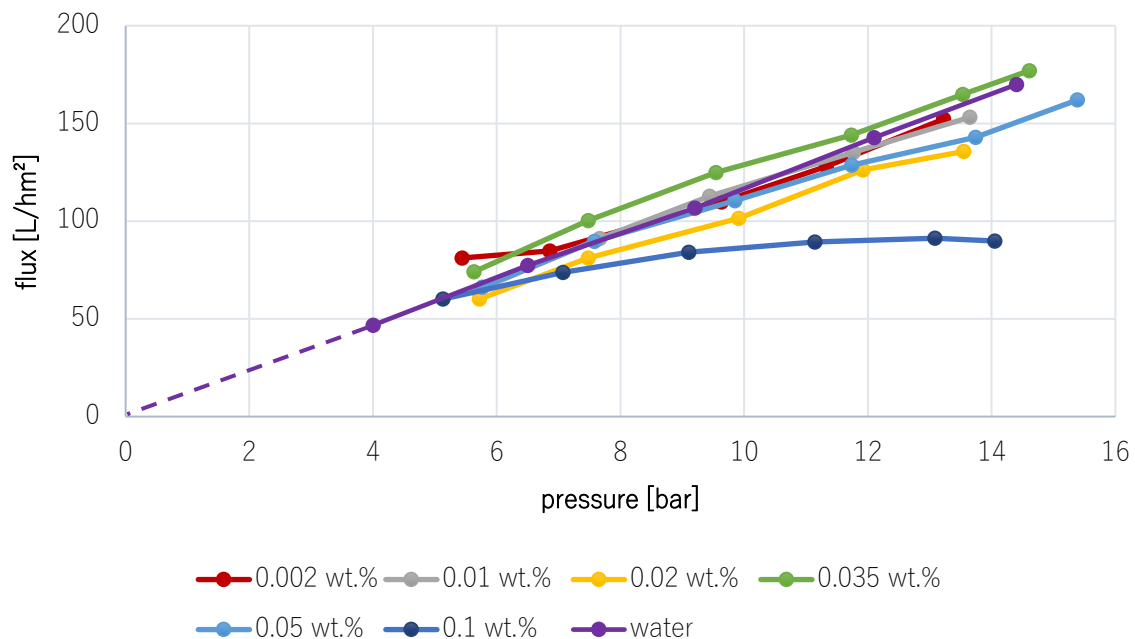


Figure 5.49 Flux for polymer solutions in dependence of applied pressure.

Filtrations performed with feed solutions with concentrations up to 0.05 wt.% show a linear increase in flux with higher applied pressure difference and are in the range of pure water flux. Although CP is strongest in the beginning of filtration, decrease within the first minute cannot be observed for polymer solutions compared to pure water flux.

However, for filtrations with 0.1 wt.% concentrated feed solutions, a critical and limiting flux can be observed. Critical flux describes the flux until deviation from pure water flux can be observed (strong form), or linear dependence with pressure starts to disappear (weak form). It is often conceptualized as the flux at which repulsive forces between solute and surface are overcome and fouling starts to become predominant.<sup>184, 185</sup> More precise, hydrodynamic drag forces overcome energy barrier, resulting from electrostatic forces and allow deposition of polyelectrolytes. In Fig. 5.49 critical flux is observed for a flux of approximately 75 L/hm<sup>2</sup> at a concentration of 0.1 wt.%.

When pressure is further increased, limiting flux is achieved at 90 L/hm<sup>2</sup>. Limiting flux can be understood as the “last reachable flux”. At limiting flux, increase in pressure will lead to growing of a gel layer by further polymer deposition and will result in a maximal operating flux. More accurate, increase of driving force (pressure) will be compensated by hydraulic resistance imposed by growing cake layer.<sup>186</sup>

However, it must be noted that all performed zwitterionic polymer filtrations do not lead to irreversible fouling and initial membrane permeabilities could be regained through intense washing. Therefore, no cake layer was formed by zwitterionic macromolecules during 30 minutes of filtration and flux reduction is solely a consequence of resistance imposed by CP. Hence, permeability reduction during modification will be a consequence of gelation reaction at the membrane surface, rather than fouling caused by zwitterionic macromolecules.

### *Estimation of CP*

Membrane modification was performed using different polymer feed concentrations and redox-initiator contents and a constant stirring rate of 200 ppm. Hence, the boundary layer thickness was assumed to be approximately 40 μm (see Tab. 5.8)). Moreover, due to limited amount of polymer batches, different polyzwitterions (ZP1 and ZP2) were used. However, this section serves as an example and a brief overview of one specific modification procedure ( $C_{f,polymer}=0.08$  wt.%) and estimation of CP conditions. Flux during modification was tracked and is depicted in Fig. 5.50. In addition, following free bulk gelation conditions (see Tab. 5.9) were used as reference and tried to be mimicked in boundary layer.

*Table 5.9 Free bulk gelation conditions.*

polymer concentration [wt.%]	APS:Acrylate ratio	gelation time [min]	completion of reaction [min]
5	0.2	~13	~45
5	0.5	~5	~28

Flux decreases sharply in the initial filtration phase and follows a logarithmical plot. Since macromolecules are completely retained by NF270 membrane, high concentration polarization is caused immediately. The CP leads to an additional hydraulic resistance and consequently, flux decreases sharply. After five minutes of modification, only a slight further linear reduction can be observed and flux stabilized around 30 to 40 L/hm<sup>2</sup>. The minimal but continuous reduction may be caused by crosslinking reaction and formation of the hydrogel layer on membrane surface.

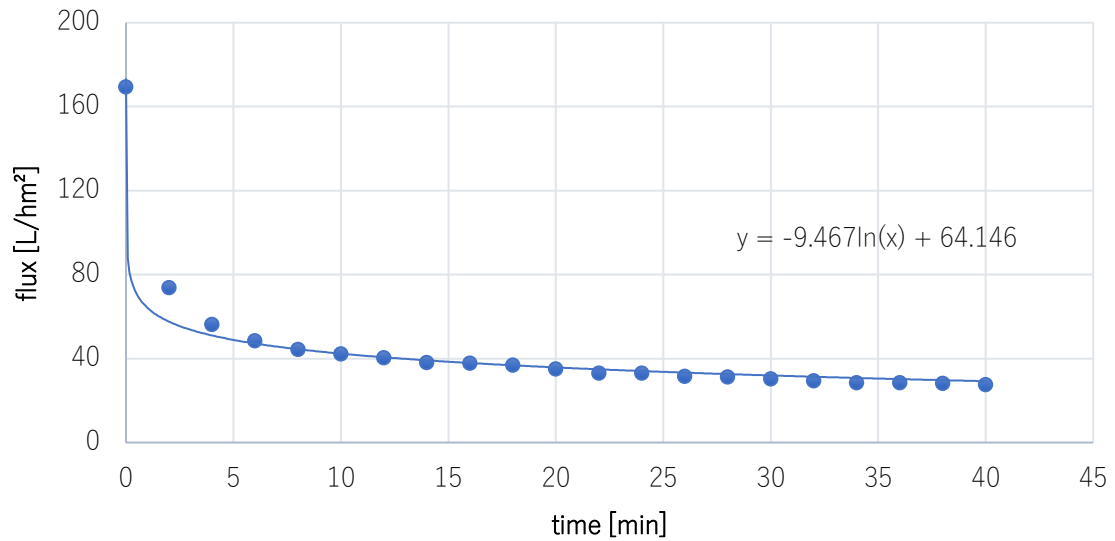


Figure 5.50 Flux during membrane modification with a polymer feed concentration of 0.08 wt.%.

Moreover, dead end filtration is a non-continuous process and stationary conditions for CP cannot be assumed. Feed concentrations are increasing with time. Hence, permanent and steady flux decrease may be caused by dynamic dead end conditions, which contribute to a constant increase of concentration at the membrane surface.

However, when flux data are entered post experimentally into CP estimation model, according to section 4.7.2, course of CP will decrease after climax, rather than increase. The CP courses for various assumed boundary layer thicknesses are shown in Fig. 5.51.

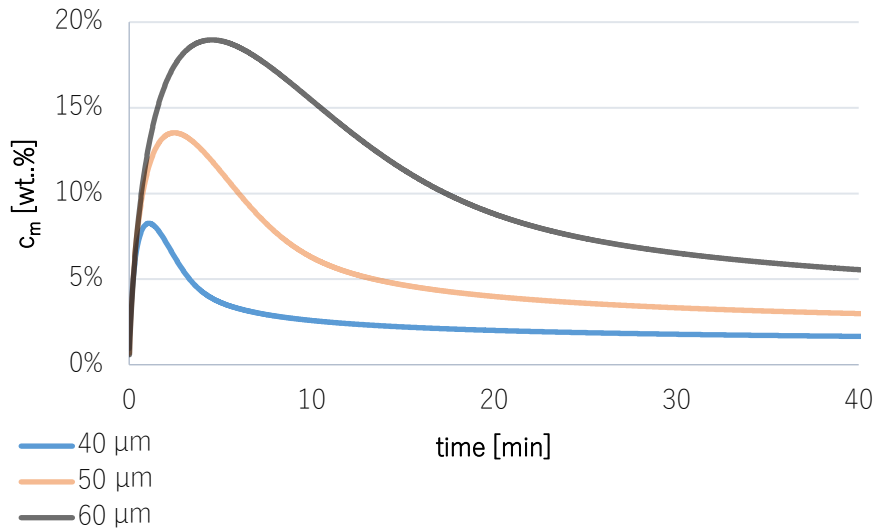


Figure 5.51 Dynamic polymer concentration at the membrane surface with a polymer feed concentration of 0.08 wt.-%.

It is worth noticing that concentration in the boundary layer varies over time due to dynamic conditions in dead end mode and their impact on back diffusion. Depending on the assumed layer thickness, concentration rises in the early stage of filtration up to 5 minutes, until back diffusion phenomena become more dominant and CP starts to decrease. For a boundary layer thickness of 40  $\mu\text{m}$ , the peak concentration during modification procedure is around 8 wt.-%, while for a thickness of 60  $\mu\text{m}$  the model predicts a concentration of approximately 19 wt.-%. In addition, average concentration over time varies from 3 wt.-% to about 9 wt.-%.

In general, a thicker layer reduces diffusive transport away from membrane surface due to longer diffusion distance. Higher polymer amount in boundary layer is obtained and accompanied by an increase in viscosity, which additionally decreases diffusion rate. Hence, with thicker boundary layers higher average as well as peak concentrations are predicted. The concentration courses, demonstrated in Fig. 5.51, are therefore massively influenced by estimated layer thickness and its contribution to diffusion.

However, for all assumed thicknesses, necessary overlap condition, investigated in rheological experiments (see section 5.3.3) were reached, at least regarding peak concentration of polyelectrolytes next to the membrane surface. In contrast, the average concentration during the whole filtration procedure does only meet critical conditions for an assumed layer thickness of 50 and 60  $\mu\text{m}$  but is too low when boundary layer thickness is assumed to be 40  $\mu\text{m}$ .

### Estimation of CP in dependence of polymer concentration

When polymer concentration and redox-initiator content are varied, the following flux courses are obtained for a modification with ZP1. The feed parameters are given in Tab. 5.10.

Table 5.10 Feed parameter in NF270 modification with const. TEMED feed concentration (0.06 wt.%).

polymer feed concentration [wt.%]	APS feed concentration [wt.%]
0.1	0.08
0.085	0.07
0.08	0.05
0.065	0.04
0.04	0.03

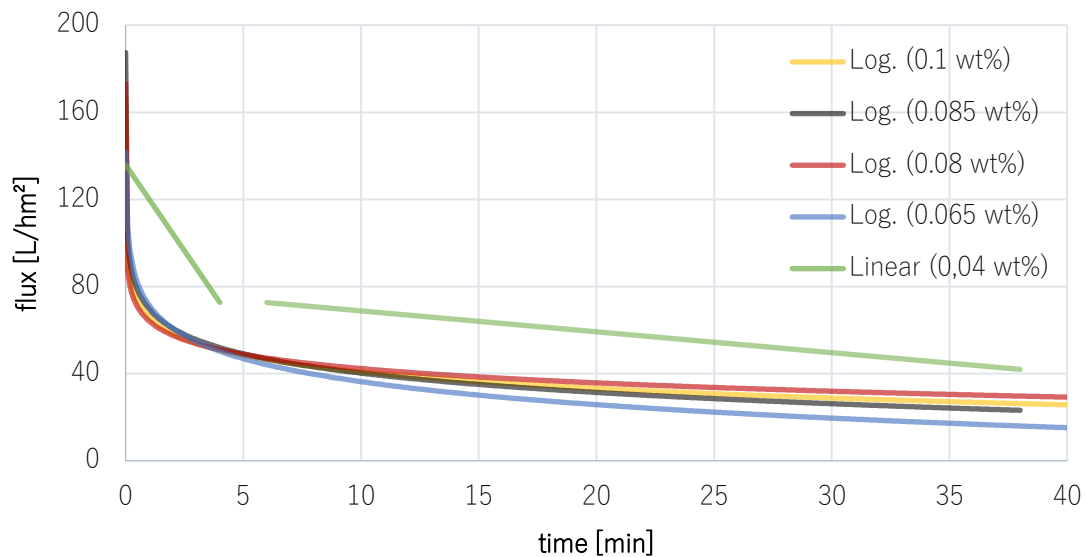


Figure 5.52 Flux courses for membrane modifications with various polymer feed concentrations.

For all modifications, except for  $c_f=0.04$  wt.%, flux as a function of time can be fitted logarithmically. Again, initial decrease of permeation rate is strong, due to additional resistance caused by concentration polarization. After 5 minutes more than two third of initial flux is lost. With a feed concentration of 0.04 wt.% initial flux reduction is less dramatic (50% loss) and can be fitted linearly. Additionally, later filtration phase shows significantly higher fluxes (~40 to 70 L/hm<sup>2</sup>) compared to courses obtained for polymer concentration above 0.065 wt.%.

When experimental flux values are inserted into the CP estimation model with an assumed layer thickness of 40  $\mu\text{m}$ , polymer concentrations at the membrane surface over time can be estimated and are shown in Fig. 5.53.

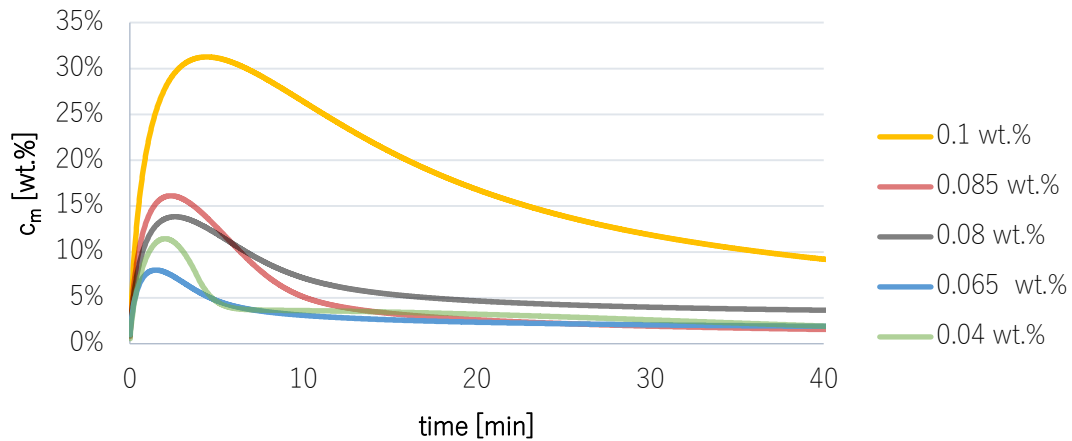


Figure 5.53 Concentration course in boundary layer for various polymer feed concentrations.

Significant high polymer content (above 30 wt.%) at the membrane surface is reached for a feed concentration of 0.1 wt.%. All peak and average concentrations are given in Tab. 5.11. Regarding peak concentration, all filtrations should allow gelation on the membrane surface. However, average concentrations are lower and only procedures, where feed concentration is higher than 0.08 wt.%, should lead to gelation on membrane surface. Interestingly, lowest feed concentration (0.04 wt.%) predicts more polymer at the membrane surface than a modification with 0.065 wt.%, attributed to its overall higher flux.

Table 5.11 Estimated concentration in boundary layer in dependence of polymer feed concentration.

polymer feed concentration [wt.%]	membrane peak concentration [wt.%]	membrane average concentration [wt.%]
0.1	31.2	18
0.085	16.1	4.2
0.08	15.2 $\pm$ 2.8	6.5 $\pm$ 1.8
0.065	7.8	2.7
0.04	9.8 $\pm$ 0.4	3.2 $\pm$ 0.1

Furthermore, modeling suggests a substantial variation of CP extent that would have more severe impact on flux during modification. However, flux variation during filtration is weak and may point to more stable CP conditions than proposed by estimation. More concretely, a

dramatic reduction of concentration polarization may stem from an overestimation of diffusion transport. Hence, flux data suggest that after an initial increase, CP will stabilize due to balance between convective and diffusive mass transport. Nevertheless, such behavior is not consistent with modeled conditions at the membrane surface, which predicted a much more dynamic extent of CP. However, it is important to notice, some of the accumulated polymer in the boundary layer will react and is therefore not able to diffuse back into bulk solution. These crosslinked chains are therefore not part of CP. However, the model does not consider the transition of CP into hydrogel. Consequently, the estimated concentration at the membrane surface may be generally overestimated.

### *Membrane modification*

Fig. 5.54 shows the maintained permeability after modification procedure for various polymer feed concentrations (see Tab. 5.11). For membranes modified using concentrations below of 0.085 wt.% membrane permeability can be regained, indicating either that no hydrogel exists on membrane surface or gelation is minimal. Nevertheless, for slightly higher polymer concentrations in feed, permeability reduction is dramatic and drops by about 80%.

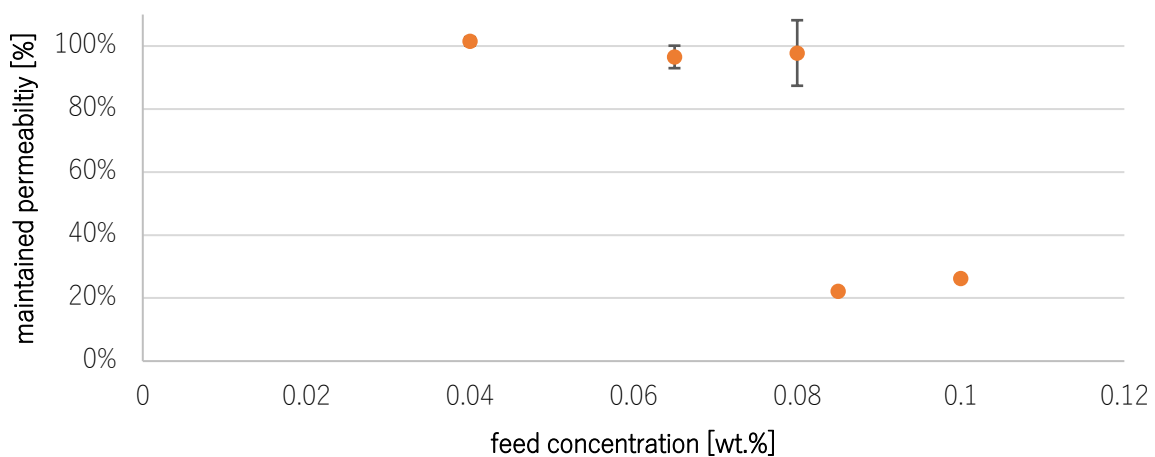


*Figure 5.54 NF270 modification: permeability recoveries in dependence of polymer feed concentrations.*

The hydrogel layer thickness of modified membranes, obtained via SEM, supports the permeability recovery data (see Fig. 5.55). Although pristine NF270 membrane is already relatively smooth compared to most PA membranes, further decrease in membrane roughness due to zwitterionic hydrogel can be observed.<sup>187</sup> Thick gel between 1.2 and 1.5  $\mu\text{m}$  ( $c_f=0.085$  or 0.1 wt.% respectively) was formed on the membrane surface that will impose additional hydraulic resistance and can therefore explain the significant and sudden drop in membrane performance.

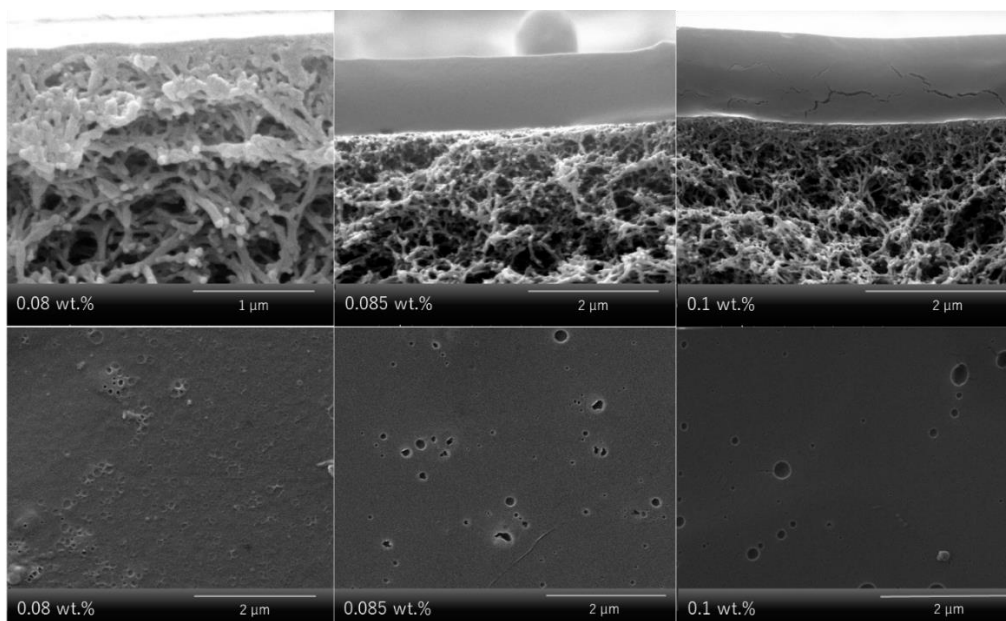


Figure 5.55 SEM images of ZHM1 membranes with different polymer feed concentrations; top: cross-section, bottom: membrane surface.

The results may lead to the conclusion that filtrations with feed concentrations above 0.08 wt.% generate critical gelation conditions in boundary layer. Nevertheless, such a statement is premature, since also redox-initiator amount was varied (and only APS:Acrylate ratio was kept constant). However, solely focusing on polymer concentration is insufficient because gelation is mainly influenced by APS and TEMED content.

#### *Redox-initiator dependency*

It may be the case that although polymer concentration at the membrane surface is high enough for all performed filtrations, redox-initiator concentrations in previous experiments were too low. This assumption is supported, because APS and TEMED are only partially retained by the NF270 membrane and consequently, lower CP was achieved for the redox-initiator compounds. Moreover, already formed radicals may pass membrane before initiating crosslinking reaction. To understand the impact of redox-initiator amount, further membrane modifications were performed at three different APS concentrations with constant polymer and TEMED contents in feed (ZP2), summarized in Tab. 5.12.

Table 5.12 Feed characteristics for NF270 modification.

polymer feed concentration [wt.%]	APS feed concentration [wt.%]
0.08	0.04

\*no TEMED added

0.08	0.06
0.08	0.09
0.08	0.06*

Flux for mentioned modifications follow logarithmical plots, which are presented in Fig. 5.56. Interestingly, flux in gelation procedures with various APS feed concentrations does not differ for the first ten filtration minutes. However, after around 20-30 minutes, flux reduces for two high initiator concentrations of 0.06 and 0.09 wt.%, which may indicate beginning of hydrogel formation. For lower APS feed content, the flux difference is diminished at approximately 40 minutes and may hint to even more postponed starting point of crosslinking reaction. However, only slight differences in overall permeation capacity between membrane modifications exist. Major resistance is imposed by CP during early filtration phase.

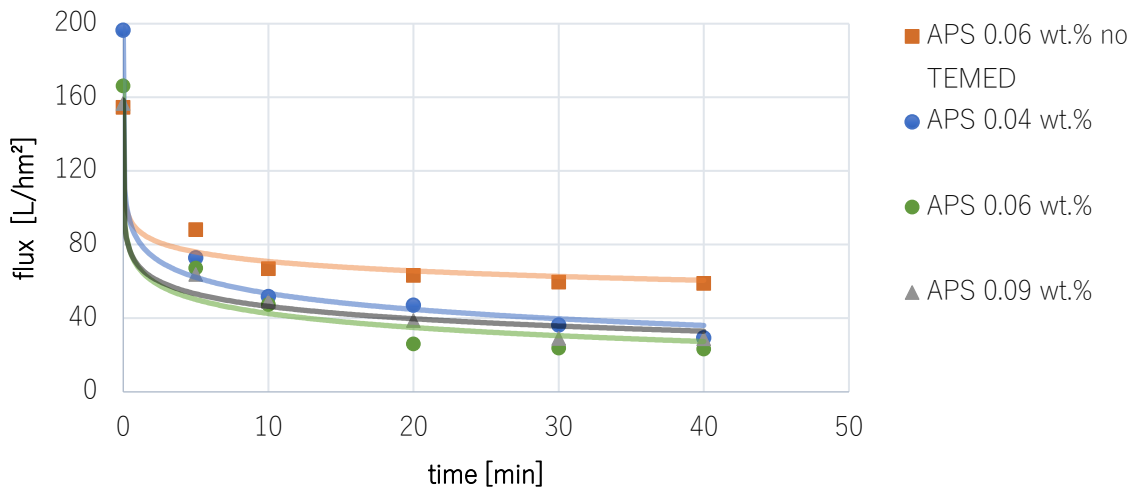


Figure 5.56 NF270 membrane modification: Flux courses for various APS content with constant polymer feed concentration of 0.08 wt.%.

Moreover, when TEMED is not added to the feed solution, membrane flux is significantly higher (up to 50%). This observation can be probably explained by two independent mechanisms. First, effective transmembrane pressure is higher in absence of TEMED since small molecular weight compounds contribute to osmotic pressure during filtration and consequently, decrease permeation driving force. A concrete estimation of osmotic pressure is made with the aid of the van't Hoff equation:

$$\pi = MRT \quad (5.16)$$

Whereby  $\pi$  is osmotic pressure, M is molarity of TEMED solution in boundary layer, R is the normal gas constant and T is temperature.

When concentration of TEMED in boundary layer is assumed to be 1 wt.%, the osmotic pressure is approximately 2 bar. Hence, the loss in effective pressure difference is about 13%. Secondly, more relevant for this work, radical initiation without co-catalyst TEMED is slow and hence, crosslinking between chains will not occur during first 40 minutes of reaction time. Thus, differences between flux values with and without TEMED are growing with filtration time, especially in between 20 to 30 minutes when crosslinking seems to begin for modification in presence of co-catalyst.

In order to understand the differences between modification, estimation of CP is given in Fig. 5.57. Modification without TEMED gives highest and continuously rising concentration for ZP2 at the membrane-liquid interface. Back diffusion would never counterbalance mass transport towards membrane, due to increased viscosity and hence polymer content increases steadily. Furthermore, above 40 wt.% solubility limits will be massively exceeded, making the estimation of concentration in the boundary layer unreasonable. The viscosity-diffusion interdependence strongly points to the limits of modeling and only allows qualitative statements.

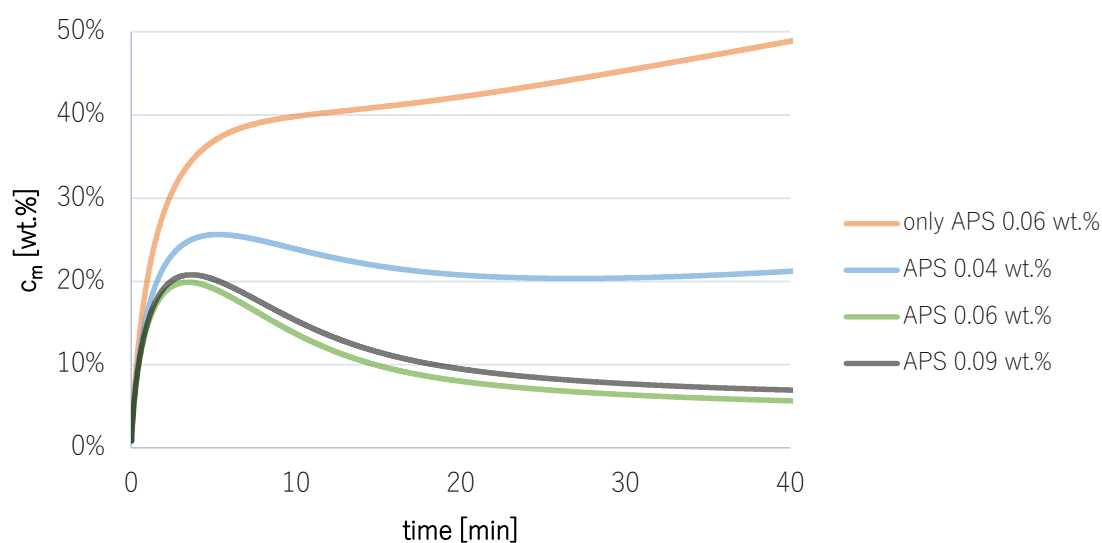


Figure 5.57 Polymer concentration at the membrane surface for const. polymer feed concentration and various APS contents.

For the modification in the presence of co-catalyst, no clear distinction between CP modelling is possible between APS feed concentrations of 0.06 and 0.09 wt.%. Peak concentration is at around 20 wt.%, while average content over time is between 10 or 11 wt.% respectively and hence, model would predict gelation, independent of APS feed concentration.

In contrast, the lowest APS feed content led to highest concentrations for ZP2 at the membrane surface. Therefore, critical polymer concentration should be reached in the boundary layer.

However, the permeability recovery, plotted in Fig. 5.58, shows no loss in membrane performance for APS feed concentration of 0.04 wt.%. On the contrary, increasing APS concentration to 0.06 and 0.09 wt.%, reduces membrane permeability by about 80% suggesting formation of a thick hydrogel layer. Such a difference strongly points to a specific critical concentration for redox-initiator, which is only obtained when APS feed content is in the range of 0.06 wt.%.

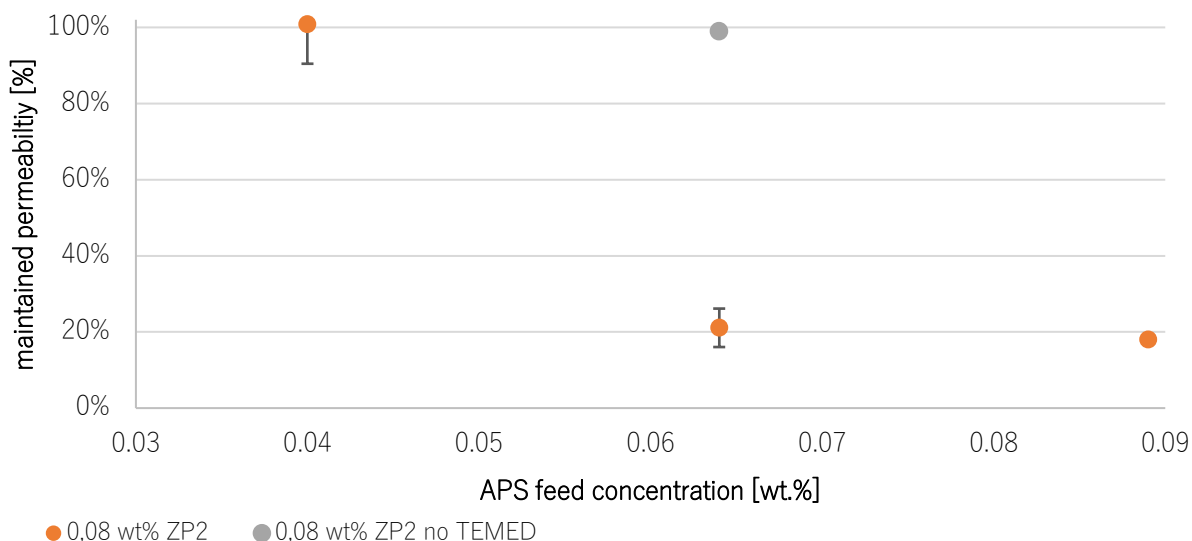


Figure 5.58 NF270 modification: Maintained permeabilities in dependence of APS feed concentration.

### *Polymer concentration dependency*

Additional modifications were performed at a constant APS feed concentration of 0.06 wt.% and various polymer contents. These experiments served the purpose of finding necessary and most-suited polymer feed conditions for successful gelation. The performed modifications and their flux courses are demonstrated in Fig. 5.59. The results allow assumptions regarding crosslinking reaction in dependence of polymer concentration.

First, all modifications showed strong initial flux decline during the early filtration phase (>3 minutes) due to concentration polarization. Differences in feed concentration only slightly affect initial flux decline. However, when filtration is proceeding, changes in permeation rate start to appear. More precisely, onset time for a second, less pronounced flux decline is influenced by polymer concentration. For lowest polymer feed content of 0.001 wt.% only a minor reduction in flux can be observed in between 30-40 minutes, while in the range of 0.003 and 0.005 wt.% the additional drop occurred at around 20 minutes. Mid-range concentrations of 0.01 and 0.02 wt.% exhibit a decrease in water permeation between 10 to 15 minutes and

highest polymer concentrations (0.04 and 0.08 wt.%) already show a flux reduction after approximately 5 minutes, with constant flux after approximately 20 minutes.

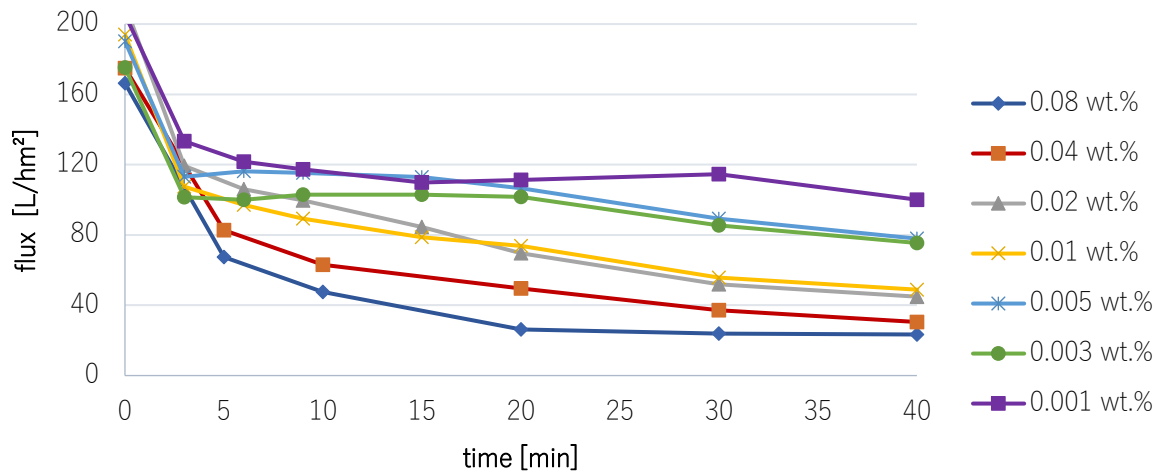


Figure 5.59 Flux during membrane modification in dependence of polymer feed concentration.

Onset time of second flux decline may hint to the beginning of crosslinking reaction between polymer chains when critical polymer concentration in boundary layer is reached. In general, higher polymer feed concentration causes more mass transport toward membrane and hence, critical gelation conditions are generated earlier during the modification process. Furthermore, more pronounced convective mass transport would also increase the extent of CP at the membrane surface and thus, decrease gelation point during modification.

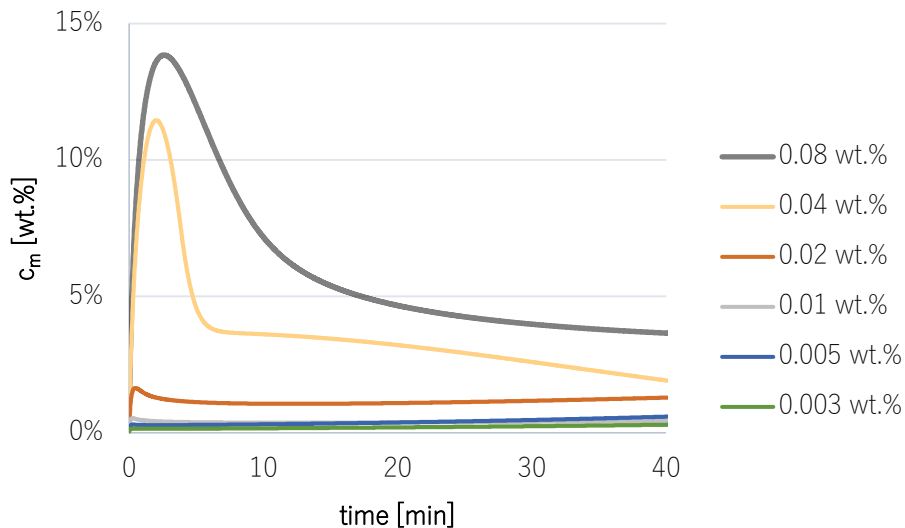


Figure 5.60 Concentration at membrane surface for various polymer feed concentrations.

The extent of CP in dependence of concentration can be demonstrated by entering experimental flux values into CP model, see Fig. 5.60. The highest mass transport is achieved for polymer feed concentrations of 0.04 and 0.08 wt.% with membrane peak concentration of 12 or

respectively 14 wt.%, which would indicate successful modification. In contrast, modelling would not suggest that smaller polymer feed content ( $>0.04$  wt.%) would lead to gelation on membrane surface since peak concentration is predicted to be around 1.5 wt.% or lower (see Fig. 5.61).

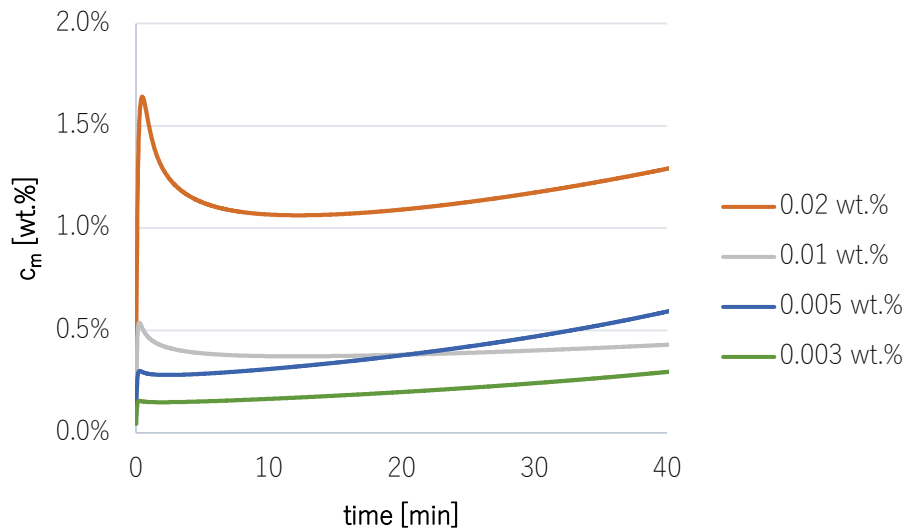


Figure 5.61 Concentration at the membrane surface for various polymer feed concentrations (see Fig. 5.60).

However, permeability recoveries in dependence of polymer feed concentration, shown in Fig. 5.62, points to successful gelation for concentrations in the range of 0.003 to 0.01 wt.%. The results support the argument that the second onset of flux decline may refer to the initiation of gelation reaction. The resistance caused by the hydrogel on top of the membrane increases linearly in dependence of polymer feed concentration, with a 24% permeability drop for  $c_f=0.003$  wt.% up to approximately 75% for  $c_f=0.01$  wt.%. When polymer content in feed is further increased, no additional loss in permeability is measured, indicating that maximal degree of modification is already reached at a concentration of about 0.01 wt.% and 40 minutes reaction time.

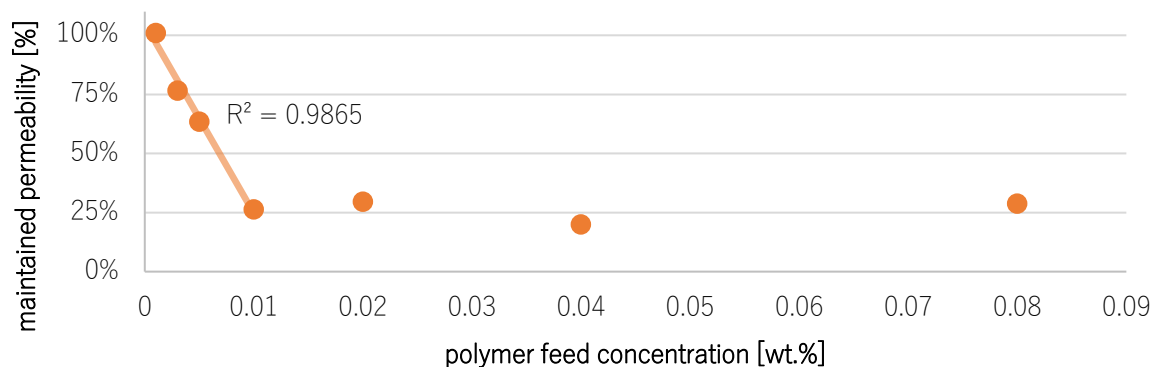


Figure 5.62 NF270 modification: Maintained permeability in dependence of polymer feed concentration with const APS content of 0.06 wt.%.

The successful hydrogel modification of NF270 for concentrations below  $c_f < 0.08$  wt.% can also be verified via SEM images, see Fig. 5.63. However, cross-section of membranes modified using feed concentrations of 0.01 and 0.02 wt.% allowed observation of hydrogel layer on top of PA surface. Thicknesses differ across membrane areas and are in the range of 0.8 or respectively 1.3  $\mu\text{m}$ . Images for membranes modified with low feed concentration have too low resolution to conclude if the gelation reaction was initiated on surface. Additionally, preparation and cutting of NF membranes for SEM analysis was complicated due to mechanical flexibility of membrane materials. Hence, cross-section images do not lead to a final judgment about necessary feed conditions, resulting in zwitterionic hydrogel modification.

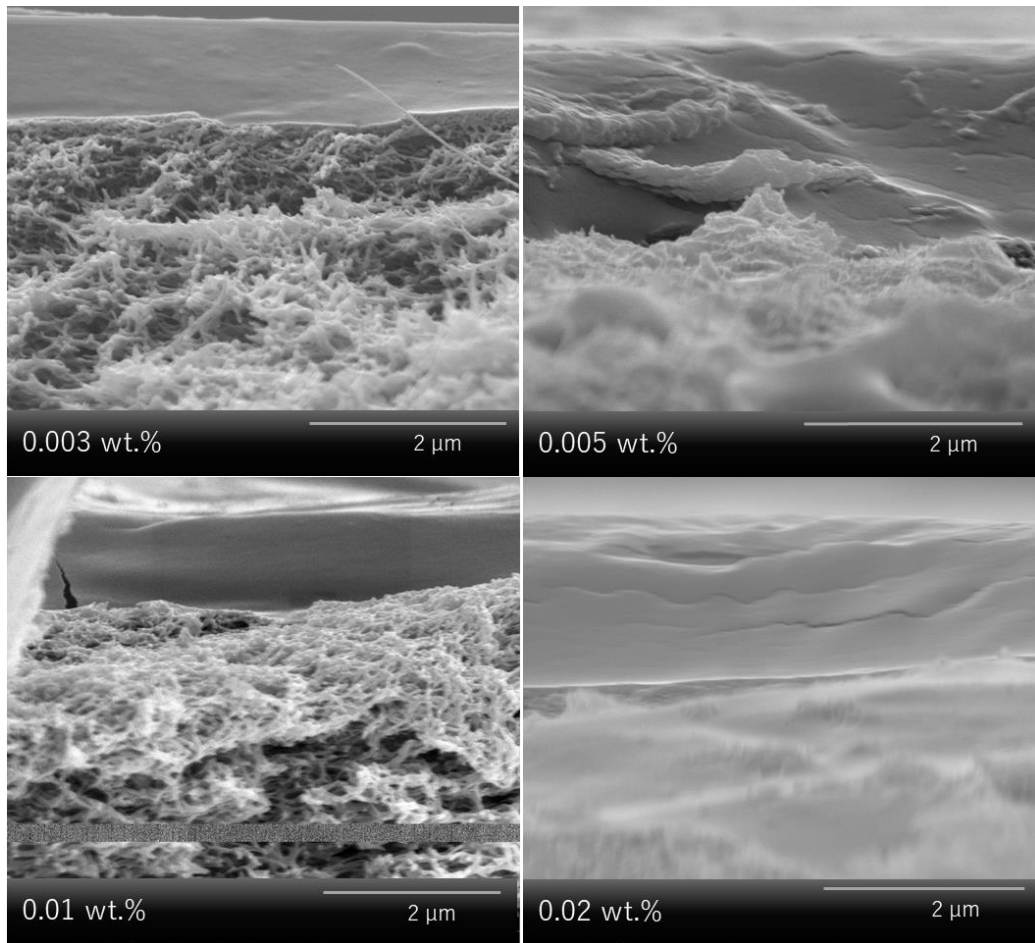


Figure 5.63 Cross-section SEM images of ZHM2 NF270 membranes with different feed concentrations.

Fig. 5.64 shows top layers of ZHM2 membranes with feed concentration of 0.003 and 0.005 wt.%. In general, both membranes differ from NF270 reference membrane surface. A membrane modified with a polymer feed concentration of 0.005 wt.% is smoothed, indicating successful crosslinking reaction onto PA layer. For lower concentrations, membranes still possess areas of slight roughness. Nevertheless, membranes do not show a crater-type surface, seen in pristine NF270 membranes. The change in surface topography may act as an additional evidence and, in combination with permeability recovery data, indicate that low feed concentrations in the range of 0.005 wt.% led to conditions in boundary layer, which met critical gelation requirements.

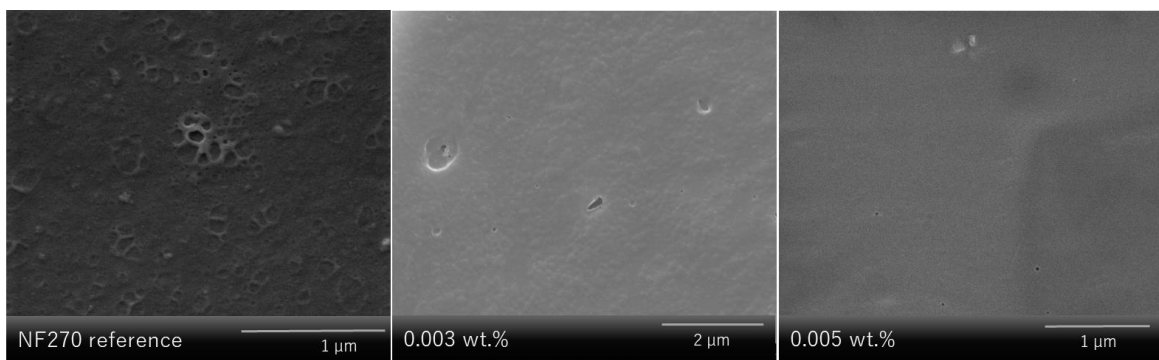


Figure 5.64 SEM images of pristine and ZHMM2 NF270 for different feed concentrations.

### *Influence of filtration time*

Besides investigating the influence of APS and polymer feed content on membrane modification, the impact of filtration time on degree of modification was studied with constant redox-initiator content (0.06 wt.%) and constant polymer concentration (0.08 wt.%). Fig. 5.65 shows the results, in which permeability recovery is dependent on filtration time. For modification times up to 15 minutes, decline in membrane flux is moderate and below 15%. A more significant drop down to approximately 50% occurs when filtration time is increased to 20 minutes. Finally, after 40 minutes, loss of initial membrane permeability is about 70%.

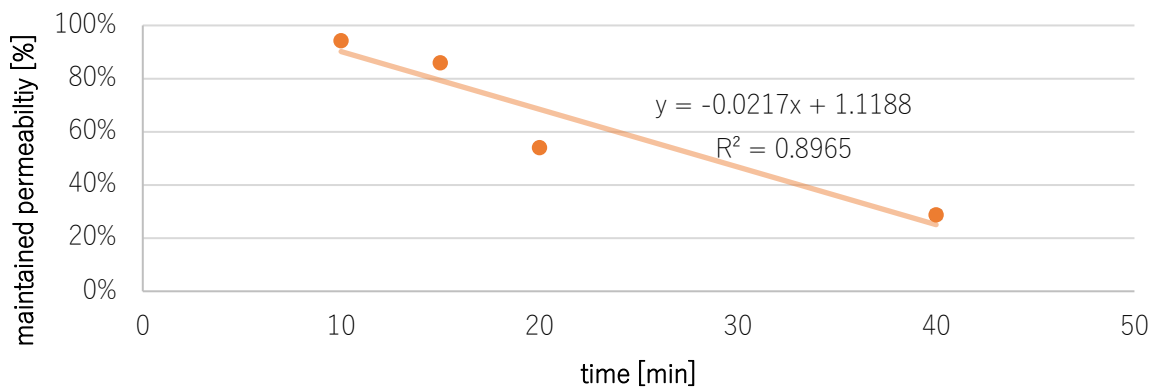


Figure 5.65 Maintained permeability in dependence of filtration time.

Due to significant decline at 20 minutes, dependency of modified permeability and reaction time is not perfectly fitted by linear regression. The early modification phase only shows a slight decrease in membrane performance, indicating beginning of hydrogel formation. This assumption is supported by flux decline after 5 to 10 minutes, seen in previous section.

When modification is proceeding, incorporation of convectively transported polymer into the hydrogel matrix may explain thicker hydrogel layers and consequently, significant permeability reduction. Once critical conditions are reached in boundary layer and gelation is initialized,

further transport of macromolecules to the membrane surface results in a growing hydrogel layer and increased hydraulic resistance.

This reasoning is well supported by SEM analysis, depicted in Fig. 5.66. For modification below 15 minutes, no relevant hydrogel thickness values can be determined that may refer to initiation of gelation reaction. However, for filtration time of 20 minutes, hydrogel layer thickness increases dramatically up to 1  $\mu\text{m}$ . Finally, additional 20 minutes of modification time lead to a hydrogel thickness of about 2.2  $\mu\text{m}$ .

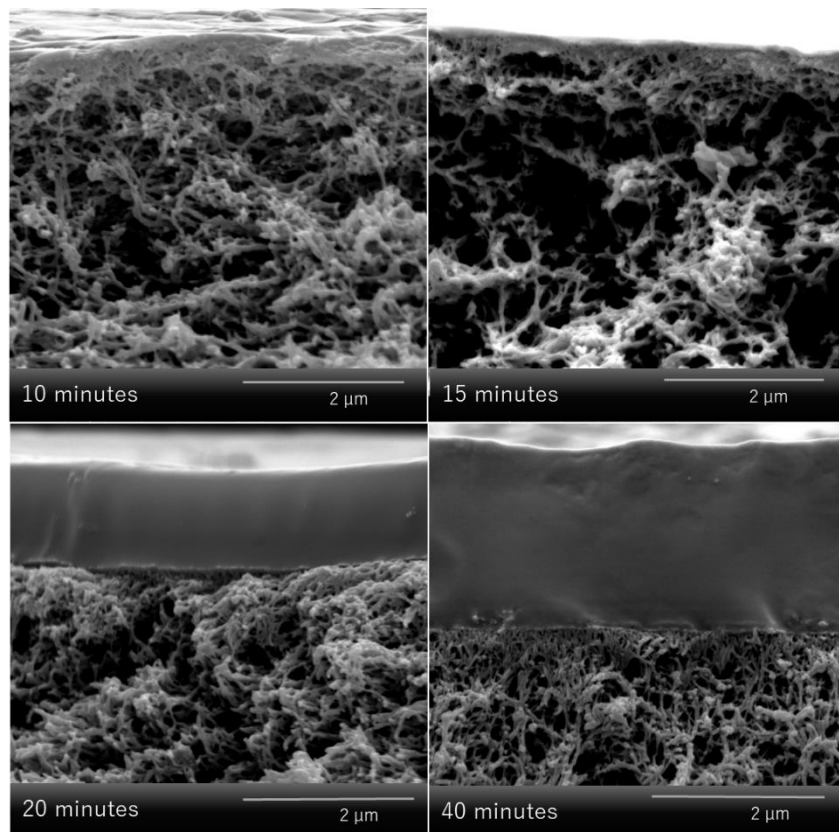


Figure 5.66 SEM images for ZHM2 membranes with different filtration times.

The impact of convective transport is also demonstrated in Fig. 5.67, in which transported mass per area is plotted against permeability recovery and a linear dependence is observed. The graph supports the hypothesis that once gelation is started, additional polymer is integrated into hydrogel structure and contributes to higher hydraulic resistance. Hence, degree of membrane modification can be well adjusted by manipulating filtration time or convective flux under the precondition that critical conditions in boundary layer are met.

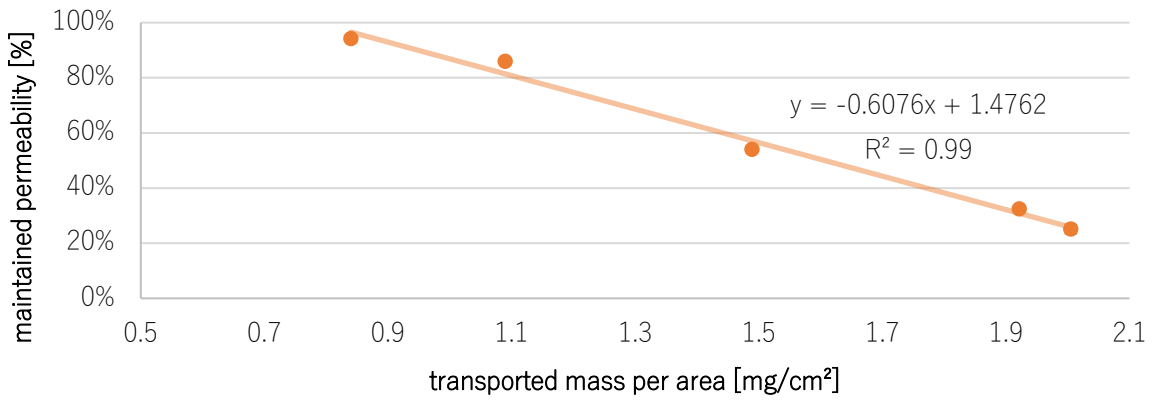


Figure 5.67 Maintained permeability in dependence of transported mass per area.

### 5.6.3 Hydraulic resistance and Darcy permeabilities

Hydraulic resistance of hydrogels was calculated with aid of resistance-in-series model (see section 2.6.3; equation 2.14 and 2.15) and maintained permeabilities. The results for NF270 membrane and gel networks obtained for different filtration times are depicted in Fig. 5.68.

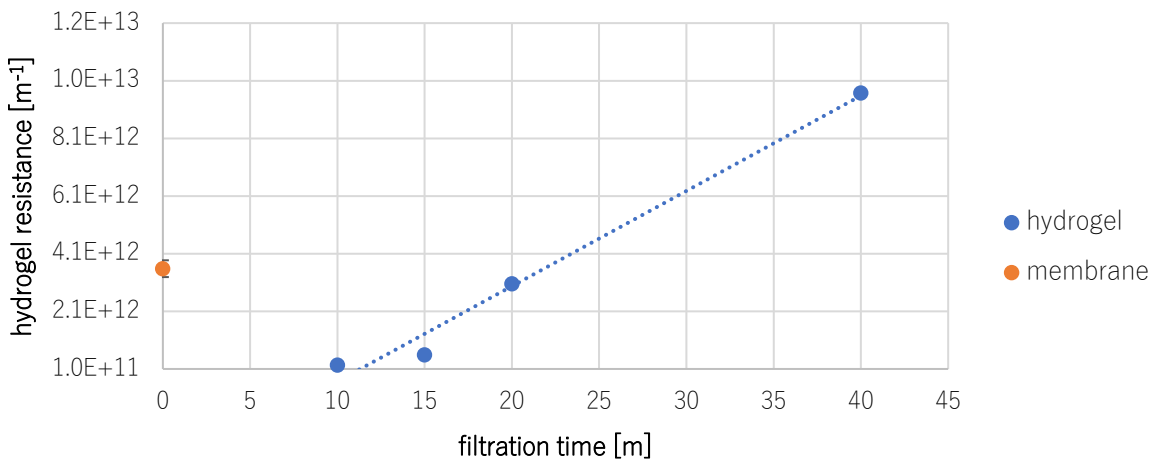


Figure 5.68 Hydrogel resistance in dependence of filtration time.

Hydrogel resistances are in the range of  $2.0 \cdot 10^{11}$  to  $1.0 \cdot 10^{13} \text{ m}^{-1}$  and increase, as expected, for thicker layers (longer filtration time). Furthermore, resistance imposed by PA layer is in a similar range ( $4.0 \cdot 10^{12} \text{ m}^{-1}$ ). However, the results do not consider specific layer thicknesses.

Hence, the thickness normalized Darcy permeabilities are calculated with equation 2.17 and are shown in Fig. 5.69. Darcy permeability allow better comparison between different hydrogel layers and PA film. In addition, since swelling abilities of hydrogels were not experimentally determined, various swelling (2, 10, 20) ratios are assumed.

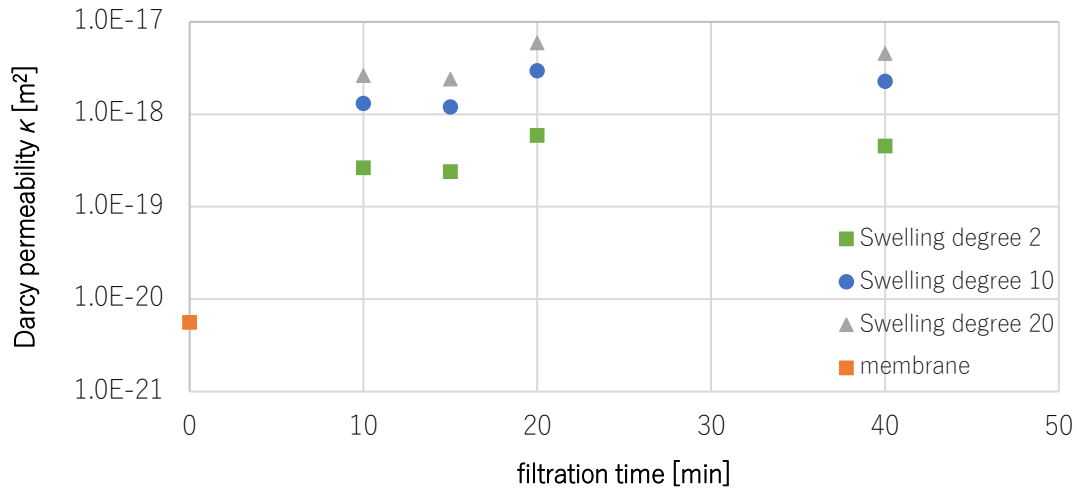


Figure 5.69 Darcy permeabilities of hydrogel in dependence of filtration time and swelling degree.

Overall, PA layer shows lowest Darcy permeability (or highest specific resistance) in the range of  $6 \cdot 10^{-21} \text{ m}^2$ . In contrast, hydrogels represent weaker hydraulic barriers, with up to three orders of magnitude higher Darcy permeabilities. For swollen networks with a swelling degree of 2, Darcy permeabilities are lowest ( $\sim 10^{-19} \text{ m}^2$ ). However, when higher swelling degrees (10 or 20) are assumed, hydrogel permeabilities increase to  $10^{-18} \text{ m}^2$ . Hence, thin hydrogels (<50 nm) do not contribute significantly to total membrane resistance, due to already high intrinsic membrane resistance.

Moreover, average Darcy permeabilities seem to increase with filtration time (see Fig. 5.70). Hydrogels formed below 10 minutes can have 2 to 3 times lower Darcy coefficients compared, to hydrogels formed in 20 or 40 minutes  $\mu\text{m}$ . This finding implies that initially formed hydrogel structures (closer to membrane surface) contribute stronger to hydraulic resistance than later formed gel networks.

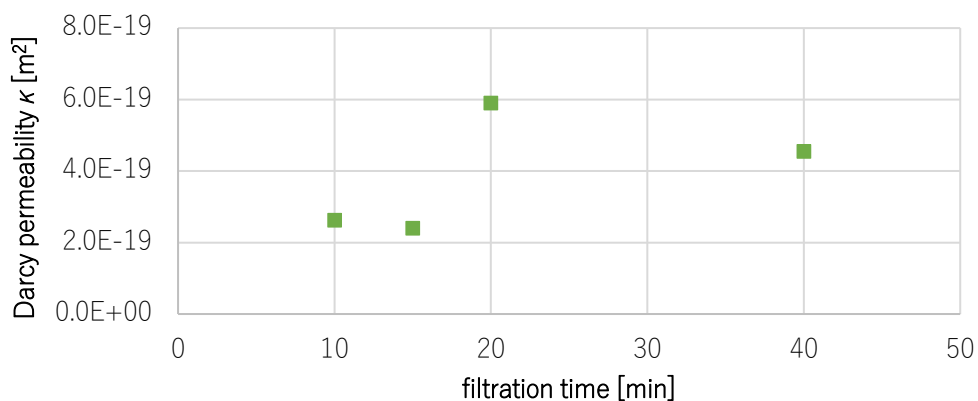


Figure 5.70 Darcy permeability in dependence of filtration time and a swelling degree of 2.

In particle fouling and cake layer formation, it is known that initially deposited foulants are more densely packed. Thus, initial layers impose a bigger hydraulic resistance than later deposited foulants for experiment with constant pressure.<sup>188</sup> In this work, the results can hint to different polymer densities within gel network structures, caused by time and location dependent concentration polarization and polymerization rates. Since CP is most pronounced at the membrane surface, initially formed hydrogels next to the surface will possess highest material density and therefore have low permeability. In contrast, later crosslinking reaction at more distant regions may compete with polymer diffusion away from boundary and consequently result in looser, more permeable networks.

#### *Comparison of hydrogel permeabilities*

In addition, comparison with hydrogels reported in literature allows to evaluate permeation properties and estimate polymer volume content. Several in literature documented hydrogels and (highest and lowest) zwitterionic network permeabilities are shown in Fig. 5.71.<sup>113, 189-191</sup>

Polyzwitterionic networks possess permeabilities that are in similar range as those of Agarose, PHEMA and PAAm hydrogels. In addition, hydrogels with lower polymer volume fraction demonstrate, as expected, lower Darcy permeation coefficients. The plot of hydrogels' Darcy permeabilities and polymer volume fraction allows to estimate a reasonable zwitterionic polymer volume fraction of approximately 0.05 up to 0.2 (dark blue area).

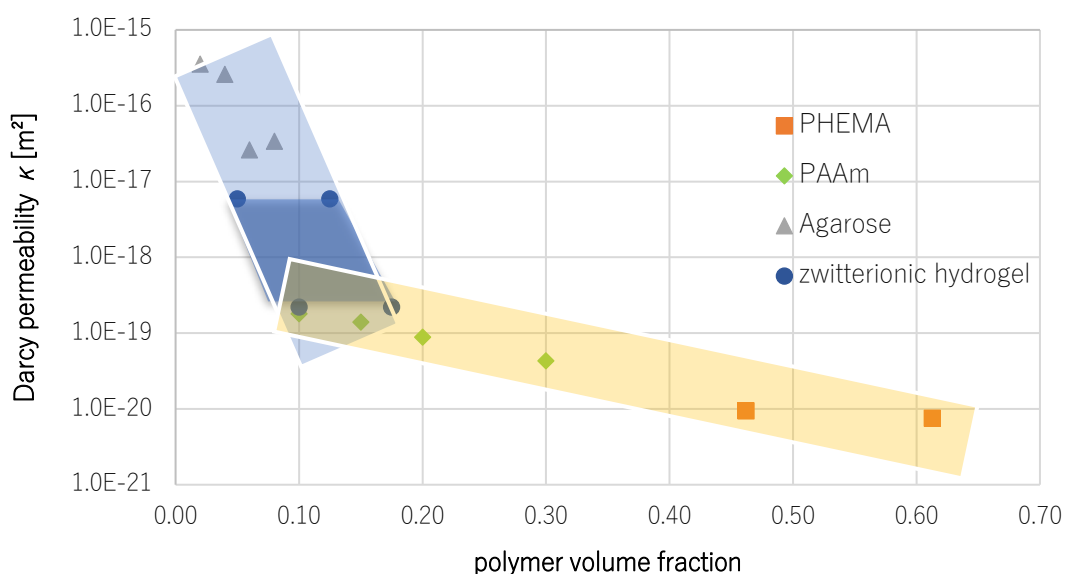


Figure 5.71 Darcy permeabilities for different hydrogels in dependence of polymer volume fraction.

Furthermore, Darcy permeabilities decrease logarithmically with higher polymer volume fraction for two types of networks. Hydrogels, generated from macromolecular building blocks (blue; Agarose and P(SBMA-co-MAMMA)), show overall higher Darcy permeabilities compared to crosslinked monomers (yellow; PHEMA and PAAm). Furthermore, the decrease in permeability with higher polymer content is more severe for macromolecular networks.

The permeation differences between hydrogels built from polymers or respectively monomers can be mainly explained in terms of network formation and its impact on mesh size variation. Due to their size, polymer solutes move significantly slower than monomers. Consequently, macromolecules do not intermingle easily with each other and hence intramolecular crosslinking (self-cyclizing) may be favored, leading to loops in network structure. Such loops (or voids) are less accessible for further polymer chains and may therefore remain “unfilled” when crosslinking reaction is finished. The resulting voids in three-dimensional network structure are contributing disproportionately to hydrogels permeation abilities.

In contrast, monomers cannot react intramolecularly, since they only possess one or two crosslinking functionalities and therefore, require additional monomers to form a hydrogel. The network therefore grows more regularly with less mesh size variety. However, if irregularities occur, they can be easily penetrated by small monomers. Thus, monomer crosslinking leads to more uniform structures than macromolecular gelation.

However, Darcy permeabilities decrease more intensely with higher material content in macromolecular networks. Such finding can point to an inverse correlation between loops (number as well as size) and polymer content. When polymer solutions are more concentrated, interchain reactions increase in probability (see section 5.4) and networks can become more regular. More precise, the number of loops decreases, forming homogenous network with more narrow mesh size distribution. The reduction of irregularities is therefore lowering Darcy permeabilities intensively in macromolecular gels. In comparison, network structures built by monomers are already homogenous, independent of monomer concentration. Though permeability decreases with higher polymer volume fraction (higher monomer/crosslinker concentration), the reduction is weak and solely stems from smaller mesh sizes.

#### 5.6.4 Membrane fouling

Fouling of modified and unmodified membranes was examined by static and dynamic adsorption experiments with protein solutions containing BSA or respectively Myoglobin in PBS buffer. However, already for unmodified NF270 membrane, no irreversible fouling in static adsorption as well as in dynamic filtration experiment was observed and membrane permeability could be regained completely after several washing steps with NaCl and water.

Compared to most commercial polyamide films that exhibit a typical nodular or ridge and valley structure, NF270 membranes possess a smooth surface. For a rough polyamide film, interactions between foulant and surface are not described by classical DLVO assumption.<sup>192</sup> Tangential forces for colloids are found to be increased in rough surface topographies and hence, fouling is more probable as a consequence of higher drag forces towards membrane. Surface roughness would cause a distribution of energy levels rather than a single energy value, for foulant-membrane interactions, resulting higher fouling potential in certain regions of characteristic PA morphology.<sup>193</sup> Additionally, higher surface roughness increases overall effective membrane surface area, which was found to be a more relevant parameter leading to organic fouling rather than average roughness.<sup>175</sup>

Besides static experiments, fouling filtration with less concentrated protein solutions were performed and are depicted in Fig. 5.72. Initial flux ( $\sim 50$  L/hm<sup>2</sup>) was same for all membranes and was adjusted by pressure. Hence, protein transport to membrane surface and extent of CP can be considered equal for all used membranes. Again, no irreversible fouling was observed after membranes were washed with water and salt solutions. However, while membrane permeability was not decreased after fouling experiments, difference in flux reduction can be seen during protein filtration experiments.

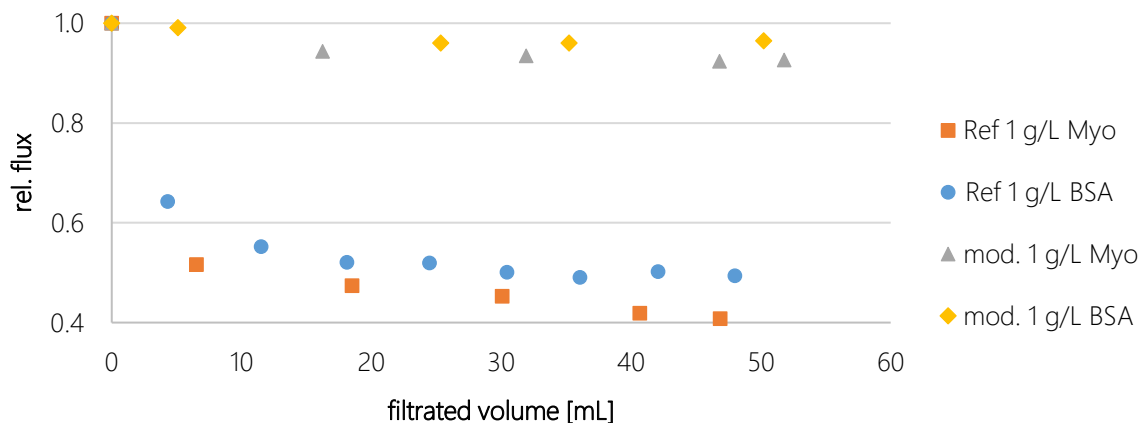


Figure 5.72 Dynamic fouling experiment: Rel. flux courses during filtration with protein solutions.

Modified membranes demonstrated minor decrease in relative flux (up to 10%), compared to pristine membrane, which shows almost 50% reduction after 5 minutes, independent of specific protein type. Zwitterionic hydrogel contributes to significant anti-fouling properties under dynamic conditions. Foulants' attachment to membrane surface is inhibited compared to NF270, since hydrogel imposes an interaction barrier for protein foulants with membrane surface by representing a steric hindrance, possessing tight water shell as well as neutral surface charge.

Additionally, flux change for different protein solutions may stem from unequal pH values of each protein solution. Myoglobin has an isoelectric point near to pH 7.<sup>194</sup> At such neutral conditions, polyamide is more negatively charged, due to its free carboxylic groups. In contrast, pH of BSA solution was adjusted to 4.8, at which NF270 membrane is almost neutral.<sup>195</sup> Hence, membrane-foulant interactions should be more attractive at pH 7 so that more pronounced flux reduction is observed for Myoglobin solution.

Myoglobin shows also stronger negative impact on flux decline in dynamic filtration experiments. Such results may be explained by sieving mechanism caused by size dependent permeation through the hydrogel network. Since BSA is bigger than Myoglobin ( $d_H=7.2$  nm or MW=66 kDa vs.  $d_H=4.4$  nm or MW=16.7 kDa), highly crosslinked zwitterionic hydrogel may exclude BSA better than Myoglobin from penetration through the network.<sup>196</sup> Consequently, flux decline during filtration is slightly higher for Myoglobin, which may be able to diffuse into the hydrogel matrix. Nevertheless, since no information about network mesh size are gathered and differences in fluxes are only minimal, such line of argumentation is speculative.

#### 5.6.5 Discussion of CP model

Successful gelation on membranes surfaces for low feed concentrations (0.003-0.02 wt.%) implies that modeling of boundary layer conditions underestimates the extent of CP. Balance of convective mass transport and back diffusion does not predict sufficiently high polymer concentration at the membrane surface.

Furthermore, for high feed concentration, the estimated extent of CP increases dramatically. However, estimated concentrations at the membrane surface area were in a reasonable range within and comparable to investigated free bulk gelation conditions. This section is an approach to discuss why applied post modeling may underestimate CP for low concentrations ( $c_f < 0.04$  wt.%) and overestimates concentration in boundary layer for polymer feed concentration above 0.08 wt.%.

Film model proposes that concentration polarization is solely dependent on mass transport towards, back diffusion away from and permeation through the membrane. Under stationary conditions, solute concentration will hence experience an exponential increase with shorter distance to the membrane surface. Unfortunately, by calculating overall mass in the boundary layer due to counterbalancing transport phenomena and knowledge about concentration at the beginning of boundary layer, not enough information is provided to estimate an exponential increase of CP. In this work, concentration in boundary layer was therefore assumed to rise linearly, which did not match the exponential nature of CP. Consequently, the estimation of concentration at the liquid-membrane interface will be lower (at least for low concentrated feed solution) than estimated by exponential Film model and may explain why model does not predict successful gelation conditions (Fig. 5.73).

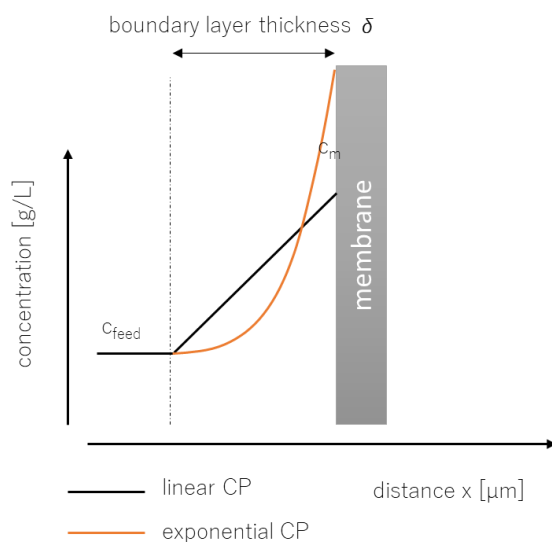


Figure 5.73 Comparison of linear and exponential concentration increase in the boundary layer.

However, such a line of argumentation would lead to even higher concentration at the membrane surface for high polymer feed content. Consequently, parallel occurring phenomena, more relevant for higher concentrations must counterbalance an estimated increase of CP caused by the exponential fitting.

One plausible explanation for too high concentration at the membrane surface may result from ignoring polymer solubility limits. As section 5.3 shows, polymer solubility is already limited for low concentrations ( $\sim 1$  wt.%), at least in water. Concentrations in such range are not high enough to form a hydrogel and hence, concentration in the boundary layer must be substantially higher. Nevertheless, polymer solubility will be reached at one point and lead to a gel layer at the membrane surface. Once transitions from CP to gel layer occurred, further mass transport will not lead to an increase in CP at the membrane surface. Such reasoning may also explain why there are no significant differences in degree of modification upon filtrations using polymer feed concentration from 0.01 to 0.08 wt.%, even though concentrations are increased eight-fold. For all polymer feed content in that range, similar or maximal extent of CP may be reached and lead to same hydrogel layer thickness and hence reduce permeability equally.

Furthermore, when no limit for the polyelectrolyte amount in boundary layer is assumed, viscosity dependent back diffusion becomes problematic. As diffusion coefficient is calculated via Stokes-Einstein equation, diffusive mass transport is inversely proportional to viscosity. Hence, at high polymer concentrations at the membrane surface, back transport into the bulk is decreased, resulting in an overestimation of CP. The impact of exemplary solubility limits and constant viscosities (5 and 10 wt.%) on the extent of modelled CP is shown in Fig. 5.74.

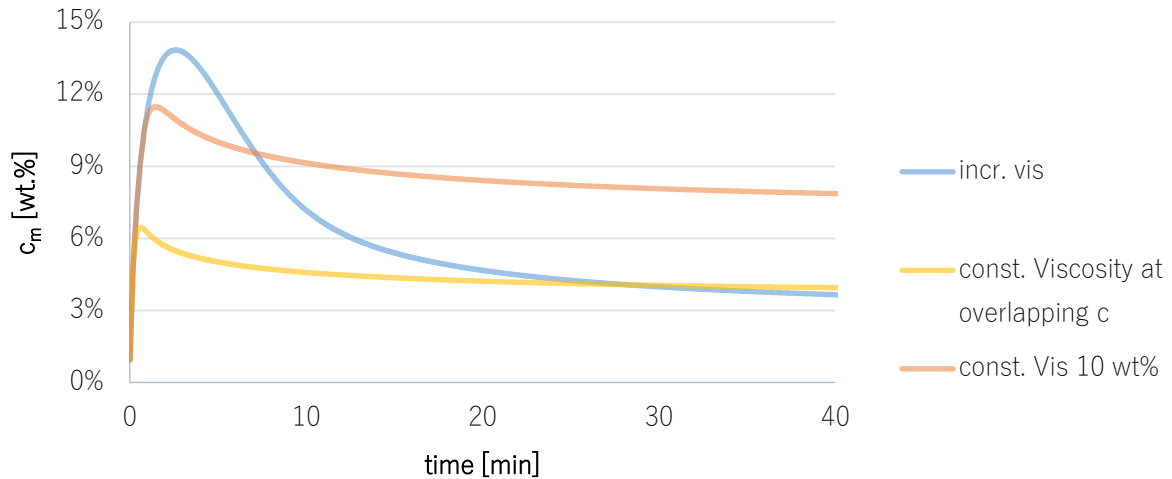


Figure 5.74 Comparison of CP courses for different solubility limits.

A solubility limit reduces maximal concentration at the membrane surface. Nevertheless, once CP maximum is reached, decrease is less dramatic since viscosity is assumed to be constant. Overall differences in solubility can demonstrate sensitivity of proposed model and point to its inaccuracies.

Furthermore, as already demonstrated, the boundary layer thickness is crucial and is measured in a separate experiment. In this work, the boundary layer for HEMA filtration and modification is assumed to be equal as well as constant over the whole filtration procedure. Nevertheless, the layer thickness is determined by hydrodynamic conditions, which will be dynamic and strongly differ for polymer and HEMA filtration experiments. These differences are not considered in the model and hence, boundary layer thickness may be misleading.

In conclusion, CP estimation operates in a reasonable range. However, accurately predicting concentration at the membrane surface is challenged by above mentioned issues. Further estimation should include more knowledge about polymer solubility limit and try to calculate boundary layer dependent for specific modification conditions.

## 5.6.6 Zwitterionic hydrogel modified NF270 membrane characteristics

### *Impact on salt rejection*

Tab. 5.13 shows rejection for mono- and divalent salts of NF270 and zwitterionic modified membrane. While almost 50% of NaCl (2 g/L) can permeate through the selective layer PA layer of pristine membrane, rejection for divalent NaSO<sub>4</sub> increases up to 90%. However, no significant change in rejection is obtained when hydrogel is attached to membrane surface. No additional sieving mechanism is introduced by hydrogel, due to bigger relative mesh size of crosslinked networks compared to PA voids. Hence, salt permeation is not reduced by physical structure properties of zwitterionic gel. Moreover, electroneutrality of hydrogel does not add additional exclusion effects based on charge. Therefore, main rejection mechanisms are still imposed by PA layer, in form of sieving as well as dielectric and Donnan effects.

Table 5.13 Comparison of salt rejection for pristine NF270 membrane and zwitterionic hydrogel modified membranes.

NF270 characteristics	ZHMM2	pristine
NaCl rejection [%]	39.3 ± 8.8	37.7 ± 7.8
Na <sub>2</sub> SO <sub>4</sub> rejection [%]	89.9 ± 7.7	89.7 ± 2.8

### *Zeta potential*

The impact of hydrogel on membrane charge is crucial since fouling propensity is enhanced by attractive interactions. Fig. 5.75 shows the zeta potential of zwitterionic, cationic premodified and pristine membrane in dependence of pH. As expected, NF270 membrane possesses an overall negatively charged surface due to free carboxylic groups, resulting from hydrolyzation during interfacial polymerization of PA. The IEP is between pH 3 to 4, which is similar to reported values in literature.<sup>197</sup> Additionally, slight reduction of IEP may be attributed to the presence of secondary amine functions, which act as proton acceptors, contributed by piperazine monomers.

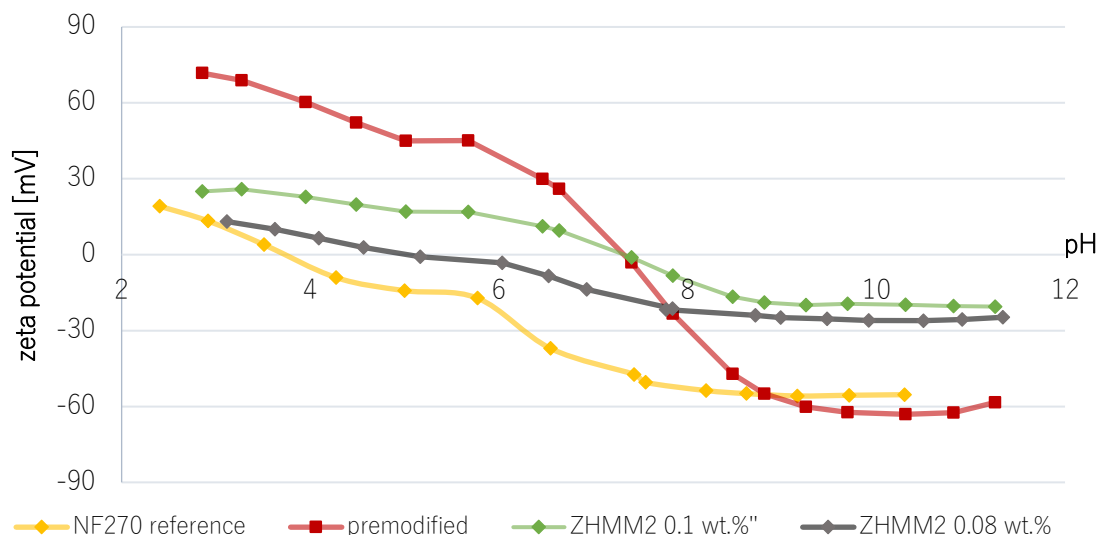


Figure 5.75 Zeta potential for pristine, premodified and modified NF270 membranes.

Overall membrane charge is decreasing until pH 8 down to -50 mV and remains constant under more basic conditions. In contrast, when the cationic surface linker is adsorbed on membrane surface, IEP shifts to a pH of 7 and the overall membrane charge is much more positively charged, with values up to 70 mV. Interestingly, zeta potential of premodified membrane is comparable to pristine PA film when solution exceeds pH values of 9. At such basic conditions the PA film itself is negatively charged due to free carboxylic acids. However, positively charged, quaternary amine functionalities of macromolecular linker may be shielded by hydroxyl anions present in the electrolyte solution and hence, interactions between membrane and cationic polymer may be weakened. This shielding could result in desorption of cationic linker and consequently measure zeta potential of pristine NF270 membrane.

For zwitterionic hydrogel modified membranes, two modifications with polymers ZP1 and ZP2 were measured, each showing a loss of about 80% in permeability. Compared to pristine and cationic, hydrogel modified membranes demonstrate strongest electroneutrality over whole pH range. Zeta potential varies from 25 mV for acidic conditions down to -25 mV for basic pH values. Moreover, IEP is obtained at almost neutral conditions, either at pH 6 for ZP1 polymer or slightly above 7 for hydrogel build-up by ZP2 polymer. Charge neutralization is a result of inter- and intrachain ion pairing of quaternary amine and sulfonic acid units.

The differences between two polymers may be either explained in terms of unfunctionalized DMAEMA units or by incorporation of TEMED into the network structure. Both possibilities would add amine chemistry into the hydrogel, which could act as proton acceptors and hence result in more positively charged membranes. Nevertheless, chemical bonding of co-catalyst

TEMED seems to be more reasonable, since no unfunctionalized DMAMEMA groups could be detected in NMR spectra.

### *IR spectroscopy*

Modified and pristine membranes were investigated by IR spectroscopy, in order to identify successful gelation on the membrane surface. In Fig. 5.76, IR of pristine NF270 membrane and a hydrogel modified membrane (~80% permeability loss) is depicted. Two additional peaks appear in the spectra of modified membrane. First, signal  $1726\text{ cm}^{-1}$  can be attributed towards carboxylic function of ester units in zwitterionic hydrogel. Additionally, broad peak at  $3400\text{ cm}^{-1}$  is representative for either quaternary amine units or respectively water molecules, integrated within gel network.<sup>146</sup>

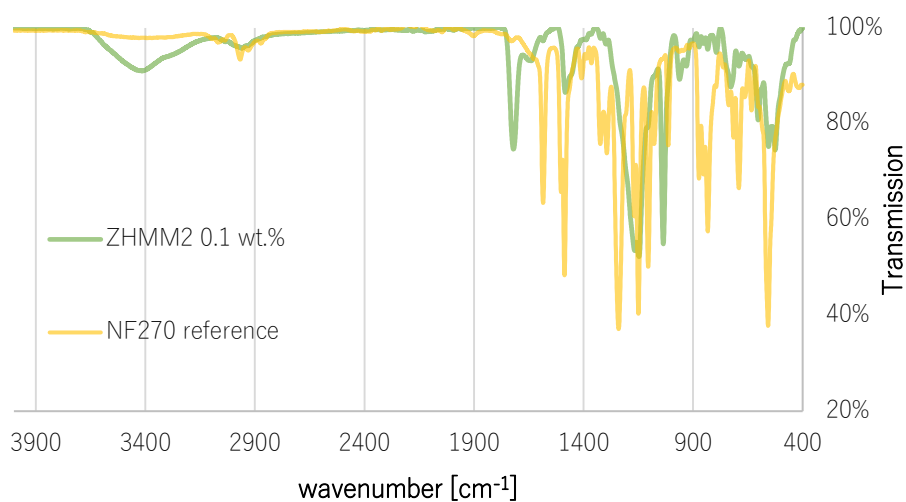


Figure 5.76 IR spectra of pristine and ZHM2 membrane

### *Contact angle*

The contact angle of premodified, modified and pristine membranes are depicted in Fig. 5.77. In general, no significant change in contact angle can be observed. Due to its semi-aromatic nature contributed by TMC monomers, NF270 possess areas, which avoid interactions with water. However, a contact angle of approximately  $33^\circ$  points to overall hydrophilic surface properties, introduced by free carboxylic groups and amine functionalities of piperazine.

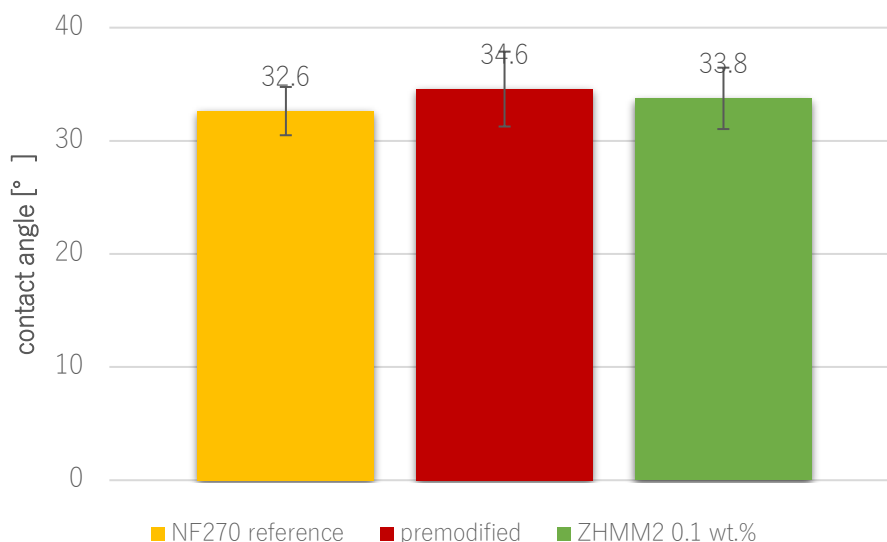


Figure 5.77 Contact angle for NF270, premodified and zwitterionic hydrogel modified membranes.

The premodified membrane also possesses a relatively hydrophilic surface with a contact angle of 34°, which is in the same range as a zwitterionic hydrogel modified membrane (ZHMM1;  $c_1=0.1$  wt.%). It was expected that covering of semi-aromatic PA layer will enhance membrane hydrophilicity. However, the expected impact could not be observed.

#### 5.6.7 NF270 membrane modification summary

With the aid of shown results following conclusion about NF270 membrane modification and CP estimation can be made:

- 1) A successful crosslinking reaction on the membrane surface is achieved for low polymer feed concentrations in the range of 0.003 to 0.01 wt.%. Additionally, the decrease in permeability seems to follow a linear line and appears to be const. for feed concentrations  $>0.01$  wt.% (70-80% reduction). However, for strongly diluted feed solutions, the proposed model does not suggest membrane modification. It is therefore assumed that the proposed model underestimates CP conditions when convective mass transport is low due to linear fitting in boundary layer.
- 2) Besides meeting critical polymer concentration criteria, the redox initiator must be present in a substantial amount. Modification in which only APS content was varied, were successfully modified when APS content was above 0.06 wt.% in feed. Below this threshold concentration NF270 was not modified at all, indicating that radical concentration was too low. The redox-initiator content sensitivity may stem from partial permeation of APS and TEMED, what lead to a less pronounced CP of both substances.

- 3) Shortening modification procedure led to a much thinner hydrogel layer onto the membrane surface and consequently, a less pronounced reduction in membrane permeability. The reaction may be already initiated after 10 to 15 minutes of modification procedure, comparable to free bulk gelation. Prolonging crosslinking time led to very thick hydrogels (1-2  $\mu\text{m}$ ), probably caused due to mass transport and consequent integration into the hydrogel network.
- 4) All membranes did not foul irreversibly. For the pristine NF270 membrane, the superior anti-fouling properties, compared to the NF90 membrane, stem from the smooth active layer, uncommon for most PA membranes. Although even reference membranes did not suffer from fouling, hydrogel abilities to minimize fouling phenomena are demonstrated in dynamic experiments. The ZHM2 hydrogel modified membranes can maintain a high flux during fouling filtration, while references permeability almost reduces up to 50%. Hence, it can be concluded that zwitterionic hydrogel is successfully attached to the membrane and improve at least flux during fouling filtration.

## 6 Conclusion

This work focused on the development of a new in situ zwitterionic hydrogel coating of NF membranes to increase anti-fouling properties. First, novel zwitterionic, crosslinkable polymer was synthesized in a three step process. Reasonable copolymer sizes (~60-100 kDa) were obtained when a minimal radical initiator concentration was used (AIBN concentration >0.2 wt.%). Otherwise PDI increased due to inhomogeneous growing of polymer chains. FRP was subsequently followed by quantitative conversion of side groups into crosslinkable methacrylate and zwitterionic sulfobetaine units.

Cloud point measurements point to low solubility limits at approximately 1 wt.% of zwitterionic polymer. DLS analysis supported formation of agglomerates, which could be reduced by pretreatment of sample or addition of salts by using anti-polyelectrolyte effect. In general, sizes of macromolecules were in the range of 10 nm. Additionally, viscosity studies were performed and showed that overlap concentration is reached around 4 wt.%.

Consequently, the gelation of synthesized bifunctional macromolecules was studied via rheological measurements in the presence of redox-initiator system APS and TEMED. It could be demonstrated that a necessary critical polymer concentration of 5 wt.% was essential to obtain a hydrogel. However, mechanical properties were low for lowest macromolecular content. More crosslinked and hence, mechanical stable hydrogels were generated above polymer concentration of 7.5 wt.%. As expected, gelation time decreased with higher polymer content and higher redox-initiator content. Again, a minimal threshold for APS seems to be crucial to create sufficiently crosslinked networks.

After successful free bulk gelation, low flux NF90 membranes were modified in a dead end cell without stirring in order to prove general possibility of surface-selective membrane coating via gelation. These experiments showed that complete coating of PA surface was only possible when feed concentration was above 0.005 wt.% and an initial flux in the range of 35 to 50 L/hm<sup>2</sup>. Below such a threshold concentration, membrane permeability decreased strongly without showing many beneficial anti-fouling properties. Hence, it was speculated that at low feed concentration only dense gelation in hot spots occurs, which predominantly minimizes permeation rate. However, when higher concentrations were used, a more regular hydrogel on membrane surface can be observed in SEM images, with maintained permeabilities in the range of 70 to 80%. These membranes showed almost no propensity to static fouling and were therefore superior to NF90 membranes when comparing trade-off parameter.

Modification of NF270 membranes was as well performed in a dead end cell, but with stirring (stirring rate 200 rpm) and by additionally estimating CP to establish gelation conditions in the boundary layer. For that purpose, an iterative approach, regarding viscosity and size dependent diffusion, experimental-inserted mass transport and boundary layer thickness, obtained from independent experiment, was developed to estimate extent of CP and concentration next to the membrane surface. The primary purpose was to mimic free bulk gelation conditions and consequently achieve control over crosslinking reaction and modification degree. While the model predicts the right order of magnitude for polymer concentration, it fails to predict exact gelation conditions.

However, modifications were successful above a polymer feed concentration of 0.003 wt.% and an initial flux in the range of 150 to 200 L/hm<sup>2</sup>, with declining permeability recovery until a concentration of 0.01 wt.% (with constant APS concentration). Above this concentration, loss in performance due to additional resistance caused by hydrogel was constant, indicating that maximal extent of CP may be reached already at 0.01 wt.%. This fact was supported by SEM analysis, which showed independent hydrogel layer thicknesses of approximately 2 μm, for concentrations above 0.01 wt.%. Additionally, it is to mention that no gelation on membrane surface was obtained when APS content was below 0.06 wt.%, pointing to a critical minimal radical content at the membrane surface.

Besides the influence of concentration on modification degree, also time as variable was studied under constant feed concentration of 0.08 wt.% and an initial flux in the range of 150 to 200 L/hm<sup>2</sup>. Starting from approximately 10 minutes, a linear decline of membrane permeability could be shown with longer filtration time. Once reaction is started, continuous filtration will transport polymer to the surface, which is consequently integrated into the network and hence, hydrogel layer is growing. For filtration times of 10 to 15 minutes, SEM images show skinny hydrogel layers. Increasing time to 20 or respectively 40 minutes leads to hydrogel layer thickness of about 1 to 2 μm. Therefore, modification degree can be adjusted by filtration time or respectively convective flux towards the membrane.

Finally, protein fouling tests with BSA and Myoglobin were performed with pristine and hydrogel modified membranes. Unfortunately, no irreversible fouling was observed for unmodified NF270 membranes. However, flux decline during protein filtration was more dramatic for pristine PA film (up to 50%) compared to zwitterionic hydrogel modified membranes (~10%). Such improved performance points to better anti-fouling abilities introduced by zwitterionic gel network.

## 7 Outlook

Water scarcity will remain a major problem in the future of our planet and membranes may be part of the technological equation. However, further innovation and improvement, especially regarding fouling propensity, are crucial. The novelty and attractiveness of this Ph.D. project was to apply already well-reported anti-fouling properties of polyelectrolytes in situ, meaning during a continuous filtration process. Hence, the investigated approach is favored for industrial applications, especially for modular platforms, since no additional fabrication steps are necessary.

### *Membrane modification*

Membrane performance and anti-fouling properties were studied solely for membranes with a thick hydrogel layer (~1-2  $\mu\text{m}$  in dry state). As a consequence of strong additional hydraulic resistance, permeability for these membranes decreased approximately 80% and made a comparison with pristine NF270 membrane redundant. Next works should, in order to allow comparison, focus on zwitterionic hydrogel modified membranes with a reasonable permeation loss in the range of 20% or less.

Additionally, the pristine NF270 PA film did not show any irreversible fouling for protein filtration tests. Hence, either fouling tests should be done with systems causing fouling (e.g. oil-in-water emulsions) or more modifications should be performed with different NF/RO membranes (which show significant fouling) or even apply hydrogel onto “tight” UF membranes, to prove transferability onto different membrane types like PES. For these membrane types, a novel macromolecular linker should be developed, combining crosslinking with additional hydrophobic functionalities, which would replace quaternary ammonium units as anchoring groups.

Furthermore, modeling under which conditions successful gelation on membrane surface will occur, is crucial to achieve controllability over modification procedure and should be improved. Although proposed CP model give insight into course and increase of concentration at membrane surface, it is yet insufficient to predict necessary conditions. Improvements could be generated when more precise and specific boundary layer thickness are applied and polymer solubility limits are considered.

Moreover, parameter variation should bring clarification into how the layer thickness is growing, either through further crosslinking of CP layer or incorporation of convectively transported matter or both. Hence, experiments with significant differences in mass transport,

adjusted by flux, should be performed at constant times and influence on hydrogel resistance should be compared. Furthermore, variation of modification time at lower concentrations (0.003-0.001 wt.%) will generate further knowledge about true impact of overall transported mass or respectively crosslinking time.

Finally, in future works, chemical and mechanical stability of zwitterionic hydrogel must be evaluated in terms of applicability. Intense washing, manifested in high shear forces or harsh pH conditions, is often used in chemical industry to minimize fouling potential. However, such cleaning methods could also destroy membrane modification by ester hydrolysis, shearing hydrogel from surface or desorption of macromolecular linker and in order to evaluate potential use, information about stability is necessary.

#### *Gelation system*

In this work, free bulk gelation was only studied for one polymer batch in dependence of polymer and initiator concentration. More information about the nature of crosslinking reaction and hydrogel properties may be gathered with further experiments regarding the number of crosslinkable groups and molecular weight of macromolecules.

Furthermore, a shift from free radical crosslinking to click reaction, e.g. thiol-ene, would promise simple and more facile to control hydrogel formation. Due to highly reactive nature of radicals, adjustment of crosslinking formation is complex, especially in a three-component system used in this project. In contrast, click-type reaction offers simple reaction conditions and can be easily regulated by pH or crosslinker amount.<sup>198</sup>

#### *Transfer to modules*

While dead end filtration modifications are sufficient in lab scale range, they fail to be applicable for larger membrane areas. Therefore, a transfer of modification conditions from dead end procedures towards cross-flow modules with higher active membrane areas is favorable from industrial perspective. For cross-flow systems extent of CP is a result of shearing forces dependent on cross-flow velocity and convective flux towards the membrane.

Therefore, in order to transfer free bulk gelation and analogous membrane modifications of dead end filtration, matching conditions for modular platforms have to be investigated in future works. Mass transfer coefficient may be estimated via Sherwood, Schmidt and Reynolds number, essentially resulting in a different boundary layer thickness than obtained in this work. Furthermore, hydrodynamic conditions such as flux (permeate volume per membrane area) and

cross-flow velocity (feed flow per membrane area) can be adjusted to match dead end filtration conditions. While flux is responsible for convective mass transport and analogous to dead end experiments, cross-flow velocity manipulates shearing on membrane surface and is equivalent to stirring rate in dead end.

## 8 Literature

1. Gleick, P. H., Oxford University Press **1998**.
2. Mekonnen, M. M.; Hoekstra, A. Y., *Science Advances* **2016**, 2, e1500323.
3. United Nations, World population prospects **2017**.
4. Service, R. F., *Science* **2006**, 313, 1088-1090.
5. Vorosmarty, C. J.; McIntyre, P. B.; Gessner, M. O.; Dudgeon, D.; Prusevich, A.; Green, P.; Glidden, S.; Bunn, S. E.; Sullivan, C. A.; Liermann, C. R.; Davies, P. M., *Nature* **2010**, 467, 555-61.
6. Werber, J. R.; Osuji, C. O.; Elimelech, M., *Nature Reviews Materials* **2016**, 1, 16018.
7. Shannon, M. A.; Bohn, P. W.; Elimelech, M.; Georgiadis, J. G.; Marinas, B. J.; Mayes, A. M., *Nature* **2008**, 452, 301-10.
8. Zhao, X.; Zhang, R.; Liu, Y.; He, M.; Su, Y.; Gao, C.; Jiang, Z., *Journal of Membrane Science* **2018**, 551, 145-171.
9. Elimelech, M.; Phillip, W. A., *Science* **2011**, 333, 712-717.
10. Freeman, B. D., *Macromolecules* **1999**, 32, 375-380.
11. Park, H. B.; Kamcev, J.; Robeson, L. M.; Elimelech, M.; Freeman, B. D., *Science* **2017**, 356, eaab0530.
12. Abdelrasoul, A.; Doan, H.; Lohi, A., *Journal of Membrane Science* **2013**, 433, 88-99.
13. Otitoju, T. A.; Saari, R. A.; Ahmad, A. L., *Journal of Industrial and Engineering Chemistry* **2018**, 67, 52-71.
14. Zhang, R.; Liu, Y.; He, M.; Su, Y.; Zhao, X.; Elimelech, M.; Jiang, Z., *Chemical Society Reviews* **2016**, 45, 5888-5924.
15. Schlenoff, J. B., *Langmuir* **2014**, 30, 9625-9636.
16. Baker, R. W., *Membrane technology and applications*. 2nd ed.; J. Wiley, **2004**.
17. Selatile, M.; Sinha Ray, S.; Ojijo, V.; Sadiku, R., *RSC Advances* **2018**, 8, 37915-37938.
18. Singh, R., *Membrane technology and engineering for water purification application, systems design and operation*. Butterworth-Heinemann: Oxford, UK; Waltham, MA, **2015**.
19. Islam, M. A.; Ulbricht, M., *Journal of Membrane Science* **2019**, 569, 104-116.
20. Wijmans, J. G.; Baker, R. W., *Journal of Membrane Science* **1995**, 107, 1-21.
21. Mohammad, A. W.; Teow, Y. H.; Ang, W. L.; Chung, Y. T.; Oatley-Radcliffe, D. L.; Hilal, N., *Desalination* **2015**, 356, 226-254.
22. Vezzani, D.; Bandini, S., *Desalination* **2002**, 149, 477-483.
23. Rautenbach, T. M., Nanofiltration. Membranverfahren. Springer, Berlin, Heidelberg **2007**.
24. Yaroshchuk, A. E., *Advances in Colloid and Interface Science* **2000**, 85, 193-230.
25. Bandini, S.; Vezzani, D., *Chemical Engineering Science* **2003**, 58, 3303-3326.
26. Silva, V., *Dielectric Exclusion Model in Membranes*. Springer, Berlin, Heidelberg, **2015**.
27. Oatley, D. L.; Llenas, L.; Pérez, R.; Williams, P. M.; Martínez-Lladó, X.; Rovira, M., *Advances in Colloid and Interface Science* **2012**, 173, 1-11.
28. Lee, K. P.; Arnot, T. C.; Mattia, D., *Journal of Membrane Science* **2011**, 370, 1-22.
29. Geise, G. M.; Lee, H.-S.; Miller, D. J.; Freeman, B. D.; McGrath, J. E.; Paul, D. R., *Journal of Polymer Science Part B: Polymer Physics* **2010**, 48, 1685-1718.
30. Khorshidi, B.; Thundat, T.; Fleck, B. A.; Sadrzadeh, M., *Scientific Reports* **2016**, 6, 22069.
31. Cadotte, J. E.; Petersen, R. J.; Larson, R. E.; Erickson, E. E., *Desalination* **1980**, 32, 25-31.
32. Lau, W. J.; Ismail, A. F.; Misdan, N.; Kassim, M. A., *Desalination* **2012**, 287, 190-199.
33. Chai, G.-Y.; Krantz, W. B., *Journal of Membrane Science* **1994**, 93, 175-192.
34. Muscatello, J.; Müller, E. A.; Mostofi, A. A.; Sutton, A. P., *Journal of Membrane Science* **2017**, 527, 180-190.

35. Ismail, A. F.; Padaki, M.; Hilal, N.; Matsuura, T.; Lau, W. J., *Desalination* **2015**, *356*, 140-148.
36. Raaijmakers, M. J. T.; Benes, N. E., *Progress in Polymer Science* **2016**, *63*, 86-142.
37. Xu, G.-R.; Xu, J.-M.; Feng, H.-J.; Zhao, H.-L.; Wu, S.-B., *Desalination* **2017**, *417*, 19-35.
38. Guo, W.; Ngo, H.-H.; Li, J., *Bioresource Technology* **2012**, *122*, 27-34.
39. Amy, G., *Desalination* **2008**, *231*, 44-51.
40. He, M.; Gao, K.; Zhou, L.; Jiao, Z.; Wu, M., *Acta Biomaterialia* **2016**, *40*, 142-152.
41. Tijing, L. D.; Woo, Y. C.; Choi, J.-S.; Lee, S.; Kim, S.-H.; Shon, H. K., *Journal of Membrane Science* **2015**, *475*, 215-244.
42. Iritani, E., *Drying Technology* **2013**, *31*, 146-162.
43. Bacchin, P.; Aimar, P.; Sanchez, V., *AIChE Journal* **1995**, *41*, 368-376.
44. Wang, F.; Tarabara, V. V., *Journal of Colloid and Interface Science* **2008**, *328*, 464-469.
45. Cohen, R. D.; Probst, R. F., *Journal of Colloid and Interface Science* **1986**, *114*, 194-207.
46. Schaefer, A.; Andritsos, N.; Karabelas, A.; Hoek, E.; Schneider, R.; Nystrom, M., F., Elsevier Science, New South Wales, 2004.
47. Chon, K.; Cho, J.; Shon, H. K.; Chon, K., *Desalination* **2012**, *301*, 59-66.
48. Nyström, M.; Kaipia, L.; Luque, S., F., *Journal of Membrane Science* **1995**, *98*, 249-262.
49. Lee, S.; Lee, C.-H., *Water Res.* **2000**, *34*, 3854-3866.
50. Sheikholeslami, R., *Heat Transfer Engineering* **2000**, *21*, 24-33.
51. Shirazi, S.; Lin, C.-J.; Chen, D., *Desalination* **2010**, *250*, 236-248.
52. Nguyen, T.; Roddick, F. A.; Fan, L., *Membranes* **2012**, *2*, 804.
53. Sadr Ghayeni, S. B.; Beatson, P. J.; Schneider, R. P.; Fane, A. G., *Journal of Membrane Science* **1998**, *138*, 29-42.
54. Nielsen, P. H.; Jahn, A., *SpringerLink* **1999**, 49-72.
55. Baker, J. S.; Dudley, L. Y., *Desalination* **1998**, *118*, 81-89.
56. Schaefer, A.; Fane, A.; Waite, T., *Nanofiltration*. Elsevier Science: 2004.
57. Hoek, E. M. V.; Elimelech, M., *Environmental Science & Technology* **2003**, *37*, 5581-5588.
58. Porter, M. C., *Product R&D* **1972**, *11*, 234-248.
59. Koyuncu, I.; Topacik, D., *Journal of Membrane Science* **2002**, *195*, 247-263.
60. Mauter, M. S.; Wang, Y.; Okemgbo, K. C.; Osuji, C. O.; Giannelis, E. P.; Elimelech, M., *ACS Applied Materials & Interfaces* **2011**, *3*, 2861-2868.
61. Damodar, R. A.; You, S. J.; Chou, H. H., *Journal of Hazardous Materials* **2009**, *172*, 1321-8.
62. Ben-Sasson, M.; Lu, X.; Bar-Zeev, E.; Zodrow, K. R.; Nejati, S.; Qi, G.; Giannelis, E. P.; Elimelech, M., *Water Research* **2014**, *62*, 260-70.
63. Choi, O.; Deng, K. K.; Kim, N. J.; Ross, L., Jr.; Surampalli, R. Y.; Hu, Z., *Water Research* **2008**, *42*, 3066-74.
64. Marambio-Jones, C.; Hoek, E. M. V., *Journal of Nanoparticle Research* **2010**, *12*, 1531-1551.
65. Nel, A.; Xia, T.; Madler, L.; Li, N., *Science* **2006**, *311*, 622-7.
66. Aslan, S.; Loebick, C. Z.; Kang, S.; Elimelech, M.; Pfefferle, L. D.; Van Tassel, P. R., *Nanoscale* **2010**, *2*, 1789-1794.
67. Silver, S.; Phung, L. T.; Silver, G., *Journal of Industrial Microbiology and Biotechnology* **2006**, *33*, 627-634.
68. Kenawy, E.-R.; Worley, S. D.; Broughton, R., *Biomacromolecules* **2007**, *8*, 1359-1384.
69. Kang, S.; Mauter, M. S.; Elimelech, M., *Environmental Science & Technology* **2008**, *42*, 7528-34.
70. Sanchez, V. C.; Jachak, A.; Hurt, R. H.; Kane, A. B., *Chemical Research in Toxicology* **2012**, *25*, 15-34.

71. Jastrzebska, A. M.; Kurtycz, P.; Olszyna, A. R., *Journal of Nanoparticle Research* **2012**, *14*, 1320.
72. Shvedova, A. A.; Castranova, V.; Kisin, E. R.; Schwegler-Berry, D.; Murray, A. R.; Gandelsman, V. Z.; Maynard, A.; Baron, P., *Journal of Toxicology and Environmental Health. Part A* **2003**, *66*, 1909-26.
73. Yarbrough, J. C.; Rolland, J. P.; DeSimone, J. M.; Callow, M. E.; Finlay, J. A.; Callow, J. A., *Macromolecules* **2006**, *39*, 2521-2528.
74. Ostuni, E.; Chapman, R. G.; Holmlin, R. E.; Takayama, S.; Whitesides, G. M., A., *Langmuir* **2001**, *17*, 5605-5620.
75. Krishnan, S.; Weinman, C. J.; Ober, C. K., *Journal of Materials Chemistry* **2008**, *18*, 3405-3413.
76. Kitano, H.; Tada, S.; Mori, T.; Takaha, K.; Gemmei-Ide, M.; Tanaka, M.; Fukuda, M.; Yokoyama, Y., *Langmuir* **2005**, *21*, 11932-11940.
77. Gunkel, G.; Weinhart, M.; Becherer, T.; Haag, R.; Huck, W. T. S., *Biomacromolecules* **2011**, *12*, 4169-4172.
78. de Vos, W. M.; Leermakers, F. A. M.; Lindhoud, S.; Prescott, S. W., *Macromolecules* **2011**, *44*, 2334-2342.
79. Murosaki, T.; Ahmed, N.; Ping Gong, J., *Science and Technology of Advanced Materials* **2012**, *12*, 064706-064706.
80. Shen, J.; Du, M.; Wu, Z.; Song, Y.; Zheng, Q., *RSC Advances* **2019**, *9*, 2081-2091.
81. Chen, W.; Su, Y.; Peng, J.; Dong, Y.; Zhao, X.; Jiang, Z., *Advanced Functional Materials* **2011**, *21*, 191-198.
82. Callow, J. A.; Callow, M. E., *Nature Communications* **2011**, *2*, 244.
83. Gudipati, C. S.; Finlay, J. A.; Callow, J. A.; Callow, M. E.; Wooley, K. L., *Langmuir* **2005**, *21*, 3044-3053.
84. Blackman, L. D.; Gunatillake, P. A.; Cass, P.; Locock, K. E. S., *Chemical Society Reviews* **2019**.
85. Yeagle, P., *The membranes of cells*. 2nd ed ed.; Academic Press: San Diego, **1993**.
86. Laschewsky, A., *Polymers* **2014**, *6*, 1544-1601.
87. Laughlin, R. G., *Langmuir* **1991**, *7*, 842-847.
88. Kudaibergenov, S.; Jaeger, W.; Laschewsky, A., Polymeric Betaines: Synthesis, Characterization, and Application. In *Supramolecular Polymers Polymeric Betains Oligomers*, Springer Berlin Heidelberg, **2006**, 157-224.
89. Weers, J. G.; Rathman, J. F.; Axe, F. U.; Crichlow, C. A.; Foland, L. D.; Scheuing, D. R.; Wiersema, R. J.; Zielske, A. G., *Langmuir* **1991**, *7*, 854-867.
90. Lowe, A. B.; McCormick, C. L., *Chemical Reviews* **2002**, *102*, 4177-4190.
91. Wang, F.; Yang, J.; Zhao, J., *Polymer International* **2015**, *64*, 999-1005.
92. Ilčíková, M.; Tkáč, J.; Kasák, P., *Polymers* **2015**, *7*, 2344-2370.
93. Marcus, Y., *Chemical Reviews* **2009**, *109*, 1346-1370.
94. Wicky, B. I. M.; Shamma, S. L.; Clarke, J., *Proceedings of the National Academy of Sciences* **2017**, 201705105.
95. Yang, Q.; Ulbricht, M., *Chemistry of Materials* **2012**, *24*, 2943-2951.
96. de Grooth, J.; Ogieglo, W.; de Vos, W. M.; M.; Nijmeijer, K.; *European Polymer Journal* **2014**, *55*, 57-65.
97. Shao, Q.; Jiang, S., *Advanced Materials* **2015**, *27*, 15-26.
98. Loh, X. J.; Scherman, O. A., *Polymeric and Self Assembled Hydrogels*. Royal Society of Chemistry: **2012**.
99. Ahmed, E. M., *Journal of Advanced Research* **2015**, *6*, 105-121.

100. Strachota, B.; Matějka, L.; Zhigunov, A.; Konefał, R.; Spěvácěk, J.; Dybal, J.; Puffr, R., *Soft Matter* **2015**, *11*, 9291-9306.
101. De Gennes, P. G., *Die Makromolekulare Chemie* **1979**, *3*, 195-196.
102. Cãmara, F. V.; Ferreira, L. J., *Hydrogels: Synthesis, Characterization and Applications*. Nova Science, **2012**.
103. Thakur Raghu Raj Singh, G. L., Ryan Donnelly, *Hydrogels: Design, Synthesis and Application in Drug Delivery and Regenerative Medicine*; Taylor & Francis Inc., **2018**.
104. Bowen, J.; Pettitt, M. E.; Kendall, K.; Leggett, G. J.; Preece, J. A.; Callow, M. E.; Callow, J. A., *Journal of the Royal Society Interface* **2007**, *4*, 473.
105. Eshet, I.; Freger, V.; Kasher, R.; Herzberg, M.; Lei, J.; Ulbricht, M., *Biomacromolecules* **2011**, *12*, 2681-2685.
106. Lei, J.; Ulbricht, M., *Journal of Membrane Science* **2014**, *455*, 207-218.
107. Quilitzsch, M.; Osmond, R.; Krug, M.; Heijnen, M.; Ulbricht, M., *Journal of Membrane Science* **2016**, *518*, 328-337.
108. Dai, W. S.; Barbari, T. A., *Journal of Membrane Science* **1999**, *156*, 67-79.
109. Ulbricht, M., *Polymer* **2006**, *47*, 2217-2262.
110. Yang, Q.; Adrus, N.; Tomicki, F.; Ulbricht, M., *Journal of Materials Chemistry* **2011**, *21*, 2783-2811.
111. Keller, M.; Panglisch, S.; Gimbel, R., *Water Supply* **2017**, *17*, 985-997.
112. Di Bella, G.; Di Trapani, D., *Membranes* **2019**, *9*, 24.
113. Yasuda, H.; Lamaze, C. E.; Peterlin, A., *Journal of Polymer Science Part A-2: Polymer Physics* **1971**, *9*, 1117-1131.
114. Hoch, G.; Chauhan, A.; Radke, C. J., *Journal of Membrane Science* **2003**, *214*, 199-209.
115. Adrus, N. B., Dissertation Stimuli-responsive hydrogels and hydrogel pore-filled composite membranes. University *Duisburg-Essen*, **2012**.
116. Walter, S., Master Thesis, University *Duisburg-Essen*, **2013**.
117. Ju, H.; Sagle, A. C.; Freeman, B. D.; Mardel, J. I.; Hill, A. J., *Journal of Membrane Science* **2010**, *358*, 131-141.
118. Wu, Y.-H.; Park, H. B.; Kai, T.; Freeman, B. D.; Kalika, D. S., *Journal of Membrane Science* **2010**, *347*, 197-208.
119. Zhang, Z.; Chao, T.; Jiang, S., *Journal of Physical Chemistry B* **2008**, *112*, 5327-5332.
120. Zhao, W.; Zhu, Y.; Zhang, J.; Xu, T.; Li, Q.; Guo, H.; Zhang, J.; Lin, C.; Zhang, L., *Journal of Materials Science* **2018**, *53*, 13813-13825.
121. Koc, J.; Schönemann, E.; Amuthalingam, A.; Clarke, J.; Finlay, J. A.; Clare, A. S.; Laschewsky, A.; Rosenhahn, A., *Langmuir* **2019**, *35*, 1552-1562.
122. Kasák, P.; Kroneková, Z.; Krupa, I.; Lacík, I., *Polymer* **2011**, *52*, 3011-3020.
123. Carr, L. R.; Xue, H.; Jiang, S., *Biomaterials* **2011**, *32*, 961-968.
124. Malkoch, M.; Vestberg, R.; Gupta, N.; Mespouille, L.; Dubois, P.; Mason, A. F.; Hedrick, J. L.; Liao, Q.; Frank, C. W.; Kingsbury, K.; Hawker, C. J., *Chemical Communications* **2006**, 2774-2776.
125. Dong, D.; Li, J.; Cui, M.; Wang, J.; Zhou, Y.; Luo, L.; Wei, Y.; Ye, L.; Sun, H.; Yao, F., *ACS Applied Materials & Interfaces* **2016**, *8*, 4442-4455.
126. Daumann, K.; May, P.; Brückerhoff, J.; Ulbricht, M., *Reactive and Functional Polymers* **2018**, *131*, 251-257.
127. Zhang, W.; Yang, Z.; Kaufman, Y.; Bernstein, R., *Journal of Colloid and Interface Science* **2018**, *517*, 155-165.
128. Lieu Le, N.; Cheng, H.; Quilitzsch, M.; Ulbricht, M.; Hong, P.-Y.; Nunes, S. P.; Chung, T.-S., *Journal of Membrane Science* **2017**, *512*, 1-11.

129. Susanto, H.; Ulbricht, M., *Langmuir* **2007**, *23*, 7818-7830.
130. Pinson, J.; Thiry, D., *Surface Modification of Polymers*. Wiley, **2020**.
131. Quilitzsch, M., Dissertation Surface selective hydrogel grafting of ultrafiltration membranes using macromolecular initiators and the application to increase fouling resistance. *University Duisburg-Essen*, **2015**.
132. Bernstein, R.; Belfer, S.; Freger, V., *Langmuir* **2010**, *26*, 12358-12365.
133. Bernstein, R.; Belfer, S.; Freger, V., *Journal of membrane science* **2012**, *405*, 79-84.
134. Baransi-Karkaby, K.; Bass, M.; Freger, V., *Membranes* **2019**, *9*, 28.
135. Mori, S.; Barth, H. G., *Size Exclusion Chromatography*. Springer Science & Business Media, **1999**.
136. Podzimek, S., *Light Scattering, Size Exclusion Chromatography and Asymmetric Flow Field Flow Fractionation*. Wiley, **2011**.
137. [https://en.wikipedia.org/wiki/Size-exclusion\\_chromatography](https://en.wikipedia.org/wiki/Size-exclusion_chromatography), **12/2019**.
138. Moore, J. C., *Journal of Polymer Science Part A: General Papers* **1964**, *2*, 835-843.
139. Grubisic, Z.; Rempp, P.; Benoit, H., *Journal of Polymer Science Part B: Polymer Letters* **1967**, *5*, 753-759.
140. Provder, T.; , *Chromatography of Polymers: Characterization by SEC and FFF, Band 521*. American Chemical Society, 1993.
141. Mezger, T. G., *The Rheology Handbook*. Vincentz Network, **2012**.
142. [https://en.wikipedia.org/wiki/Couette\\_flow](https://en.wikipedia.org/wiki/Couette_flow), **12/2019**.
143. Dorfmueller, T.; Berne B. J.; Pecora R., *Dynamic Light Scattering, John Wiley and Sons Ltd.*, **1977**, *81*, 101-101.
144. Opong, W. S.; Zydney, A. L., *AIChE Journal* **1991**, *37*, 1497-1510.
145. Pennycook, S. J.; Nellist, P. D., Springer, New York, NY, **2011**.
146. Stuart, B. H., *Infrared Spectroscopy: Fundamentals and Applications*, **2004**.
147. PerkinElmer, FT-IR Spectroscopy, Attenuated Total Reflectance (ATR); PerkinElmer Life and Analytical Sciences. **2005**.
148. Hunter, R. J.; Ottewill, R. H.; Rowell, R. L., *Zeta Potential in Colloid Science*. Academic Press: **1988**.
149. Duy Thanh, L.; Sprik, R., Zeta Potential Measurement Using Streaming Potential in Porous Media. **2015**, *31*.
150. Atkins, P.; de Paula, J.; Keeler, J., *Atkins' Physical Chemistry*. Oxford University Press: **2017**.
151. Tonelli, A. E., *NMR Spectroscopy and Polymer Microstructure: The Conformational Connection*. Wiley: **1989**.
152. Bloembergen, N.; Purcell, E. M.; Pound, R. V., *Physical Review* **1948**, *73*, 679-712.
153. Karlsson, O. J.; Stubbs, J. M.; Karlsson, L. E.; Sundberg, D. C., *Polymer* **2001**, *42*, 4915-4923.
154. Martín-Gomis, L.; Cuervo-Rodríguez, R.; Fernández-Monreal, M. C.; Madruga, E. L.; Fernández-García, M., *Journal of Polymer Science Part A: Polymer Chemistry* **2003**, *41*, 2659-2666.
155. Barton, A. F. M., *Handbook of Polymer-Liquid Interaction Parameters and Solubility Parameters*. CRC Press: **2018**.
156. Yamamoto, D. H., <https://pirika.com>, **01/2020**.
157. Bhanu, V. A.; Kishore, K., *Chemical Reviews* **1991**, *91*, 99-117.
158. Daumann, K., Dissertation Zwitterionische und vernetzbare Copolymer-Bausteine für Antifouling-Beschichtungen, *University Duisburg-Essen*, **2018**.
159. Miller-Chou, B. A.; Koenig, J. L., *Progress in Polymer Science* **2003**, *28*, 1223-1270.
160. Eckelt, A.; Eckelt, J.; Wolf, B., Solubility of Polymers. *Wiley Online Library*, **2011**.
161. Delgado, J. D.; Schlenoff, J. B., *Macromolecules* **2017**, *50*, 4454-4464.

162. Sakai, T.; Katashima, T.; Matsushita, T.; Chung, U., *Polymer Journal* **2016**, *48*, 629-634.
163. Zhang, H.; Wehrman, M. D.; Schultz, K. M., *Frontiers in Chemistry* **2019**, *7*.
164. Odian, G., *Principles of Polymerization*, John Wiley & Sons, Inc, **2004**.
165. Sandrin, D.; Wagner, D.; Sitta, C. E.; Thoma, R.; Felekyan, S.; Hermes, H. E.; Janiak, C.; de Sousa Amadeu, N.; Kühnemuth, R.; Löwen, H.; Egelhaaf, S. U.; Seidel, C. A. M., *Physical Chemistry Chemical Physics* **2016**, *18*, 12860-12876.
166. Krieg, H. M.; Modise, S. J.; Keizer, K.; Neomagus, H. W. J. P., *Desalination* **2005**, *171*, 205-215.
167. Marín, N. G.-V.; López-Ramírez, J. A., *Water Science & Technology Water Supply* **2011**, *11*, 473.
168. DuPont Water Solutions Customer Portal. **01/2020**.
169. Tu, K. L.; Nghiem, L. D.; Chivas, A. R., *Chemical Engineering Journal*, **2011**, *168*, 700-706.
170. Vrijenhoek, E. M.; Hong, S.; Elimelech, M., *Journal of Membrane Science* **2001**, *188*, 115-128.
171. Ben-David, A.; Bernstein, R.; Oren, Y.; Belfer, S.; Dosoretz, C.; Freger, V., *Journal of Membrane Science* **2010**, *357*, 152-159.
172. Guo, H.; Peng, L.; Yao, Z.; Yang, Z.; Ma, X.; Tang, C., *Environmental Science & Technology* **2019**, *53*.
173. Farrukh, M. A., *Nanofiltration*. IntechOpen: 2018.
174. Purkait, M. K.; Sinha, M. K.; Mondal, P.; Singh, R., Chapter 1 - Introduction to Membranes. *Interface Science and Technology* **2018**, *25*, 1-37.
175. Hobbs, C.; Taylor, J.; Hong, S., *Journal of Water Supply: Research and Technology-Aqua* **2006**, *55*, 559-570.
176. Mouhoumed, E. I.; Szymczyk, A.; Schäfer, A. I.; Paugam, L.; La, Y.-H., *Journal of Membrane Science* **2014**, *461*, 130-138.
177. Mänttari, M.; Pekuri, T.; Nyström, M., NF270, *Journal of Membrane Science* **2004**, *242*, 107-116.
178. Semiao, A.; Schaefer, A., *Journal of Membrane Science* **2011**, *381*, 132-141.
179. Dolar, D.; Kosutic, K.; Asperger, D., *Water Air and Soil Pollution* **2012**, *224*, 1377.
180. Yusoff, I.; Rohani, R.; Mohammad, A., *Malaysian Journal of Analytical Sciences* **2017**, *21*, 484-495.
181. Al-Zoubi, H.; Hilal, N.; Darwish, N. A.; Mohammad, A. W., *Desalination* **2007**, *206*, 42-60.
182. Hilal, N.; Al-Zoubi, H.; Darwish, N.; Mohammad, A., *Separation Science and Technology* **2005**, *40*, 3299-3321.
183. Zhao, Y.Y.; Kong, F.X.; Wang, Z.; Yang, H.W.; Wang, X.M.; Xie, Y. F.; Waite, T. D., *Frontiers of Environmental Science & Engineering* **2017**, *11*, 20.
184. Bacchin, P.; Aimar, P.; Field, R. W., *Journal of Membrane Science* **2006**, *281*, 42-69.
185. Field, R. W.; Wu, D.; Howell, J. A.; Gupta, B. B., *Journal of Membrane Science* **1995**, *100*, 259-272.
186. Tang, C. Y.; Leckie, J. O., *Environmental Science & Technology* **2007**, *41*, 4767-4773.
187. Chen, Z.; Luo, J.; Hang, X.; Wan, Y., *Journal of Membrane Science* **2018**, *547*, 51-63.
188. Yim, S.-S.; Kim, J.-H., *Korean Journal of Chemical Engineering* **2000**, *17*, 393-400.
189. Refojo, M. F.; Yasuda, H., *Journal of Applied Polymer Science* **1965**, *9*, 2425-2435.
190. Johnson, E. M.; Deen, W. M., *AIChE Journal* **1996**, *42*, 1220-1224.
191. White, M. L., *Journal of Physical Chemistry* **1960**, *64*, 1563-1565.
192. Hoek, E. M. V.; Agarwal, G. K., *Journal of Colloid and Interface Science* **2006**, *298*, 50-58.
193. Elimelech, M.; Zhu, X.; Childress, A. E.; Hong, S., *Journal of Membrane Science* **1997**, *127*, 101-109.
194. Kandori, K.; Oda, S.; Tsuyama, S., *Journal of Physical Chemistry* **2008**, *112*, 2542-2547.
195. Phan, H. T. M.; Bartelt-Hunt, S.; Rodenhausen, K. B.; Schubert, M.; Bartz, J. C., *PLoS ONE* **2015**, *10*.
196. Charalel, R. A.; Engberg, K.; Noolandi, J.; Cochran, J. R.; Frank, C.; Ta, C. N., *Ophthalmic Research* **2012**, *48*, 50.
197. Chen, Z.; Luo, J.; Hang, X.; Yinhu, W., *Journal of Membrane Science* **2017**, *547*.

198. Nair, D. P.; Podgórski, M.; Chatani, S.; Gong, T.; Xi, W.; Fenoli, C. R.; Bowman, C. N., *Chemistry of Materials* **2014**, 26, 724-744.

## 9 Appendix

### 9.1 List of figures

<b>Figure 2.1:</b> Pressure driven membrane processes and their characteristic separation range .....	3
<b>Figure 2.2:</b> Schematic representation of membrane tortuosity (top), porosity and pore size (bottom) .....	5
<b>Figure 2.3:</b> Size exclusion mechanism in a porous membrane .....	6
<b>Figure 2.4:</b> Capture mechanisms inside a membrane .....	7
<b>Figure 2.5:</b> Schematic representation of PA film formation between TMC and MPD .....	10
<b>Figure 2.6:</b> Course of Gibbs free energy in stepwise adsorption of a protein onto different surface types .....	11
<b>Figure 2.7:</b> Adsorption of a protein onto a surface and change of its conformation .....	11
<b>Figure 2.8:</b> Colloid Fouling mechanism – a) complete blocking, b) standard pore blocking, c) intermediate pore blocking, d) cake layer formation .....	13
<b>Figure 2.9:</b> Schematic representation of concentration polarization during filtration .....	16
<b>Figure 2.10:</b> Passive anti-fouling strategies: a) fouling resistance; b) fouling release .....	19
<b>Figure 2.11:</b> Most frequent type and examples for polybetaines .....	21
<b>Figure 2.12:</b> Anti-polyelectrolyte effect of NaCl – Impact on intra- and intermolecular inter-actions and polyelectrolyte swelling .....	22
<b>Figure 2.13:</b> Hofmeister series .....	23
<b>Figure 2.14:</b> Water orientation in zwitterionic and positively charged side groups .....	24
<b>Figure 2.15:</b> Protein adsorption and “counterion evaporation” for polyelectrolyte and negatively charged brushes .....	24
<b>Figure 2.16:</b> Redox reaction of APS and TEMED and formation of radicals .....	25
<b>Figure 2.17:</b> Concentration areas in polymer solution after deGennes .....	26
<b>Figure 2.18:</b> Irregular hydrogel network types .....	26
<b>Figure 2.19:</b> Relative settlement of barnacles onto hydrogel with different chemical groups .....	28
<b>Figure 2.20:</b> Barnacle settlement in dependence of elastic modulus .....	29
<b>Figure 2.21:</b> Deposition coefficient of <i>Pseudomonas fluorescens</i> in dependence of swelling degree and chemistry .....	30
<b>Figure 2.22:</b> Various clickable polyelectrolyte structures developed by Daumann et al. ....	34
<b>Figure 2.23:</b> Surface initiated crosslinking developed by Quilitzsch et al. ....	37
<b>Figure 3.1:</b> Zwitterionic crosslinkable target molecule .....	39

<b>Figure 3.2:</b> Concentration polarization enabled modification of membrane surface with polyzwitterionic and crosslinkable macromolecules .....	39
<b>Figure 3.3:</b> Polymer synthesis reaction scheme .....	42
<b>Figure 3.4:</b> Cationic macromolecular surface linker .....	42
<b>Figure 4.1:</b> Free radical polymerization of HEMA and DMAEMA .....	46
<b>Figure 4.2:</b> Acrylation of HEMA side functionalities .....	47
<b>Figure 4.3:</b> Sulfobetainization of DMAEMA side units .....	47
<b>Figure 4.4:</b> Quaternization of DMAEMA units .....	48
<b>Figure 4.5:</b> Principle of SEC and example for obtained chromatogram .....	49
<b>Figure 4.6:</b> Schematic representation of planar Couette flow and consequent resistance of a fluid to shear deformation .....	51
<b>Figure 4.7:</b> Membrane modification procedure: flux in dependence of time with rinsing after adsorption and modification step .....	56
<b>Figure 4.8:</b> Concentration polarization – a) exponential course resulting from the Film model; b) homogenous distribution in the boundary layer; c) linear increase in boundary layer used in this work .....	59
<b>Figure 4.9:</b> Development of streaming and conduction current in a channel(top); schematic representation of electrical double layer and distance dependence of electrical potential (bottom) .....	65
<b>Figure 5.1:</b> NMR-Spectra of P(DMAEMA-co-HEMA) .....	67
<b>Figure 5.2:</b> NMR peaks for monomers and polymer backbone .....	69
<b>Figure 5.3:</b> Monomer conversion over time .....	69
<b>Figure 5.4:</b> Relative conversion of HEMA and DMAEMA for polymerization with 0.15 wt. % AIBN .....	70
<b>Figure 5.5:</b> Molecular weight in dependence of AIBN concentration for 20% HEMA content .....	72
<b>Figure 5.6:</b> PDI of copolymers with 20% HEMA content and different initiator concentrations .....	74
<b>Figure 5.7:</b> Intrinsic viscosities and Mark-Houwink parameters for copolymers with 20% HEMA side units at different AIBN concentrations .....	74
<b>Figure 5.8:</b> Influence of HEMA content on molecular weight of P(DMAEMA-co-HEMA) at constant AIBN amount of 0.4 wt.% .....	75
<b>Figure 5.9:</b> Influence of HEMA content on PDI .....	76
<b>Figure 5.10:</b> Influence of HEMA content on the Mark-Houwink parameter .....	76

<b>Figure 5.11:</b> <sup>1</sup> H-NMR spectroscopy and structural analysis of P(DMAEMA-co-MAMMA)	77
<b>Figure 5.12:</b> <sup>1</sup> H-NMR spectroscopy and structural analysis of P(SBMA-co-MAMMA)	78
<b>Figure 5.13:</b> <sup>1</sup> H-NMR spectroscopy and structural analysis of surface linker	80
<b>Figure 5.14:</b> Polymer solubility: Cloud point measurements of various concentrated copolymer solutions	82
<b>Figure 5.15:</b> DLS intensity (top) and number (bottom) plot for different zwitterionic polymers in water	83
<b>Figure 5.16:</b> DLS intensity and number plot for ZP2 in water and KCl solutions	85
<b>Figure 5.17:</b> Break down of zwitterionic agglomerates by addition of salt and screening of interchain interactions	86
<b>Figure 5.18:</b> DLS intensity and number plot for ZP2 in water and KCl solutions after prefiltration	87
<b>Figure 5.19:</b> Schematic representation of the anti-polyelectrolyte effect	88
<b>Figure 5.20:</b> Shear stress vs. strain rate of ZP1 samples with different concentrations	89
<b>Figure 5.21:</b> Viscosity of aqueous polymer solutions (ZP1 and ZP2) in dependence of Polymer concentration with strain rate of 800 s <sup>-1</sup>	89
<b>Figure 5.22:</b> Rheological investigation of gelation reaction; ZP1 (5 wt.%), APS:Acrylate ratio (1:2) and APS:TEMED ratio (8:1)	91
<b>Figure 5.23:</b> Gelation time in dependence of the APS:Acrylate ratio	92
<b>Figure 5.24:</b> Gelation time in dependence of polymer concentration	93
<b>Figure 5.25:</b> Completion of hydrogel reaction in dependence of APS:Acrylate ratio	94
<b>Figure 5.26:</b> Completion of gelation in dependence of polymer concentration	94
<b>Figure 5.27:</b> Damping factor in dependence of APS:Acrylate ratio for various polymer concentrations	95
<b>Figure 5.28:</b> Final storage modulus in dependence of APS:Acrylate ratio	96
<b>Figure 5.29:</b> Change in storage modulus in dependence of APS:Acrylate ratio	97
<b>Figure 5.30:</b> Damping factor in dependence of polymer content	97
<b>Figure 5.31:</b> Storage modulus in dependence of polymer concentration	98
<b>Figure 5.32:</b> Intra- and interchain crosslinking and its impact on network structure	98
<b>Figure 5.33:</b> NF90 membrane modification: maintained permeability in dependence of polymer and redox-initiator feed concentration	101

<b>Figure 5.34:</b> Schematic representation of heterogenous hot spot (top) and regular hydrogel modification (bottom) onto ridge and valley topographies .....	102
<b>Figure 5.35:</b> SEM images of NF90 membrane and zwitterionic hydrogel modified membranes (ZHMM1 NF90) at different polymer feed concentrations .....	103
<b>Figure 5.36:</b> SEM images of NF90 membrane and zwitterionic hydrogel modified membranes (ZHMM1 NF90) at a feed concentration of 0.0075 wt.% .....	104
<b>Figure 5.37:</b> NF90 membrane modification: Maintained permeability in dependence of transported mass per area .....	105
<b>Figure 5.38:</b> NF90 membrane modification: Maintained permeability in dependence of filtration time and a constant polymer feed concentration (0.005 wt.%) .....	106
<b>Figure 5.39:</b> Comparison of NF90 membrane modification: Maintained permeability in dependence of transported mass per area and a constant polymer feed concentration (0.05 wt.%, blue) and different polymer feed concentration (orange) .....	106
<b>Figure 5.40:</b> RFR in dependency of polymer feed concentration for static BSA adsorption .....	107
<b>Figure 5.41:</b> SEM image of NF90 membrane and zwitterionic hydrogel modified membranes (ZHMM1 NF90) at a feed concentration of 0.005 wt.% but without premodification .....	108
<b>Figure 5.42:</b> RFR in dependency of filtration time with constant polymer feed concentration (0.005 wt.%) .....	109
<b>Figure 5.43:</b> Trade-off in dependence of polymer concentration .....	110
<b>Figure 5.44:</b> Trade-off in dependence of filtration time .....	111
<b>Figure 5.45:</b> Zeta potential measurements for pristine NF90, pre-modified and ZHM1 hydrogel coated membranes .....	112
<b>Figure 5.46:</b> IR spectra of two IR ranges showing differences between NF90 and ZHMM1 (0.005 wt.%) membrane (left: Carbonyl stretching vibration of the zwitterionic hydrogel at 1726 cm <sup>-1</sup> ; right: N-H stretching vibration of pristine PA membrane) .....	113
<b>Figure 5.47:</b> Contact angle of NF90 reference, premodified and ZHM1 membranes (0.005 wt.%) .....	114
<b>Figure 5.48:</b> Permeation of HEMA as a function of flux and stirring rate .....	117
<b>Figure 5.49:</b> Flux for polymer solutions in dependence of applied pressure .....	118
<b>Figure 5.50:</b> Flux during membrane modification with a polymer feed concentration of 0.08 wt.% .....	120

<b>Figure 5.51:</b> Dynamic polymer concentration at the membrane surface with a polymer feed concentration of 0.08 wt.% .....	120
<b>Figure 5.52:</b> Flux courses for membrane modifications with various polymer feed concentrations .....	122
<b>Figure 5.53:</b> Concentration course in boundary layer for various polymer feed concentrations .....	122
<b>Figure 5.54:</b> NF270 modification: permeability recoveries in dependence of polymer feed concentrations .....	124
<b>Figure 5.55:</b> SEM images of ZHM1 membranes with different polymer feed concentrations; top: cross-section, bottom: membrane surface .....	124
<b>Figure 5.56:</b> NF270 membrane modification: Flux courses for various APS content with constant polymer feed concentration of 0.08 wt.% .....	126
<b>Figure 5.57:</b> Polymer concentration at the membrane surface for const. polymer feed concentration and various APS contents .....	127
<b>Figure 5.58:</b> NF270 modification: Maintained permeability recoveries in dependence of APS feed concentration .....	128
<b>Figure 5.59:</b> Flux during membrane modification in dependence of polymer feed concentration .....	129
<b>Figure 5.60:</b> Concentration at membrane surface for various polymer feed concentrations .....	129
<b>Figure 5.61:</b> Concentration at the membrane surface for various polymer feed concentrations .....	130
<b>Figure 5.62:</b> NF270 modification: Maintained permeability recovery in dependence of polymer feed concentration with const APS-content of 0.06 wt.% .....	130
<b>Figure 5.63:</b> Cross-section SEM images of ZHM2 NF270 membranes with different feed concentrations .....	131
<b>Figure 5.64:</b> SEM images of pristine and ZHMM2 NF270 for different feed concentrations .....	132
<b>Figure 5.65:</b> Maintained permeability recovery in dependence of filtration time .....	132
<b>Figure 5.66:</b> SEM images for ZHM2 membranes with different filtration times .....	133
<b>Figure 5.67:</b> Maintained permeability recovery in dependence of transported mass per area .....	134
<b>Figure 5.68:</b> Hydrogel resistance in dependence of filtration time .....	134

<b>Figure 5.69:</b> Darcy permeabilities of hydrogel in dependence of filtration time and swelling degree .....	135
<b>Figure 5.70:</b> Darcy permeability in dependence of filtration time and a swelling degree of 2 .....	136
<b>Figure 5.71:</b> Darcy permeabilities for different hydrogels in dependence of polymer volume fraction .....	137
<b>Figure 5.72:</b> Dynamic fouling experiment: Rel. flux courses during filtration with protein solutions .....	139
<b>Figure 5.73:</b> Comparison of linear and exponential concentration increase in the boundary layer .....	141
<b>Figure 5.74:</b> Comparison of CP courses for different solubility limits .....	142
<b>Figure 5.75:</b> Zeta potential for pristine, premodified and modified NF270 membranes .....	144
<b>Figure 5.76:</b> IR spectra of pristine and ZHM2 membrane .....	145
<b>Figure 5.77:</b> Contact angle for NF270, premodified and zwitterionic hydrogel modified membranes .....	146

## 9.2 List of tables

<b>Table 2.1:</b> Zwitterionic chemistry and its influence on network properties .....	33
<b>Table 4.1:</b> Chemicals used in this work .....	45
<b>Table 4.2:</b> Free bulk gelation conditions .....	54
<b>Table 4.3:</b> NF90 membrane modification feed parameter .....	57
<b>Table 5.1:</b> Hansen solubility parameter for P(HEMA), P(DMAEMA) and P(MMA) in DMAc .....	72
<b>Table 5.2:</b> Molecular weight, PDI and composition of used polymer batches .....	79
<b>Table 5.3:</b> Molecular weights, PDIs and compositions of macromolecular surface linker ....	81
<b>Table 5.4:</b> NF90 characteristics from experiments and literature .....	100
<b>Table 5.5:</b> Comparison of salt rejection for pristine NF90 and zwitterionic hydrogel modified membranes .....	111
<b>Table 5.6:</b> NF270 characteristics from experiments and literature .....	115
<b>Table 5.7:</b> HEMA rejection in dependence of stirring rate .....	116
<b>Table 5.8:</b> Mass transfer coefficient and boundary layer thickness in dependence of stirring rate .....	117
<b>Table 5.9:</b> Free bulk gelation conditions .....	119
<b>Table 5.10:</b> Feed water parameters in NF270 modification with const. TEMED feed concentration (0.06 wt.%) .....	121
<b>Table 5.11:</b> Estimated concentration in boundary layer in dependence of polymer feed concentration .....	123
<b>Table 5.12:</b> Feed water characteristics for NF270 modification .....	125
<b>Table 5.13:</b> Comparison of salt rejection for pristine NF270 membrane and zwitterionic hydrogel modified membranes .....	143

### 9.3 List of abbreviations

AIBN	=	azobisisobutyronitrile
APS	=	ammonium persulfate
ATP	=	adenosine triphosphate
ATR	=	attenuated total reflection
ATRP	=	atom transfer radical polymerization
BMA	=	N-butylmethacrylate
BSA	=	bovine serum albumin
CBAA	=	carboxybetaine acrylamide
CBMA	=	carboxybetaine methacrylate
CNT	=	carbon nanotubes
CP	=	concentration polarization
CPM	=	cationic polymeric material
DLS	=	dynamic light scattering
DMAc	=	dimethylacetamide
DMAEMA	=	N,N-(dimethylamino)ethyl methacrylate
DNA	=	deoxyribonucleic acid
EfOM	=	effluent organic matter
EPS	=	extracellular polymer substances
FRP	=	free radical polymerization
GO	=	graphene oxide
HEMA	=	hydroxyethyl methacrylate
IEP	=	isoelectric point
IR	=	infrared spectroscopy
MAC	=	methacryloyl chloride
MBAA	=	N,N-methylenbisacrylamide
METMA	=	2-(methacryloyloxy)ethyl trimethylammonium chloride
MF	=	microfiltration
MPC	=	2-methacryloyloxyethyl phosphorylcholine
MPD	=	m-phenylenediamine
MW	=	molecular weight
MWCO	=	molecular weight cut-off
NF	=	nanofiltration
NMR	=	nuclear magnetic resonance
NOM	=	natural organic matter
PA	=	polyamide
PAAm	=	poly(acrylamide)
PBS	=	phosphate buffered saline
P(DMAEMA-co-HEMA)	=	poly(dimethylamino)ethyl methacrylate-co-hydroxyethyl methacrylate
P(DMAEMA-co-MAMMA)	=	poly(dimethylamino)ethyl methacrylate-co-2-methacryloylmethyl methacrylate
PEG	=	poly(ethylene glycol)
PEGMA	=	poly(ethylene glycol methacrylate)

PES	=	poly(ethersulfone)
PMMA	=	poly(methyl methacrylate)
PDI	=	polydispersity index
P(SBMA-co-MAMMA)	=	poly(sulfobetainethylmethacrylate-co-2-methacryloylmethyl methacrylate)
PSPE	=	poly(2-(methacryloyloxy)ethyl dimethyl-(3-sulfopropyl)propanesulfonate)
RFR	=	relative flux reduction
RNA	=	ribonucleic acid
RO	=	reverse osmosis
ROS	=	reactive oxygen species
SBMA	=	sulfobetaine methacrylate
SEC	=	size exclusion chromatography
SEM	=	scanning electron microscopy
SPE	=	2-(methacryloyloxy)ethyl dimethyl-(3-sulfopropyl)propanesulfonate
SPP	=	N-(3-methacryloylimino)propyl-N,N-(dimethylamino)propanesulfonate
TEMED	=	tetramethylenediamine
TFC	=	thin-film composite
THF	=	tetrahydrofuran
TMC	=	trimesoyl chloride
TOC	=	total organic carbon
UF	=	ultrafiltration
VSA	=	vinylsulfonic acid
ZHMM	=	zwitterionic hydrogel modified membrane
ZP	=	zwitterionic polymer

#### 9.4. List of equations

<b>Equation 2.1:</b> Flux through a membrane.....	4
<b>Equation 2.2:</b> Hagen-Poiseuille equation.....	5
<b>Equation 2.3:</b> Flux through an ideal membrane .....	6
<b>Equation 2.4:</b> Fick's Law .....	7
<b>Equation 2.5:</b> Water flux in solution-diffusion model.....	7
<b>Equation 2.6:</b> Salt flux in solution-diffusion model.....	8
<b>Equation 2.7:</b> Darcy's law.....	13
<b>Equation 2.8:</b> Film theory model.....	16
<b>Equation 2.9:</b> Concentration polarization modulus.....	16
<b>Equation 2.10:</b> Concentration polarization modulus for complete rejection.....	17
<b>Equation 2.11:</b> Observed membrane rejection .....	17
<b>Equation 2.12:</b> Real membrane rejection .....	17
<b>Equation 2.13:</b> Mass transfer coefficient dependent rejection relationship.....	17
<b>Equation 2.14:</b> Resistance-in-series model.....	31
<b>Equation 2.15:</b> Darcy's law .....	31
<b>Equation 2.16:</b> Hydraulic permeability .....	32
<b>Equation 2.17:</b> Darcy permeability.....	32
<b>Equation 2.8:</b> Film theory model.....	16
<b>Equation 4.1:</b> Mark-Houwink plot .....	50
<b>Equation 4.2:</b> Viscosity.....	51
<b>Equation 4.3:</b> Shear stress.....	52
<b>Equation 4.4:</b> Shear rate.....	52
<b>Equation 4.5:</b> Complex shear modulus.....	52
<b>Equation 4.6:</b> Damping factor.....	53
<b>Equation 4.7:</b> Water permeability .....	55
<b>Equation 4.8:</b> Calculation of membrane rejection for salts.....	55
<b>Equation 4.9:</b> Calculation of membrane rejection for organic compounds.....	55
<b>Equation 4.10:</b> Maintained permeability .....	57
<b>Equation 4.11:</b> Stirring rate dependency of mass transfer coefficient .....	58
<b>Equation 4.12:</b> Boundary layer thickness.....	58
<b>Equation 4.13:</b> Convectively transported mass towards membrane .....	60
<b>Equation 4.14:</b> Polymer concentration at the membrane surface .....	60
<b>Equation 4.15:</b> Average polymer concentration at the membrane surface .....	60

<b>Equation 4.16:</b> Back diffused mass .....	60
<b>Equation 4.17:</b> Stokes-Einstein equation .....	60
<b>Equation 4.18:</b> Viscosity in dependence of polymer concentration .....	60
<b>Equation 4.19:</b> Net transported mass .....	61
<b>Equation 4.20:</b> Corrected concentration at the membrane surface.....	61
<b>Equation 4.21:</b> Concentration at the membrane surface for next iteration .....	61
<b>Equation 4.22:</b> Feed concentration for next iteration.....	61
<b>Equation 4.23:</b> Linear increase of concentration within boundary layer.....	61
<b>Equation 4.24:</b> Concentration at the beginning of boundary layer.....	61
<b>Equation 4.25:</b> Net mass in boundary layer thickness .....	61
<b>Equation 4.26:</b> Slope of linear concentration increase.....	61
<b>Equation 4.27:</b> Linear corrected concentration at the membrane surface .....	62
<b>Equation 4.28:</b> Relative flux reduction in static protein adsorption .....	62
<b>Equation 4.29:</b> Relative flux reduction in protein filtration.....	63
<b>Equation 4.30:</b> Penetration depth in IR.....	64
<b>Equation 4.31:</b> Helmholtz-Smoluchowski equation.....	65
<b>Equation 5.1:</b> Percentage of HEMA units.....	68
<b>Equation 5.2:</b> Percentage of DMAEMA units.....	68
<b>Equation 5.3:</b> Monomer Conversion .....	68
<b>Equation 5.4:</b> HEMA conversion .....	70
<b>Equation 5.5:</b> Hansen-solubility parameter.....	72
<b>Equation 5.6:</b> PDI.....	73
<b>Equation 5.7:</b> Percentage of methacrylate units.....	77
<b>Equation 5.8:</b> Percentage of HEMA units.....	77
<b>Equation 5.9:</b> Percentage of zwitterionic units .....	78
<b>Equation 5.10:</b> Molecular weight of functionalized polymer.....	79
<b>Equation 5.11:</b> Percentage of ammonium units .....	80
<b>Equation 5.12:</b> Molecular weight of cationic polymer.....	80
<b>Equation 5.13:</b> Storage ratio.....	96
<b>Equation 5.14:</b> Transported mass per membrane area.....	104
<b>Equation 5.15:</b> RFR-permeability trade-off .....	109
<b>Equation 5.16:</b> van't Hoff equation .....	126

## 9.5 List of Symbols

<b>Symbol</b>	<b>Description</b>	<b>Unit</b>
$A$	Area	$m^2$
$A_m$	Water permeability constant	$L/hm^2bar$
$B_m$	Salt permeation constant	$m/s$
$c_f$	Feed concentration	$g/L$
$c_m$	Concentration at membrane surface	$g/L$
$c_m(t_j)$	Concentration at the membrane surface at time interval j	$g/L$
$\bar{c}_m(t_j)$	Average interval concentration	$g/L$
$c_{m,corr}(t_j)$	Corrected concentration at membrane surface at time interval j	$g/L$
$c_p$	Permeate concentration	$g/L$
$d_p$	Pore diameter	$m$
$D_p(t_j)$	Diffusion coefficient of polymer at time interval j	$m^2/s$
$F$	Force	$N$
$G^*$	Complex shear modulus	$Pa\ s$
$G'$	Storage modulus	$Pa$
$G''$	Loss modulus	$Pa$
$h$	Distance between plates	$m$
$J_i$	Transmembrane flux of i	$L/hm^2$
$J_{water}$	Transmembrane water flux	$L/hm^2$
$k$	Mass transfer coefficient	$m/s$
$k'_d$	cell specific mass transfer coefficient	$m/s$
$K$	Mark Houwink constant	$L/g$
$K_B$	Boltzmann constant	$J/K$
$K_{hyd}$	Hydraulic permeability	xxx
$l$	Active layer thickness	$m$
$M$	Molarity	$mol/L$
$m(t_j)$	Convectively transported mass in time interval j	$g$
$m_D$	Back diffused mass	$g$
$\bar{M}_{n,cationic}$	Average molecular weight (number) of PTMAEMA-co-MAHEMA	$g/mol$
$\bar{M}_n$	Average molecular weight (number)	$g/mol$

$\bar{M}_{n,0}$	Average molecular weight (number) of PDMAEMA-co-HEMA	g/mol
$m_{net}(t_j)$	net transported mass at time interval j	g
$\bar{M}_w$	Average molecular weight (weight)	g/mol
$\bar{M}_{n,functionalized}$	Average molecular weight (number) of PSBMA-co-MAHEMA	g/mol
$\overline{MW}_{side-chain}$	Average molecular weight of side-chains	g/mol
$n_i$	Refractive index i	
P	Permeability	L/m <sup>2</sup> h bar
$P_0$	Initial Permeability	L/hm <sup>2</sup> bar
$P_{FF}$	Permeability after fouling filtration	L/hm <sup>2</sup> bar
$P_{mod}$	Permeability after modification	L/hm <sup>2</sup> bar
$P_{SA}$	Permeability after static adsorption	L/hm <sup>2</sup> bar
$P_{water}$	Water Permeability	L/hm <sup>2</sup> bar
pd	Penetration depth IR	m
PDI	Polydispersity index	
R	Normal gas constant	J/Kmol
r	Radius	m
$R_0$	Real rejection	%
$R_a$	Hansen solubility distance parameter	
$R_{ad}$	Resistance caused by adsorbed species	1/m
$R_{cake}$	Resistance caused by cake layer	1/m
$R_{ch}$	Electrical Resistance of channel	$\Omega$
$R_{hyd}$	Resistance caused by hydrogel	1/m
$R_i$	Rejection of compound i	%
$R_m$	Membrane resistance	1/m
$R_{obs}$	Observed rejection	%
$R_p$	Rejection of polymer	%
$R_{pp}$	Resistance caused by plugged pores	1/m
$R_{salt}$	Salt rejection	%
$R_{TOC}$	Total organic carbon rejection	%
$R_{tot}$	Total membrane resistance	1/m
RFR	Relative flux reduction	%
t	Time	s

$t_j$	Time interval j	s
T	Temperature	K
$TOC_f$	TOC concentration feed	g/L
$TOC_p$	TOC concentration permeate	g/L
u	velocity of plate	m/s
$\Delta U_s$	Streaming current	A
$\dot{V}$	Volume flux	L/h
$V(t_j)$	Permeated volume in time interval j	L
$V_\delta$	Volume in boundary layer	L
$\Delta x$	Hydrogel thickness	m
$\alpha$	Mark Houwink constant	
$\gamma$	Shear rate	1/s
$\delta$	Boundary layer thickness	m
$\varepsilon$	Relative permittivity	
$\varepsilon_0$	Vacuum permittivity	F/m
$\varepsilon_{mem}$	Membrane porosity	
$\delta_h$	Hydrogen bond interaction energy	
$\delta_p$	Polar interaction energy	
$\delta_h$	Hydrogen bond interaction energy	
$\zeta$	Zeta potential	V
$[\eta]$	Intrinsic viscosity	L/g
$\eta$	Dynamic viscosity	Pa s
$\eta(t_j)$	Dynamic viscosity at time interval j	Pa s
$\eta_{water}$	Dynamic viscosity of water	Pa s
$\Theta$	angle of incidence	°
$\kappa$	Darcy permeability	m <sup>2</sup>
$\lambda$	Wavelength	m
$\pi$	Osmotic pressure	bar
$\rho_{water}$	Water density	g/L
$\sigma_f$	Conductivity feed	S/m
$\sigma_p$	Conductivity permeate	S/m
$\tau$	Shear stress	Pa
$\omega$	Stirring rate	rpm

**"Der Lebenslauf ist in der Online-Version aus Gründen des Datenschutzes nicht enthalten."**